Wuermian glaciation and climate in the western Mediterranean based on investigations in the mountain chain of Corsica

Dissertation

zur Erlangung des Grades eines Doktors der Naturwissenschaften

der Geowissenschaftlichen Fakultät
der Eberhard-Karls-Universität Tübingen

vorgelegt von
Ingrid Krumrei
aus Köln

2009

Tag der mündlichen Prüfung: 27. April 2009

Dekan: Prof. Dr. Peter Grathwohl

1. Berichterstatter: Prof. Dr. Joachim Kuhlemann

2. Berichterstatter: Prof. Dr. Wolfgang Frisch

Abstract

Based on new reconstructions of the ultimate glaciation and the corresponding ELA depression in Corsica constrained by cosmogenic and luminescence age dating, a new climatic model is evolved for the Last Glacial Maximum (LGM) in the Western Mediterranean.

Dating of Corsican glacial sediments and glacially abraded rock surfaces generally confirmed the previously described four glacier advances during the Wuermian, but revealed mainly younger ages. Large, well preserved moraines and moraine quartets belong to a widespread glaciation that started around 24 kyr and lasted until 19 kyr with subsequent moraine stabilisation by about 18 kyr. This glaciation correlates with the cold phase of Heinrich event (HE) 2 and the LGM of the Mediterranean and the North Atlantic. Two subsequent phases of smaller valley glacier advances from 17 to 14 kyr and from 13 to 11 kyr are correlated with the Oldest (OD) and Younger Dryas (YD) continental cold spells, and marine cold spells of HE1 and HE0. Locally, the Wuermian maximum ice extent precedes the global LGM as in few valleys one or two degraded moraines were found down-valley below LGM moraines. Luminescence dating suggests an age around 30 kyr (HE3) whereas a glacier advance in the early Wuermian (HE6/~MIS4) is not confirmed by age dating. The difference in extent between HE3 and HE2/LGM is quite variable as in some cases the older moraines have a short distance to those of the LGM; in other cases the pre-LGM moraine relics indicate advances 1 – 2.5 km further down-valley. Stronger glacier advances during the penultimate and older glaciations, as postulated in older works particularly for the Rissian (~MIS6), has been substantiated with few more data, but the timing and the extent remain unknown for most of Corsica.

Dating results and mapping enabled a reconstruction of the glacier extent for three phases of the Wuermian glaciation, which are the LGM, the OD, and the YD. These results served as a base for equilibrium line altitude (ELA) reconstructions. With an average ELA of 1573 m the LGM was 9.5 °C colder than the Present, if the effect of precipitation of the ELA was excluded. The temperature lowering in the OD (8.2 °C) and the YD (7.6 °C) show a temperature trend that is mainly in line with that of the sea surface temperature (SST) in the Western Mediterranean. Regional changes in the ELA pattern and their associated first-order de-convolution of underlying temperature and precipitation components of the three cold phases from the LGM over the Oldest to the Younger Dryas revealed a trend towards a dryer Mistral (NW wind) and increasing moisture supply from the SW. The climate reconstructions for the Oldest and Younger Dryas indicate a stepwise transition from full glacial (LGM) to interglacial (Present) atmospheric conditions.

The climatic conditions especially at the margins of the island differ considerably between the LGM and the Present and are explained by changes of the larger scale atmospheric circulation that is reflected by the ELA pattern in Mediterranean scale. All available Mediterranean ELA data were incorporated in a new Mediterranean ELA map of the LGM. The ELA depression as the elevation difference between the ELA in the LGM and at Present was recalculated as temperature draw-down of the higher altitudes and combined with data on LGM cooling at sea level (SST proxies), and low-elevation terrestrial proxy-data, in order to provide direct constraints on the vertical structure of the LGM atmosphere. The glacial SST dropped considerably less than the calculated T_{ELA} over part of the Mediterranean, which has implications for the atmospheric stability, circulation patterns and local precipitation. The new synoptic climate model suggests that cyclones followed preferential

storm tracks across the basin grossly similar to the Present. Due to the more southerly position of the polar front over the western Mediterranean during cold phases like the LGM, northerly polar air outbreaks over the western basin have probably been more frequent and/or persistent than today. The incursion of polar air masses would have favoured convection of moist air in regions with relatively warm SSTs, so that considerable local LGM precipitation can be predicted in eastern and northern Corsica, the Apennines, the Dinarides, and Greece. The observed climate pattern in the LGM could be explained with a frequent occurrence of a strongly sinuous Rossby wave lobe, forming a trough of polar air over the western Mediterranean basin. This setting would have had strong impact on the accumulation of snow, and would superimpose the climatic effects of longer phases of zonal circulation (westerlies) with lower and broadly scattered precipitation.

Zusammenfassung

Neue Rekonstruktionen der letzten Vergletscherung auf Korsika und deren dazugehörige Gleichgewichtshöhenverschiebung, die sich aus Datierungen mit kosmogenen Nukliden und Lumineszenz ergeben, sind die Basis für ein neues Klimamodell des Letzen Glazialen Maximums (LGM) im westlichen Mittelmeer.

Die Datierung korsischer glazialer Sedimente und gletschergeschliffener Gesteinsoberflächen konnte die in älterer Literatur vermutete Anzahl von vier Gletschervorstößen während des Würms bestätigen, ergab jedoch meist jüngere Alter für die einzelnen Vorstöße. Große, gut erhaltene Moränen und vierfach gegliederte Moränen gehören zu einer ausgedehnten Vergletscherung, die um 24 ka begann und bis ungefähr 19 ka dauerte, wobei die anschließende Stabilisierung des Moränenmaterials bis 18 ka dauerte. Diese Vergletscherung korreliert mit der Kaltphase während des Heinrich-Ereignisses (HE) 2 und des LGM sowohl des westlichen Mittelmeeres als auch des Nordatlantiks. Zwei darauf folgende Phasen mit kleineren Talgletschern von 17 bis 14 ka und von 13 bis 11 ka korrelieren mit den kontinentalen Kaltphasen der Ältesten und Jüngeren Dryas sowie den marinen Kaltphasen HE1 und HE0. Lokal ist der weiteste Gletschervorstoß während des Würms älter als das globale LGM, da in einigen Tälern ein oder zwei stark degradierte Moränenwälle unterhalb der LGM Moränen gefunden wurden. Lumineszenzdatierungen deuten auf ein Alter von ungefähr 30 ka (HE3) hin, wohingegen ein Gletschervorstoß im frühen Würm (HE6/~MIS4) nicht mit Datierungen belegt werden konnte. Die Größenunterschiede zwischen den Vorstößen des HE3 und des HE2/LGM sind sehr unterschiedlich. In einigen Fällen liegen die älteren Moränen in kleinem Abstand zu denen des LGM, in anderen Fällen zeigen die älteren Moränenreste Vorstöße bis zu 1 - 2.5 km weiter vor an. Vergletscherungen älter und größer als die des Würm, wie sie in älteren Arbeiten vor allem für das Riss (~MIS6) vorgeschlagen wurden, konnte mit wenigen Altersdaten untermauert werden. Das Alter und die Ausdehnung sind jedoch weiterhin unbekannt.

Mit den Datierungsergebnissen und Kartierungen konnte für drei Phasen des späten Würms die Ausbreitung der Gletscher rekonstruiert werden: für LGM, Älteste Dryas und Jüngere Dryas. Diese Ergebnisse wiederum dienten als Basis für Rekonstruktionen der Lage der Gleichgewichtshöhen (ELA). Mit einer durchschnittlichen Gleichgewichtshöhe von 1573 m war das LGM 9.5 °C kälter als heute. Die Temperaturabsenkungen in Ältester (8.2 °C) und Jüngerer Dryas (7.6 °C) zeigen eine Temperaturentwicklung, die größtenteils mit der der Meerwasseroberflächentempereatur (SST) im westlichen Mittelmeer übereinstimmt. Regionale Veränderungen im ELA Muster der drei Kaltphasen und der ihnen zugrundeliegenden Temperatur- und Niederschlagskomponenten lassen vom LGM über die Älteste Dryas bis zur Jüngeren Dyas eine Entwicklung hin zu trockenerem Mistral (NW Wind) und zunehmend von SW kommender Feuchte erkennen. Die Klimarekonstruktionen für Älteste und Jüngere Dryas zeigen den Übergang von voll glazialen (LGM) zu interglazialen Atmosphärenbedingungen.

Vor allem an den Rändern der Insel unterscheiden sich die klimatischen Bedingungen zwischen LGM und heute deutlich. Sie werden anhand von großräumigen Zirkulationen in der Atmosphäre erklärt, wie sie sich im Mittelmeer-weiten ELA Muster wiederspiegeln. Alle verfügbaren ELA Daten aus dem Mittelmeerraum wurden in einer neuen ELA Karte für das LGM im Mittelmeer zusammengefasst. Die Verringerung der ELA als Höhendifferenz zwischen der ELA des LGM und der heute wurde umgerechnet in eine Temperaturverringerung in hohen Höhen und mit Daten der Abkühlung auf Meerespiegelniveau (SST-Proxies) im LGM und terrestrischen Klimadaten niedrigerer Höhen kombiniert, um direkte Rückschlüsse auf die vertikale Struktur der Atmosphäre

im LGM ziehen zu können. Die glazialen SST sanken in Teilen des Mittelmeeres deutlich weniger als die aus den Gleichgewichtslinien errechneten Temperaturen, was Auswirkungen auf die Stabilität der Atmosphäre, das Zirkulationsmuster und lokale Niederschläge hat. Das neue synoptische Klimamodell deutet darauf hin, dass Tiefdruckgebiete ähnliche Sturmbahnen über das Meeresbecken bevorzugten wie heute. Ausbrüche kalter Nordpolarluft über das westliche Mittelmeerbecken waren durch die südlichere Lage der Polarfront über dem Mittelmeer während Kaltphasen wie des LGM wahrscheinlich häufiger oder ausdauernder als heute. Der Einfall hochreichender Kaltluftmassen würde Konvektion feuchter Luft in Regionen mit relativ warmen SSTs unterstützen, so dass beachtliche lokale Niederschläge im LGM für das östliche und nördliche Korsika, den Appenin, die Dinariden und Griechenland prognostiziert werden. Das beobachtete Klimamuster im LGM könnte mit einem häufigen Auftreten einer stark lobaten Rossby-Welle erklärt werden, die einen Trog polarer Luft über dem westlichen Mittelmeer formt. Dieses Szenario würde einen starken Einfluss auf die Schneeakkumulation haben und klimatische Effekte von längeren Phasen zonaler Zirkulation (Westwinde) mit wenig und weit verteiltem Niederschlag überlagern.

Contents

1. Introduction

Mountain climate reconstructions provide evidence of atmospheric processes at various elevations and contribute a vertical dimension to diverse data sets generated from marine and terrestrial archives from near-coast sites. Palaeoclimate archives from the mountains as ancient alpine glaciers, peat bogs, and freshwater archives thus help to validate atmospheric circulation models of variable resolution, which are used for palaeoclimate reconstructions. Since the use of palaeoclimate reconstructions requires a regionalisation to manage future climate change, there is an increasing interest for a higher spatial resolution of atmospheric circulation models.

The island of Corsica (France) provides important constraints on late Wuermian temperature gradients across Western Europe (e.g., Klaer 1956, Messerli 1967) due to its central position in the western Mediterranean basin (~42º N, 9° E) and its high altitudes up to 2706 m a.s.l. (Mte. Cinto). Modelling of climate in central Europe during the Last Glacial Maximum (LGM) indicates frequent high pressure and dryness in central Europe and a southward shift and intensification of polar front-triggered cyclones (Mediterranean Genoa-type cyclones) (CLIMAP Project 1976, COHMAP Members, 1988, Schäfer-Neth and Paul 2003, Ramstein et al., 2007). As a result, the Central Alps received more precipitation from the south than from the north (Florineth and Schlüchter, 1998, 2000), whereas today the distribution of precipitation at both flanks of the Swiss Alps is almost symmetric (Frei and Schär, 1998). The N-S oriented main drainage divide of Corsica formed an obstacle to the southward shifted and intensified polar front activity, similar to the Apuane Alps in Italy. Hence, the former altitude range of Wuermian glaciers in Corsica can be used to constrain the equilibrium line altitude (ELA), which provides insights into regional precipitation patterns (Kuhlemann et al., 2005a).

The present study shall contribute to a better understanding of mountain glaciation in response to climate change in the Late Pleistocene at various spatial scales. Homogenous geology (quartz- and feldspar-rich crystalline rocks) and prevailing chemical weathering support cosmogenic dating. Preserved moraine ridges partly suitable for dating are the base for a reconstruction of the glaciation along the whole mountain chain. Steep mountainous relief and high altitudes are favourable for valley glacier formation that is particularly suited for equilibrium line altitude reconstruction. Together with a conception of forest history throughout the late Wuermian and Holocene (Reille et al., 1997) these conditions make Corsica a key site for late Pleistocene climate reconstructions of the western Mediterranean. During the Wuermian, rapid western Mediterranean climate changes, as recorded by high-resolution alkenone data, suggest that maximum cooling occurred contemporaneous and casually linked with Heinrich events in the North Atlantic (Cacho et al., 2002). The mountain glaciation in the regions surrounding the western Mediterranean should be correlated with these cold spells, since sea surface temperatures (SSTs) in the Mediterranean are governed by wind (Kuhlemann et al., 2008). This applies particularly to Corsica.

Terrestrial records in the surrounding mountain chains (Pyrenees, western Alps and Apennine) are scarce, and often lack precise dating (^{14}C, luminescence, or terrestrial cosmogenic nuclides (TCN)). Correlation only based on morphological and sedimentological criteria might be inaccurate because they are determined by barely comparable factors like erosion and weathering rates, rock type, tectonic, and primary cover. Correlation of different proxies as well as correlation between different regions requires precise dating. During the last years many studies tried to close the dating gap in the Pyrenees revealing a conflict when correlating the different

"precise" data sets (discussed by Hughes and Woodward, 2008). Radiocarbon and luminescence data suggest a Wuermian maximum ice extent (MIE) preceding the global Last Glacial Maximum (LGM), in several areas by tens of thousand of years (^{14}C: e.g. Reille and Andrieu, 1995; González-Sampériz et al., 2006; luminescence: Sancho et al., 2002, Peña et al., 2004), whereas TCN dating seems to suggest a Wuermian MIE correlating with the global LGM (Pallàs et al., 2007; Delmas et al., 2008). All studies postulate a fast deglaciation and ice retreat into the cirques.

Data from the Maritime Alps and the Italian Apennines are fragmentary. ^{10}Be ages from the Maritime Alps, where the glaciers were part of the main Alpine ice sheet, show a Wuermian MIE around 18 kyr (Granger et al., 2006) which is near the LGM maximum at the northern Alpine margin (Ivy-Ochs et al., 2008). Recessional stages are correlated to the Oldest and Younger Dryas. In the central Italian Apennines ^{14}C ages suggest a Wuermian MIE prior to the global LGM with the advance beginning shortly after Heinrich event 3 (~30 kyr) and reaching its maximum before Heinrich event 2 (~24 kyr) (Giraudi and Frezzotti, 1997). The glaciation on Corsica might be a link between all the three mountain ranges, as the island has an intermediate position.

High mountains building up the largest part of the Corsican Island consist mainly of Variscan granites providing the quartz needed for dating with the cosmogenic nuclide ^{10}Be as well as the feldspar and quartz needed for the luminescence dating. Other typical lithologies like the rhyolites in the north or the metamorphic rocks in the north-west are difficult to date by these methods, as they lack large quartz crystals as well as frequent quartz veins.

Glacial morphology and sediments were mapped by Conchon (Conchon, 1975, 1978, 1979, 1984 – 1989; Conchon et al., 1986) but her glacial chronology lacks precise dating. Several advances are distinguished and correlated on the basis of the topographical position of the moraines and the state of weathering. A rough placement in the international stratigraphy is possible by correlation with lake sediments of Lake Creno dated around 15 kyr B.P. (17 cal. kyr) (Reille, 1975).

In this study, the Wuermian glaciation on Corsica is dated and the climate consecutively deduced from the glacier reconstruction. Dating was done by determining the exposure age of moraine boulders or abraded bed rock with the cosmogenic nuclide ^{10}Be. Additionally, glacial and fluvio-glacial sediments were dated by luminescence. As constrained from the dated glaciers, the glacier extent along the mountain chain was reconstructed by correlating moraines valley-to-valley on the basis of mapping including interpretation of stereo air-photos. The best documented glacier advances again were used to reconstruct equilibrium line altitudes (ELAs). Based on the resulting ELA distribution and a tentative differentiation of precipitation and temperature effects, the ELA depression was transferred into atmosphere cooling at 1500 to 2000 m elevation. This information is interpreted in context of the western Mediterranean by comparing it with marine sea surface temperatures (SST).

Open questions

Four glacier advances during the Wuermian are proposed by Conchon (N4-N7; e.g. 1975) without the possibility of absolute dating. How many glacier advances can be confirmed after dating? At which age? When has the maximum extent happened? Is there a correlation with Heinrich events or Dansgaard-Oeschger stadials of the marine and ice core record? As Conchon postulated also the possibility of glacier advances older than

Wuermian, however without preserved moraines, is it possible to date the corresponding glacial morphology, especially trimlines, or the fluvial terraces?

To get an answer to these questions, bedrock can be dated with ^{10}Be or fluvial sediments with OSL. The applicability of cosmogenic exposure dating strongly depends on the weathering rate. Post-depositional weathering of glacially abraded rock surfaces (roches moutonnées and glacial boulders) is important to obtain meaningful exposure ages. Published mean erosion values for crystalline rocks are mainly less than 10 mm/kyr (e.g. Small et al., 1997), common values used in exposure age studies less than 5 mm/kyr (e.g. Kaplan et al., 2004) or even zero (e.g. Ivy-Ochs et al., 1999; Kelly et al., 2004). The mean erosion rate in Corsican calc-alkaline granites is 15 mm/kyr (Kuhlemann et al., 2007). Which value is reasonable for calculating the exposure ages?

On the base of equilibrium line altitude (ELA) reconstruction, local and regional differentiation of mountain climate in Corsica is reconstructed. From this reconstruction answers to the question about climatic differences between the past and today, e.g. how much lower the temperature was compared to the Present.

Pollen analyses indicate cold and arid climatic conditions during Heinrich events and Dansgaard-Oeschger stadials in the Alboran Sea (Sánchez Goñi et al., 2002), the Spanish Pyrenees (González-Sampériz et al., 2006) and also for southern Italy (Allen et al., 2000). If Heinrich events are linked with glacier advances in Corsica, how would this fit in the context of a generally drier climate while glacier advances need moisture?

2. Geological setting, climate and previous studies

2.1. Topography and geology

The 183 km long and 84 km wide island Corsica is located between 43°01' and 41°22' northern latitude and 8°33' and 9°34' eastern longitude in the western Mediterranean, 180 km from the French and 82 km from the Italian mainland. Towards the south, the island Sardinia is only 12 km away. With a rugged relief, 20 peaks over 2000 m, and an average altitude of 565 m, Corsica is the most mountainous island in the Mediterranean, often referred to as "mountain in the sea". Monte Cinto, with 2706 m the highest peak, lies within 25 km from the western coast.

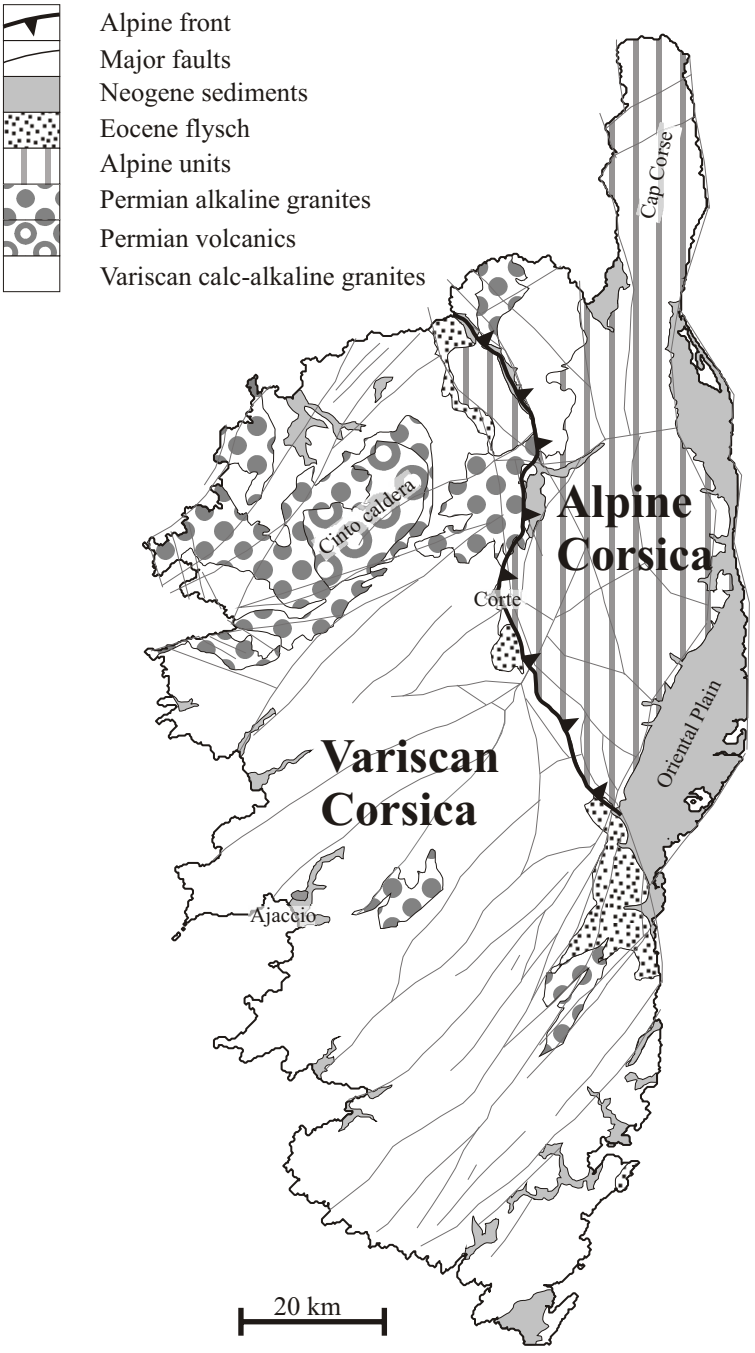

Fig. 1: Schematic map of major lithotectonic units (modified after Rossi et al., 1980) showing the two principal domains in Corsica.

Geographically and geologically, Corsica is divided into two parts (Fig. 1):

1) The western part accounting for nearly 2/3 of the island is called Variscan Corsica, because Variscan crystalline basement rocks prevail. It is mainly composed of unmetamorphosed granitoid rocks, Variscan calc-alkaline granites, Permian alkaline granites, and Permian volcanics (Fig. 1). The latter form the most rugged relief and highest mountains typical of the Cinto massif. Weathering of the granites works mainly by chemical weathering and single grain disintegration (grusification). The weathering rate and the amount of erosion depend not only on climatic conditions but also on lithology and the state of brittle deformation of the granite (Kuhlemann et al., 2007). Lowest values are found in alkaline granites. The calc-alkaline granites show a variation between 9 mm/kyr and 24 mm/kyr with an average around 15 mm/kyr. High values come from samples that reveal a high degree of shearing on microscopic

scale. On the other hand, calc-alkaline granites can be extremely durable, if microscopic cracks are filled with kataklasite and vein quartz strongly cementing the texture as it is normally typical for pseudotachylite. Preservation of glacial striation was observed quite often on these silicified granites.

2) The eastern part, the so-called Alpine Corsica, is a southern extension of the Alpine chain. Similarly, the mountains consist of metamorphic nappe slices originating mostly from oceanic crust and its sedimentary cover (Durand-Delga, 1978, Durand-Delga, 1984). In the east, it is overlain by Neogene sediments forming the Oriental Plain (Fig. 1).

Morphologically, both parts of the island differ strongly. Alpine Corsica is generally characterised by a moderate relief with Monte San Petrone (1767 m) as the highest peak resulting in a significantly lower mean elevation than in the west. In contrast, Variscan Corsica is characterised by high-mountainous relief in wide areas. There, the main valleys with the lowest passes follow NE striking faults (Fig. 1) dividing the ~NW-SE oriented mountain chain into several segments. From north to south these are: Monte Cinto massif – Col de Vergio – Monte Rotondo massif – Monte d'Oro massif – Col de Vizzavona – Monte Renoso massif – Col de Verde – Verde chain, Monte Incudine massif, and Bavella. South of the Bavella, mountains are lower and the landscape is dominated by flat plateaus. The elevation of the mountain peaks generally decreases towards the south.

The steepest relief gradients are found in the NW and the SE of Corsica. The western side of the Cinto massif exposes an elevation rise from coast up to 2700 m in only 24 km distance. The valleys there are narrow and deeply incised having steep head waters and rock walls favoured by the alkaline granite and rhyolite. A similar topography is found on the eastern slope of the Bavella where also alkaline granites crop out. Owing to the steep relief, advection of air masses forces uprise, and torrential rain as well as foehn effects in the lee are frequently observed. The Verde chain and peaks of the Alpine Corsica have a more moderate relief, however with steep topographic gradients, which favour convection close to the shore or the margin of the coastal plain.

2.2. Climate

The present climate in Corsica at sea-level is characterised by subtropic Mediterranean-type conditions with dry and warm summers (May to September) and oceanic-type temperate, wet winters (October-April). Mean annual precipitation is largely controlled by elevation and increases from 600 mm yr^{-1} near the coast to ~1500 mm yr^{-1} at 2000 m a.s.l. (centre and south) and to ~1100 mm yr^{-1} at 2000 m in the north and east (Bruno et al., 2001). The high mountain chain of Corsica forms an obstacle to main paths of Atlantic cyclones, subtropical Mediterranean cyclones from the SW, and locally formed Genoa cyclones. Thus, luv and lee effects are well established, especially in areas with a high relief gradient. The topography-related gradient is up to 50 mm yr^{-1} per 100 m altitude decreasing above 2000 m because of lack of barriers. Main precipitation in the high mountains comes down as snow. Above 1900 m there is a closed snow cover between December and April. Maximum snow thickness is reached in mid March, typically 2 m, much snow accumulates in cirques due to wind. The north-eastern parts of the mountain range are somewhat drier than the central and southern parts. The extent of snow fields in late summer indicates that the highest cirques exposed towards the N to NE typically contain most snow. Remnants of snow frequently outlast the summer. Thunderstorms with heavy rainfall that can cause serious linear erosion of soil and unconsolidated sediment are the main source for precipitation in summer.

During the LGM, western Mediterranean SSTs show largest cooling during the summer season, while winter temperature anomalies were less pronounced (Hayes et al., 2005). Lake level investigations indicate that along a stripe following the winterly subtropical jet (and probably the winterly NW Mediterranean polar jet) climatic conditions were wetter than today in southern Spain and Greece (Harrison et al., 1996). Reduced LGM evaporation from the colder Mediterranean Sea is suggested from studies of the net freshwater budget (Rohling et al., 2008) might also be the reason for higher lake levels. Studies about palynoflora suggest that along the wet stripes winterly precipitation (Oct-April) was about similar to the recent setting, whereas away from these moisture stripes it was drier also in winter times (Peyron et al., 1998; Wu et al., 2007). For the LGM setting of central Corsica such a scenario would mean up to 90 % of the annual precipitation above 1700 m a.s.l. would have fallen as snow (~1300 mm or 4 m of fresh wet snow or 2.5 m typical snow profile).

2.3. Previous studies

2.3.1. Palaeo-glacial studies

At the end of the 19th and the beginning of the 20th century, the first geomorphological observations of glacial relicts on Corsica were published by Pumpelly (1859); Lucerna (1911), and Hollande (1917). In the midst of the 20th century, Klaer (1956), Rondeau (1961) and Michard (1965) described single moraines on the Renoso massif. Systematic research on Corsican Quaternary sediments was done by O. Conchon in the 1970s considering especially the glacial history: Cinto, Rotondo, and d'Oro massif (Conchon, 1975, doctoral thesis); Renoso, Verde, and Incudine (Conchon, 1977; Conchon and Gauthier, 1977); more details as well as corrections were published in the following 20 years (Conchon, 1978, 1979, 1984, 1985, 1986a, 1986b, 1988a, 1988b, 1989, 1999; Conchon et al., 1986). The results of these 30 years of work are summarized in a 1:250,000 geologic overview map (Rossi et al., 1980), and in several 1:25,000 geological map sheets (e.g., Amaudric du Chaffaut et al., 1985; Rossi et al., 1995). Despite Conchon's glacial chronology is the only one existing for Corsica so far, it should be considered as tentative. It is described in the following:

The chronology of glacial advances is based on morphological and sedimentological studies with focus on colour and degree of weathering of the glacial and corresponding fluvial sediments. Morphological indicators are cirques with lakes, polished rock surfaces, U-shaped valley cross-profiles, and longitudinal valley profiles revealing alternation of basins and rock swells. Glacial sediments are divided into glacial deposits and fluvioglacial deposits differing in pebble and boulder shape, sorting, and bedding. Fluvial and marine terrace sediments are also considered.

Seven fluvial terrace levels are the basis for the chronology order (N1 – N7). Since they correlate in their degree of weathering and colour of associated soils as well with marine terraces as with glacial sediments, the stratigraphic order is transferred from fluvial terraces on to the glacial sediments (G3 – G7) (Tab. 1). Conchon circumvents simple numeration by connecting her stratigraphy with dated sediments (Tab. 1): the climatic curve of a marine sediment core off-shore Ajaccio for N5 (middle Wuermian) and N6 (late Wuermian, probably last glacial maximum), amino-stratigraphy and U-Pb ages of palaeostrand-sediments for N4 fluvial sediments (MIS 5e), and pollenstratigraphy and two ^{14}C-ages of a pozzi (peat bog) core for the youngest glacial sediments N7

Tab. 1: Stratigraphy of fluvial and glacial deposits in Corsica based on colour and degree of weathering, and their correlation to the marine oxygen isotope stages, after Conchon (1989).

fluvial terrace	glacial advance	colour, degree of weathering	glacier form	stratigraphy	$\delta^{18}O$ stage
N7		grey, not altered		Holocene	1
	G7		cirque glacier	Oldest Dryas	
N6	G6	grey, not altered	valley glacier	late Wuermian	2
N5	G5	brown, slightly altered	larger valley glacier	middle Wuermian	3
				early Wuermian	4
N4		red, altered	no moraines	last interglacial	5e
N3	G3	red, strongly altered	blocks of Restonica valley	penultimate glacial	6
N2		red, quite strongly altered		glacial	8
N1		red, quite strongly altered (highest terraces)		glacial	10

Tab. 2: Altitudinal position of the N5, N6, and N7 moraines and the estimated ELA for glacier advance N6 of the Corsican mountain massifs following Conchon (1975, 1977).

massif	altitudinal position of moraines [m a.s.l.]			ELA for N6 [m a.s.l.]
	N5	N6	N7	
Cinto/ Rotondo/ d'Oro	900-1000	1100-1200	1700-2100	1700-1800
Renoso	1000-1150	1150-1650		1800-2000
Verde		1200-1400		1600-1700

(Oldest Dryas). N1 – N3 are taken for pre-Wuermian. The best linkage is between the N7 moraine and the peat bog as they are in direct neighbourhood. Relics of glacier advances lower than the N7 advance are additionally sorted by altitudinal position of the moraine (Tab. 2). For the N6 advance, represented by single moraines of medium size, Conchon reconstructed ice margins and permanent snow-lines as well as equilibrium line altitudes (Tab. 2). The larger laterofrontal moraines of the N5 advance which are often staged moraine complexes were not used for any kind of reconstruction.

2.3.2. Dating

All existing absolute datings on Corsica are ^{14}C-ages from peat bogs and lake sediments (Reille, 1975; Reille et al., 1997; Reille et al., 1999 and references therein). The oldest lake sediments come from Lake Creno (1310 m a.s.l.) in the Rotondo massif with an uncalibrated age of 14,560 ± 100 yr B.P. (17,437 ± 139 cal. yr B.P.) that overlay glacial pebbles and sand without organic remains (Reille et al., 1997; Reille et al., 1999). At Lac de Nino (1770 m a.s.l.), the most complete core covers a sequence interpreted as Allerød, Younger Dryas, Preboreal, Atlantic, Subboreal and Subatlantic (Reille, 1975). The peats of the Atlantic part of the sequence have ages of 7,110 ± 80 yr B.P. at the bottom and 6,250 ± 80 yr B.P. in the middle. These ages give an independent time frame for the glaciation of the Tavignano plateau.

3. Methods

Fieldwork and studies of 1:25,000 topographic maps, stereoscopic air photos, and satellite images are the base of all applied methods. In the following chapter, a short introduction into the dating and glacier reconstruction methods is given.

3.1. Dating with terrestrial cosmogenic nuclides

Cosmogenic radionuclides, such as ^{10}Be, are produced in the atmosphere and in mineral lattice by nuclear reactions as a result of bombardment by secondary cosmic rays. Secondary radiation results from initial interactions of primary radiation particles with atoms of the earth's atmosphere. When entering the earth's atmosphere, the primary radiation particles produce cascades of nuclear reactions in which the main part of the secondary particles causes further nuclear reactions. Owing to this cascading, the decrease of the cosmic-ray flux with atmospheric depth is not exactly exponential. Towards the base of the atmosphere, interactions with the atmospheric nuclei then cause a rapid attenuation. As the cosmic particles are charged particles, they are deflected by the earth's geomagnetic field resulting in vertical and horizontal intensity variations. Simplified, the magnetic equator gains high averaged energetic flux, the higher latitudes a wider energy spectrum.

^{10}Be is mainly produced by spallation and muon reactions on ^{16}O and ^{28}Si. Spallation reactions are prevalent energy processes in which a nucleon (mainly neutrons) collides with a target nucleus. As a consequence several lighter particles break from the target nucleus, leaving a lighter residual nucleus. For the production of ^{10}Be in quartz, fast neutrons play the most important role. Muons resemble electrons (both are leptons and negatively charged) but have a much larger mass. Muon-produced cosmogenic nuclides are produced by capture of slow negative muons, to a minor degree by reactions with fast muons. Fast neutrons do not penetrate deeply into the lithosphere since they are highly reactive. Established values for the depth in which the production rate will decrease by a factor of e^{-1} (attenuation length) lie between 150 and 170 g cm^{-2} (Gosse and Phillips, 2001). Muons penetrate much deeper than fast neutrons as their reactivity is low. Their attenuation lengths are 1510 g cm^{-2} for capture of slow negative muons and 4320 g cm^{-2} for fast muon reactions (Heisinger et al., 2002a, and b). Due to the shorter attenuation length of the neutrons, the concentration of cosmogenic nuclides is highest in the upper half metre of the surface, so that samples for exposure dating are taken from the uppermost few centimetres.

Three general methods yield estimates of cosmogenic nuclide production rates: 1) geological calibration (e.g. Ivy-Ochs, 1996; Kubik et al., 1998), 2) experiments (e.g. Nishiizumi et al., 1996), and 3) numerical simulations (e.g. Masarik and Reedy, 1995). The widely used spallogenic production rates are estimates from geological calibration done by measurements of the nuclide concentration in a natural rock surface with a known simple and independently dated exposure history.

Cosmic radiation and hence the production rates of terrestrial cosmogenic nuclides are subject to temporal variations that originate from variations in the intensity of the primary cosmic radiation, changes in the solar modulation of cosmic radiation, changes in the geomagnetic field, variations in atmospheric shielding, and variations in the character of the landform surface over time. As for the first two aspects the influences are either under discussion or seem to average out they are usually assumed to be constant over the exposure time of inter-

est or disregarded, respectively (Gosse and Phillips, 2001). Geomagnetic field changes have to be differentiated into variations in dipole intensity, dipole axis position, and variations in the presence and strength of non-dipole components of the geomagnetic field. To be able to include non-dipole geomagnetic field changes into cosmogenic exposure age calculations the concept of cut-off rigidities is used to describe the shielding effect of the earth‘s magnetic field. Geomagnetic rigidity is the minimum energy a primary proton must have to create a cascade which can reach sea level at that location. It can be understood as an energy filter where the minimum energy equals the numerical value of the cut-off rigidity. Thus, the reconstruction of the cosmic ray flux with the cut-off rigidity includes also non-dipole components.

Corrections for variations in dipole axis position are especially important for exposure ages <10 kyr. For exposure ages >20 kyr the hypothesis of the geocentric axial dipole is generally accepted assuming the identicalness of geographic and geomagnetic poles on long-term averages. Since data are missing for the period from 10 to 20 kyr it is also the best existing estimate for this period (Dunai, 2001)

Records of virtual axial dipole moments (VADM) reproduce the changes in dipole intensity. They are available from palaeomagnetic data sets like the SINT-800 (Guyodo and Valet, 1999). Better resolution for samples younger than 12 kyr give the data set of Yang et al. (2000) and the spherical harmonic field model of Korte and Constable (2005a).

In high latitudes (>60°), the cosmogenic nuclide production rate is insensitive to variations in the terrestrial magnetic field strength since the dipole field lines become steeper near the magnetic poles lowering the particle rigidity. Therefore, the standard ^{10}Be production rate is scaled to sea level in high latitudes (SLHL). Values for SLHL production rates of ^{10}Be in quartz range between 4.74 at g^{-1} yr^{-1} and 6.5 at g^{-1} yr^{-1} (Gosse and Phillips, 2001). As the scaling system for the SLHL production rate has to be the same as for the age calculation, the SLHL production rates for spallation used in the CRONUS-Earth calculator (http://hess.ess.washington.edu) are scaled separately from the existing calibration data sets according to one of their five scaling systems (Balco et al., 2007). Their spallation production rates range between 4.84 at g^{-1} yr^{-1} and 5.39 at g^{-1} yr^{-1}.

Variations in atmospheric shielding due to changing air pressure occur vertically and horizontally and have influence on the amount of radiation reaching the earth’s surface. Most scaling models of the production rate use the global Standard Atmosphere model (1013.25 hPa, 15 °C, 0.0065 °C/km; ISO 2533:1975) for calculating atmospheric depth. Persistent pressure and temperature deviations from the Standard Atmosphere change the production rate what has to be considered mainly if deviations are large. An anomaly of 20-40 hPa results in a 25-30 % different production rate as reported for Antarctica (Stone, 2000). Recent mean sea-level air pressure on Corsica lies between 1015 hPa and 1016 hPa. This deviation from the standard of 1.75-2.75 hPa may cause an error of 2 %. Assuming more frequent cyclones due to a southward shifted polar high the mean annual pressure during the last glaciation should have been lower than today. This lowering is assumed to be in the range of 2-3 hPa resulting in air pressure values quite near the standard. Based on the recent mean sea-level temperature of 16 °C, palaeo-temperatures at sea-level are derived from sea surface temperatures of Hayes et al. (2005). Assuming glacial conditions (1013 hPa, 10 °C) over the whole exposure time would result in ~2.3 % younger ages. Considering the general warming, atmospheric values should better be integrated over time lowering the error to 0.5 % to 1.5 %. Using Standard Atmosphere is therefore an admissible approximation for Corsican atmospheric

values over the last 30 kyr.

The CRONUS-Earth calculator takes account of regional atmospheric variations outside Antarctica by using a recent data set containing the mean sea level pressure and 1000 mbar temperature field (Balco et al., 2007). Using these data with the basic formula of the Standard Atmosphere they achieve a better fit to production rates calculated with the observed pressure at a weather station, get a better estimate of the production rate at high elevations, and are able to improve the match between some scaling systems and the calibration data set. The height-pressure relationship fails in high-relief continental areas (Balco et al. 2007). If one wants to calculate exposure ages in such regions or has indications for persistent air pressure changes in the past, it might be more accurate to use the air pressure of the site instead of elevation.

For exposure age dating, the sea level high latitude (SLHL) production rate has to be adapted to local conditions of the sampling site. As described above the local production rate depends on geomagnetic latitude (often referred to as latitude if position of geomagnetic poles is stable), local geomagnetic field, and altitude, but also on erosion, sample thickness, and shielding by relief, inclination of the sampled surface, sediment, vegetation, and snow. There does not exist a standard procedure for calculating ^{10}Be exposure ages, several are in use. They differ in 1) the way the local production rate is scaled from the SLHL production rate, 2) the SLHL production rate itself, 3) the muon contribution and 4) the choice of correction factors.

Lal (1991) published the first generally accepted scaling system for cosmogenic nuclide production consisting of a set of polynoms with metrical altitude as the only free parameter. The polynoms are empirically fitted to measured „star“ production in the atmosphere, which is assumed to be caused by neutron spallation only. For each ten-degree latitude step, one polynom is given. Lal (1991) hypothesises an additional contribution of 15.6 % of the production rate at sea level due to the capture of slow negative muons. He scaled it vertically as a separate fraction using an attenuation length of 247 g cm^{-2}.

Stone (2000) changed the free parameter of Lal's (1991) scaling system from altitude to atmospheric depth permitting changes in standard atmospheric values. He also calculated a new value of 2.6 % for the contribution of negative muon capture to the total SLHL production rate. This value minimized the error of the mean of all calibration studies for SLHL production rates published until then.

To overcome the problem of interpolation between the ten-degree steps, Dunai (2000) chose two free parameters, geomagnetic inclination, and atmospheric depth for his scaling system which bases on a more extensive database of cosmic ray measurements. Dunai (2001) refined his scaling system by changing geomagnetic inclination into local cut-off rigidity. Using this parameter non-dipole effects as well as temporal changes in the dipole and non-dipole moments can be considered since the local cut-off rigidity directly links field strength and cosmogenic nuclide production. Geomagnetic inclination and horizontal field strength are the two parameters to calculate the cut-off rigidities. Production due to muons in only one fraction, scaled with an atmospheric attenuation length of 247 g cm^{-2}, is still assumed, but in contrast to Stone (2000) the latitude dependence for the negative muon capture and the neutron spallation fractions is treated as the same (Dunai, 2000).

Similar to Dunai (2000, 2001), the scaling system of Desilets and Zreda (2003) has atmospheric depth and local cutoff rigidity as free parameters. It uses more complex fitting functions to a more extensive database and calculates the cutoff rigidity in a different way. The production due to fast muon reactions and capture of slow

negative muons is scaled separately as requested by Heisinger et al. (2002a, b).

By interpolating the lithospheric muon flux to the rock - atmosphere interface, Heisinger et al. (2002a, b) derived SLHL production rates of ^{10}Be in quartz of 0.106 atoms g^{-1} yr^{-1} due to the capture of slow negative muons, and of 0.093 atoms g^{-1} yr^{-1} due to fast muon reactions. In the atmosphere, they consider production due to fast muons to be included in the „star“ production. However, they derive an atmospheric attenuation length of 1463 g cm^{-2} for slow negative muons. The values of Heisinger et al. (2002b) were implemented in another scaling system by Schaller et al. (2002) in which, though, all three production fractions were scaled separately.

Lifton et al. (2005) criticise all existing scaling models that they do not reproduce the natural variability in Earth's cosmic ray environment, because they do not use the full available cosmic ray intensity data. Therefore, they are only able to take account of the spatial and temporal variability in the geomagnetic field, but not the solar modulation of the primary cosmic ray flux and fluctuations in the galactic cosmic ray energy spectrum. The new scaling system includes a new spallogenic nucleon scaling model using a relative solar activity coefficient (Lifton et al., 2005) to describe the influence of the solar activity on in situ cosmogenic nuclide production rates that is largest at high geomagnetic latitudes to which the production rates are normally referenced. Furthermore, new models for scaling fast- and slow muon intensities as well as a model for uncertainties in time-integrated effective vertical cutoff rigidity values are developed by Lifton et al. (2005).

3.1.1. Correction factors

Additionally to the scaling for latitude and altitude, erosion, sample thickness, and shielding should be considered and the standard production rate should be corrected for. For samples from tectonically active areas correction for tectonic uplift has also to be considered. The shape factor (Masarik and Wieler, 2003) is still a controversial correction factor.

Geometric shielding by topographic obstructions as well as by an inclined sampling surface requires correction factors for the production rate P and attenuation length Λ. Maximum flux of cosmic radiation is only given for objects that are located on a flat, planar landform with an unobstructed view of the sky in all directions. Both, surface rate of production and effective attenuation length are changed by geometric shielding. Following Dunne et al. (1999) the correction factor F_P for the production rate is given by equation 1:

$$F_P = 1 - \frac{1}{360°} \sum_{i=1}^{n} \Delta\phi_i \sin^{m+1}\theta_i \quad , \tag{1}$$

and the correction factor for the attenuation length F_Λ is given by equation 2:

$$F_\Lambda = \frac{1 - \sum_{i=1}^{n} \frac{\Delta\phi_i}{360°} \sin^{m+2}\theta_i}{1 - \sum_{i=1}^{n} \frac{\Delta\phi_i}{360°} \sin^{m+1}\theta_i} \quad , \tag{2}$$

where $\Delta\phi_i$ are n equal parts of the azimuth circle for which the mean angle between the horizon and the horizontal is θ_i (Fig. 2A). The exponent m is 2.3 for the neutron component of the cosmic radiation (Nishiizumi et al.,

1989) and around 2.1 for the muon components (Heisinger et al., 2002b). As the model assumption includes production below a horizontal planar surface, an inclined sampling surface needs also correction. The inclined surface itself has a shielding effect as well since the upper part of the surface shields a part of the incident radiation. Furthermore, the normal of the depth penetration is changed from the vertical to the normal of the inclined surface resulting in a somewhat different attenuation length. With an inclined sampling surface calculation of topographic shielding according to equation 1 and 2 requires modification: θ_i has to be measured between the horizon angle of the surface γ and the actual horizon (angle β in Fig. 2B). The horizon angle γ is given by the following relation:

$$\tan\gamma = \cos\phi_\alpha \tan\alpha \quad , \tag{3}$$

where α is the maximum slope angle (dip of the surface) and ϕ_α the azimuth angle with the direction of α (dip direction). Two cases have to be distinguished (Fig. 2B and C): 1) if the horizon angle is larger than α, then the topographic shielding using β and the surface shielding has to be calculated; 2) if α is larger than the horizon angle, only surface shielding has to be taken into account. Equations for shielding of an inclined surface and their graphical solutions are presented in detail by Dunne et al. (1999).

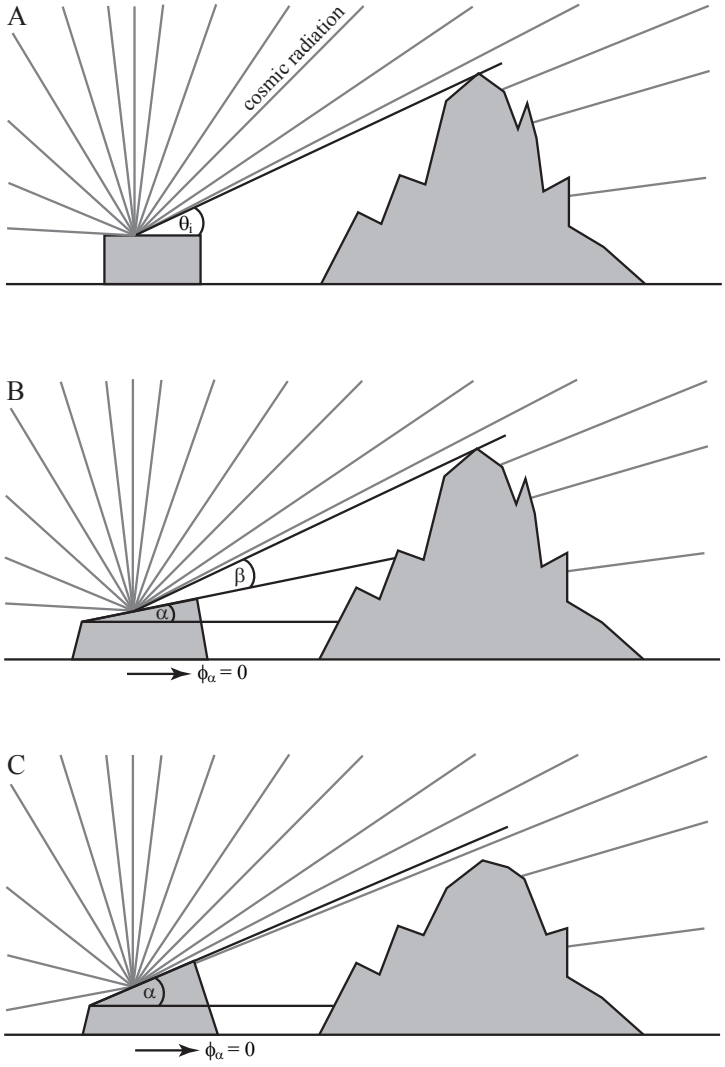

Fig. 2: Schematic illustration of shielding. A: Topographic shielding for a planar surface. B: Topographic shielding for an inclined surface with an inclination angle smaller than the horizon. C: Shielding for an inclined suface with an inclination angle larger than the horizon. See text for explanation of the angles.

Since cosmic radiation particles are absorbed with increasing depth, correction of the production rate is necessary for sample thickness and surface cover. Sediment, vegetation, and snow are typical surface covers. Snow and vegetation have low average densities, their influence can be calculated assuming single exponential decrease of the production. As it is difficult to estimate for older samples, annual average snow cover is mainly considered for Holocene samples where recent data are available. Correction for snow cover is important for polished bedrock surfaces, which are not wind exposed. For boulders it is usually assumed that the snow is blown off by wind. Because of its low density, vegetation cover is commonly also not considered

when calculating the local production rate.

To correct for absorption by high-density covers as soil or sediment and the sample itself a different approach is required. Physical Monte Carlo models of cosmogenic nuclide production in the lithosphere show a relatively flat depth dependence profile in the first 12 g cm^{-2} below the surface-air interface for high-density materials, related to reflection of neutrons at the surface (Masarik and Reedy, 1995). Owing to the increased relative influence of muon reactions (Heisinger et al., 2002a, b) at greater depth, the production profile is not exactly exponential. Schaller et al. (2002) introduced the following equation, which calculates the depth dependence down to a depth of 20 m fitting the evaluated fast and stopped muons depth profile of Heisinger et al. (2002a, and b) to within 1 %:

$$C_{dep} = \left[\left(P_{Nuc}(0) \cdot \sum_{i=1}^{2} a_i e^{\frac{-z\rho}{b_i}} \right) + \left(P_{\mu stopped}(0) \cdot \sum_{j=1}^{3} a_j e^{\frac{-z\rho}{b_j}} \right) + \left(P_{\mu fast}(0) \cdot \sum_{k=1}^{3} a_k e^{\frac{-z\rho}{b_k}} \right) \right] \cdot \frac{\left(1 - e^{-\lambda t}\right)}{\lambda} \quad , \quad (4)$$

where z [cm] is the depth below surface, t [yr] is the time since exposition, ρ [g cm^{-3}] is the rock/sediment density, λ [yr^{-1}] is the decay constant for the nuclide, and $P_{nuc}(0)$, $P_{\mu stopped}(0)$ and $P_{\mu fast}(0)$ [atoms g^{-1} yr^{-1}] are the local surface production rates of cosmogenic nuclides by spallation, stopped and fast muons, respectively: $a_{i,j,k}$ [dimensionless] and $b_{i,j,k}$ [g cm^{-2}] are coefficients for the depth scaling of the production rates (Appendix 1 of Schaller et al., 2002).

The depth dependency of the production has also to be considered calculating SLHL production rates from geological calibration samples as the measured ^{10}Be concentration comes from the whole sample with its finite thickness. The concentration has to be integrated over sample thickness with a model for the depth profile which can be exponential or not. The ratio of the measured concentration to the calculated profile is then the production rate at surface. Hence, SLHL production rates calculated with an exponential depth dependency should not be corrected using Masarik and Reedy (1995) and Schaller et al. (2002).

3.1.2. Erosion

The age equation is only solvable when one of the two variables, erosion and exposure time, is set to a constant. Calculation of exposure ages is based on the assumption of constant erosion. The erosion rate becomes an increasingly larger factor over time since erosion removes the outermost part of the boulder or bedrock which contains the highest concentrations of cosmogenic nuclides. The difference between “true” exposure age and apparent exposure age (without erosion) increases with increasing erosion rate. Hence, quantifying the erosion rate is essential to correct for this removal. Surface textures like preserved glacial polish are geological evidence that surfaces have not suffered significant erosion. Differences in weathering resistance as shown by quartz-veins protruding from their surrounding host-rock can be used as an approximation for erosion rates if the exposure age of the protruding part is roughly known. The influence of possible past as well as recent vegetation cover on the erosion rate should be considered in the estimation. When no other geological evidence is given, a widely used value for the erosion rate during the last 20 kyr in European alpine environments is 3 mm kyr^{-1} published by Ivy-Ochs et al. (2004).

Independent data of erosion rates for the crystalline rocks indicate that zero erosion and even 3 mm kyr^{-1}

are unrealistic on Corsica (Kuhlemann et al., 2007). With mafic inclusions rising above freshly exposed cal-calkaline granite erosion rates of wind-exposed insolated roches moutonnées could be determined in the range of 6 mm kyr^{-1} for the last 5000 years. Kuhlemann et al. (2007) observed ^{10}Be erosion rates between 9 and 20 mm kyr^{-1} on continuously exposed rock castles in subalpine altitudes on Corsica. An erosion rate of 10 mm kyr^{-1} means removal of 20 cm in 20 kyr causing a significant apparent younging of exposure ages if the erosion is not considered in the calculation. Serious interpretation problems arise when weathering rates increase to 20 mm kyr^{-1} as the uncertainty becomes so large that the ages are neither precise enough to date short cold events like the Heinrich events nor to distinguish between two temporally close events. The values of 6 and 20 mm kyr^{-1} seem to be rare extreme values and not representative for the sampled boulders and polished rocks. As a compromise, all ages have been calculated with an erosion rate of 10 mm kyr^{-1} if not indicated differently.

3.1.3. Shape factor

Numeric models of the production rate of cosmogenic nuclides show that shape and size of a boulder affects the production rate beyond the self-shielding (Masarik and Wieler, 2003). Neutron flux is lower in targets from non-flat geometries than for those from flat geometries because the number of scattered neutrons lost from the target to the atmosphere is larger in non-flat targets. This effect is largest at the surface of the boulder. Required corrections amount to up to 10-12 % (Masarik and Wieler, 2003) and are so in the same order than other corrections e.g. for snow or vegetation cover or intensity changes of the palaeomagnetic field. These corrections are often not applied because of their small influence on the final exposure age. This might be the reason why the shape factor is discussed controversially and is mainly not used (i.e. the CRONUS-Earth calculator does not include it). It is rather incorporated in the sampling strategy aiming for samples from the inner part of a flat face of a boulder.

3.1.4. Correction for crustal movements

In tectonically active areas scaling for altitude is not enough since the altitude is changing over the whole exposure time. By varying the atmospheric depth in the scaling systems according to the altitude changes crustal movements (mainly uplift) can be integrated into the age calculations. As a first approximation a linear uplift model is feasible. On Corsica there are no indications of significant tectonic uplift during the Quaternary, except for the NW coast where post-Eemian uplift rates reach up to 0.3 mm yr^{-1}, whereas typical rates range between 0.05 and 0.1 mm yr^{-1} (Kuhlemann et al., 2005b).

Glacial isostatic adjustment, mainly isostatic balance of the lithosphere induced by eustatic sea level change or melting ice, could also require correction. Lowering of sea level results in raising of coastal areas what is compensated further inland. Around the watershed where most of the samples come from the inelastic Corsican crust is assumed to minimize this effect. Post-glacial rebound due to melting glacier ice is estimated to amount to 0.5 m (pers. comm. Kuhlemann 2006). Hence, glacial isostatic adjustment was not considered in the age calculation.

3.1.5. Age calculation

All exposure ages of this study are calculated with the CRONUS-Earth online calculator (http://hess.ess.washington.edu/), version 2.1. The calculator is described in detail by Balco et al. (2007). In the following, only the most important aspects are given.

The concentration of cosmogenic isotopes in minerals of exposed rock surfaces increases with time. The exposure age can be calculated by solving the following equation for exposure age T:

$$N = S_{thick} S_G P_{ref,sp,Xx} \int_0^T S_{Xx}(t) e^{(-\lambda t)} e^{\left(\frac{-\varepsilon t}{\Lambda_{sp}}\right)} dt + P_\mu \int_0^T e^{(-\lambda t)} e^{\left(\frac{-\varepsilon t - z/2}{\Lambda_\mu}\right)} dt \quad , \tag{5}$$

where N is the measured nuclide concentration in atoms per gram, S_{thick} the thickness correction, S_G a geometric shielding correction, $P_{ref,sp,Xx}$ the reference production rate due to spallation for scaling scheme Xx in atoms g^{-1} yr^{-1}, $S_{Xx}(t)$ is the scaling factor for scaling scheme Xx, λ the decay constant of the nuclide in yr^{-1}, ε the erosion rate in g cm^{-2} yr^{-1}, λ_{sp} the effective attenuation length for spallogenic production in g cm^{-2}, P_μ the surface production rate in the sample due to muons in atoms g^{-1} yr^{-1}, z the sample thickness in g cm^{-2}, and λ_μ is an effective attenuation length for production by muons in g cm^{-2} (Balco et al., 2007).

Production due to muons is scaled in a single scaling system after Heisinger et al. (2002a, b) using energy-dependent atmospheric attenuation length from Boezio et al. (2000) without considering magnetic field effects on the muon flux. Spallogenic nuclide production is scaled using five different scaling systems according to Stone (2000), Dunai (2001), Desilets et al. (2006), Lifton et al. (2005), and the altitude scaling of Lal (1991) combined with a simple palaeomagnetic correction following Nishiizumi et al. (1989). For the time-dependent scaling systems, a single set of magnetic field reconstructions is used which resembles that used by Lifton et al. (2005) complemented with spherical harmonic field models from Korte and Constable (2005). Sea-level high-latitude (SLHL) ^{10}Be production rates are scaled according to each of these scaling systems (Table 6 in Balco et al., 2007). Depth correction for production by spallation is calculated using an attenuation length value of 160 g cm^{-2} and assuming downward exponential decrease of nuclide production. Samples of this study are normally not more than 2 to 3 cm thick and rock density is estimated with 2.7 g cm^{-3}. Related to the production by muons some simplifications are assumed: it is not affected by topographic shielding, its depth-dependence is exponential with a single attenuation length, and its depth-dependence within the sample is linear.

The online calculator reports two different uncertainties. The ‘internal uncertainty’ is calculated using only the AMS measurement uncertainty in the nuclide concentration. This should be used when comparing samples from a single study area. The ‘external uncertainty’ additionally uses the uncertainty in the spallogenic SLHL nuclide production rate and the uncertainty in the nuclide production rate by muons. This should be used when comparing samples from widely separated locations, or when exposure ages are compared to ages calculated from other dating techniques.

3.1.6. Sample preparation

In this study, quartz is the target mineral used for all samples. The advances of the ubiquitous mineral quartz are its simple mineral chemistry, its high concentration of oxygen as the source of ^{10}Be, and that it incorporates

no Al in its lattice.

Samples of 100-300 g granite were taken from the topmost centimetres of polished bedrock surfaces or of glacial boulders which rise at least 1.5 m, but normally more than 2 m above the surrounding regolith to ensure exposure since deposition. Sampling near edges was avoided since the calculation of the local production rate is only valid for infinite flat areas. The whole rock samples were crushed until all grains were smaller than 630 µm. For further separation, the grain size fraction between 630 and 250 µm was used. Chemical treatments of samples during mineral separation generally followed after Kohl and Nishiizumi (1992). After optical evaluation and XRFA control measurements on Al and trace element contents, the purified quartz samples of 15 to 40 grams were prepared after von Blanckenburg et al. (2004) to extract the Be. The extraction was done under normal laboratory conditions with ultrapure chemicals. A detailed description of the complete preparation routine is given in Appendix A. The AMS measurements were done at the PSI/ETH AMS facility in Zurich. The used ^{10}Be standard (S555) is a secondary standard to the standard material BEST433 (Hofmann et al., 1987).

3.2. Luminescence dating

The phenomenon of luminescence can be observed in many solids. This emission of light is caused by supply of energy and based on the possibility of crystalline electric nonconducting solids to store part of the energy of ionising radiation in the crystal lattice over millions of years and to release part of this energy in form of light after stimulation. Quartz and feldspar are the only minerals showing this phenomenon. Depending on the way of stimulation luminescence is subdivided into thermoluminescence (TL, stimulation by heat), optically stimulated luminescence (OSL, stimulation by visible light) and infrared optically stimulated luminescence (IR-OSL, stimulation by infrared light). In this work the quartz samples are dated with OSL, the feldspar samples with IR-OSL. The basic principles of luminescence methods are explained in the following, the physical basis is explained in Appendix B.

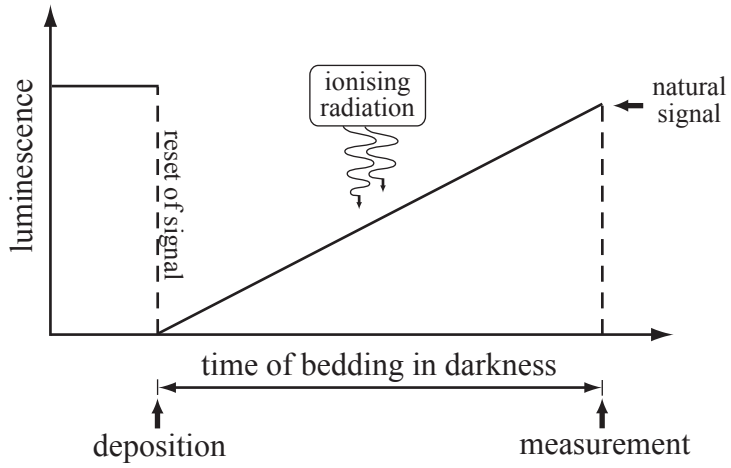

Fig. 3: Dating principle of luminescence dating methods. Reset of signal due to exposition to light, e.g. during (re-)deposition of the sediment, and buildup of the luminescence signal by ionising radiation during the time of bedding in darkness.

3.2.1. Principles of luminescence dating

With luminescence dating methods the depositional time of sediment is determined. Presumption is the complete deletion of the luminescence signal by exposure to light during the transport of the material prior to deposition. Due to ionising radiation a new signal builds up after sediment deposition (Fig. 3).

After optical stimulation in the laboratory, the signal is measured as emission of luminescence. By synthetic radiation with selected dose rates in the laboratory, the build up of the luminescence signal is simulated as well as the rate determined which produces a signal equivalent to the natural luminescence signal (palaeo- or equivalent dose). In addition, the concentration of natural radionuclides within the sediment sample is determined and the cosmic dose rate is estimated, both to be able to calculate the total dose rate. The age of the sample T is calculated using the following equation:

$$T = \frac{D_e}{D_{tot}} \quad , \tag{6}$$

where D_{tot} is the total dose rate [Gy/kyr] and D_e the palaeodose or equivalent dose [Gy]. D_{tot} can be subdivided into the effective dose rate components of α-, β- and γ-rays D_α, D_β, and D_γ, the internal dose rate D_i, and the cosmic ray dose rate D_c changing equation 6 to

$$T = \frac{D_e}{D_\alpha + D_\beta + D_\gamma + D_i + D_c} \quad , \tag{7}$$

3.2.1.2. The palaeodose or equivalent dose D_e

The palaeodose D_e is the dose used in the laboratory which produces a luminescence signal equivalent to the natural signal. Therefore, it is also called equivalent dose. It represents the energy accumulated since the last reset of the signal in the mineral measured in Gray [Gy], with 1 Gy = 1 J kg^{-1}. The luminescence signal of a sample depends on properties characteristic for the mineral as saturation characteristics, stability of the signal and the luminescence capability, i.e. there is not a common relation between equivalent dose and luminescence signal. To investigate the equivalent dose, the functional correlation between the absorbed dose and the intensity of the luminescence has to be determined empirically. This is done by developing a growth curve from laboratory irradiations with distinct doses of the sample split into several parts (aliquots). Generally, additive and

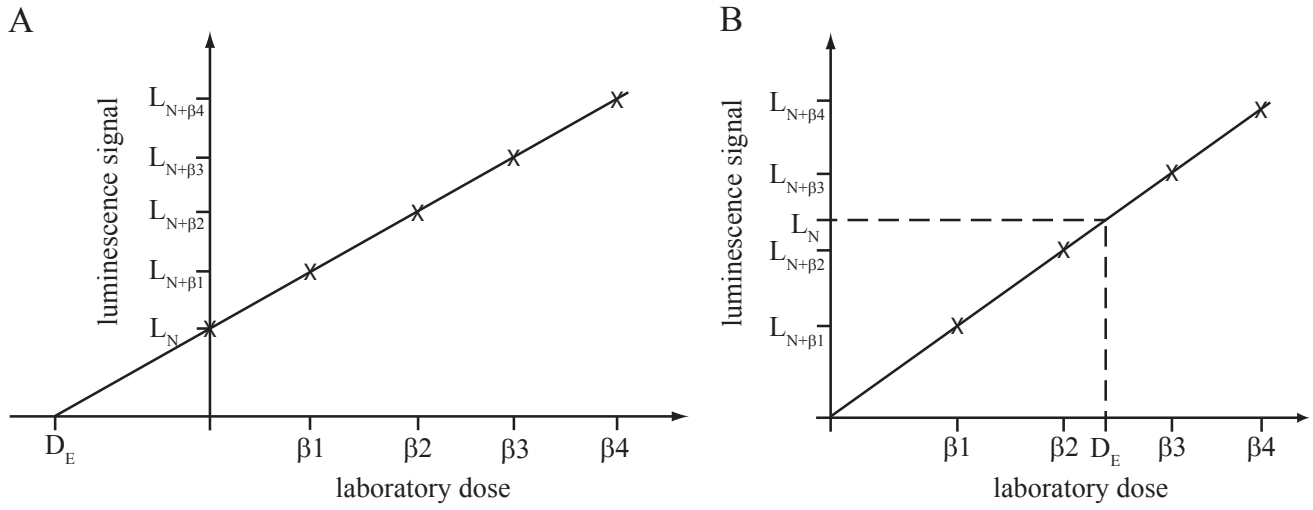

Fig. 4: Schematic illustration of the determination of the palaeodose De with A) additive methods and B) regenerative methods.

regenerative methods are distinguished. The additive methods simulate the aging of a sample in the laboratory. Additionally to the measurement of the natural luminescence signal (L_N), aliquots are irradiated with defined dose rates (β_i) and their luminescence signals ($L_{N+\beta i}$) measured subsequently. Plotting the light signal strength against the laboratory dose and following interpolation gives the growth curve. The equivalent dose is the intersection point of the extrapolated growth curve with the dose axis (Fig. 4A).

Regenerative methods simulate the growth of the luminescence signal after natural resetting under laboratory conditions. A subset of the aliquots is bleached to remove the luminescence signal; the rest is kept as natural reference. The bleached aliquots are grouped and given various doses, until the luminescence signal is reached, that equals the signal of the natural aliquots. The luminescence signal is plotted against the irradiation dose. The intersection point of the growth curve with the natural luminescence signal, plotted on the abscissa, gives the equivalent dose (Fig. 4B).

3.2.1.2. The dose rate

The dose rate is the amount of energy that is saved in the sediment due to the effect of ionizing radiation per mass and time. The unit is Gray/second, with 1 Gy s^{-1} = 1 J kg^{-1} s^{-1}. Sources of ionizing radiation are transformation processes of radioactive nuclides as well as cosmic rays. The calculation of the total dose rate is explained in Appendix D.

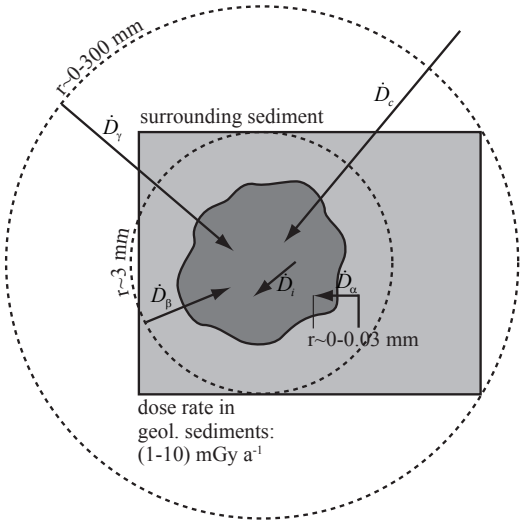

Fig. 5: Components of the dose rate having impact on the mineral grain, and their reach (after Krbetschek, 1995, and Aitken, 1998).

For the dose rate, the radioactive nuclides of the ^{235}U-, ^{238}U- and ^{232}Th- decay chains as well as ^{40}K and ^{87}Rb are important. The decay of these nuclides is connected with the emission of α-, β-, and γ- radiation. As the types of radiation differ basically in characteristics (mass, charge, energy) and range, also their contribution to the dose rate differs. α- (^{4}He) and β- (electron) radiation have short ranges (up to 0.03 mm and up to 3 mm, respectively) whereas the γ-radiation, as a kind of electromagnetic radiation, is absorbed in the material exponentially (Fig. 5). The filling of the pore space is crucial for the range of radiation since different pore fillings absorb each single type of radiation in a different strength. The attenuation effect of water is exceedingly high.

The contribution of the cosmic rays to the dose rate depends on the type of particle, as protons and electrons are absorbed in the uppermost decimetres of the lithosphere, but the higher energetic muons are able to penetrate up to some kilometres and ionize the sediment. As for terrestrial cosmogenic nuclide dating, the intensity of the cosmic rays depends on latitude, altitude and depth below surface.

3.2.2. Sources of error

3.2.2.1. Instability of the signal

Precondition for reliable luminescence dating is the temporal stability of the luminescence signal over the desired period of dating. The stability of the signal is defined by the average residence time of the electrons in the traps which depends on the energy level of the traps, and is affected by the temperature. That is, the lower the temperature of the surrounding and the higher the required activation energy, the larger is the average residence time. The latter should be ten times larger than the period of dating (Aitken, 1998). Beside the deeper traps relevant for dating, the synthetic radiation also occupies traps that are not stable due to their small depth and recombine spontaneously within a short time. To empty these unstable traps, the sample is stored for an adequate time or pre-heated. Recommended values range between 16 hours of storing at 160 °C (Stokes, 1994) and 220 °C for 5 minutes (Roberts et al., 1994). Independently of the mean residence time of the electrons in the traps, anomalous fading, an athermal lost of signal, can occur in feldspars resulting in an underestimation of the age. The origin of this phenomenon is not exactly known. Models under discussion are quantum-mechanical tunnelling (Visocekas, 1985), located transitions (Templer, 1986) and the decay of centres of luminescence (Wintle, 1977). Comparison of luminescence signals of two sets of aliquots radiated with the same dose, measured with delay of several weeks (fading test), is used to test the sample for anomalous fading. Anomalous fading is not observed in quartz (Aitken, 1998).

3.2.2.2. Incomplete bleaching

Requirement of dating methods using luminescence is the complete bleaching (= reset) of the luminescence signal during the transport of sand and silt particles. The degree of bleaching depends on intensity and wavelength of the light as well as the duration of exposure. UV-light bleaches faster than light with long wavelengths (Spooner, 1994). Depending on transport medium different portions of the sun light are effective. Sufficiently bleached with the whole spectrum are normally mineral grains of aeolian sediments. For short transport distances or times, further factors as season, time of day, altitude and cloudiness have to be considered. In full sun-light, the OSL-signal is reduced to 1 % of the original signal after 10 seconds in quartz and after 9 minutes in feldspar, whereas a cloudy sky lengthens the bleaching time (Godfrey-Smith et al., 1988). Furthermore, the mineral grains of the sediment can be differently strongly bleached because some were longer exposed to the light than others. The age of the sediment is overestimated if the incomplete bleaching is not recognised. For multiple-aliquot-methods the test for incomplete bleaching is the plateau-test. Equivalent doses calculated from different integrals of the shine down curve are plotted against time and compared. If the values of the equivalent dose do not significantly differ in between their error, then a plateau exists and the sample is well bleached.

3.2.2.3. Changes in sensitivity

Changes in sensitivity are changes in luminescence characteristics of a mineral grain despite the same applied dose. They are produced by procedures like pre-heating, radiation and stimulation which influence the

grain. The sensitivity is controlled by the degree of activation of the recombination level which in turn depends on temperature. Thus, changes in sensitivity play a role especially in single-aliquot-protocols, where repeated pre-heating procedures lead to increasing sensitivity (Aitken, 1998). Particularly the duration of the impact of temperature seems to be crucial (Wintle and Murray, 1999). In the same way the existence of charges in light sensitive as well as in light insensitive traps affects the sensitivity. Pre-heating induces transitions of charge from shallow and light insensitive traps to light sensitive and thermal stable traps (thermal transfer). This phenomenon is mainly found in quartz.

3.2.2.4. Disequilibria

Since single members of the decay chain have different properties, the equilibrium can be disturbed by physical or chemical processes when isotopes are removed from the system or added. Those disequilibria are a possible source of error for the determination of the dose rate (Krbetschek et al., 1994), since the dose rate cannot be assumed to be constant over the whole dating period. The sample has to be tested for possible disequilibria.

The development of disequilibria is determined by the mobility of the radionuclides. Particularly the 238U-decay chain, one of the three decay chains relevant for the dose rate, has some mobile nuclides causing radioactive disequilibrium. Responsible are the following effects:

- the weaker bond of ^{234}U in the crystal lattice in contrast to ^{238}U due to α-recoil; recoil of ^{234}U into the pore space and preferred hexavalent oxidation state (U^{6+}) favouring the formation of water soluble complexes;
- the limited mobility of ^{230}Th due to easy absorption on minerals;
- the good solubility of ^{226}Ra (disequilibria especially in those parts of the sediment influenced by back- and groundwater), the transport being limited by different effects (e.g. adsorption);
- the high ability of the noble gas ^{222}Rn to migrate;
- the flow of radon from the earth surface into the atmosphere result in a permanent fractionation of ^{222}Rn and ^{210}Pb as the latter is rapidly deposited.

3.2.3. Water content

The latent water in the pore space of the sediment absorbs the ionising radiation partly attenuating the radiation released by radioactive decay. This effect has to be considered since otherwise the age can be misinterpreted. Although the water content can be measured and be used for corrections, this value is not representative over the whole dating period due to seasonal or climatic fluctuations. To get an indication for the possible water content, it can be estimated from the in-situ water content together with the maximum saturation level considering also the geological conditions. The maximum saturation level of the sediment is the total amount of moisture the sediment can contain which can be determined in the laboratory. The dose rates of the single radiation components can then be corrected with a moisture factor (Appendix D).

3.2.4. Sampling

Mainly road cuts or steep walls along rivers provided profiles of glacigenic sediments suitable for luminescence dating. Geographic coordinates were taken from topographic maps, altitudes determined with digital barometric altimeters. Before sampling, the topmost decimetre of the sediment was removed to avoid completely bleached sediment. Sampling was done with steel tubes, 12 cm long and 5 cm in diameter, that were hammered into the sediment. The steel tubes were closed impervious to light. When opened in the laboratory, the outermost centimetres of sediment were discarded since they could have been partly bleached. Determination of total dose rate was done with the coarse sieving residue. Since the in situ water content fluctuates depending on season and/or weather, the water content used for calculation was estimated over the whole expected deposition time.

3.2.5. Sample preparation

20 samples (OSL1-13, 15-21) were prepared and measured at the luminescence laboratory of the GGA Institute Hannover, section Geochronology and Isotope Hydrology. Eight samples (Cruz1-4, Guagno, Guagno-Q, Cann1-3) were prepared and measured at the luminescence laboratory of the Institute of Geography, University of Cologne. All steps of preparation were done under shaded red light to avoid early exposure to light of the mineral grains. Preparation steps with long chemical reaction times were carried out under complete darkness. During sample preparation the sediment material is separated into a fine grained polymineralic fraction and two coarse grained fractions of quartz and feldspar. Finally, the extracted fractions have to be mounted on sample carriers to prepare the aliquots for the luminescence measurements. A schematic description of the preparation procedure is given in Appendix C. For this study, only the coarse grained fraction (quartz and feldspar) between 100 and 200 μm was prepared for dating.

3.2.6. Determination of equivalent dose rates

In the luminescence laboratory of the University of Cologne all luminescence measurements were carried out on automated Risø TL/OSL readers (TLDA-12 or 15, Bøtter-Jensen et al. 2003), equipped with 90Sr/90Y β-sources for irradiation, infra-red (880 ± 80 nm) and blue light emitting diodes (470 ± 30 nm) for optical stimulation of the feldspar and quartz samples, respectively. For detection of the luminescence emissions EMI 9235 photomultiplier tubes were used with two different detection windows; for quartz samples in the UV (290 to 370 nm) and for the feldspars in the violet to blue wavelength range. In order to minimise the possibility of age underestimations caused by the detection of unstable signal components of the feldspar emission as such in the UV band, interference filters were used in all feldspar measurements that allow transmission in a very narrow part of the emission band only (± 410 nm) as recommended by Krbetschek et al. (1997). The 20 samples prepared in the GGA luminescence laboratory in Hannover were measured on automated Risø TL/OSL-DA-15 readers with a filter combination of BG-39 and Corning 7-59 for the feldspars and with filter U-340 for quartz.

The measurement parameters have been determined based on the single aliquot regenerative dose (SAR) protocols described by Murray and Wintle (2000, 2003) for quartz and Wallinga et al. (2000, 2007) for K-rich feldspars in both laboratories. Additionally, in Hannover the feldspars were measured following the multiple

additive aliquot (MAA) protocol with seven regenerative dose steps per five aliquots. Different numbers of D_e values were measured for each sample in Cologne, whereas in Hannover the standard was 25 D_e values per sample. The final value used for age determinations was calculated as median of the dose distributions obtained for the feldspar samples and from the lowest 22 % of the dose distribution for the quartz measured in Cologne. For the Hannover samples, the final D_e value was calculated as the weighted average after elimination of outliers accepting recycling ratios between 0.85 and 1.15.

Prior to the luminescence measurements, all aliquots were preheated in order to remove thermally unstable luminescence signals which are not suitable for dating purposes. These signals are induced by the laboratory irradiation, but due to their thermal instability they are not present in the natural samples, which were irradiated by the environmental dose only. Temperatures for the pre-heat regeneration cycle and the cut-heat test dose cycle for the feldspars were as follows: pre-heat and cut-heat 270 °C (Cologne), pre-heat 290 °C, cut-heat 210 °C (Hannover). For quartz, the following temperatures were used: pre-heat 240 °C, cut-heat 160 °C (Cologne), pre-heat 240 °C, cut-heat 210 °C (Hannover).

Preheat plateau tests and dose recovery tests (DRT = aliquots artificially bleached and irradiated with a defined laboratory β-dose prior to luminescence measurements) provide the basis for setting the measurement parameters. In Cologne, these tests were done for all mineral fractions. In Hannover, two preheat tests and two dose recovery tests were made with feldspars, and five preheat tests and four dose recovery tests with quartz.

3.2.7. Determination of total dose rates

In order to estimate the annual dose derived from the decay of lithogenic radionuclides for the samples measured in Cologne, the concentration of U, Th, and K in the sediment samples was measured by neutron activation analysis (NAA, Becquerel Laboratories, Canada). The results are summarized in Tab. E4. In Hannover, the U-, Th-, and K- concentrations were determined from 50 g sediment with high-resolution low-level gamma spectrometry under the assumption of radioactive equilibrium. The results are summarized in Tab. E7.

The dose rate values shown in Tab. E5 and E7 include the contribution of cosmic rays which was determined for each sample as a function of sampling depth and geographical position according to Prescott and Hutton (1988, 1994). All dose rate values were calculated assuming secular equilibrium for the U and Th decay chains. In contrast to the quartz extracts, the K-rich feldspars have not been etched in HF to remove the outer alpha-irradiated layer. Hence, for feldspar samples the alpha dose contribution has to be included in the dose rate determination using an alpha-efficiency factor of 0.07 ± 0.02 (Cologne, Preusser et al. 2005) and of 0.2 ± 0.1 (Hannover).

For the ^{238}U and ^{232}Th decay chains, NAA gives the concentration of the parent nuclides only. Thus, NAA is not useful in terms of the identification of radioactive disequilibria, which, if present and not corrected for, cause erroneous dose rate calculation and hence, age estimates. While disequilibrium in the ^{232}Th decay chain is unlikely to be important in sediments (a.o. Olley et al., 1996), serious disequilibria in the ^{238}U decay chain are to be expected at sampling sites showing wet conditions (e.g. due to present-day groundwater flow) or which probably have been wet for a significant time in their past. In such a depositional context, disequilibria can occur due to post-sedimentary geochemical processes involving percolating water, or carbonate precipitation or dissolution

(e.g. Krbetschek et al., 1994). As the low-level gamma-spectrometry used for the 20 samples measured in Hannover does not indicate any disequilibrium this is also suggested for the samples measured in Cologne.

Water present in pore voids attenuates the radiation dose to the individual grains more effectively than air. Hence, the overall dose rate is reduced with rising moisture content in the sediments. Therefore the water content of the sediment to be dated has to be taken into account for dose rate calculation. The 'as collected' water content of a sample can be measured and its influence on the radiation attenuation calculated by applying the appropriate attenuation factors. But in terms of dose-rate assessment for dating, the variation in wetness over the whole time-span of burial has to be considered, which is problematic. The uncertainty related with this parameter represents a fundamental limitation in improving the luminescence-age error limits to below the level of about 5 % (Aitken, 1998) as quantification of the range of variations in moisture is almost impossible. Based on field observations and sediment characteristics the dose attenuation was finally calculated assuming moisture content of 20 ± 2 % by weight (Cologne) and 20 ± 5 % by weight (Hannover).

3.2.8. Bleachability

The quartz samples investigated in this study turned out to be less suitable for OSL dating, at least when using the SAR protocol. During the measurements of the eight Cologne samples it revealed that most of the aliquots showed untypical shine down curves. The depletion of the OSL signal was much slower than typically observed for quartz. This slow decay of the OSL intensity can be caused by feldspar contamination of the quartz fraction or feldspar inclusions within certain quartz grains. As feldspar will also emit light when optically stimulated with blue LEDs and generally gives rise to bright luminescence signal even only little contamination causes erroneous equivalent dose estimates. A common test for feldspar contamination is the IR stimulation of the quartz extracts. As pure quartz is insensitive to IR any measurable signal has to be attributed to the presence of feldspars in the sample. The IRSL tests carried out on the samples of this study showed that feldspar contamination is a problem. The slow depletion rate of the OSL signals could also be caused by a lack of the fast OSL component and a dominance of the medium and slow components. The quartz OSL decay curve was found to be rather complicated because of different components contributing to it. Smith and Rhodes (1994) described the OSL emission as the sum of three exponential decay curves, referred to as fast, medium, and slow component according to their relative optical depletion rates. For the successful application of the SAR protocol for OSL dating the quartz sample has to be characterised by a dominant fast component since it is related to the typical trap that is used for OSL dating. Dominance of slow components would cause erroneous equivalent dose estimates when OSL measurements are carried out following the SAR procedure which concentrates on the initial OSL signal intensity and is appropriate only for those samples showing a strong fast component. Application of the SAR protocol to such samples results in an underestimation of the depositional age (Klasen 2007). Despite sample Guagno the SAR procedure is inappropriate for the quartz samples investigated in this study. This result was transferred to the samples measured in Hannover and all of the quartz-SAR ages were discarded.

3.2.9. Fading

The major problem in feldspar dating is the loss of some signal components with time, a phenomenon called anomalous fading (Wintle 1973), which affects feldspars of at least some geological origins and causes an underestimation of the luminescence age if this is not corrected for. Despite a few studies on volcanic quartz that reported fading, it is not known to affect quartz samples (e.g. Duller 2004). Testing of feldspar samples for the occurrence of fading is necessary. But in general the results of such experiments are more qualitative than quantitative. With that it is difficult to correct for fading unless independent age control is available. Nevertheless, several procedures have been suggested that provide a test for the occurrence of fading and, if present, to correct for the signal loss (see for example Auclair et al., 2003, Huntley and Lamothe, 2001, Lamothe et al., 2003). Fading tests have been carried out for two samples, Cruz1 and Cann3, after the protocol of Auclair et al. (2003). With these measurement results the equivalent dose was corrected after Lamothe et al. (2003) and a fading corrected age calculated. For Cruz1 the fading rate is 3.3 % per decade, resulting in a total fading rate of 35 %. As sample Cann3 yielded an old age of >100 kyr, its decadal fading rate of 5.8 % increases the corrected age by 75 %. Whether the corrections make sense in a stratigraphical context is discussed in chapter 4.2.

3.2.10. Age calculation

The final age calculation was done with software “age calculation, version 1999” (Cologne; Grün, 1992) and software “Adele” (Hannover; Degering et al., 2006).

3.3. Equilibrium line altitude

Size and volume of a glacier through past times provide climate signals since they reflect changes in precipitation, temperature, and radiation. A tool for reconstructing former climates in glaciated areas is the glacier equilibrium line altitude (ELA), the position on the glacier where the mass accumulation is equal to the mass loss. The height of the ELA is mainly determined by the amount of snow accumulation and the summer temperature (Loewe, 1971). Moreover, the difference between modern and palaeo-ELA can be interpreted as a proxy for climate change.

Recent glacier ELAs are exactly determined by measuring the glacier mass balance. To estimate ELAs of former glaciers, many methods exist (i.e. Kaser and Osmaston, 2002), of which the most rigorous are based on the reconstructed three-dimensional form of the glacier. Further combination with assumed mass balance – altitude relationships is possible using mass balance gradient and balance ratio (Osmaston, 2005). The mass balance gradient is defined by the ablation and accumulation gradient, what are the rates at which annual ablation and accumulation change with altitude. Generally, these two gradients have different values with the ELA situated at the inflection point (Benn and Evans, 1998). The ratio between the gradients is defined as balance ratio. Non-linearities in the gradients caused by debris cover, shading, proximity to rock walls, altitudinal variations in cloudiness and humidity or avalanche supply are neglected. Despite the balance ratio summarizes the overall mass balance curve of a glacier it is a useful tool to describe the glacier activity. High balance ratios represent

small ablation areas compared with the area of the glacier; lower balance ratios represent larger ablation areas which are less than the half of the whole area. For maritime mid-latitude glaciers in general a value of 2 may be representative (Benn and Evans, 1998)

Methods for reconstructing former glacier ELAs have been subject of several extensive reviews (e.g. Meierding, 1982; Porter, 2001; Kaser and Osmaston, 2002) and will therefore not be discussed in detail here. The two methods used in this study, Accumulation Area Ratios (AAR) and Area-Altitude Balance Ratios (AABR), are shortly discussed below.

3.3.1. AAR method

Under steady-state conditions the accumulation area of the glacier occupies some fixed proportion of the glacier area (Meier and Post, 1962). Steady-state AARs for mid- and high-latitude glaciers lie in the range 0.5-0.8 with typical values between 0.55-0.65 (Porter, 1975). As the value depends on the hypsometry of the glacier surface and debris cover of the tongue, factors that may have changed in the same region through time, the most suitable ratio has to be chosen carefully. The calculation requires the glacier outline and contours as well as a broad hypsometry (distribution of surface area with respect to altitude). Since the typical hypsometry of Wuermian glaciers on Corsica resemble modern glaciers in regions of similar relief in the Alps, an AAR of 0.6 seems to be a reasonable value (Wilhelm, 1975).

3.3.2. AABR method

This method, introduced and developed by Osmaston (1965, 1975), is based on the principle that parts of a glacier which are far above or below the ELA have greater spot net balances. These parts have more influence on the total mass balance of a glacier, and hence on the ELA, than those which are close. Therefore, the AABR method weights the mass balance in areas far above or below the ELA more than in areas close to the ELA using the detailed hypsometry of a glacier (Osmaston, 2005). From the position of the margin of a glacier and the contour data for the ice surface the area and mean altitude of successive contour belts of the ice surface are determined. The mass balance/altitude curve is assumed to consist of two approximately linear segments, usually with different slopes above and below the ELA. The relation between the two slopes is described by the balance ratio (BR). The opportunity of applying any desired BR in the ELA calculation accounts for this fact. Mid-latitude glaciers normally have BRs in the range 1.5-3.5 (Osmaston, 2005). Nevertheless, it is recommended to choose the BR by statistical means (Osmaston, 2005). The BR with the lowest standard deviation of the estimated ELAs should then be used. For the reconstructed Corsican glaciers it appeared that always the lowest BR was the one with the lowest standard deviation. This was the case even for ratios <1 normally attributed to debris-covered glaciers, but there is no evidence of relevant debris-cover on Corsican glaciers. Grouping of the glaciers results in quite small data sets making conclusions from statistical calculations questionable. Finally, a BR of 2 was chosen for the calculation.

3.3.3. Error

Spatial distribution of ELAs is best obtained from medium-sized simply shaped glaciers. Since the data base for a regional reconstruction of the ELA pattern only using simply shaped glaciers would have been quite small also more complex glaciers were used as well as some glacier systems. The resulting ELA for the latter then estimates the average ELA of the whole system.

Nevertheless, ELA reconstructions are quite robust for Alpine-type mountain glaciers (Kerschner et al., 2000), since ±100 m ELA difference means ±200 m elevation difference for the tongue of typical Alpine glaciers, equivalent to ±0.6 ºC temperature difference or +11 %/ -9 % precipitation difference (Ohmura et al., 1992). For smaller glaciers and those with a regular vertical profile and typical shape in map view, the error of the ELA calculation is ±50 m, increasing to ±100 m for large and complex-shaped glaciers.

4. Results and discussion of dating

4.1. Mapping

Fieldwork and studies of 1:25,000 topographic maps, stereoscopic air photos and satellite images enabled to distinguish glacial landforms including trimlines. Observations have been evaluated and compared with published data on glacial and glacio-fluvial deposits (Bieda et al., 1977; Conchon and Gauthier, 1977; Conchon, 1975, 1976, 1977, 1979, 1985, 1986, 1988, 1989) in the field. The trimlines and the moraine limits define highstands of the Wuermian glaciation. Wuermian frontal moraines of large glaciers are poorly preserved in narrow valleys. In such places with poor outcrop conditions moraine deposits are difficult to separate from glacio-fluvial deposits formed in front of glacier tongues (Conchon and Gauthier, 1977). On the other hand, perfect preservation of moraines is observed in wide and flat valleys.

4.2. Dating

Only moraine sequences located in granitic basement areas are potentially feasible for cosmogenic exposure dating. Rhyolitic or metamorphic rocks in Corsica do not provide the free quartz needed for dating with ^{10}Be. Samples have been taken all over the island in crucial settings, some of them as a set from large moraines. Nevertheless, the samples are discussed in groups as all samples from one massif or one large valley system might represent the glacial history over a longer time. In Tab. 3 the results of the exposure dating are summarised, the detailed sample documentation is given in Appendix E.

Dating with luminescence requires complete exposition to sunlight of the sediment before deposition and small grain sizes. Therefore sampling aimed for river terraces, proglacial fluvial sediments with direct relation to preserved moraines, or glacio-fluvial sand lenses in moraines. Sand lenses in moraines may represent deposits of melt water streams typical for temperate glaciers or former proglacial sands incorporated into the moraine during a glacier advance. Since quartz of Corsican rocks is not suitable for luminescence dating (see chapter 3.2.8.) the cross-check between the two minerals quartz and feldspar was not possible to recognise incomplete bleaching or fading in feldspars. Only the comparison with nearby cosmogenic samples allows a quality check. In Tab. 4 the results of the luminescence dating are summarised, the detailed sample documentation is given in Appendix E.

Boulder ages are interpreted as the time of final moraine stabilisation directly following a glacier advance; in contrast ages from polished rock are interpreted as the time of glacier retreat. Proglacial and glacio-fluvial sediments are directly related to glaciers and should therefore give the time of the glaciation. Glacier advances as well as retreat phases should correlate to cold and warm climatic phases, respectively. The last Wuermian cold phases lasting several thousand years are the Last Glacial Maximum (LGM), a chronozone defined by the minimum glacial sea level (Mix et al., 2001), and the Oldest Dryas, originally defined as a European pollen zone ending with the abrupt warming of the Bølling (Tab. 5). Its onset is stated differently in the literature, but might be around 17 kyr (Severinghaus et al., 1998; Stanford et al., 2006). Another pollen zone, the Younger Dryas,

Tab. 3: Sampling location, erosion rate, exposure age (scaling with time-dependent Lal (1991)/Stone (2000) of Balco et al., 2007), and internal and external uncertainty of all dated cosmogenic samples from Corsica.

sample	lat	long	erosion rate	exposure age	uncertainty	
	[°]	[°]	[mm/kyr]	[kyr]	internal [kyr]	external [kyr]
Ku10	42.30	8.88	10	20.5	1.1	2.4
Ku11	42.17	9.10	10	28.4	1.8	3.6
Ku16	42.26	8.93	10	14.6	0.6	1.5
Ku27	42.12	9.13	15	14.1	3.6	3.9
Ku29	42.28	9.11	3	25.0	1.4	2.6
Ku34	42.31	8.95	10	25.9	2.0	3.4
Ku37	42.20	8.92	10	19.3	1.0	2.2
Ku41	42.23	9.06	10	1.7	0.8	0.8
Ku47	42.03	9.19	10	23.1	1.1	2.7
Ku49	41.97	9.09	10	14.5	0.9	1.7
Ku51	42.02	9.11	10	14.8	1.3	1.9
Ku52	42.02	9.11	10	18.2	1.2	2.2
Ku53	42.01	9.10	8	121	14	29
Ku63	42.24	9.06	10	3.2	0.3	0.4
Ku81	41.85	9.18	10	16.9	1.0	1.9
Ku84	41.87	9.18	10	24.1	1.2	2.8
Ku85	42.20	9.05	10	11.7	0.6	1.3
Ku86	42.15	9.06	10	19.4	1.4	2.4
Ku88	42.03	9.15	10	15.5	0.9	1.7
Ku89	42.30	8.88	3	238.7	33.6	50.1
Ku90	42.30	8.90	10	18.6	1.7	2.5
Ku91	42.30	8.90	10	21.1	1.6	2.6
Ku93	42.25	8.96	10	13.9	0.9	1.6
Ku95	42.24	8.98	10	16.9	0.8	1.8
Ku98	42.21	9.06	6	8.1	1.3	1.4
Ku99	42.21	9.06	6	4.1	0.7	0.8
Ku100	42.18	9.06	10	115.2	34.6	39.8
Ku102	42.15	9.08	10	5.2	0.6	0.7
Ku103	42.11	9.12	10	18.1	1.5	2.3
Ku104	42.13	9.13	15	26.0	2.6	4.0
Ku105	42.22	9.02	3	48.3	2.3	5.2
Ku106	42.23	9.09	10	11.2	1.0	1.4
Ku107	42.04	9.14	10	15.6	2.2	2.6
Ku110	42.12	9.12	15	23.2	2.7	3.8
Ku111	42.12	9.12	15	19.4	2.5	3.3
Ku112	42.12	9.12	15	21.3	3.2	4.0
Ku117	42.01	9.23	10	20.3	1.1	2.3
Ku118	42.24	9.06	10	17.7	1.0	2.0
Ku119	42.28	8.93	10	27.9	5.4	6.0
Ku121	42.06	9.13	10	10.5	0.4	1.1
Ku122	42.28	9.11	3	9.5	1.6	1.8
Ku123	42.28	9.00	10	13.2	1.1	1.7
Ku125	42.28	9.01	10	20.0	1.0	2.2
Ku126	42.28	9.02	10	13.8	1.2	1.8
Ku127	42.28	9.02	10	18.1	1.1	2.1
Ku128	42.06	9.13	10	6.5	0.9	1.0
Ku129	42.21	9.06	0	15.3	0.7	1.5
Ku131	42.21	9.06	0	11.1	0.6	1.1
Ku132	42.21	9.03	0	13.8	0.9	1.5
Ku133	42.21	9.02	0	10.1	0.6	1.0
Ku135	42.06	9.17	10	14.3	2.0	2.4
Ku138	42.28	9.01	10	19.5	1.2	2.3
CO-Gro	42.23	9.03	10	2.6	0.4	0.4
CO-Ver	42.30	8.88	10	17.4	1.1	2.0

Tab. 4: Sampling location and feldspar luminescence ages measured with the regenerative single-aliquot (SAR) protocoll and the additive multiple-aliquot (MAA) protocoll.

sample	lat [°]	long [°]	luminescence age			
			Fsp-SAR	error	Fsp-MAA	error
Hannover			[kyr]	[kyr]	[kyr]	[kyr]
OSL1	41°49'04"	9°15'36"	18.9	1.0	16.7	1.1
OSL2	42°06'03"	9°05'41"	19.8	1.0	22.2	1.3
OSL3	42°06'00"	9°06'05"	86.3	5.3	116.0	6.0
OSL4	42°07'39"	9°09'43"	12.0	0.6	10.9	0.7
OSL5	42°12'43"	9°11'43"	-	-	63.4	3.2
OSL6	42°17'33"	9°06'19"	24.6	1.3	27.3	1.5
OSL7	42°12'55"	8°55'26"	78.6	4.6	99.5	5.0
OSL8	42°04'41"	9°11'51"	22.1	1.2	25.8	1.4
OSL9	42°00'23"	9°11'45"	43.0	2.5	47.6	2.4
OSL10	42°14'46"	9°10'25"	23.2	1.3	26.4	1.5
OSL11	42°07'57"	9°08'56"	20.8	1.1	20.3	1.1
OSL12	42°20'16"	9°20'24"	-	-	78.2	4.3
OSL13	42°05'53"	9°13'41"	0.4	0.02	0.3	0.5
OSL15	41°57'54"	9°15'39"	11.7	0.6	13.4	0.7
OSL16	41°59'17"	9°15'38"	30.2	1.7	30.5	1.8
OSL17	41°52'55"	9°16'19"	25.2	1.4	25.5	1.3
OSL18	41°47'27"	9°12'19"	13.5	0.7	14.3	0.8
OSL19	42°02'22"	9°11'43"	29.3	1.7	36.4	2.1
OSL20	42°08'30"	9°06'02"	24.4	1.3	25.6	1.3
OSL21	42°07'04"	9°08'03"	19.7	1.1	22.3	1.2
Cologne						
Cruz1	42°08'30"	9°06'10"	33.6	2.9	-	-
Cruz2	42°08'30"	9°06'10"	30.7	2.2	-	-
Cruz3	42°08'30"	9°06'10"	30.3	3.0	-	-
Cruz4	42°08'30"	9°06'10"	24.8	2.9	-	-
Guagno	42°10'30"	8°54'30"	44.2	3.2	-	-
Cann1	42°03'30"	9°10'20"	15.5	1.7	-	-
Cann2	42°03'30"	9°10'20"	32.7	3.7	-	-
Cann3	42°03'30"	9°10'20"	106.0	11.0	-	-

representing the termination of the last glacial period, is correlated with the youngest Heinrich event. Heinrich events (HEs) are short cold pulses in the North Atlantic Ocean characterised by a high percentage of ice rafted debris in marine sediments. The events are numerated with increasing age (Tab. 5). Reconstructed sea surface temperatures (SSTs) from the Western Mediterranean show minima that correlate well in time and duration with the North Atlantic HEs (Tab. 5; Cacho et al., 2002). As the glaciers in Corsica are mainly relatively small valley glaciers with a high sensitivity to climatic fluctuations, a correlation of the advances with the marine cold phases of the Mediterranean and the North Atlantic is expected.

River terraces form when a large amount of water transports large amounts of sediment. In glaciated areas this happens in larger scale during climatic changes from cold to warm when glaciers disappear and large amounts of melt water transport glacial sediments down-valley. When the glaciers are completely melted, more regular runoff results in incision of the terraces. Luminescence ages of river terraces reflect therefore the timing of the late phase and end of a glaciation. River terraces provide the opportunity to date old glaciations without

Tab. 5: Late Wuermian cold phases in the North Atlantic and the Western Mediterranean

	North Atlantic	Western Mediterranean
LGM chronozone	23-19 kyr[a]	
Oldest Dryas "before Bölling"	~17-14.7 kyr[b,c]	
Youngest Dryas = HE 0	12.7-11.6 kyr[b,c]	12.9-12.1 kyr[f]
HE 1	around 16 kyr[b,d]	16.8-16.2 kyr[f]
HE 2	24.2-23.5 kyr[e] 24.8-24 kyr[d]	24.2-23.5 kyr[f]
HE 3	31-29 kyr[e]	30.9-29.1 kyr[f]

LGM: Last Glacial Maximum; HE: Heinrich event
[a]: Mix et al., 2003; [b]: Stanford et al., 2006; [c]: Severinghaus et al., 1998; [d]: Bond and Lotti, 1995; [e]: Bond et al., 1993; [f]: Cacho et al., 2002

preserved moraines. Older than HE3 are the events HE4, HE5, and HE6 during the middle and early Wuermian: 39.9 – 38.4 kyr and 46.5 – 45.4 kyr for HE4 and HE5 in the Western Mediterranean, respectively (Cacho et al., 2002); HE6 corresponds to the Marine Isotope Stage MIS4, ~68 – 60 kyr. Preceding the Wuermian, the Rissian cold stage (~180 – 140 kyr) is assumed to have left behind preserved river terraces (Conchon 1975, 1989) numbered as local stage N3 (Tab. 1).

In the following, the regional groups are discussed in detail. As recommended by Balco et al. (2007) for comparison of the cosmogenic ages among each other the internal uncertainty is used, the external uncertainty is used when the ages are compared to ages derived from other methods.

4.2.1. Golo valley

In the Cinto massif, moraines are mainly preserved in broader valleys at the eastern and southern side. If there are moraines in the narrow and steep western valleys, they are strongly degraded. All of these moraines consist of rhyolithic debris and boulders and are therefore not suitable for exposure dating. Only the moraines of the Golo valley and its tributary Catamalzi NW and W of the relatively dry and warm Niolu at the southern rim of the Cinto massif consist of granitic material and are well-developed. The samples Ku90 and Ku91 have been taken from the large latero-frontal moraine complex in the Golo valley at 1210 and 1230 m a.s.l., respectively (Fig. 6A). The moraine complex consists of five parallel ridges. Boulder Ku91 is situated slightly off the crest on the outer side of the second ridge, its vertical axis standing above the ground between 1.10 and 4 m (Fig. 6B). The short axis has a length of 0.8 to 1.8 m. This geometry results in a stable position, so that turning of the boulder after deposition seems unlikely. Sample Ku90 was taken from a 4x2x2 m boulder on the fourth ridge (Fig. 6C). At this place, the crest is formed by a row of large glacial boulders. The fine-grained matrix has been washed out, but boulders should have always raised above it for at least 0.8 m. Sample Ku10 was taken from a three metres high boulder at the upper end of the lateral moraine at 1370 m a.s.l. Here, the different ridges merge into one single ridge (Fig. 6A). The glacier tongue might have had the same ice thickness during all advances or the fluctuations were so small that movement of the tongue formed new moraine ridges only at the very end.

The maximum glacier advance in the tributary Catamalzi valley, correlated with the moraine complex in the Golo valley, reached 1300 m as indicated by degraded moraine relicts. At 1550 m, a quite perfect moraine

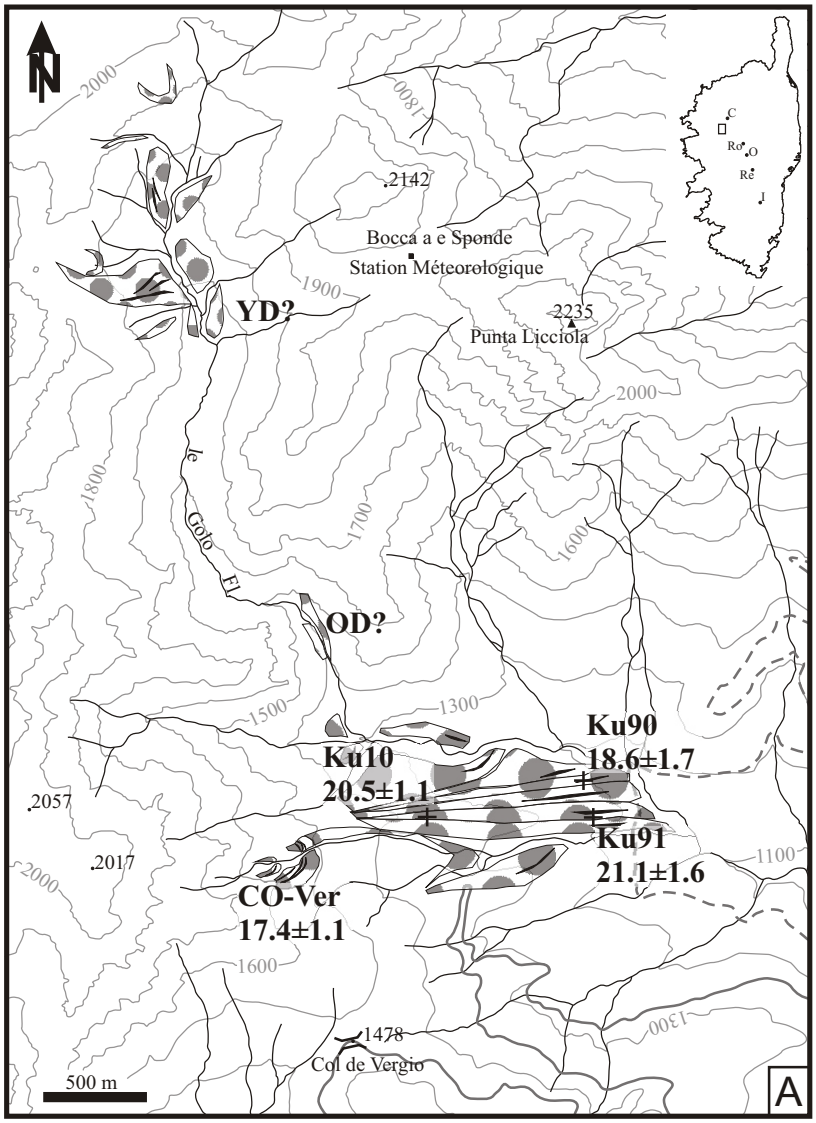

Fig. 6: A: Map of the glacial setting in the Golo valley, southern Cinto massif. B: Boulder Ku91 on the outermost ridge of the Golo moraine. C: The sampled surface of boulder Ku90 is marked by the hammer. D: View towards the NW over the moraine amphitheatre of the Catamalzi tributary, where sample CO-Ver was collected from several calc-alkaline boulders. Legend see Fig. 8.

amphitheatre was formed during a later re-advance (Fig. 6D). The first sample taken on a very large boulder of alkaline granite yielded an age that clearly shows inheritance (Ku89, 238.7 ± 33.6 kyr, Tab. 3). The transport distance in the small catchment may be shorter than 500 m (Fig. 6A). Material for a new sample taken during an excursion in spring 2008 comes from about 20 large boulders of calc-alkaline granite along the moraine ridges. This strategy was chosen as a compromise between having no age or a further age with inheritance which might be an ubiquitous phenomenon difficult to exclude during sampling in such a small catchment. Possible inheritance of single boulders should largely average out. Nevertheless, the age of sample CO-Ver should only be taken as a maximum age estimate.

Sample CO-Ver is expected to give the youngest age, followed by the group of the three samples Ku10, Ku90 and Ku91. The age of ~17 kyr for sample CO-Ver is slightly older than the beginning of HE1 (16.8 kyr) in the western Mediterranean (Cacho et al., 2002) but fits within error. On the other hand it is only slightly younger than the youngest age of the large moraine complex. The deposition of the moraine complex in the Golo valley dates between 18.6 ± 1.7 kyr (Ku90) and 21.1 ± 1.6 kyr (Ku91). The 20.5 ± 1.1 kyr of Ku10 lie in between. The five ridges of the moraine complex represent short-time fluctuations of the glacier over small distances during the LGM with the outermost formed in the middle of the LGM and the innermost at the very end of the LGM. Moraine stabilisation seems to have finished shortly after glacier retreat.

Younger advances leaving glacial sediments behind have been mapped in the upper Golo valley (Fig. 6A). Boulders are either not present or not suitable for cosmogenic dating. Glacial sediments at 1450 m a.s.l. are correlated to the OD. At this site the valley is narrow allowing only a narrow glacier tongue. The small amount of sediments is also poorly preserved. Preserved moraine ridges were found around 1700 m a.s.l., forming a larger complex that is correlated to the YD. Moraine relics and glacial sediments found higher up should therefore reflect Holocene depositional age.

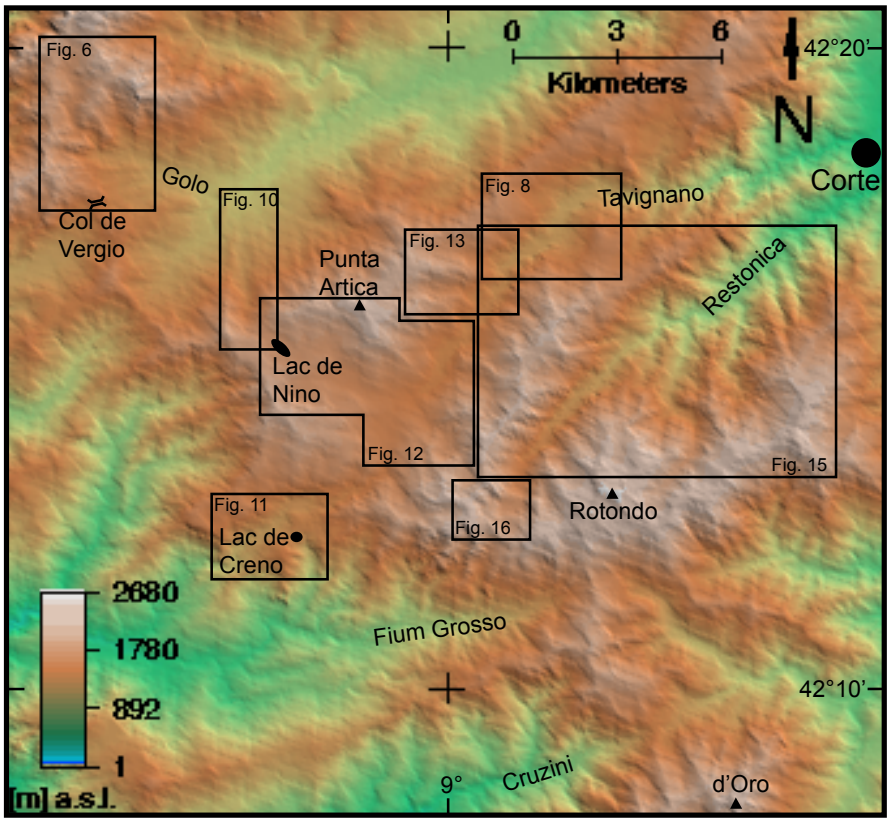

Fig. 7: Topography of the Rotondo massif in central Corsica with the Tavignano plateau in its northern part. Frames show position of following detail maps.

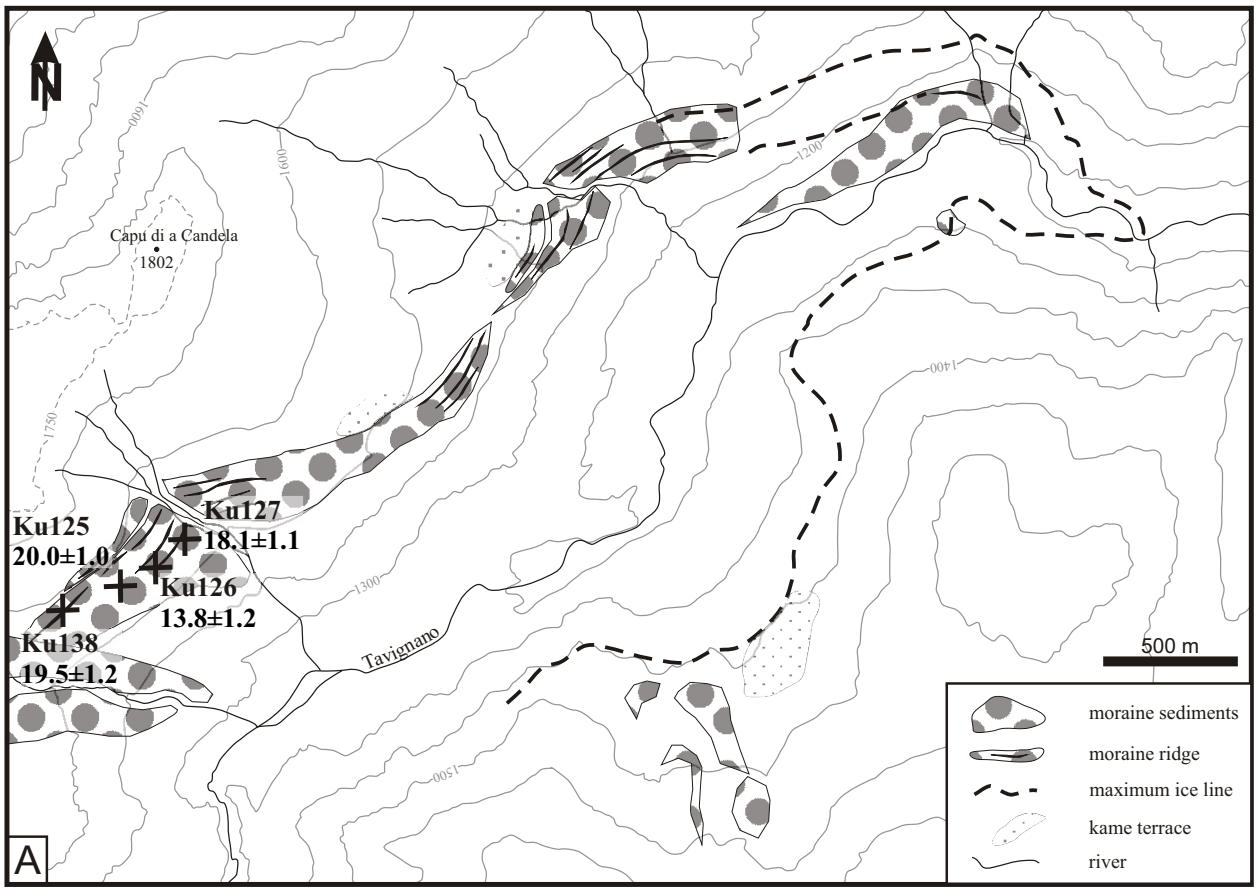

Fig. 8: Lateral moraines of the Tavignano valley. A: Sketch map showing the glacial morphology of the valley, maximum ice extent and the position of the sampled boulders; B: boulder Ku138; C: boulder Ku125; D: boulder Ku126; E: boulder Ku127. All boulders were sampled on the topmost and flattest surface.

4.2.2. Tavignano-Plateau

In the northern Rotondo massif, the headwaters of the Tavignano River have their sources on a partly glacially modified, high elevated palaeosurface with valley floors above 1600 m forming a small plateau, which is surrounded by mountain peaks exceeding 2500 m a.s.l. (Fig. 7). In several tributary valleys as well as on the plateau glacial sediments and/or moraines have been mapped (Figs. 8, 9, 10, 11, 12, 13). The lowest and therefore oldest moraines are in the Tavignano, Colga, and Zoicu valleys resulting in maximum glacier advances reaching 1050, 1000, and 900 m a.s.l., respectively. Five moraine boulders and one bedrock surface were sampled from glacial landforms that are related to the maximum advance. Furthermore, two boulders and one bedrock surface on the plateau and bedrock in a tributary valley were sampled to get information about later re-advances of glaciers.

Boulders Ku125, Ku126, Ku127 and Ku 138 are located on a lateral moraine complex on the northern shoulder of the Tavignano valley, some 350 m above the valley floor at 1550 to 1590 m a.s.l. (Fig. 8A). Downward of the valley shoulder, slopes become progressively steeper and unfavourable for a preservation of lateral moraines. The sampled lateral moraines have been intensively washed out by melt water beside the glacier, which formed kame terraces and left larger boulders as sieve deposits on top of the moraine ridges behind (Fig. 9). The topmost kame terrace is largely covered by regolith which likely migrated under periglacial conditions, due to the fair slope angles. Average boulders on the Tavignano moraines are not larger than 1 m in diameter, but the sampled boulders rise well above the regolith (Fig. 8B, C, D and E). Boulder Ku138 lies on the outmost ridge. This block seemingly exposes in-soil weathering stages of different age, with upward increasing degree of limonite formation at the rock surface. Finally, the block, which had been standing upright, tilted over to the side (Fig. 8B).

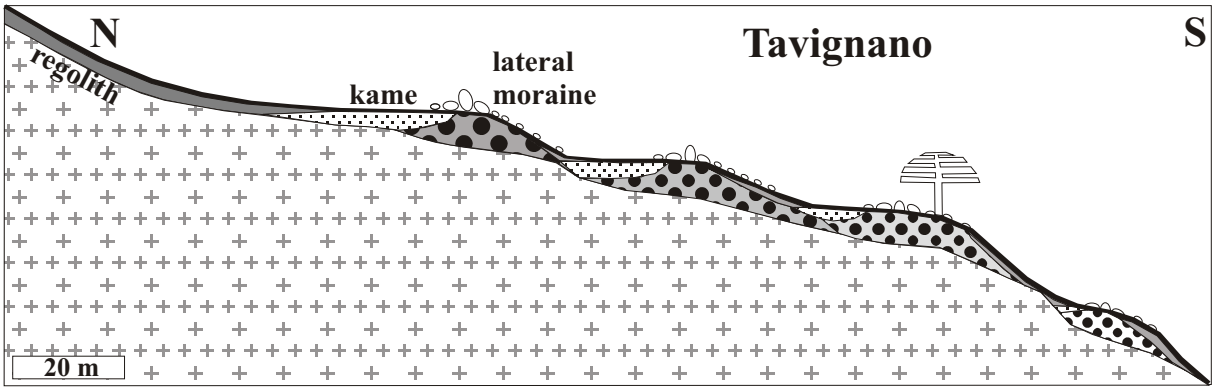

Fig. 9: Profile sketch through the lateral moraines of the Tavignano valley at the sampling site.

The exposure ages of the Tavignano boulders scatter between 18.1 ± 1.1 kyr and 20.0 ± 1.0 kyr indicating deposition and final moraine stabilisation during the late LGM. As the age of 13.8 ± 1.2 kyr for boulder Ku126 lies out of the 1σ-range given by the three other boulders, its too young age requires an explanation. All boulders Ku 125, 126, 127 and 138 lie on one moraine and should therefore show only a small scatter in age. Reasons for exposure ages that are “too young” are spallation, soil cover, boulder movement or tilting due to periglacial processes, or loss of Be during sample preparation. Granites on Corsica weather by grusification, and

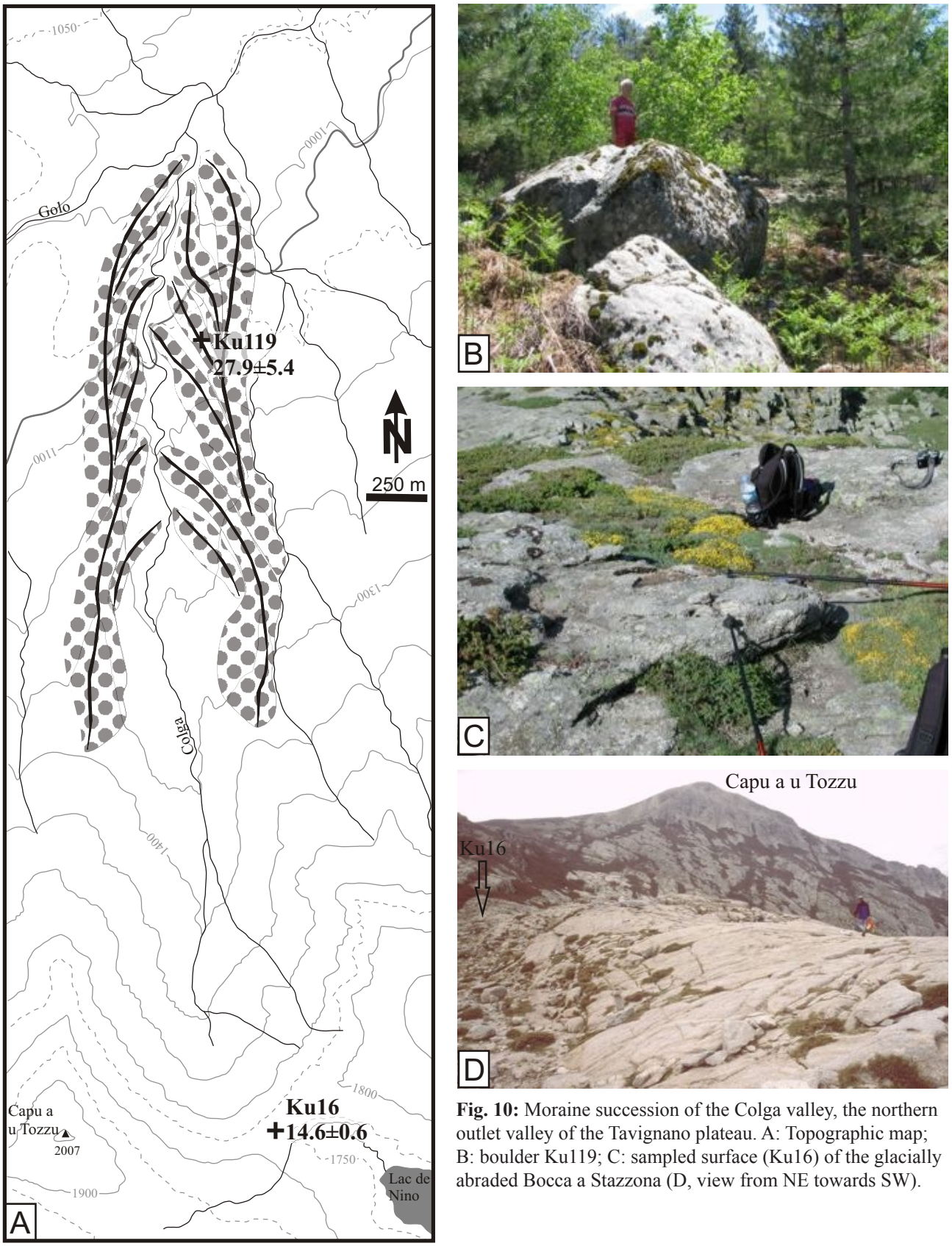

Fig. 10: Moraine succession of the Colga valley, the northern outlet valley of the Tavignano plateau. A: Topographic map; B: boulder Ku119; C: sampled surface (Ku16) of the glacially abraded Bocca a Stazzona (D, view from NE towards SW).

spallation is an untypical process, however observed locally. The sampled surface did not show any indication of spallation. Furthermore, in the case of spallation chips of rock should have been found around the boulder. Soil cover on the boulder would mean that there had been removed an unreasonable high amount of sediment around the boulder since the boulder was exposed to cosmic radiation. There are no hints on loss of ^{10}Be during sample preparation. Toppling is the most possible scenario for boulder Ku126, since it is situated on a slope.

In the Colga valley, the northern outlet of the Tavignano plateau, glaciers deposited six moraine ridges at around 1100 m a.s.l. (Fig. 10A). The two outmost moraine deposits are flat broad ridges which are largely washed out. They reach down to nearly 1000 m a.s.l. The two middle ridges are better preserved, and the two innermost ridges are almost unaltered by periglacial processes. Boulders on all moraine ridges have average diameters smaller than 1 m. Only few of them are larger and hence suitable for sampling. The sampled boulder Ku119 lies on the outmost eastern well-preserved moraine ridge (Fig. 10A). The obtained age of 27.9 ± 5.4 kyr covers a long time span including HE3, HE2 and the beginning of the LGM since the error is quite large due to a high analytical error of 15.6 %. The moraine should have been formed during a cold phase so the obtained age of ~28 kyr cannot be the true age. It is closer to the older Heinrich event but morphological features favour a younger event. This contradicting information does not allow a straightforward interpretation. A possible scenario might be a three-membered formation of the moraine set: The two outmost flat moraines are presumably of middle Wuermian age, the next slightly degraded ridge formed during HE2 followed by three advances of the LGM.

Sample Ku16 from the Bocca a Stazzona (Stazzona pass), yielding an exposure age of 14.6 ± 0.6 kyr was taken from abraded bedrock (Fig. 10C and D). The pass was formed by glacier ice spilling over from the plateau, resulting in a smooth rounded shoulder. Striations are not preserved due to weathering of grusy granite. As exposure ages of bedrock indicate the time when glacial abrasion stopped, the age of sample Ku16 has to be interpreted as the time of glacier retreat. Following this idea, the pass became finally free of ice with the end of the Oldest Dryas. Assuming a thin sediment layer for several thousand years after glacier retreat would result in an age about 1000 years older and therefore does not change the general interpretation.

The entire western outlet valley of the plateau (Zoicu valley, Fig. 11) was filled with ice indicated by glacial sediments forming kame terraces above and west of the Creno Lake and a latero-frontal moraine in the main valley. The ice spilled over local divides in places such as the Creno outlet as the lowermost one. The kame terraces lack boulder cover and the latero-frontal moraine of the Zoicu valley contains few and relatively small boulders not suitable for exposure dating. On the floor of the Zoicu valley bare rock is exposed (Fig. 11B), where glacial striation is visible on the rock surface. At this site, the polished rock has been sampled (Ku37, Fig. 11C), yielding an age of 19.3 ± 1.0 kyr. The age has to be interpreted as the timing of the glacier retreat indicating the final ice retreat from the lower Zoicu valley by the end of the LGM. Possible cover with a thin sediment layer would alter the age for less than 500 years and can therefore be neglected. Maximum extension of the last glacier advance reaching the sampling point with the highest possibility is marked by the blue line in Fig. 11A, mainly based on the form of the latero-frontal moraine. The advance marked by the red line on the lateral moraine/kame terrace might have reached the sampling point with the very end of the glacier tongue, but there is no proof in the morphology or glacial sediments. The oldest lake sediments of Lake Creno, blue inorganic clay, dated with ^{14}C at around 17 cal. yr BP (Reille et al., 1999) support the glacier retreat at the end of the LGM with the two last fluctuations (red and orange line in Fig. 11A) having been considerably smaller than the previous one. Luminescence dating of the moraine failed, as the two feldspar ages of sample OSL7 show a great difference among each other (Fsp-MAA 99.5 ± 5 kyr, Fsp-SAR 78.6 ± 4.6 kyr) and in comparison with the ^{10}Be and ^{14}C ages. Both indicate insufficient bleaching.

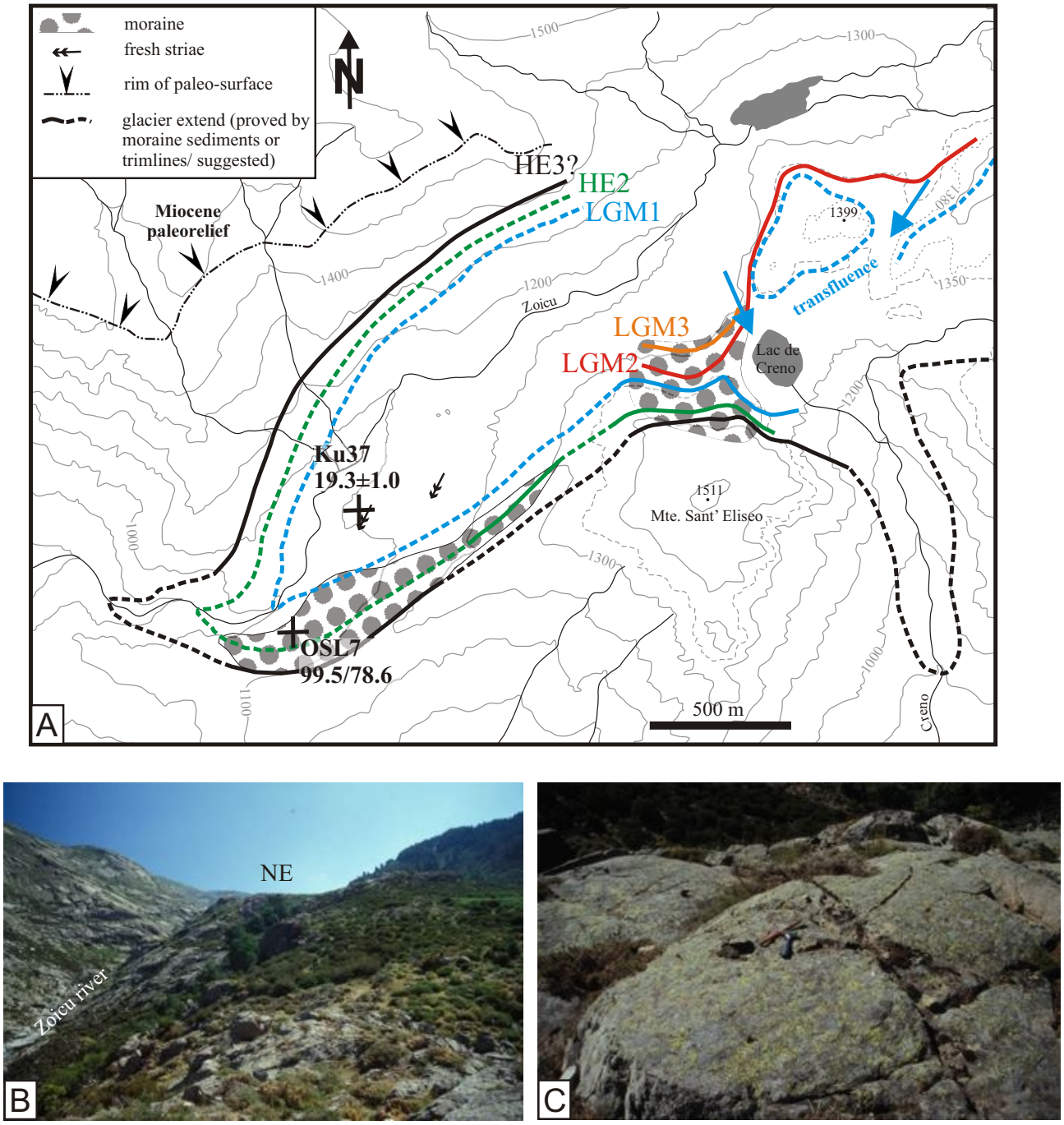

Fig. 11: A) Moraines and different glacier extents deduced from the glacial morphology of the Zoicu valley, the southern outlet valley of the Tavignano plateau. B) View from the sampling site of Ku37 (C) upvalley with the sampled glacially abraded flat.

On the plateau itself, large glacial sediment deposits and moraine complexes were mapped (Fig. 12A). Around 1550 m a.s.l. strongly degraded moraine ridges indicate glaciers coming down the tributary valleys from the SE (Lombarduccio 2261 m, Capu a i Sorbi 2267 m) and the N (southwestern slope of Punta Artica, 2327 m). The glacier tongues just did not meet to form a single tongue. Instead, the moraines interfingered and ponded a shallow glacial lake. Due to the strong degradation the complex set of moraine ridges is better visible on the air photo than in the field where some moraine relicts only consist of arrays of large boulders lying on very flat and broad ridges. The finer material has been washed away.

In addition to sample Ku16 from polished bedrock at Bocca a Stazzona, two samples from boulders were taken to get information about the glacier retreat on the plateau. Sample Ku95 was taken from a large boulder

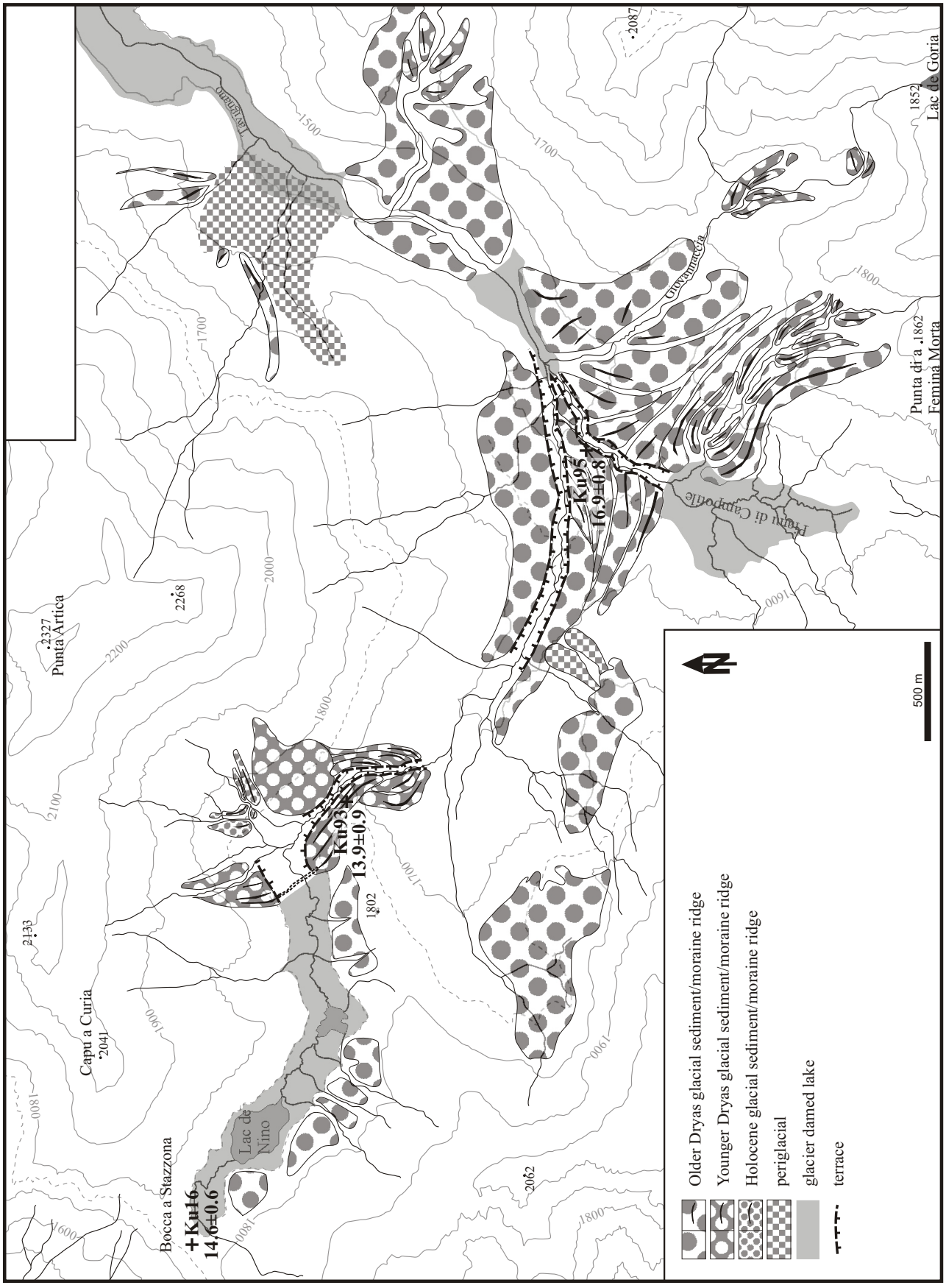

Fig. 12 (continued on next page): A) Moraine complexes and glacial sediment deposits on the Tavignano plateau with sampling sites and glacially ponded lakes. B) Boulders as sieve deposit on degraded moraine ridges of the central part of the plateau among which boulder Ku95 (2x3x3 m) was found. C) View from the Holocene morianes at the W flank of Punta Artica towards the area of the former glacial lake Nino.

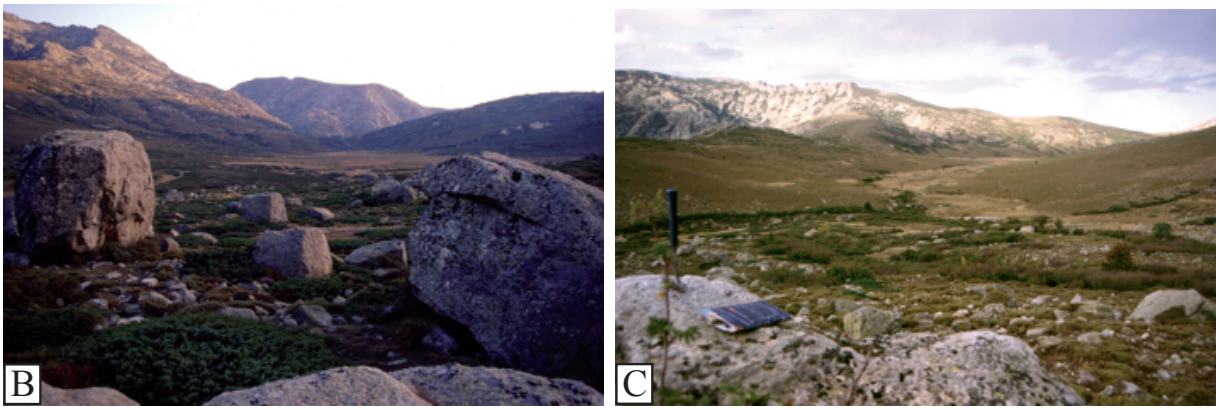

Fig. 12 continued.

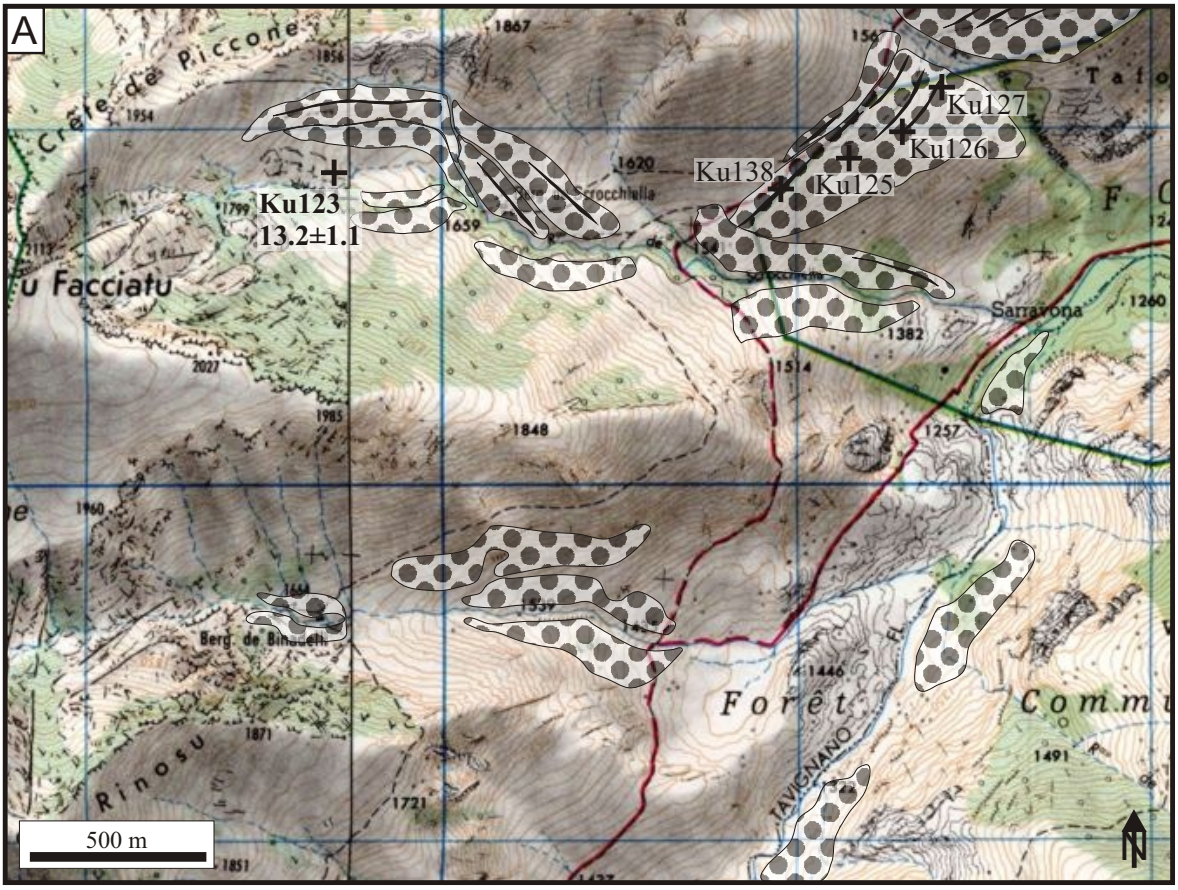

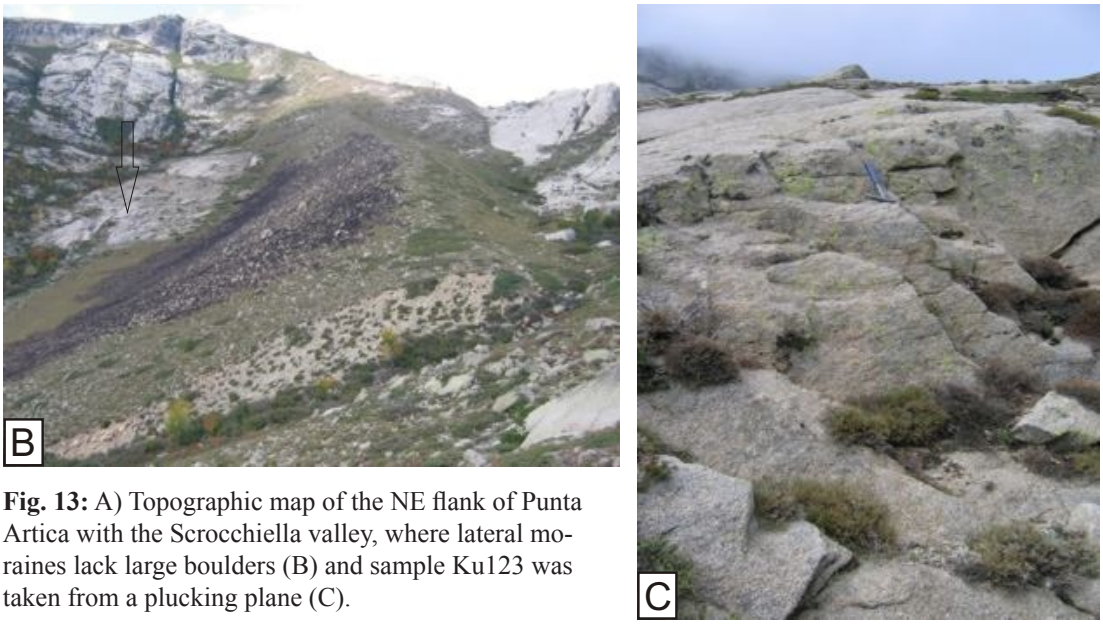

Fig. 13: A) Topographic map of the NE flank of Punta Artica with the Scrocchiella valley, where lateral moraines lack large boulders (B) and sample Ku123 was taken from a plucking plane (C).

(2x3x3 m) on a degraded moraine ridge in the central part of the plateau formed by ice coming down the south-western slope of Punta Artica (Fig. 12A and B). On one of three small degraded latero-frontal moraines 1500 m up-valley sample Ku93 was taken from the largest block. The obtained age of 16.9 ± 0.8 kyr for Ku95 fits well to the HE1 event in the Western Mediterranean (Cacho et al., 2002) but it is also possible that it overestimates the true depositional age of the moraine due to the strongly washed character of the moraine. However, the moraines are assumed not to be younger than 14.7 kyr, which is the end of the Atlantic OD. The age of sample Ku16 (14.6 ± 0.6 kyr) gives the time around which the glacier finally retreated from the pass and successively from the area of Lac de Nino (Lake Nino). A pollen sequence from sediments cored near Lake Nino has been interpreted as representing the succession of Allerød-YD-Preboreal-Atlantic-Subboreal-Subatlantic-Holocene (Reille, 1975) indicating that the area around the lake was free of ice during the YD. Therefore, the YD glacier should have been restricted to the area marked by the moraines around 1750 m a.s.l. (Fig. 12A). With 13.9 ± 0.9 kyr the age of sample Ku93 includes the YD in its uncertainty (external uncertainty 1.6 kyr) but is slightly too old. Like in other small catchments (e.g. Catamalzi, Fig. 6A) the transport distance seems to be too short to abrade enough rock to reset the cosmogenic clock. In a hanging tributary valley of the Tavignano valley, the Scrocchiella valley (Fig. 13A), boulders on a well preserved lateral moraine were not suitable for exposure dating since their diameter does not exceed 0.5 m (Fig. 13B). Glacially abraded bedrock at 1741 m a.s.l. provided the opportunity to date with ^{10}Be. Sample Ku123 was taken from a former plucking plane (Fig. 13C). At such a sampling point shielding due to the steeply inclined surface is larger than shielding by surrounding topography and becomes an important factor. The age is expected to indicate the glacier retreat. Instead, Ku123 yielded an age of 13.2 ± 1.1 kyr that is closer to the beginning of the YD where glacier advance is expected. The YD was a quite short cold event of 800 years in the Western Mediterranean (Cacho et al., 2002) and 1100 years in the North Atlantic (Stanford et al., 2006). Since uncertainties of cosmogenic ages are of the same range or even larger, the ages of Ku93 and Ku123 are used to reconstruct the YD glaciation.

The strong degradation of the moraines in the central part of the plateau can be explained by glacial outburst floods. During the OD, the glaciers coming down the valleys from the NE and SW dammed a lake on the Pianu di Campotile (Campotile plain, Fig. 12A). In the Lake Nino area a large glacial lake was dammed by the YD moraines. Outburst floods could occur during glacier retreat phases when the moraines were instable. The YD moraine was partly removed by the last outburst flood, which also incised a channel into the lower OD moraine (Fig. 12A and C). One more glacial lake can be reconstructed for the OD glaciation in the Tavignano valley. The glacier coming down the NE flank of Punta Artica advanced far enough to dam the main valley. Its frontal moraines are nearly completely eroded.

4.2.2.1. Glaciation history of the Tavignano plateau

The three glaciers in the outlet valleys can only be reconstructed under the assumption of the existence of an ice field on the plateau resembling a plateau glacier (Fig. 14). The total volume of this ice field, including its three outlet tongues, would be about 8 km³ (Kuhlemann et al., 2005b). Its formation was possible when valley glaciers on the plateau grew together and the surface of the ice rose above the ELA. Further growth of the ice field then was due to self-amplification. Its extraordinary thickness enabled transfluence across local divides and

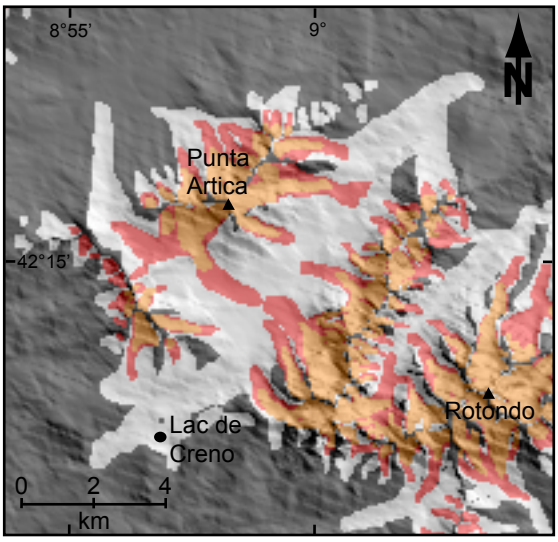

Fig. 14: The plateau glacier on the Tavignano plateau and its separation into several valley glaciers during deglaciation. White: LGM; red: Oldest Dryas; orange: Younger Dryas.

the main drainage divide towards the west, triggering catchment cannibalism. Exposure ages from moraines of the three outlet glaciers give the time of plateau glacier formation, whereas samples from the plateau itself give the time when glaciation was not strong enough to build up the plateau glacier. Depending on the interpretation of Ku119 in the Colga valley, the ice field might have existed during HE3 as well as during HE2 and the whole LGM. Latero-frontal moraines stabilised at the end of the LGM as indicated in the Tavignano valley, when the glaciers began to retreat (Zoicu valley and Lake Creno). Retreat might have begun around 19 kyr and is assumed to have been rapid. Moraine stabilisation should have been finished around 18 kyr. The glaciers advancing on the plateau during HE1/Oldest Dryas were too small to lower the ELA by self-amplification. Several valley glaciers formed new moraine ridges in the tributary valleys, some of them damming the main valley (Fig. 14). Glacial outburst floods destroyed or strongly degraded the Oldest Dryas glacial sediments. Younger Dryas glaciers were even smaller and their moraines also affected by glacial floods.

4.2.3. Restonica valley and northern flank of Monte Rotondo

South of Tavignano plateau and valley, there is the NE-SW oriented Restonica valley. The narrow main valley is ~16 km long and together with its large southern tributary valleys it drains the whole area between Punta alle Porta (2312 m), Punta Muzzella (2425 m), the complete north- and north-eastern flank of Mte. Rotondo (2622 m), the north-western flank of Mte. Cardo, and Corte (Fig. 7). As the main valley is narrow as well as many of the tributaries are, conditions for preservation of moraines or other glacial sediments are poor. Sediments near the river could be mistaken for fluvial deposits as during floods the river is able to transport large boulders. Few moraine relics were found in the main valley and the Rivisecco valley, well-preserved lateral moraines in the Timozzo valley near the Bergerie de Timozzo (Fig. 15A). As single moraines do not have many boulders suitable for cosmogenic dating, the sampling strategy aimed for a sequence in the whole catchment including polished rock surfaces. Four out of eight samples are bedrock samples.

During sampling especially the alkali feldspar granite at the upper end of the Restonia valley turned out to be extremely durable despite its coarse grain size. This silicified granite consists of partly fresh biotite, orthoclase, anorthoclase and quartz, and also contains hornblende. Thin sections revealed fissures filled with small white mica, chlorite and zoisite grains as well as larger cracks filled with a fine-grained matrix of angular broken quartz and K-feldspar chips, small white mica, chlorite and zoisite flakes. The micro-breccia contains also iron oxide/hydroxides. The texture of the crack fillings resembles pseudotachylite but lacks glass. Since this granite is durable despite the cracks, the crack filling seems to strongly cement the texture as it is typical

Fig. 15: A) Topographic map of the Restonica valley and its tributaries. As the valleys are mainly narrow moraines or other glacial sediments are scarce and poorly preserved. B) Boulder Ku29 and C) boulder Ku122 of the lateral moraine at 650 m a.s.l. D) Sampling situation of sample OSL6 from a sand pocket (inlet) below a large boulder. E) View upvalley along the steep flank of the lateral moraine (Ku63) in the Timozzo valley with the Bergerie where F) boulder Ku118 on the flat top surface. G) Sampled glacially abraded surface (Ku106) in the Rivisecco valley.

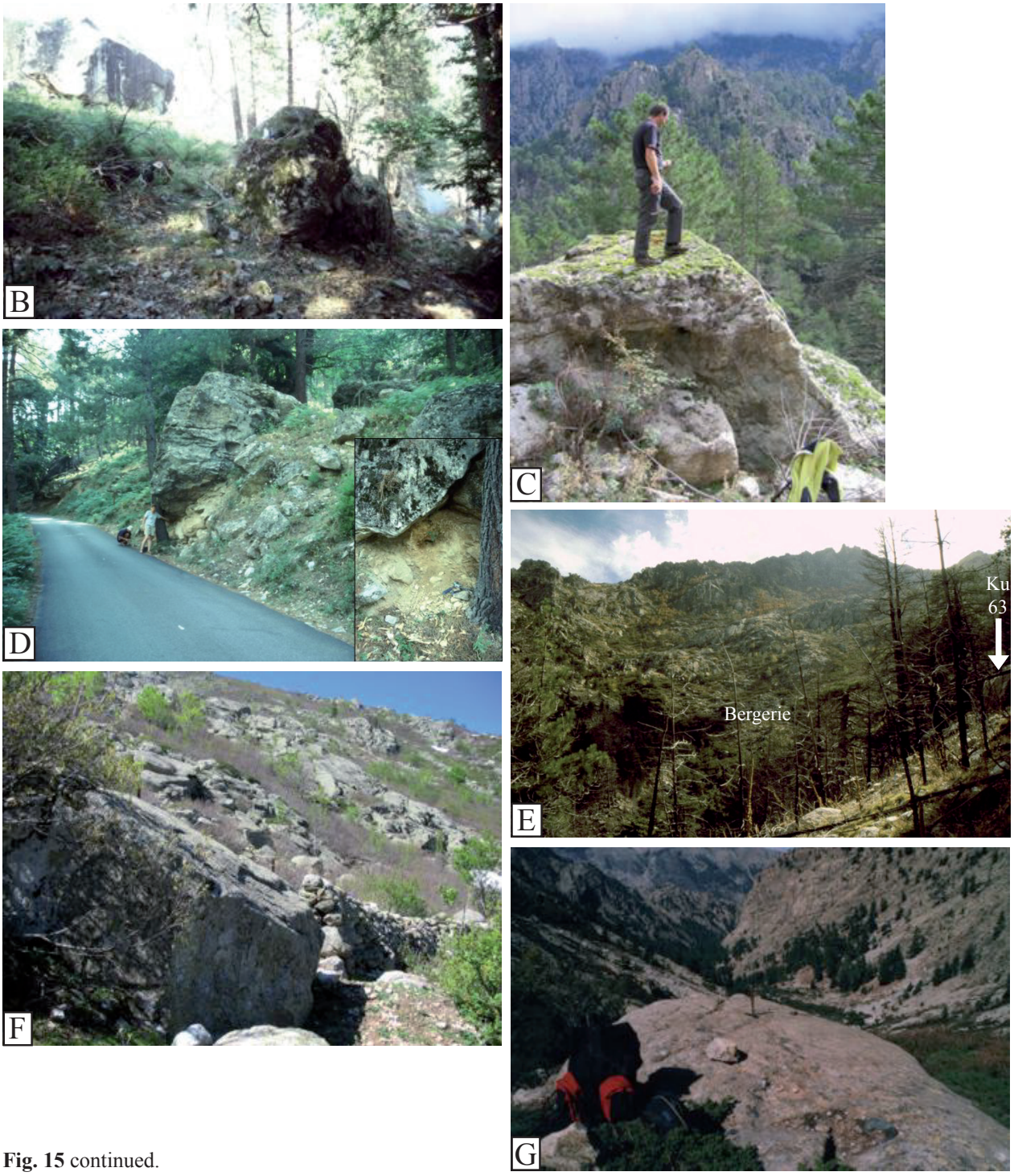

Fig. 15 continued.

for pseudotachylite. Therefore, the ages for the samples from the Restonica valley, Ku29, 105, and 122 are calculated with 3 ± 1 mm/kyr erosion. Samples Ku132 and Ku133 come from surfaces showing the original glacial striation, and therefore theses samples are calculated without erosion. The three samples from the tributary valleys were calculated with 10 mm/kyr.

The lowest glacial sediments found in the Restonica valley are moraine relics on the valley floor and a lateral moraine at 650 m a.s.l. The lateral moraine lies 15 m above the recent river and seems to be several tens of metres thick. On top of the moraine huge outwashed blocks with volumes between 10 and 100 m³ are only weakly rounded assuming short transport distance or transport on the ice. The two samples from this moraine, Ku29 and Ku122, come from the lower and the upper part, respectively. Sample Ku29 (Fig. 15B) yielded an age

of 25.0 ± 1.4 kyr which lies between HE3 and HE2. Since the boulder is situated in the lower part of the moraine it is assumed that glacial abrasion should have been large enough to reset the cosmogenic clock. Inheritance is therefore excluded. Another explanation is the incorporation of older sediment material into the moraine formed by a younger advance. The two feldspar IRSL-ages of sample OSL6 (Fig. 15D), 27.3 kyr (Fsp-MAA) and 24.6 kyr (Fsp-SAR), support this mixing of sediment since they also lie between HE3 and HE2. The age of sample Ku122 obtained from a boulder on top of the lateral moraine should give the age of the younger advance (Fig. 15C). The boulder was chosen because its surface showed different degrees of weathering. The freshest and roughest side should be the former contact to the rock and was sampled to avoid inheritance. The exposure age should be interpreted as the time when the boulder fell onto the glacier. The obtained age of 9.5 ± 1.6 kyr is far too young in comparison with sample Ku29 so that it cannot be the age of the advance reworking the older moraine material. Furthermore, this age falls in a time of rising temperature following the YD event. This age shows that the sampling assumption was invalid. Instead, it was recognised as a part of a rock-fall which is much younger than the glacial deposit.

Beside further relics of glacial sediments at around 1100 m a.s.l. four degraded latero-frontal moraine ridges above the Bergerie de Grotelle at around 1500 m a.s.l. were found. The uppermost part of the Restonica valley forms large cirques with two ice-scour lakes, Lac de Melo at 1711 m a.s.l. and Lac de Capitello at 1930 m a.s.l. each partly surrounded by moraines (Fig. 16A). Original polished surfaces are common if not dominant in higher areas, and cover 20 % of the local surface in lower areas. Larger outcrops of glacial abraded bedrock are also found below the cirque which ends with a 20 m high scarp. Sampling these rock surfaces (Fig. 16B, C, and D) offered the possibility to date the post-LGM glacier retreat in the Restonica valley. The time of retreat of the glacier forming the 1500 m-moraines should be the age of samples Ku105 and Ku132, that of the glacier scouring the depression of Lac de Melo the age of sample Ku133. The obtained ages of 48.4 ± 2.3 kyr for Ku105 (Fig. 16D), and 13.8 ± 0.9 kyr for Ku132 (Fig. 16B) differ extremely. Furthermore, Ku105 conflicts with the samples down-valley as it is older. A possible fraction of inherited nuclides implies that the rock was too hard to be eroded by the glacier. The 13.8 kyr of Ku132 are assumed to give the glacier retreat after the (Atlantic) OD cold phase back from the 1500 m-moraines since they are slightly older than YD and younger than OD. The OD seems to be more reasonable than HE1 because the marine HE1 in the Western Mediterranean ended at 16.2 kyr (Cacho et al., 2002). The Heinrich event might have initiated the glacier advance of the OD on Corsica, but final glacier retreat occurred with the beginning of the Bølling. As Ku132 was taken in front of small moraine ridges damming Lac de Melo, these moraines are consequently interpreted as YD moraines. With 10.1 ± 0.6 kyr the age of Ku133 (Fig. 16C) is 2000 years younger than the end of the marine YD (12.1 kyr, Cacho et al., 2002), suggesting either a longer terrestrial cold phase than marine, or some abrasion in the early Holocene.

In the tributary Timozzo valley a degraded lateral moraine between 1150 m and 1290 m a.s.l. as well as latero-frontal moraines near the Bergerie between 1350 and 1550 m a.s.l. mark the end of glacier advances coming down the northern flank of Mte. Rotondo (Fig. 15A). The catchment area is similar to the Dryas moraines in the Restonica valley but the accumulation area reaches higher up resulting in a lower moraine position assuming a similar ELA. Therefore a valley-to-valley correlation would suggest an OD age also for the lower degraded Timozzo moraines and a YD age of the upper moraines. Boulders on the moraines are mainly smaller than 1 m

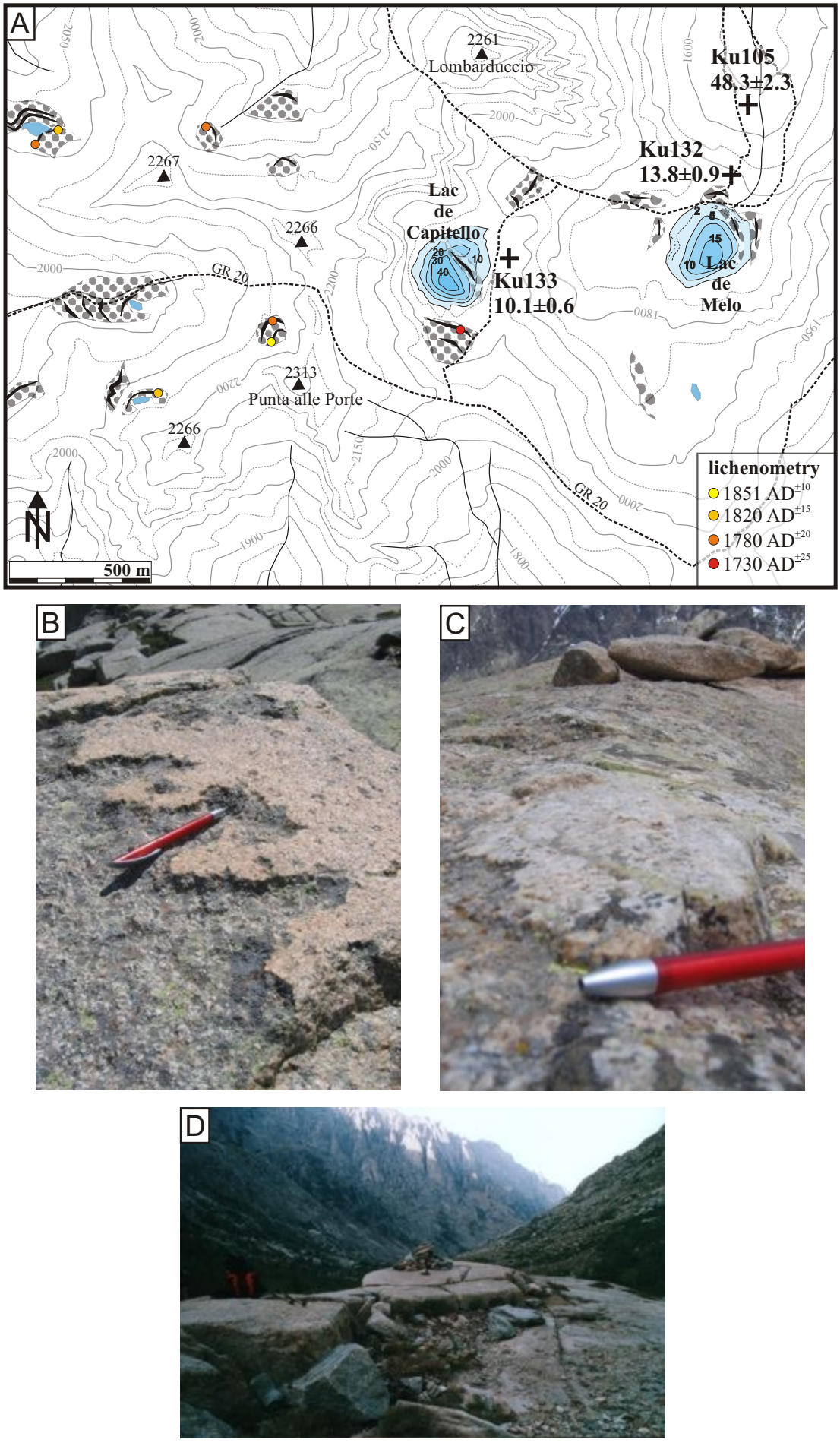

Fig. 16: A) Topographic map of the area around Punta alle Porte with the glacial cirques of Lac de Capitello and Lac de Melo. Lichenometric data from an unpublished diploma thesis. Rock surfaces with striae at Lac de Melo (Ku132, B) and Lac de Capitello (Ku133, C). D) Sample Ku105 was taken on the elevated surface at the right side of the backpack.

in diameter; nevertheless, along the large western moraine one larger boulder seemed suitable for dating (Ku63) with the limitation that it might have rolled due to its position at the moraine slope (Fig. 15E). The quite young obtained age of 3.2 ± 0.4 kyr confirms this allochtony. The bergerie was built on unstructured moraine material that might be a rest of a former basal moraine. There, another large boulder could be sampled (Ku118, Fig. 15F). Transport by men seems unlikely due to its size. Quarrying would result in a "too-young"-age. In contrast, the obtained age of 17.7 ± 1.0 kyr is too old in relation to the suggested YD age. Possibly, inheritance is relevant.

In the Rivisecco valley east of the Timozzo valley, many moraine relics at different altitudes are evidence of several glacier advances fed by a large accumulation area east of Mte. Rotondo which is surrounded by several peaks higher than 2300 m. The glacial sediments are washed out and the ridges are strongly degraded below 1250 m a.s.l. Two better preserved ridges at around 1320 m a.s.l. consist of small boulders. Small glacial sediment deposits between 1400 and 1720 m a.s.l. were also not suitable for dating. Polished bare rock crops out at 1480 m a.s.l. dated at 11.2 ± 1.0 kyr (Ku106, Fig. 15G) suggesting a glacier retreat after the YD advance going down as far down as 1320 m a.s.l.

As the obtained ages in and around the Restonica valley show a broad scatter and are also without a straightforward chronology, it is difficult to develop an age model for the glaciation. Moreover, the glacial deposits are poorly preserved. To be able to decide which age in the group is an outlier the topographic position of the single sample in relation to the other samples is the only base for argumentation as independent dating exists only for the Holocene (Reille 1992). So the following model is quite speculative, but reasonable in terms of equilibrium line altitudes (see chapter 5.2.) and regional glacier reconstruction.

The largest glacier advance should have reached its lowest position at 640 m during a time of maximal Wuermian cooling. Since the obtained ages of the lateral moraine relic suggest a reworking of older material, the HE3 and HE2/LGM advances seem to have been of quite similar extent. During these advances all tributary valleys above 800 m were filled with glaciers joining the main glacier. Very poor or even no preservation of retreat moraines does not allow a reconstruction of the late phase of the LGM. Conclusions about the following advances are only indirect because bedrock had to be sampled instead of boulders or boulder ages contradict morphological conclusions. The lowest moraine relics in the tributary valleys with few degraded moraine ridges are correlated to the HE1/OD cold phase as well as the set of degraded moraine ridges at 1500 m in the Restonica valley. Mostly well preserved moraine ridges somewhat up-valley of the OD moraines are correlated to the YD cold phase that might have been longer on the island than suggested by the marine record (Cacho et al., 2002). Moraines and glacially formed surfaces above 1900 m a.s.l. are therefore of Holocene age.

4.2.4. Eastern flank of Monte Cardo

At the eastern rim of the Rotondo massif Monte Cardo marks the highest peak (2453 m a.s.l.). On its eastern flank several moraine relics are preserved (Fig. 17A). The lowest latero-frontal moraines were found down the Misongno valley below the village Santo-Pietro-di-Venaco between 740 and 650 m a.s.l. National road N193 cuts into 8 m high moraine material (Fig. 17B). An in-situ formed cross-bedded sand lens in the moraine (Fig. 17C) provided a perfect opportunity to sample for luminescence dating. Sample OSL11 yielded congruent feldspar ages of 20.3 ± 1.1 kyr (MAR) and 20.8 ± 1.1 kyr (SAR) that place the deposition of the moraine into

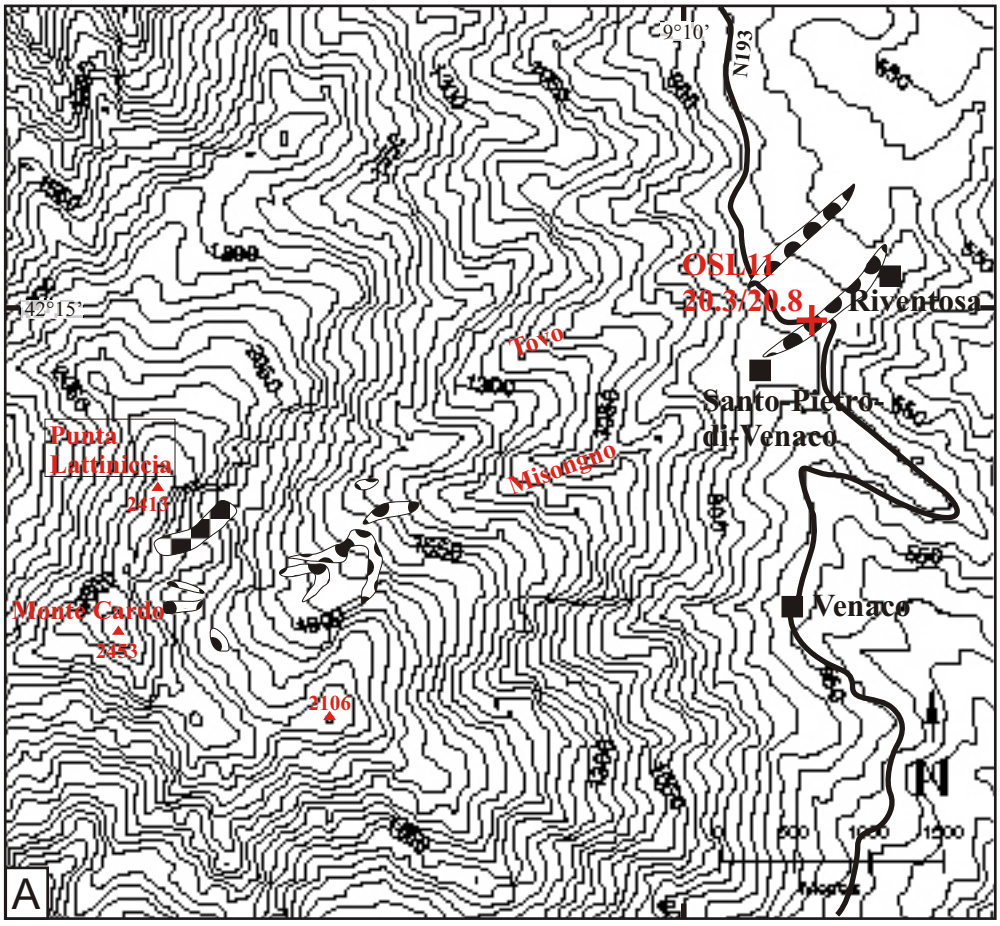

Fig. 17: Eastern flank of Monte Cardo situated SE of Corte. A) Sketch map with moraines and sampling site. B) Exposure of moraine sediment along a road cut. C) Detail of B showing cross-bedding of glacio-fluvial sands in the moraine. Hole marks position of sample OSL11.

the LGM. The moraines between 1400 and 1700 m a.s.l. have a similar altitudinal position as the Dryas moraines in the Restonica valley and its tributaries. Therefore the suggested age for the lower moraine is OD and for the upper moraine YD. Moraines higher up including the rock glacier sediments are then of Holocene age.

Fig. 18: A) Topographic map of the area between southern flank of Monte Rotondo and northern flank of Monte d'Oro indicating position of moraine ridges, glacial sediments and sampling sites. B) Sampled surface of the roche moutonnée at the Bergerie de Tolla (Ku11). C) View from the small pozzi (peat-bog) towards the sampled roche moutonnée (Ku85). D) Moraine ridge at the NW flank of Pointe de Pinzi Corbini with mainly angular boulders. Sampled boulder surface in the front with hammer. E) View from the sampling point of Ku102 (hammer) downvalley towards the N with the large lateral moraine coming from the left.

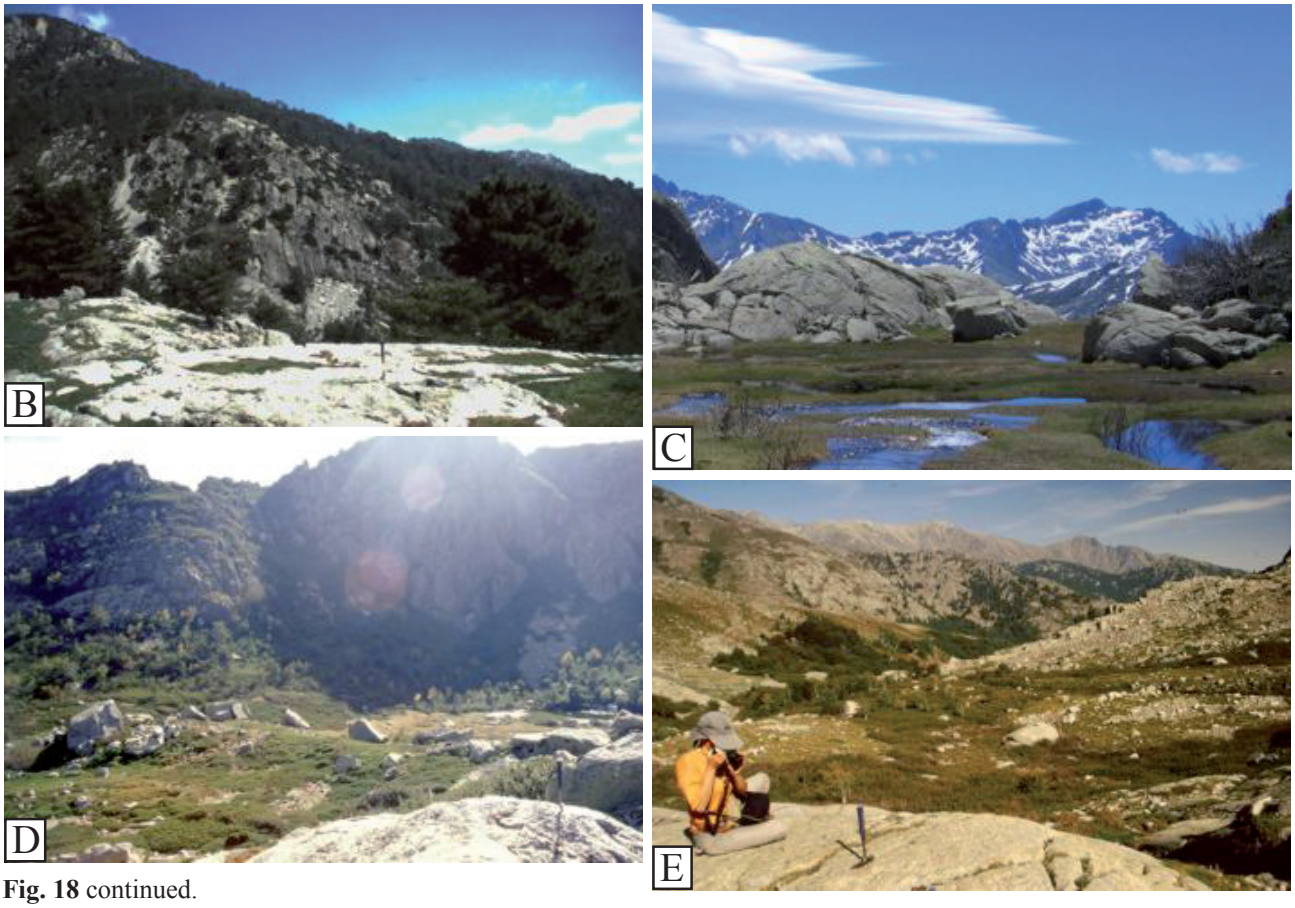

Fig. 18 continued.

4.2.5. Area between southern flank of Monte Rotondo and northern flank of Monte d'Oro

At the southern flank of Mte. Rotondo (2622 m) the headwaters of the Manganello valley are dominated by several peaks higher than 2400 m and a large kar at 2320 m a.s.l. where an ice-scour lake is surrounded by moraines and glacial sediments (Fig. 18A). Between 1250 and 1600 m a.s.l. the main valley is filled with large amount of moraine sediments, showing only strongly degraded ridges or any structure. The Bergerie de Giano and the Refuge de Petra Piana were built on moraine relics. Further down, four broad and degraded moraine ridges are preserved north of the Manganello River between 1050 and 1000 m a.s.l. They are partly overprinted by a small fan. The U-shape of the main valley, with a broad and flat bottom and steep walls, ends with this moraine deposit. The valley morphology downwards resembles a degraded U as the valley is narrower and the slopes more gentle. Despite this, there is a deposit of glacial sediment at 730 m. All moraines in the Manganello valley lack larger boulders and therefore can not be dated with cosmogenic ^{10}Be. Instead, two polished rock surfaces were sampled. Sample Ku11 was taken on a ridge-like roche moutonnée at 1031 m a.s.l. located near the Bergeries de Tolla where fresh polished surfaces display glacial abrasion (Fig. 18B). Since this roche moutonnèe is situated almost in the centre of the Manganello valley glacier ice should have flowed above and around it (Fig. 18A). The sample yielded an age of 28.4 ± 1.8 kyr clearly referring to the glacier retreat following the HE3 cold phase (30.9 – 29.1 kyr, Cacho et al., 2002). The moraine material above 1050 m is therefore interpreted to be of HE2/LGM age. Along the western headwater of the Manganello River, in the Valle di Petra Piana, a roche moutonnée at 1910 m a.s.l. borders the outlet of a small pozzi (Fig. 18C). Its exposition age of 11.7 ± 0.6 kyr (Ku85) marks the end of the YD cold phase. The corresponding moraines of the glacier advance should be the next ones down-valley at 1600 m a.s.l. The corresponding YD moraines of the eastern headwater are situated at

1400 m a.s.l. For the OD, it is suggested that the glaciers joined and advanced down to 1250 m. It results in a similar small difference in extent of glaciation between OD and YD like on the northern side of Mte. Rotondo.

In the western tributary valley down the NW flank of Pointe de Pinzi Corbini, above unstructured moraine relics, large mostly angular boulders were found on a pair of moraine ridges (Fig. 18A). As datable boulders are rare in this region, sample Ku100 is not only an opportunity to date and reconstruct the advance in the tributary but also supplies important information for the regional reconstruction of glaciation. The ELA corresponding to the advance should be similar to the ELAs of the neighbouring valleys what would allow an indirect dating of the moraines without datable boulders via correlating ELAs. A fairly rounded boulder out of angular large boulders was selected for sampling in order to avoid inheritance (Fig. 18D). However, the obtained age of 115 ± 35 kyr shows that the boulder was not eroded sufficiently to reset the cosmogenic clock.

Glaciers coming down the two northern valleys of the Mte. d'Oro massif, Grottaccia and Meli valley, deposited large amounts of sediment into moraines and moraine complexes (Fig. 18A). Like in the Manganello valley boulders on the moraines are either small or lack completely. The large stacked lateral moraine complex below the Bergerie/ Refuge de l'Onda in the Grottaccia valley is correlated to the LGM moraine relics at 1050 m in the Manganello valley as they have a similar number of ridges. Degraded latero-frontal moraine ridges of shorter and narrow glacier tongues above 1400 m a.s.l. enclose polished bed rock (Fig. 18E). The obtained age of 5.2 ± 0.6 kyr (Ku102) for this polished rock is too young to be a realistic estimate for the glacier retreat. The only explanation for a "too young" bedrock sample is a sediment or soil cover that shielded for a long time and was then removed. As the sampling point is in the vicinity of a shepherd's hut (bergerie), deforestation and intensive grazing might be the trigger for a rapid erosion of the soil and underlying sediment. In analogy to the Manganello valley the suggested age of the moraines would be OD and YD.

Large volumes of moraine material have been found in the Cruzini valley (Fig. 18A, Fig. 19A). A well-preserved lateral moraine ridge is found at the intersection of the main valley with the tributary Coracchia valley coming down the northern flank of Pointe Migliarello (2254 m, Fig. 18A). Unfortunately, the moraine ridge had no large boulders. Thus one boulder rising only little more than 1 m above the moraine matrix has been sampled (Fig. 19B). This boulder experienced 19.4 ± 1.4 kyr of exposure. Due to the small size of the boulder, this age should be considered as minimum age. Small boulders might have been covered with sediment for some time shielding the sampled surface what leads to an apparent younging. However, the age of deposition for the block and hence the moraine is assumed to fall into the LGM.

At the confluence, the moraine exceeded 50 m thickness and formerly blocked the headwaters of the main valley to form a lake (Fig. 19A). Each time the glacier advanced down into the main valley a small lake was dammed potentially causing glacial outburst floods (GLOF). The formation and persistence of glacier-dammed lakes is linked to glacier oscillations. After the ice retreat, typically one flood event occurs when the dam of moraine material collapses. Due to the high discharge of such a sudden flood, large amounts of sediment are transported down-valley, including large boulders.

A map of the Cruzini valley indicates that the LGM glacier advance protruded less far than at least one in the Wuermian prior to LGM. For geometric reasons, the LGM advance of a glacier from the steep high tributary valley to the short main valley should have caused a GLOF too, but for the same geometric reasons any wider

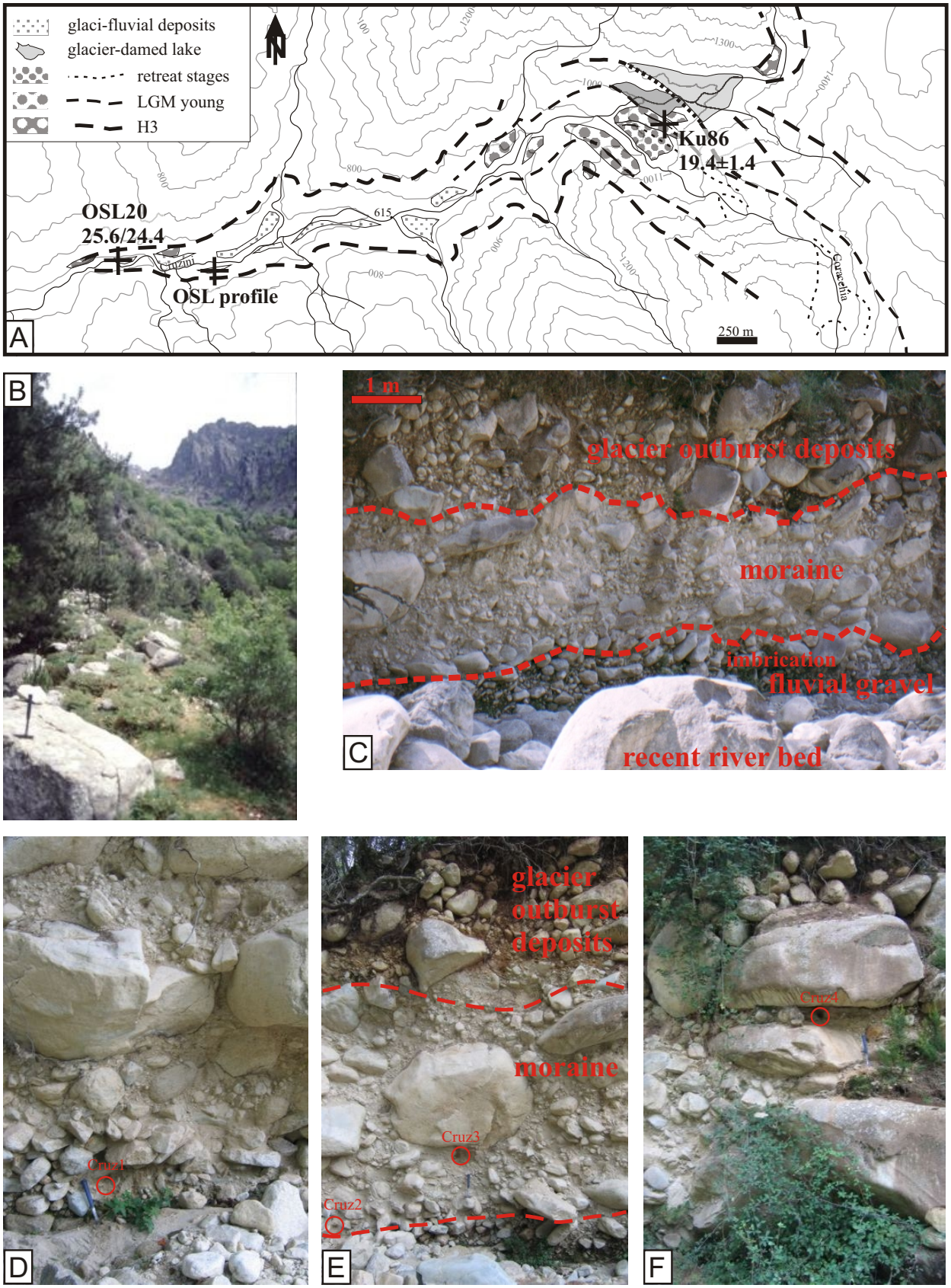

Fig. 19: A) Topographic map indicating position of glacial sediments and reconstructed glacier extents in the Cruzini valley. B) Boulder Ku86 with hammer on sampled surface. C) Sediment sequence with fluvial gravel, moraine, and flood deposits exposed along the recent river bed. D, E. and F) sampling location of luminescence samples Cruz1 (fluvial), Cruz2 and Cruz3 (glacial), and Cruz4 (base of flood deposit).

(and thus higher) glacier advance would have caused ice-damming of a higher water volume in the main valley. Additional sampling has been performed especially to constrain the depositional ages of sediments below (fluvial gravel) and at the top of the GLOF. The ^{10}Be exposure age (Ku86) confirms that the LGM glacier did not reach as low as at least one Wuermian glacier before. The excellent outcrop conditions enabled sampling of the basal fluvial gravel (Cruz1, Fig. 19D), a sand pocket incorporated at the base of the basal moraine (Cruz2, Fig. 19E), a similar sand pocket below a large glacial boulder within the moraine (Cruz3, Fig. 19E), and a sand pocket at the top of the moraine just below the GLOF deposit (Cruz4, Fig. 19F). Sample OSL20 comes from an outcrop of the GLOF down-valley. Sand deposits in basal moraines and outburst sediments are likely to consist of mineral grains that are only partly bleached. The transport should be long enough in the Cruzini valley to bleach normal fluvial sediment, but sand deposited below the ice was transported not only on top of the ice but also in and below the ice. Outburst sediments are transported in a muddy suspension. Insufficient bleaching seems to be quite possible for all of the samples. Partially bleached sand yields luminescence ages that overestimate the depositional age. Fading tests carried out with sample Cruz1 show that the feldspars lost 3.3 % of its luminescence per decade. However, ages corrected according to this fading value conflict with the geological and morphological findings in the outcrops. An explanation might be that the effects of incomplete bleaching and fading on the trapped energy amount cancelled each other resulting in an age that is suggested to be the depositional age. Therefore ages calculated without fading correction were used for the interpretation.

The obtained age of 33.6 ± 2.9 kyr for sample Cruz1 suggests a deposition of fluvial gravel in the warm phase before the cold spell of HE3. The ages for the moraine, 30.7 ± 2.2 kyr and 30.3 ± 3.0 kyr (sample Cruz2 and 3, respectively), match HE3. The ages for the GLOF, 25.6 ± 1.3 kyr (Fsp-MAA) and 24.4 ± 1.3 kyr (Fsp-SAR) for sample OSL20, 24.8 ± 2.9 kyr for sample Cruz4, indicate a link to a glacial advance during HE2 despite that they are slightly too old. This interpretation fits to the depositional setting in the upper valley, were less perfect outcrop conditions and morphology suggest that the LGM moraine set directly covers the GLOF deposit. A cross section of the LGM moraine exposed directly at the creek indicates that a likely GLOF at the end of the LGM mobilized much less moraine material than the one after HE2 and is therefore poorly preserved or completely eroded. Data set and setting suggest that the glacier advance of HE2 was somewhat stronger than those of the subsequently following LGM, and particularly accumulated a lot of material.

4.2.6. Vizzavona pass

The latero-frontal moraine succession at Vizzavona pass in central Corsica (Fig. 20A) is characterised by a particularly moist setting in a beech forest (Fagus sylvatica) with lichens on trees and with moss cover on quite grusy granite boulders (Fig. 20B and C). In this setting very high postglacial weathering rates of at least 15 mm/kyr are assumed for granitic samples Ku27, Ku104, Ku110, Ku111, and Ku112. The depositional setting exposes a quartet of fairly well-preserved moraine ridges with the outermost sitting on the plain of the broad pass and the inner ridges joining downward into the Agnone River (Fig. 20A). The outer flank of the moraine quartet is exposed along a major road and shows that the fairly fresh ridge has been deposited above older glacifluvial coarse sands and a moraine deposit (Fig. 20D). The pass itself is washed out and only isolated large glacial boulders remained. The end of the outermost moraine ridge marks an ice extent reaching down to

1000 m a.s.l. Further down-valley, two degraded moraine ridges mark the maximum ice extent in the Agnone valley with glacier advances down to 900 m a.s.l. Moraine relics in the Gravona valley on the south-western side of the pass suggest transfluence over the pass prior to the deposition of the moraine quartet and a large glacier advancing as far down as 800 m a.s.l. Six samples for cosmogenic dating and two luminescence samples should unravel the glacial history in the Agnone valley, two further luminescence samples from the Gravona valley should date the maximum ice extent.

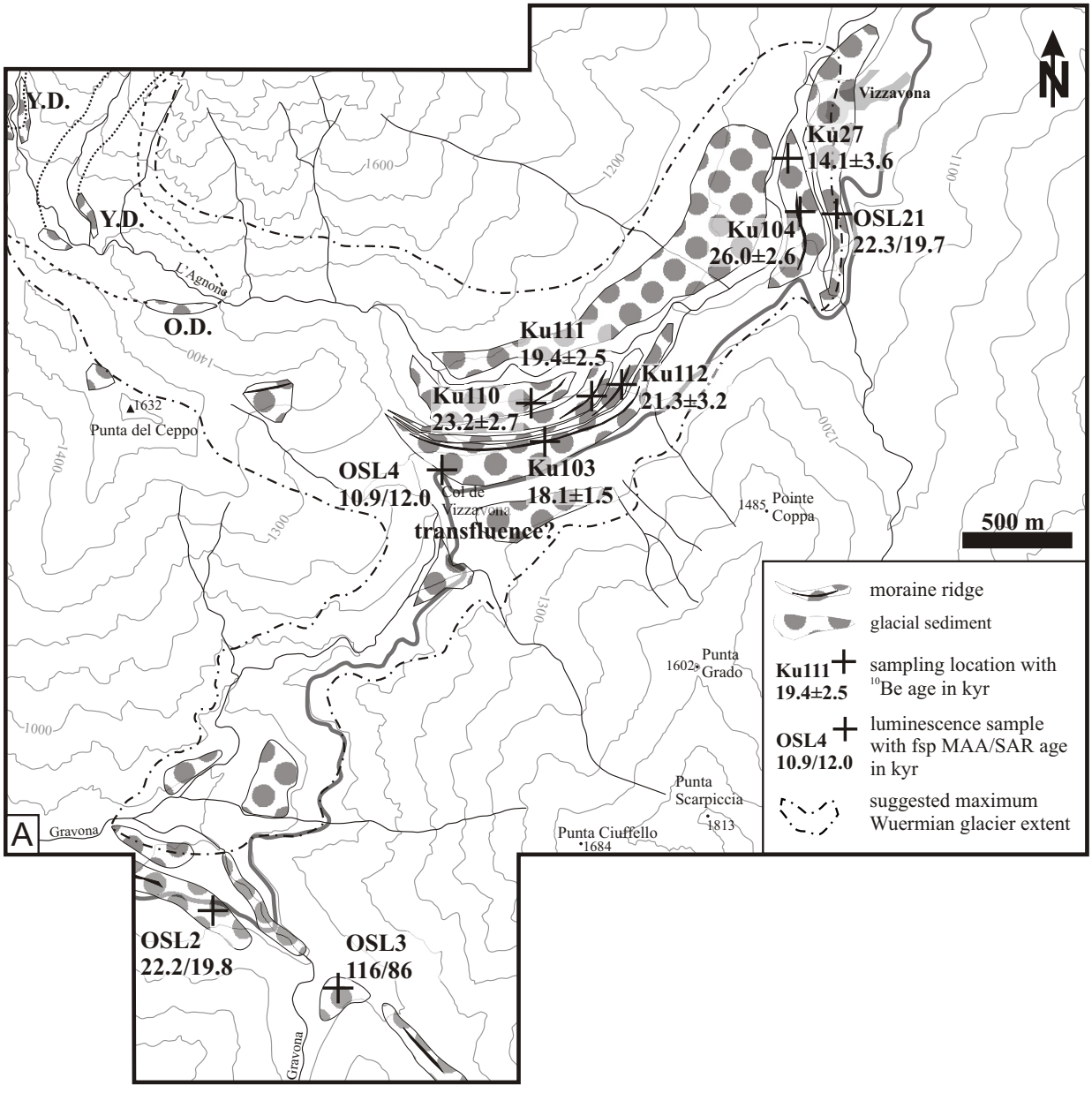

Fig. 20 (continued on next page): A) Topographic map of the area around Vizzavona pass between Oro- and Renoso massif with the Agnone (NE) and Gravona valley (SW) illustrating the glacial morphology and obtained ages. B) Boulders on the mainly densely forested moraines in the Agnone valley are covered with moss and C) consist of quite grusy granite. D) Section through the outermost moraine ridge of the stacked moraine along a road cut showing the youngest moraine deposit at its top overlying glacifluvial sands and older moraine deposits. E) Pre-Variscan gneiss boulder (Ku103) on the deforested top of the outmost moraine ridge that seems to hover above the ground indicating erosion of about 1.5 m of loose materail. F) Sampling site of sample OSL4. G) Boulder Ku104 from one of the degraded lower moraine ridges. H) Sample OSL21. I) Moraine relics along the valley slope of the Gravona where sample OSL2 was taken from a sandy layer (inlet). J) Sample OSL3 was taken from a sand lense in moraine relics at the confluence of Gravona and Lariccione.

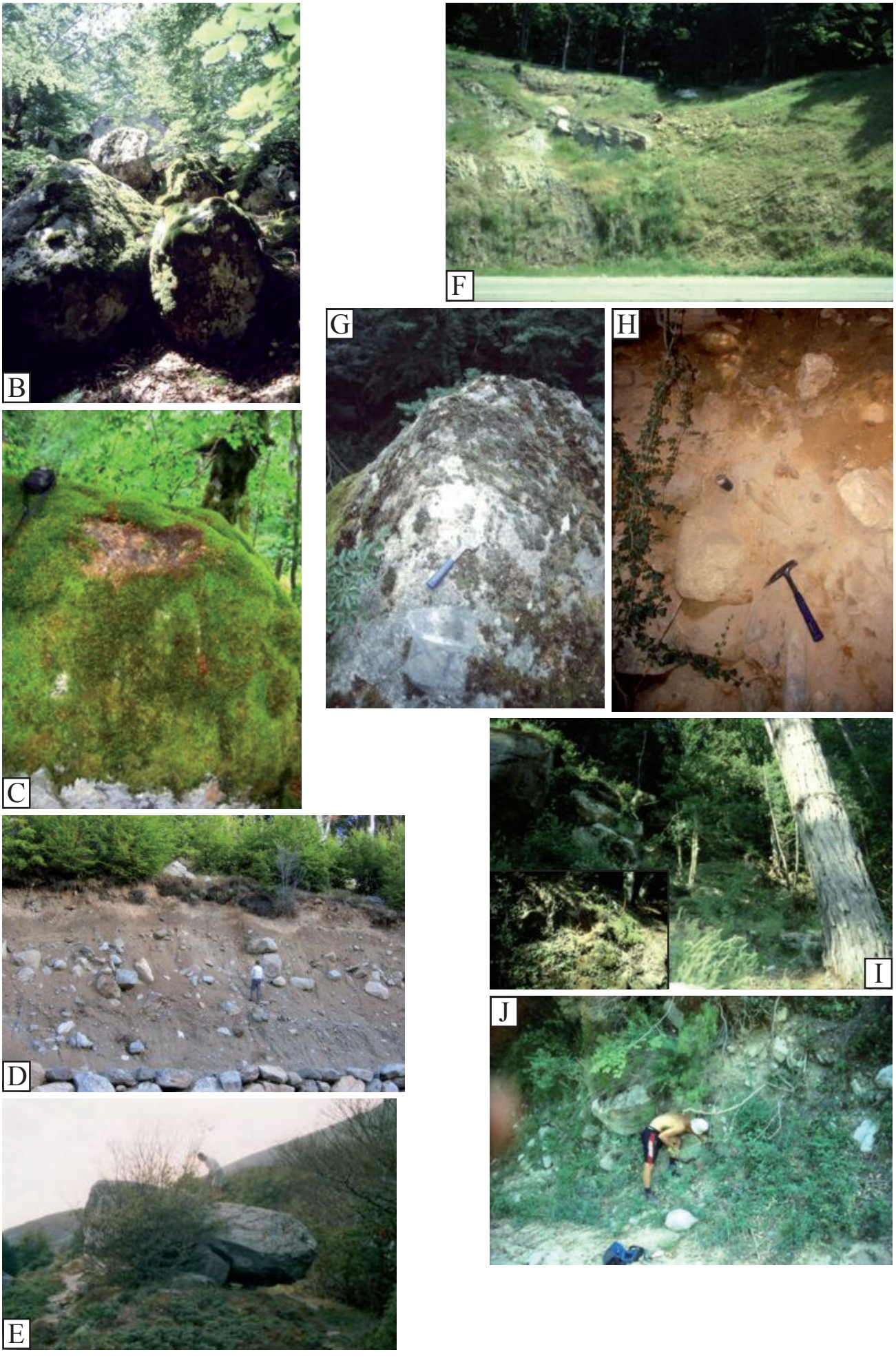

Fig. 20 continued

Sample Ku103 is from a pre-Variscan gneiss boulder from the top of the outmost moraine ridge of the moraine quartet (Fig. 20E). This large boulder is bedded on small boulders giving the impression to hover above the moraine indicating that about 1.5 m of debris an soil has been weathered and washed away. Also on the inner three ridges the fine-grained matrix has been washed out resulting in crests formed by rows of large grusy granitic boulders. Nevertheless, several boulders in these moraine ridges larger than 2 m across were suitable for sampling as they should have always been rising above it (Ku110, 111, 112). The four exposure ages scatter between 18.1 ± 1.5 kyr and 23.2 ± 2.7 kyr. The deposition of the moraine and its stabilisation occurred during the LGM. An age succession with the outermost sample being the oldest and the innermost being the youngest as the morphology suggests is not given. Additionally, the ages imply that the ridges were deposited in short time spans of less than 1000 years which cannot be distinguished with ages overlapping with the given uncertainty of the method. The luminescence age obtained directly at Vizzavona pass (OSL4, Fig. 20F) falls with 10.9 ± 0.7 kyr (Fsp-MAA) and 12.0 ± 0.7 kyr (Fsp-SAR) into the late glacial although the sample is taken in the outmost and thus oldest LGM advance. The ages are calculated without fading correction. As fading of feldspars can cause up to 30 % apparent younging of the sample, these ages are minimum ages. Adding maximum correction of 30 % would result in ages of 14 and 16 kyr, still much younger than suggested by the exposure ages. Outcrop conditions in this site were not the best. A steep slope, partial grass cover, and closeness as well to an 18th century fortress as to a modern street make natural slumping and artificial modification possible.

Towards the east, the valley bottom is flat, and voluminous washed-out moraine deposits are preserved. As they are less well preserved than the LGM moraine quartet and are deposited in some distance to it they should be older than LGM. Sample Ku104 taken from an extremely grusy but large block on a flat moraine ridge yielded an exposure age of 26.0 ± 2.6 kyr. Sample Ku27 (Fig. 20G) from the lower end of the same moraine ridge should show a similar depositional age, but despite of its large size the exposure age of 14.1 ± 3.6 kyr reflects post-LGM exhumation. At a fairly new forest road cut into the inner side of the outer moraine ridge, sample OSL21 represents a small sandy pocket within the moraine (Fig. 20H). The ages without fading correction of 22.3 ± 1.2 kyr (Fsp-MAA) and 19.7 ± 1.1 kyr (Fsp-SAR) suggest deposition during LGM contrast the morphological conclusions. Ages including maximum fading, 29 and 26 kyr, respectively, correspond to the expositional age of sample Ku104 and would support deposition prior to the LGM. However, neither a clear correlation to HE2 nor to HE3 is possible. If the choice of maximum fading would be correct, only one age would correlate to the older HE3. If fading would be lower, the younger event would be the most likely.

As suggested in the map of Fig. 20A, the two older moraine ridges at Vizzavona might correspond to the moraine relics at 800 m a.s.l. in the Gravona valley. The sample pair OSL2 and OSL3 was taken under the assumption that the glacier advance down the Gravona valley correlates to the advance down Vizzavona pass. Sample OSL2 comes from sand deposited on a lateral moraine (Fig. 20I) and yielded ages of 22.2 ± 1.3 kyr (Fsp-MAA) and 19.8 ± 1.0 kyr (Fsp-SAR) without fading. These ages are consistent with the no fading-ages of sample OSL21, so ages corrected with fading would be also. Therefore the assumption of correlating maximum advances seems to be correct. The obtained ages of sample OSL3 (Fig. 20J) of 116 kyr (Fsp-MAA) and 86 kyr (Fsp-SAR) have large difference between the two feldspar ages indicating incomplete bleaching. Furthermore, these high ages fall into the last interglacial (marine isotope stage 5) although its geographic position suggests

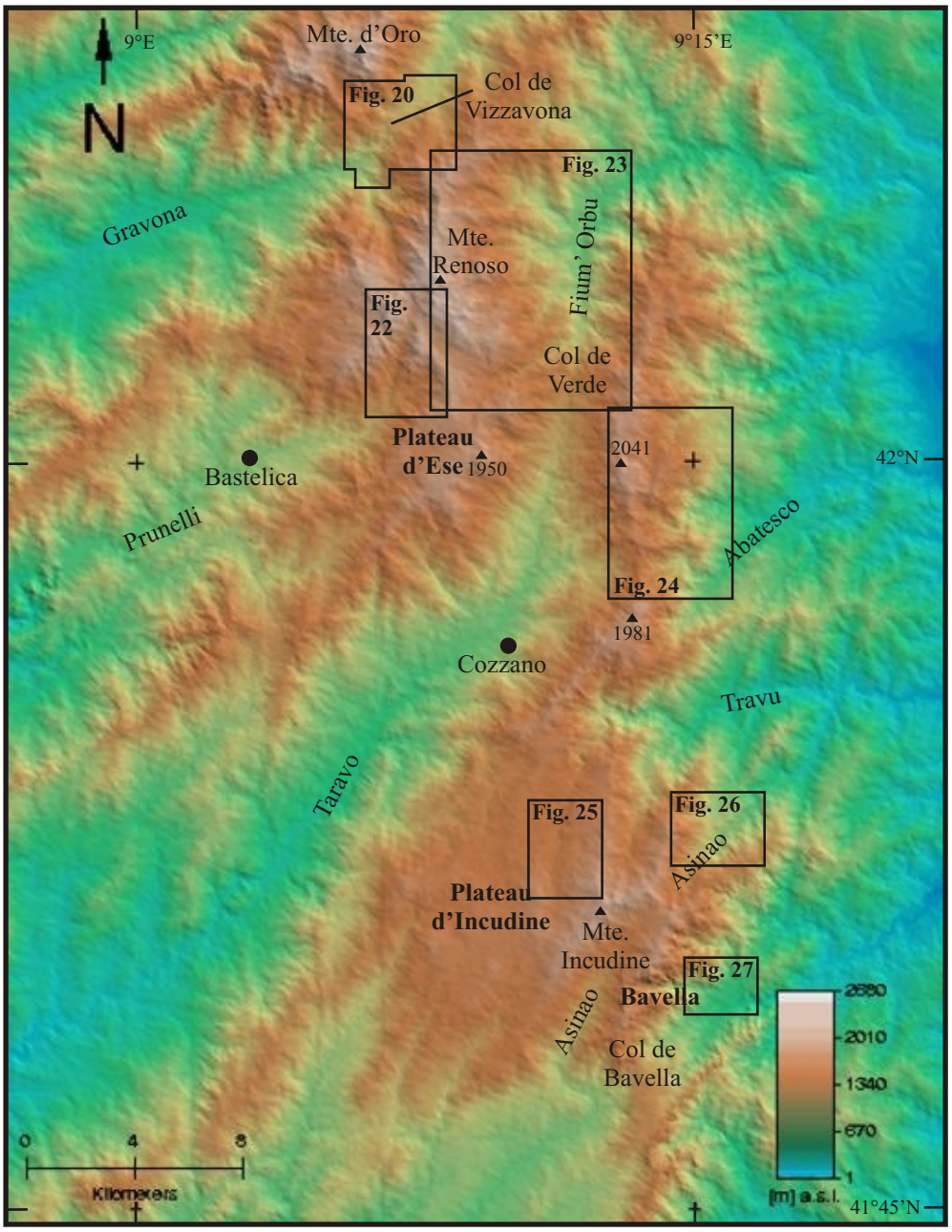

Fig. 21: Topographic overview of the southern part of the Corsican mountain chain with the Renoso massif, Verde chain and Incudine massif. Frames show locations of further detailed maps.

a depositional age younger or similar to sample OSL2. In this case, possibly a subglacially formed sand deposit has been sampled.

Moraine relics that might correlate to the OD and YD glacier advances were found in the Agnone valley between 1300 and 1600 m a.s.l. (Fig. 20A). The proposed glacier extents are reasonable in terms of the regional ELA pattern.

4.2.7. Renoso massif

South of Col de Vizzavona (Vizzavona pass), the Renoso massif with its highest peak Monte Renoso (2352 m) and several other peaks above 2100 m is characterized by palaeosurface remnants mainly in the central, western and southern part (e.g. the Plateau d'Ese), the eastern flank has a rugged and steep relief (Fig. 21). All valleys show glacial morphology, and at numerous sites moraines, moraine relics and other glacial sediments were found (Fig. 22A, Fig. 23A). Six samples dated with cosmogenic ^{10}Be and six luminescence samples should

clear the correlation between cold phases and glacier advances.

In the Prunelli valley draining the western side of the massif, the moraines at 1200 – 1300 m a.s.l. are the best preserved latero-frontal moraines in Corsica together with the Vizzavona moraines. The morphologic setting of the moraines is similar to Vizzavona pass, with two periglacially flattened older ridges aside a fresh inner quartet on the right valley side and one large ridge on the left side (Fig. 22A). Recent annual precipitation rates in this valley lie around 1500 mm/yr (Bruno et al., 2001) and dense pre-medieval forestation, largely of beech trees due to easterly aspect, is assumed. The similarity with the Vizzavona moraines strongly suggests that the age is the same, with the inner quartet representing the LGM and the two outer ones, according of their outward increasing degree of degradation, representing earlier advances. The boulders on the sharp inner quartet of moraine ridges are only up to 2 m large and rise less than 1.5 m above the moraine matrix. Therefore, samples Ku51 and Ku52 were taken from the largest boulders but sediment cover cannot be excluded. Additionally, the

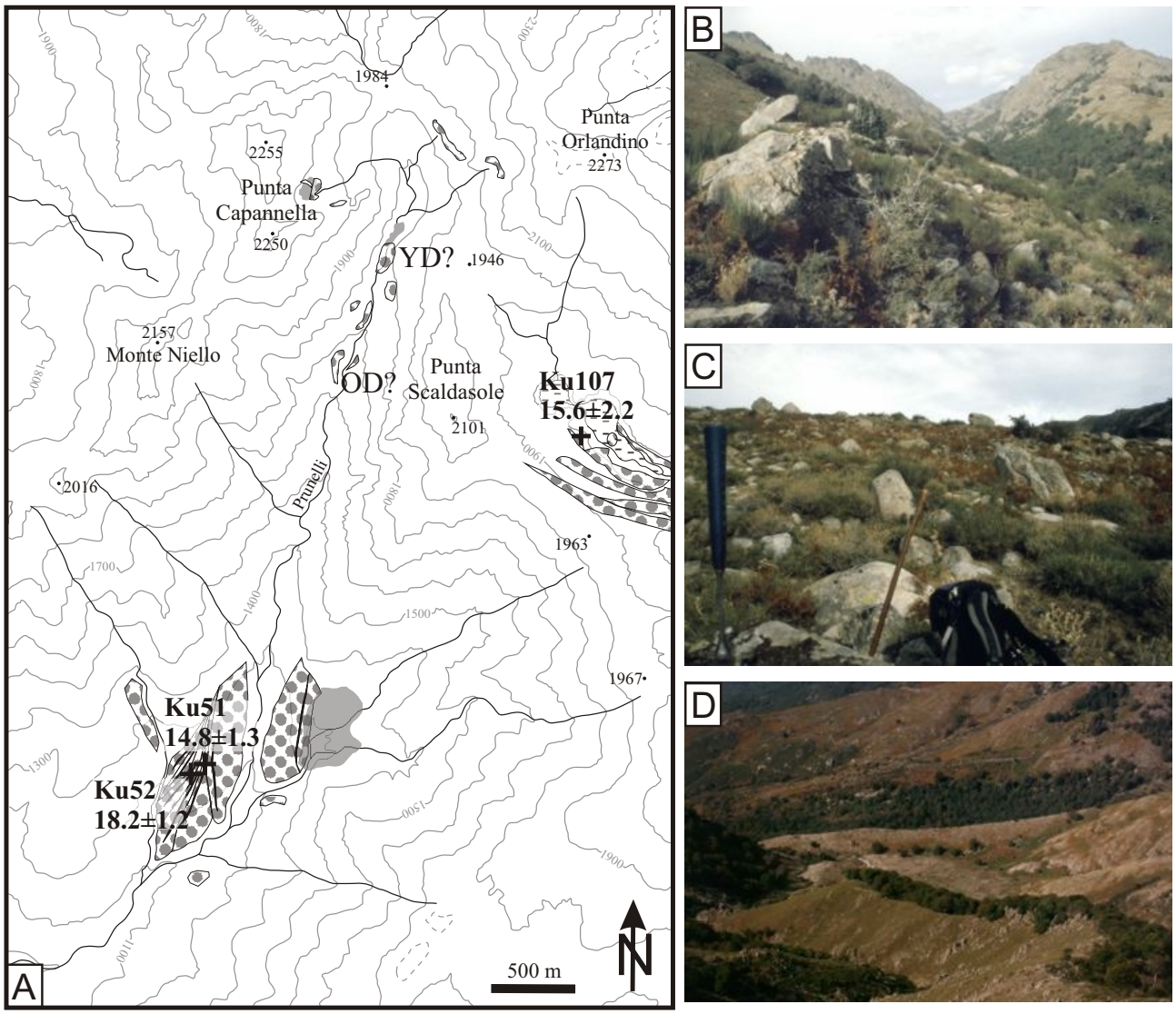

Fig. 22: In the Prunelli valley (A), two periglacially flattened older ridges aside a fresh inner quartet on the right valley side and one large ridge on the left side mark the end of a large valley glacier coming down the western side of the Renoso massif. B) Sample Ku51 comes from the boulder on the highest moraine crest at the left front of the picture. C) The surface of boulder Ku52 (front with hammer) rises not more than 1.5 m above the ground. D) View from E over the former lake area, the damming moraine ridge, the valley with its green vegetation, and the moraine quartet on the other valley side.

Fig. 23: Glacial sediments are common on the eastern flank of the Renoso massif (A) documenting early large advances as well as the whole time of deglaciation and cold phases during the Holocene. Moraine relics of the large advance can often be grouped to successions of four or more ridges like in the Prunelli valley or at Vizzavona pass. The profile through the moraine complex of the Cannareccia valley is illustrated in detail in Fig. 30 and discussed in chapter 4.2.10.

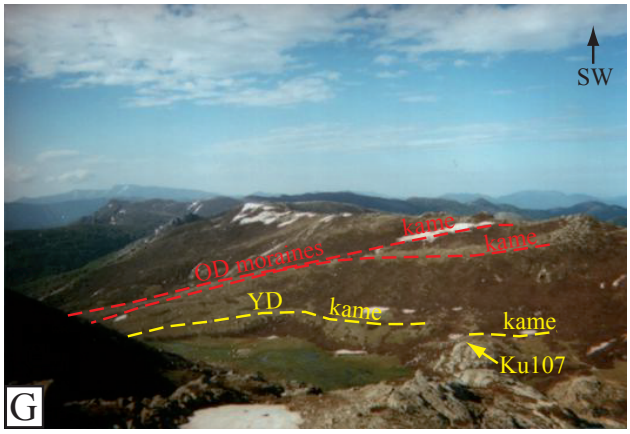

Fig. 23 (continued): Boulder Ku135 (B) yielding a quite young age conflicting with the low position of the moraine complex was sampled on the flat top surface as well as boulder Ku47 (C) one of the largest boulders sampled in the study. Glacial sediments near the Marmano river (D) were sampled for luminescence dating (sample OSL19) to confirm a correlation as basal moraine to boulder Ku47. With the two exposure samples Ku88 (E) and Ku107 (F and G) the glaciation of the Oldest and Younger Dryas of the Marmano headwaters around the Bergerie de Pozzi (E) should be dated since two different glacier extents could be mapped according to the morphology (G). A sand lense below a large boulder (H) was sampled in the Ariola valley near the confluence with the Fium'Orbu (OSL9). For sample OSL8 see Fig. 32.

boulders are often not well rounded like sample Ku51 (Fig 22B). Hence, the obtained young age of this sample, 14.8 ± 1.3 kyr, might not only be a result of sediment cover but also of insufficient glacial erosion. Boulder Ku52 (Fig. 22C) from an outer ridge yielded an age of 18.2 ± 1.2 kyr suggesting a moraine deposition at the end of the LGM. Assuming sediment cover the deposition might have been during the LGM and the age more indicates the stabilisation and first degradation of the moraine. Conditions for preservation of younger moraines above the LGM moraines are bad since the valley is steep and narrow between 1400 and 1800 m a.s.l. Quite small relics of glacial sediments were found between 1600 and 1800 m a.s.l. that might correlate to the two Dryas cold phases (Fig. 22A).

The lateral moraine ridge at the left dammed a small catchment hosting only small glaciers. The flat surface of the lower part of the catchment suggests that a shallow lake formed behind the dam (Fig. 22D). The moraine did not collapse completely after glacier retreat; instead the lake water eroded a channel along the contact between valley wall and sediment. Down-valley, fluvial terraces show a quite washed out surface. On the surface, large blocks with diameters up to 2 m testify for (fluvio-) glacial transport as the blocks are too large for fluvial transport in this low gradient part of the valley. This may hint on a flood event caused by a sudden release of the dammed lake through the small outlet.

On the eastern flank of the Renoso massif a complex pattern of glacial sediments is evidence of a long history of glaciation (Fig. 23A). Moraine relics of the largest advances are often a succession of four or more ridges similar to the Prunelli, Vizzavona, Golo or Tavignano moraines. The largest glaciers rooting above 2100 m advanced as far down as 850 m a.s.l. In the northern part the smaller catchments just reaching 2100 m hosted only glaciers advancing down to 1140 m a.s.l. (Fig. 23A). The best preserved moraine succession was found in the Cannereccia valley with six ridges with different grades of preservation. The dated boulder Ku135 yielded an age of 14.3 ± 2.0 kyr (Fig. 23B). This age is not only much younger than expected it also falls into the relatively warm period between OD and YD during which an advance seems unrealistic. Furthermore, a glacier advance reaching such a large extent during one of the Dryas events would conflict with all hitherto findings about the Dryas glaciation on Corsica which indicate a much smaller extent. The dating results of the luminescence profile Cann1-3 cannot be interpreted straightforward and are discussed separately in chapter 4.2.10.

On the southern ridge of the Marmano valley, south of the Cannareccia valley, near Col de la Flasca, huge boulders witness a glacier filling the whole valley. The obtained age of 23.1 ± 1.1 kyr of one of these boulders suggests such a large glacier during the LGM (Ku47, Fig. 23C). This glacier would be consistent with a LGM glacier that deposited the large moraine succession in the Cannereccia valley. Moraine material with sand lenses in-between found aside the bridge over the Marmano River would correlate to the lateral moraine boulders on the ridge as basal moraine. The sampled sand (OSL19, Fig. 23D) yielded feldspar luminescence ages of 36.4 ± 2.1 kyr (MAA) and 29.3 ± 1.7 kyr (SAR) suggesting a much older depositional age than the boulder. There are two different explanations for the discrepancy: First, it could be sediment of an older advance (HE3) that was preserved despite a younger glacier overriding it; second, inheritance caused an overestimation of the depositional age since incomplete bleaching is likely for basal moraine material. The latter is assumed to be the correct explanation since the difference of about 5 kyr between MAA and SAR age argues for incomplete bleaching.

Moraines of suggested OD and YD age are preserved in nearly every valley of the Renoso massif, but datable were only the advances in the Marmano headwaters around the Bergerie de Pozzi (Fig. 23A). Sample Ku88 comes from a large boulder in the vicinity of the shepherd's huts (Fig. 23E), which were built directly on the moraine ridge. The obtained age of 15.5 ± 0.9 kyr is slightly younger than the HE1 cold phase (Cacho et al., 2002) but falls still into the cold phase of the Atlantic OD. The age might therefore be the time of moraine stabilisation after the glacier retreat. The second sample, Ku107, aiming for the YD advance, was taken from polished bedrock outcropping at the southern valley flank (Fig. 23F). A small moraine ridge only few metres above the sampling point was considered to be of YD age with the bedrock being exposed since the final ice retreat after the YD (Fig. 23G). Instead, the obtained age of 15.6 ± 2.2 kyr is identical to the boulder age of Ku88, so that either the sampling assumption was incorrect or the younger advance did not erode any rock material at this point.

4.2.8. Verde Range

The Verde range is a north-south oriented mountain range east and southeast of the Renoso massif. Its highest peak, Punta Capella, reaches 2014 m, all other peaks are below 2000 m (Fig. 21). Summit surface relics are preserved above 1700 m a.s.l. Catchments towards the west are short, narrow, and steep whereas at the eastern flank the steep and narrow headwaters merge in flat valleys ending at the eastern coast. Moreover, the eastern flank forms an altered, tectonically induced steep E-W staircase pattern, controlled by subvertical N-S strike-slip faults with some east-down vertical component. This morphological pattern favours the preservation of glacial sediments at the eastern flank but in most cases they are poorly preserved. The poor preservation of moraines in this range can be explained by frequent torrential rain in this area. The only fairly well-preserved moraines were found in the upper Nursoli valley where each of two glacier tongues deposited four moraine ridges (Fig. 24A). These moraine quartets have been deposited on a mid-elevation flat at the confluence of two tributary valleys. The staircase shape of the valley floor may be the reason for the relatively good preservation as well as the protection against the torrential rains by a coastward ridge. Granite boulders in this area are sheared and show moderate grusy weathering making the chosen erosion rate of 10 mm/kyr a minimum estimate and therefore the age as well. However, the obtained exposure age of sample Ku117 fits with 20.3 ± 1.1 kyr well into the LGM (Fig. 24B). This age of the moraine quartet correlates with the moraine quartets at Vizzavona pass, in the Tavignano, or Prunelli valley.

In the valleys further to the south either mid-elevation flats lack or large moraine relics are not preserved on it. The glaciers appear to have overwhelmed the flat entering narrow steep valleys further down below as large amounts of undifferentiated moraine material have been deposited at surprisingly low elevations (550-700 m a.s.l.). At San-Gavino-di-Fiumorbo such low elevation moraine deposits could be dated by luminescence (sample OSL16, Fig. 24A and C) that yielded feldspar ages of 30.5 ± 1.8 kyr (MAA) and 30.2 ± 1.7 kyr (SAR) suggesting a deposition during HE3. In the Nursoli valley, smaller amounts of moraine deposits around 900 m a.s.l. might be relics of the corresponding glacier advance (Fig. 24A). Since large boulders and sand lenses are lacking, this sediment could not be dated with any of the methods in this study. At 515 m a.s.l. in the Abatesco valley, south of San-Gavino-di-Fiumorbo, sediment 10 m above the recent river bed was dated (OSL15). In the

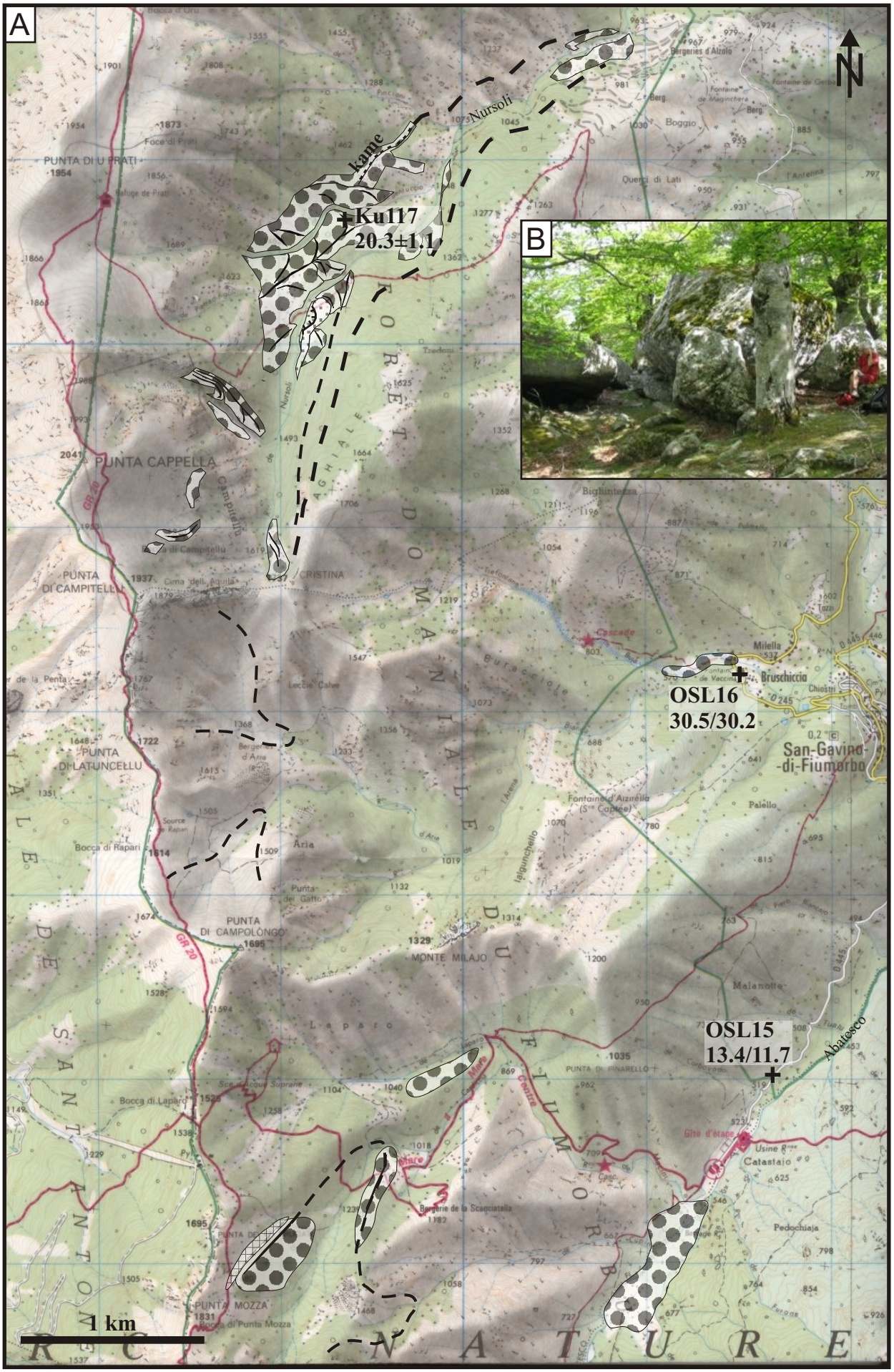
A
B
Nursoli
kame
Ku117
20.3±1.1
OSL16
30.5/30.2
OSL15
13.4/11.7
1 km
PUNTA DI U PRATI
PUNTA CAPPELLA
PUNTA DI CAMPITELLU
PUNTA DI LATUNCELLU
PUNTA DI CAMPOLONGO
MONTE MILAJO
PUNTA MOZZA
San-Gavino-di-Fiumarbo
Catastaio
Bruschiccia
Milella
Malanotte
Pedochiaja
Aria
Bocca di Rapari
Bocca di Laparo
RÉSERVE NATURELLE DES SANTONS
CHAÎNE TORRETOMANIALE
CRÊTE DU FIUMORBO

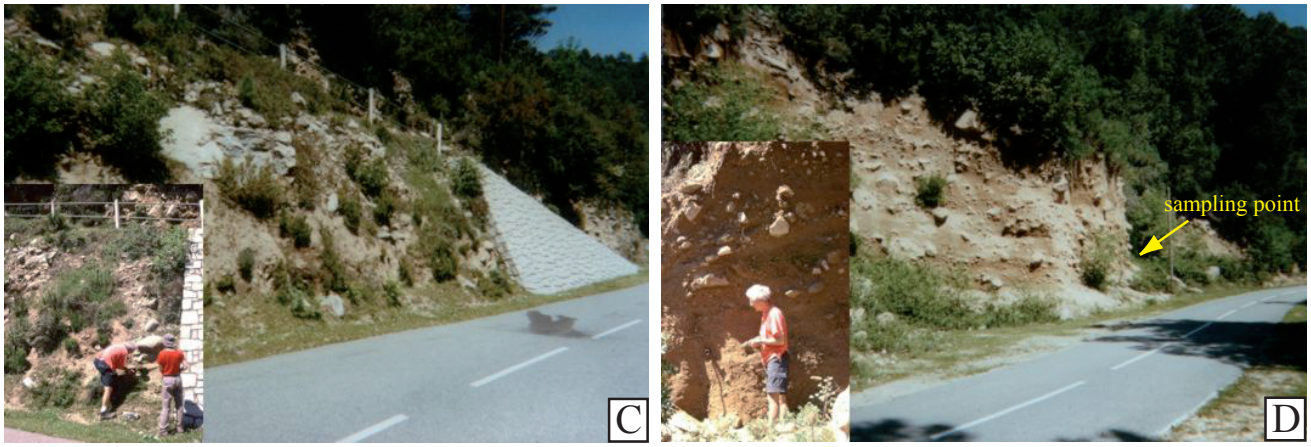

Fig. 24 (previous and this page): A) Along the eastern flank of the central Verde range, glacial sediments are mainly poorly preserved. The only well-preserved moraines were found in the Nursoli valley. B) The boulder in the centre of the picture was sampled on the top surface for exposure dating (Ku117). C) Exposure of glacial sediment near San-Gavino-di Fiumorbo, that could be sampled for luminescence dating (OSL16). D) Sediments near the Gite in the Abatesco valley were interpreted as pro-glacial sequence and sampled for luminescence dating (OSL15).

field it was interpreted as ice marginal glacio-fluvial deposits because of intercalated sand and conglomerate lenses (Fig. 24A and D). Talus material was identified on top of the sequence. Strongly degraded moraine relics are present around 600 m that could correlate to the ice marginal sediment. In contrast to the field interpretation the obtained ages of 13.4 ± 0.7 kyr (Fsp-MAA) and 11.7 ± 0.6 kyr (Fsp-SAR) indicate a deposition around the YD. An assumed total fading rate of 30 % would alter the age to OD. Since a glacier advance from accumulation areas just reaching 1980 m a.s.l. down to 600 m is impossible during the both Dryas, the field interpretation and sampling assumption must have been wrong. However, it is difficult to find a reasonable explanation for the obtained age. Large mass movements like land slides that occurred during the YD and left behind such sediments should be visible in the morphology but since the valley slope is quite uniform this possibility can be ruled out.

4.2.9. Monte Incudine

The southernmost high-mountainous region is the Incudine massif with its peak Mte. Incudine (2134 m). The massif is divided into two unequal parts along the two NE striking Asinao valleys that separate the large Incudine plateau in the W/NW from the Bavella in the SE (Fig. 21). Rock castles are common on the plateau that evolved from a palaeosurface. The alkaline granites of the Bavella form one of the most rugged and steep relief on Corsica (“Aiguilles de Bavella” – needles of Bavella) with deeply incised narrow valleys where sunlight reaches the bottom only in summer. In such a steep terrain it is possible to have long and quite low elevated glacier tongues despite low accumulation areas (below 1880 m a.s.l.).

The plateau has not been glaciated during the last glaciation as proved by the existence of the rock castles. Glaciers were restricted to the valleys in the vicinity of Mte. Incudine where glacial sediments and moraine ridges were found. The glacier advances on the western flank of Mte. Incudine, which is part of the plateau surface, could be dated with two cosmogenic samples (Fig. 25A). Around 1450 m a.s.l. lines of large boulders partly on low ridges trace former latero-frontal moraines. Sample Ku84 was taken on a 2,5x3x2 m boulder of

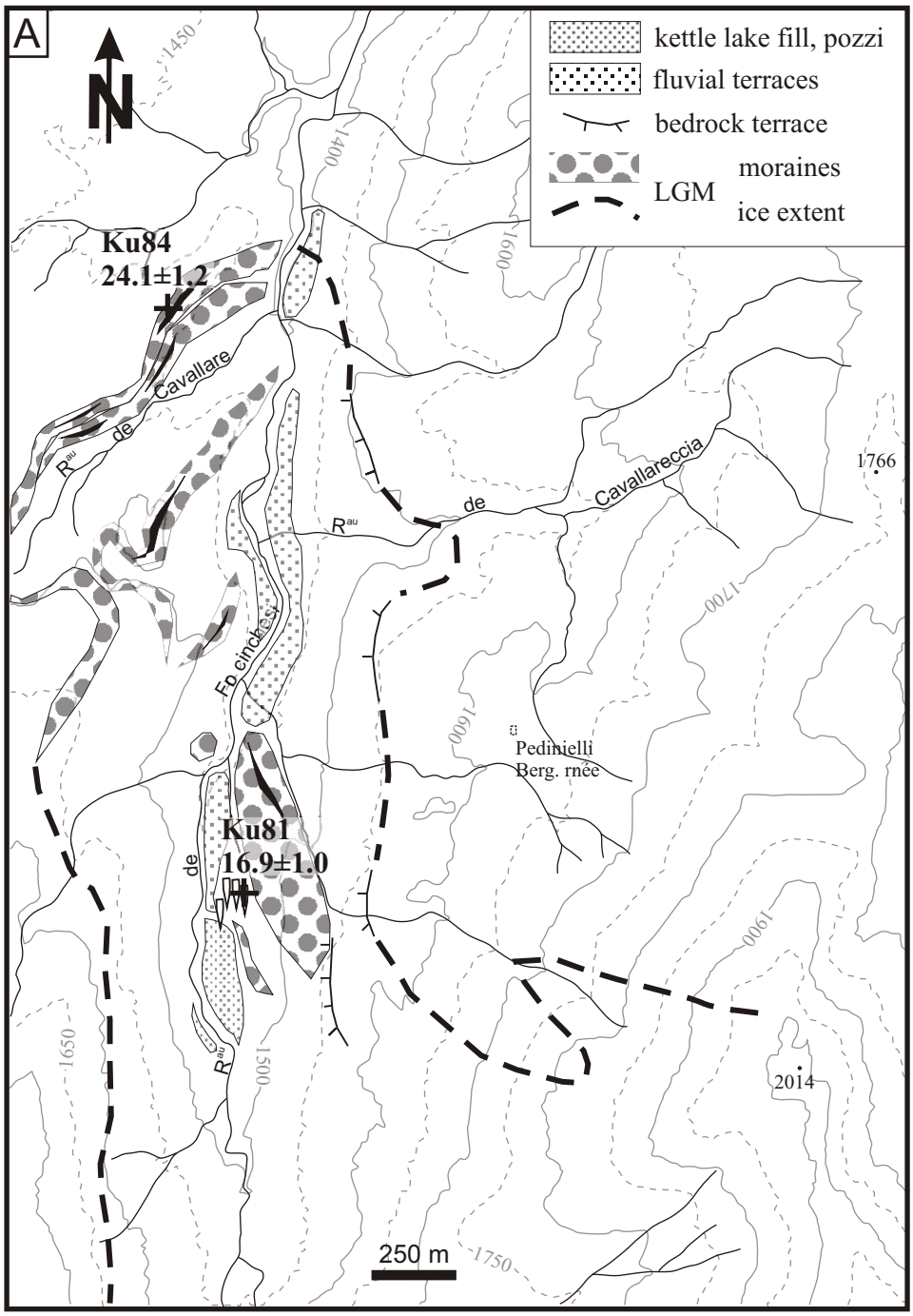

Fig. 25: A) Depositional setting at the NW flank of Monte Incudine with maximum ice extent, sampling sites and obtained exposure ages. B) View from the whale back (Ku81) towards the north over the fluvial terrace.

the maximum advance and produced an age of 24.1 ± 1.2 kyr indicating HE2 as the time of the largest glacier. As there were no relics of glaciers found further down, this HE2 advance was the largest advance during the Wuermian. Relics of a glacial readvance are a latero-frontal moraine and whale backs around 1500 m a.s.l.

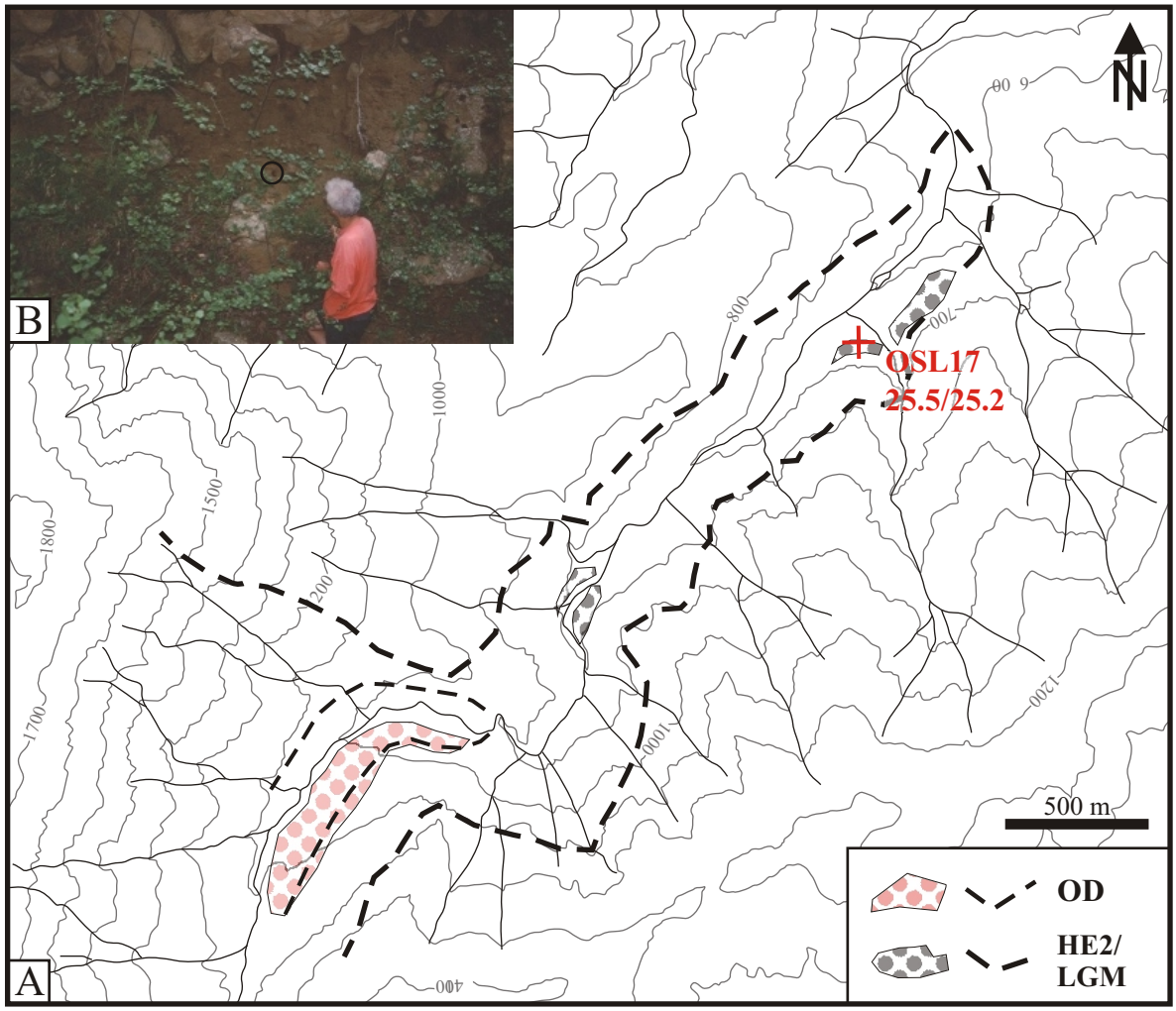

Fig. 26: A quite long and narrow glacier tongue was reconstructed for the HE2/LGM advance in the northern Asinao valley (A) since fluvial sands overlain by glacial sediments at 650 m a.s.l. (B) yielded luminescence ages only slightly older than HE2) (OSL17).

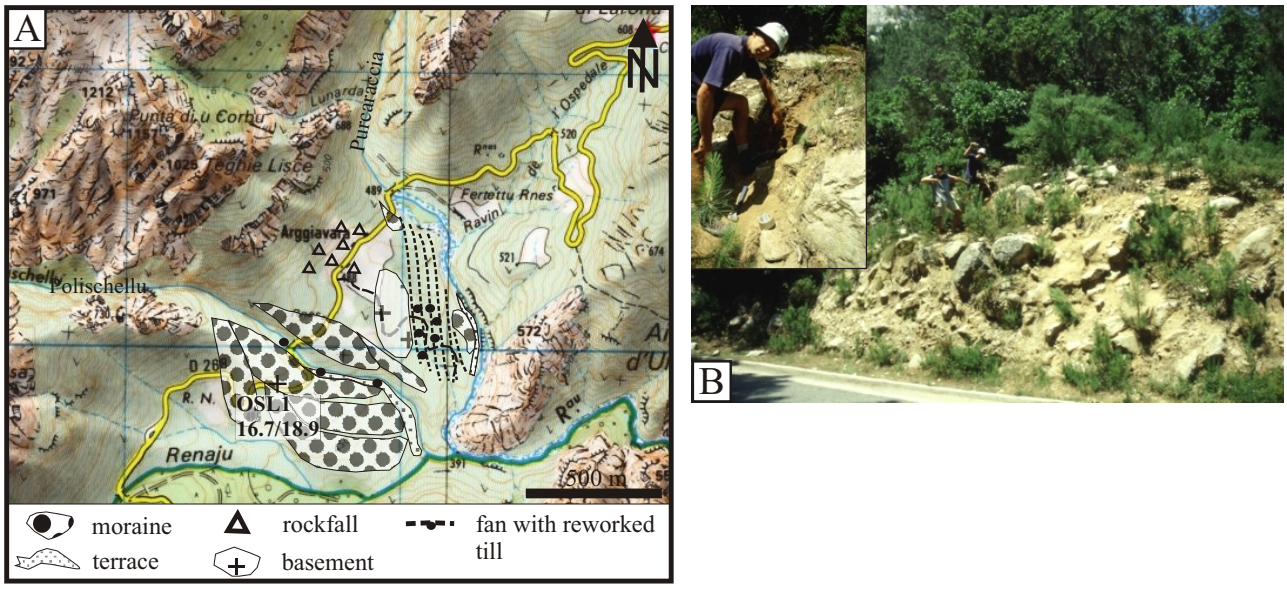

Fig. 27: A) Depositional setting at the confluence of Polischellu and Purcaraccia in the Bavella with sampling site and obtained luminescence age. B) Sample OSL1 was taken from a sand lense (inlet) below a boulder of the Polischellu moraines.

(Fig. 25A and B). The whale backs are exposed since 16.9 ± 1.0 kyr (sample Ku81) that is the beginning of the OD cold phase. As the glacier which formed the moraine covered the whale back probably during the OD this age is assumed to be slightly too old indicating low glacial erosion at the end of the glacier tongue.

In the northern Asinao valley (Fig. 21, Fig. 26A) fluvial sands are overlain by glacial sediments at 650 m a.s.l. (Fig. 26B). Because of the low elevated sampling location the assumption was to date a very old advance. However, the results for sample OSL17 suggest a large glacier advance during HE2 since the ages for the underlying sand are 25.5 ± 1.3 kyr (Fsp-MAA) and 25.2 ± 1.4 kyr (Fsp-SAR). In addition to a relatively low ELA the generation of such a large glacier during HE2 needs precipitation above average.

Due to the steep relief, preservation of glacial sediments in the narrow valleys of the Bavella is nearly impossible. At the junction of the two main valleys of the Bavella, Polischellu and Purcaraccia valley, into the broad SW-striking valley, glacial sediments are preserved as moraines and reworked till (Fig. 27A). The moraines of the Polischellu glacier could be dated with one luminescence sample (OSL1). The sand out of topmost metre of the innermost moraine ridge was deposited between 16.7 ± 1.1 kyr (Fsp-MAA) and 18.9 ± 1.0 kyr (Fsp-SAR), shortly after the end of the LGM (Fig. 27B). Therefore, the whole set of moraines is suggested to be of LGM/HE2 age despite its position at low elevation of 500 m a.s.l. Moraine relics at altitudes above 1400 m a.s.l. visible on air photos are correlated to the OD, those in the highest cirques to the YD.

4.2.10. Pre-30 kyr glacial features in Corsica

The Alpine and the northern hemispheric climate history as well as the marine oxygen isotope record prove colder temperatures during pre-Wuermian cold phases than during the Wuermian (e.g., Dahl-Jensen et al., 1998) suggesting glaciations of larger extents. The early Wuermian cold phase of the HE6 (~MIS4) was similar to the LGM in terms of temperature but due to its longer duration a slightly larger glaciation could also be expected. Northwest-European ice shields of early and middle Weichselian age (around 90 kyr and 60 kyr, respectively, corresponding to the Alpine early Wuermian) were significantly smaller during their maximum extent than those of the Late Saalian (>140 kyr, corresponding to the Alpine Rissian) and the LGM (around 20 kyr) (Svendsen et al., 2004). Also the glaciers on the northern side of the Alps are suggested to have been smaller during early Wuermian than those of the LGM (Preusser and Schlüchter, 2004). Based on minimum ages obtained from overlying sediments or calcareous cements a presumably Rissian glaciation, significantly larger than the Wuermian glaciation, is reported from the Italian Apennines (Giraudi, 1998; Kotarba et al., 2001). Furthermore, geomorphological and sedimentological observations from few other sites in the Italian Apennines suggest a larger pre-Wuermian glaciation (Federici, 1977, 1980; Palmentola and Acquafredda, 1983; Giraudi, 1998). These observations support the absence of large glacier advances during the early Wuermian (MIS5a-d) also for Corsica.

In Corsica, various generations of glacial erosional landforms and poorly preserved relics of higher, pre-30 kyr trimlines have been observed which were discriminated from younger trimlines as they do not have a geometric relation to moraine deposits. Morphological features like U-shaped valley relics might be dated with cosmogenic nuclides. The obtained ages of two samples taken from such old landforms show, that erosion mainly by spallation prevents the preservation of the original surfaces over time-spans longer than 30 kyr, whereas the landform seems to be preserved: sample Ku34 from the Niolo yielded 25.9 ± 2.0 kyr, sample Ku49

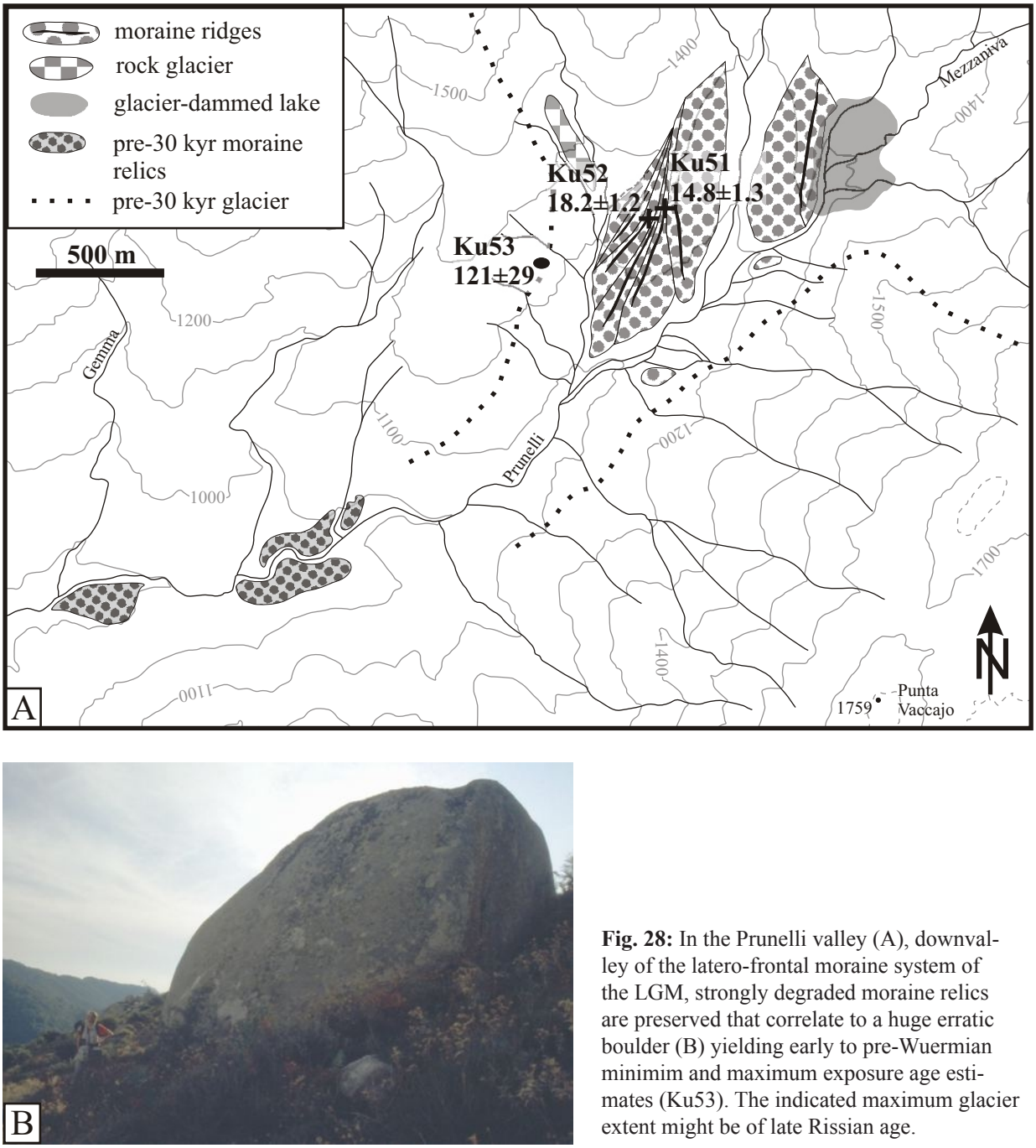

Fig. 28: In the Prunelli valley (A), downvalley of the latero-frontal moraine system of the LGM, strongly degraded moraine relics are preserved that correlate to a huge erratic boulder (B) yielding early to pre-Wuermian minimim and maximum exposure age estimates (Ku53). The indicated maximum glacier extent might be of late Rissian age.

from the Val d'Ese even yielded only 14.5 ± 0.9 kyr.

The only pre-30 kyr age of a cosmogenic nuclide sample (Ku53) comes from a large glacial boulder in the Prunelli valley in SW Corsica (size 7x4.5x>3 m, Fig. 28A and B). This durable, apparently fresh granitic glacial boulder is placed on a terrace-like feature in granite, which approaches the valley floor in SW direction, where some highly degraded boulder accumulation reaches from a terrace 10 m above the valley floor about 50 m uphill. This boulder accumulation appears to be an outwashed, weathered moraine relict (Fig. 28A). On the crest above the valley, Kuhlemann et al. (2007) found a high local weathering rate of nearly 20 mm/kyr probably reflecting a regional precipitation maximum. With the standard 10 mm/kyr, which is roughly half this rate, the uncertainty of the calculated age is larger than the age itself, the calculation therefore incorrect. The highest erosion rate, resulting in an age with a just acceptable uncertainty, is 8 mm/kyr resulting in an age of 121 ± 29 kyr. The durable granite might justify an even lower erosion rate but 6 mm/kyr is assumed to be the minimum for

granites, which are not silicified, resulting in an age of 93 ± 15 kyr. Regional and sample specific findings about the erosion rate contrast each other, so it is not possible to decide which one the "real" rate is. Therefore, the two ages can be taken as minimum and maximum estimate of the exposure age. The minimum age estimate suggests a deposition considerably before the oldest Wuermian Heinrich event 6 (~68 – 60 kyr) during MIS5. As this interglacial is a period without large glaciations, the expositional age around 90 kyr seems unreasonable. A more reasonable boulder deposition during the Rissian (~140 kyr) is indicated by the maximum age estimate due to its larger uncertainty.

Geomorphic evidence supports a pre-Wuermian age of deposition. The extent of late Wuermian glaciers in the Prunelli valley is known as a well-preserved set of latero-frontal moraines (samples Ku51 and Ku52, see chapter 4.2.7.). The four inner moraines form steep ridges, and two more, preserved at the outer western margin, form flat ridges. Their shape suggests periglacial overprint. The two older glacier advances which left the degraded moraine ridges behind occurred at climatic conditions similar to the LGM since the ELA must have been similar. Most likely, they represent advances during cold spells within the Wuermian (Heinrich-events) since $\delta^{18}O$-curves from the Greenland ice cores (e.g. Grootes et al., 1993) as well as data from marine sediment cores (e.g. Cacho et al., 2002) suggest only slightly differing strength for these events. These data suggest that HE3, HE4, or HE6 reached a degree of cooling similar to the LGM but there are no clues to decide which one deposited the two flat moraine ridges in the Prunelli valley. Generation of a much larger glacier that could have transported and deposited the boulder Ku53 (Fig. 28A), needs lower temperatures as reported for some

Tab. 6: Terrace levels with their potential age (MIS and Alpine glaciation) from selected valleys in Corsica and the resulting incision rate.

level group	MIS ?	Alpine glaciations	valley age [kyr]	incision [mm/kyr]	number of terraces								
					Asin.	Nurs.	Tara.	F. Orbu	Prun.	Grav.	Vecc.	Cruz.	F. Grosso
3-9 m	2	LGM	20	150 - 550	3	1	2	1	4	3	5	6	4
40-50 m	6	Riss II	160	250 - 313	1	3	1	1	1	3			2
60-70 m	8	Riss I	220	270 - 320		1	3	2	1	1	3	2	1
100-120 m	10				2	5	4	2	3	3	3	4	
130-170 m	12	Mindel	420	310 - 400	3	3	2		1	4	1	2	2
180-200 m					1		2	2	1	1	2	3	
220-240 m	16	Günz	650	340 - 370		1	1	2	1				
c. 300 m	22		870	350								2	1

Asin. - southern Asinao, Nurs. - Nursoli, Tara. - Taravo, F.Orbu - Fium Orbu, Prun - Prunelli, Grav. - Gravona, Vecc. - Vecchio, Cruz. - Cruzini, F. Grosso - Fium Grosso valley

pre-Wuermian cold stages (e.g., Dahl-Jensen et al., 1998). Pre-Wuermian, probably Rissian depositional age for the boulder Ku53 is also supported by the generally smaller extent of the glaciation during the early Wuermian (MIS5a-d) in Northern Eurasia and the Alps (Preusser and Schlüchter, 2004; Svendsen et al., 2004) as well as by the observation of a larger pre-Wuermian glaciation in Italy (Federici, 1977, 1980; Palmentola and Acquafredda, 1983; Giraudi, 1998; Kotarba et al., 2001)

Old valley forms can also be dated by luminescence if sediments are preserved in-situ. In the Fiume Grossu valley southwest of the Tavignano plateau several generations of valley floors were found in the near of the villages of Murzo and Guagno-les-Bains (Fig. 29A). On some of these valley floors glacial sediments interpreted

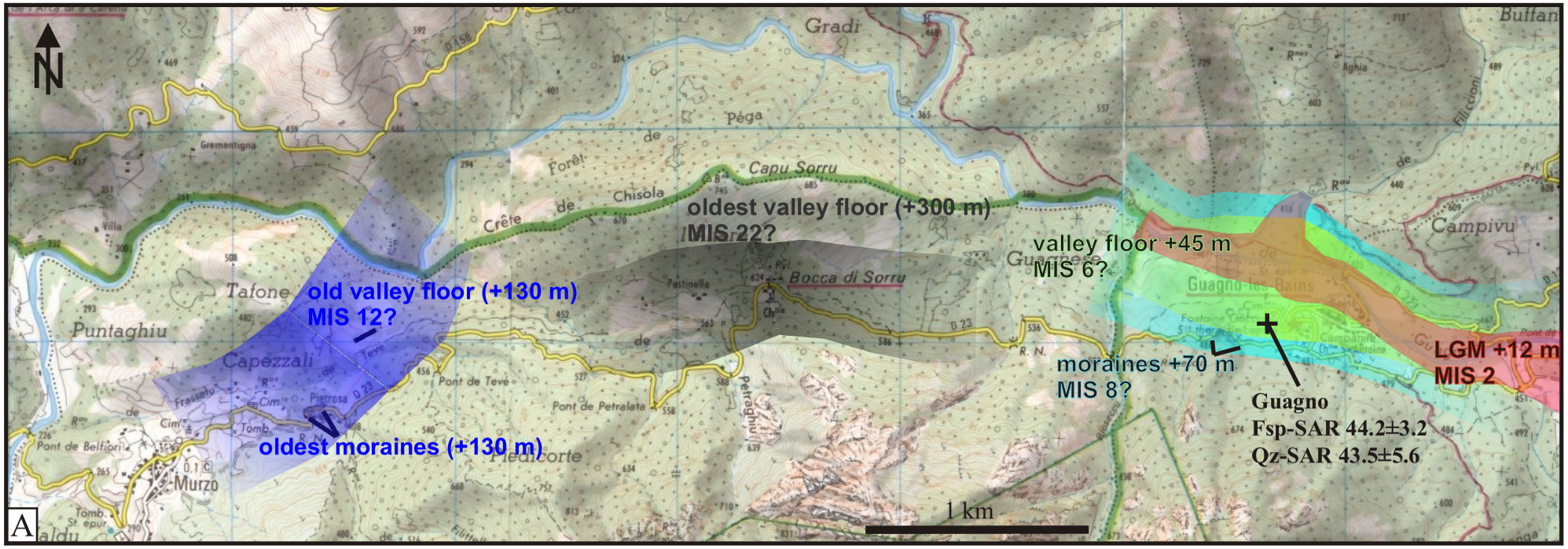

Fig. 29: A) Presumed valley floors of the Fium Grosso valley near Guagno-les-Bains south of the Tavignano plateau. The found moriane relics 130 m above the recent river are the oldest on Corsica. B) The glacial sediments in Guagno-les-Bains were deposited on granitic basement (inlet). The hammer points to the sampling location of sample Guagno. C) Evidence of periglacial activity provides this cryoturbation structure.

as moraine relics were found. As discussed by Kuhlemann et al (2007), post-LGM bedrock incision rates range between 3 and 9 m, with an average of 6.5 m, several metre-thick gravel beds excluded, reflecting an incision rate of 360 mm/kyr. Extrapolating this rate, a 45 m high terrace is expected to have formed by 162 kyr, matching Riss or MIS 6 respectively. 130 m above the river, even older glacial sediment relics are preserved which expose the virtually oldest moraine in Corsica. Linear extrapolation of the river incision rate in Corsica would mean 468 kyr, somewhat older than MIS 12 (Mindel, ~420 kyr). Certainly, river incision rates vary during the middle and late Quaternary, and a considerable regional variability is to be expected. Nevertheless, a sample of nine valleys from central and southern Corsica (all calc- alkaline granite) show typical terrace levels present in several valleys (Tab. 6). Up to 170 m above local base level, these terrace levels seem quite reliable. Higher up, the picture gets vague.

At Guagno-les-Bains, 45 m above the recent river bed (450 m a.s.l.), a sand lens in glacial sediments deposited on granitic basement was sampled for luminescence dating (Fig. 29B). Sample Guagno yielded ages of 44.2 ± 3.2 kyr (Fsp-SAR) and 43.5 ± 5.6 kyr (Qz-SAR) suggesting deposition during HE4 or HE5 (39.9-38.4 kyr and 46.5-45.4 kyr, respectively, Cacho et al., 2002). Moraines correlated to the HE2/LGM glaciation were found above 920 m a.s.l., ~10 km up-valley. The low altitude and the resulting large glacier together with the terrace level indicate that the age hardly represents the age of deposition of the moraines. As evidence of periglacial activity is provided by a cryoturbation structure exposed on this terrace (Fig. 29C) the re-deposition of older, probably Rissian moraines seems to be a reasonable explanation.

A further luminescence age of sand in moraine relics indicating deposition during HE5 at a quite low position was obtained in a tributary valley of the Fium'Orbu. At the interception of the tributary Ariola River with the Fium'Orbu, just behind a strong degraded lateral moraine ridge, a sand lens below a large boulder (Fig. 23A and H) was sampled. Sample OSL9 yielded ages of 47.6 ± 2.4 kyr (Fsp-MAA) and 43.0 ± 2.5 kyr (Fsp-SAR).

On the eastern slope of Mte. Renoso, in the Cannareccia valley, a newly enlarged forest road provides an almost 500 m long continuous outcrop of glacial deposits (Fig. 23A) which include four lateral moraines, separated by two 0.1 to 0.5 m thin coarse pebbly sand layers and a complex, up to 3 m thick unique fluvial deposit with soil relict structures in its central part (Fig. 30A and C). Especially the soil, but also the other fluvial sediments are deposits of warm climatic phases between cold phases generating glaciers. Since temperatures of the warm phases during the Wuermian were still too low, the Eemian interglacial (~126-110 kyr, analogous to MIS5e, ~135-115 kyr, Shackleton et al., 2003) would be the most reasonable age estimate for the soil layer. Three luminescence samples were taken out of each of the sandy layers. All samples are of excellent quality, better than any other luminescence sample analysed in this study. Any natural or anthropogenic disturbance can be ruled out. Despite these good external circumstances, the dating results are confusing. Sample Cann1 from the uppermost sand layer yielded an age of 15.5 ± 1.7 kyr meaning that moraine IV should be of YD age (Fig. 30A

Fig. 30 (next page): A) Sketch of exposure of moraine succession I-IV with fluvial sand layers inbetween along a forest road in the Cannareccia valley. Distance along the road is about 500 m. B) Schematic cross-section of the moraine succession. C) Map view. D) Sample Cann1 from the sand layer between moraine IV and III. E) Sample Cann2 from sand layer between moraine III and II. F) Sample Cann3 from the soil layer in the central part of the fluvial deposits between moraine II and I.

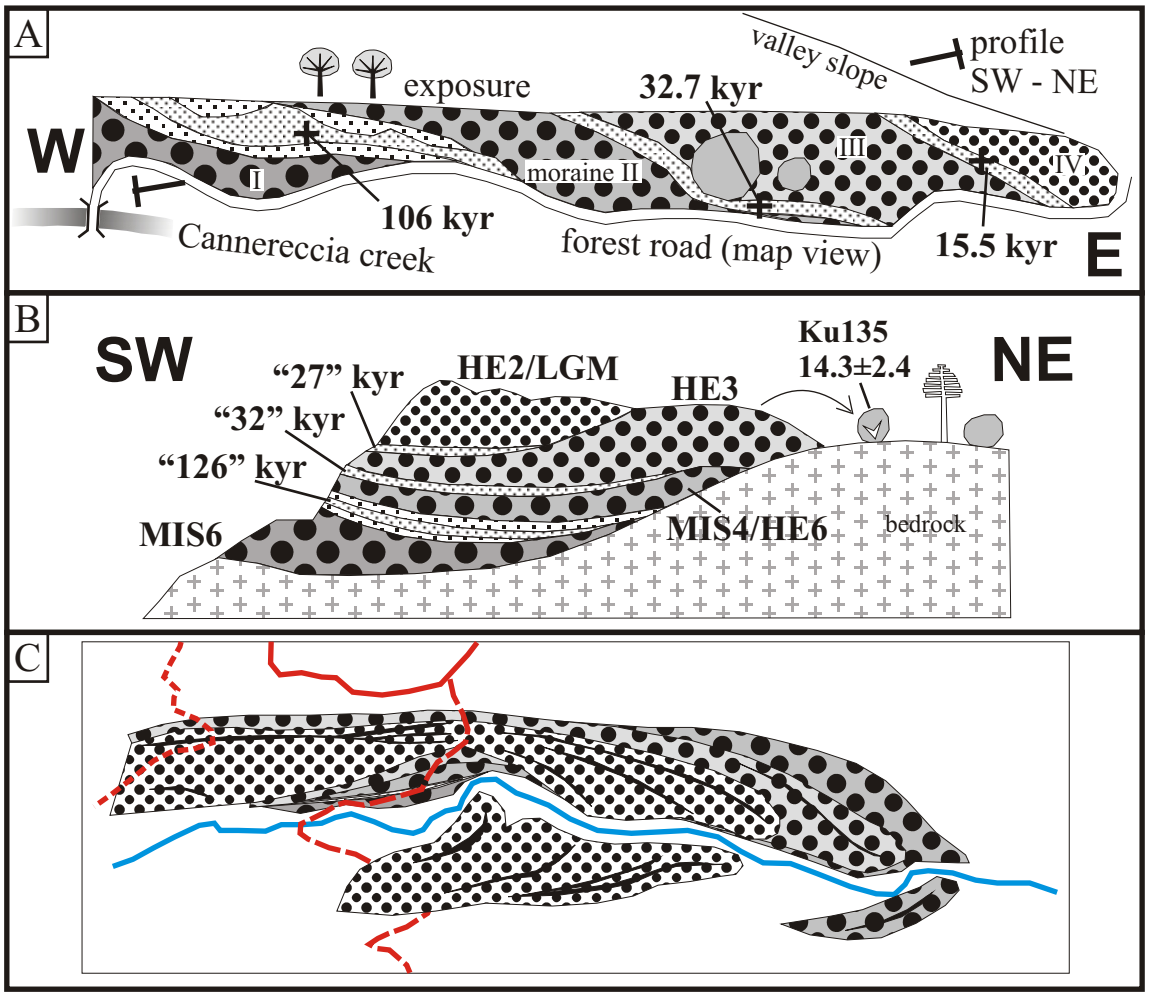
A
W
exposure
32.7 kyr
valley slope
profile
SW - NE
I
moraine II
III
IV
106 kyr
Cannereccia creek
forest road (map view)
15.5 kyr
E
B
SW
"27" kyr
HE2/LGM
HE3
Ku135
14.3±2.4
NE
"32" kyr
"126" kyr
MIS6
MIS4/HE6
bedrock
C


D


E


F

and D). Sample Cann2 yielded an age of 32.7 ± 3.7 kyr so that moraine III could be either OD, LGM, HE2 or HE3 (Fig. 30A and E). The third sample Cann3 taken from the soil layer (Fig. 30A and F) obtained an age of 106 ± 11 kyr which is quite close to the Eemian. It should be considered that bioturbation may have mixed the soil throughout the entire Eemian and even longer. A fading test for this sample shows a fading rate of 5.8 % per decade resulting in a corrected age of 186 ± 23 kyr which is a Rissian age. As the formation of a soil needs warm temperatures, this fading corrected Rissian age can not be considered as the depositional age, the fading rather seems to overestimate the age. Reasonable estimates of the total fading rate would be between 15 and 20 %. With an Eemian age for sample Cann3, moraine II would be either HE4, 5 or 6 and moraine I of Rissian age. HE6 was the longest and strongest cold event in the Atlantic (Bond et al., 1993) so it seems the most likely age for moraine II. The ages for samples Cann2 and Cann3 seem to be plausible without or with moderate fading, but the uncorrected age of sample Cann1 is unreasonably in the context of the island wide reconstruction of the YD glaciation. It suggests a YD glacier advance too far down as it could be explained with reasonable lowering of temperature and increase in precipitation. To get a plausible age a total fading rate of 80 %, as proposed for sample Cann3 by the test, but minimum of 50 % would be required. Under this assumption the most reasonable moraine stratigraphy along the road cut in the Cannareccia valley would be: HE2/LGM (moraine IV), HE3 (moraine III), MIS4/HE6 (moraine II), MIS6/Riss (moraine I) (Fig. 30B). However, preservation of Rissian moraine

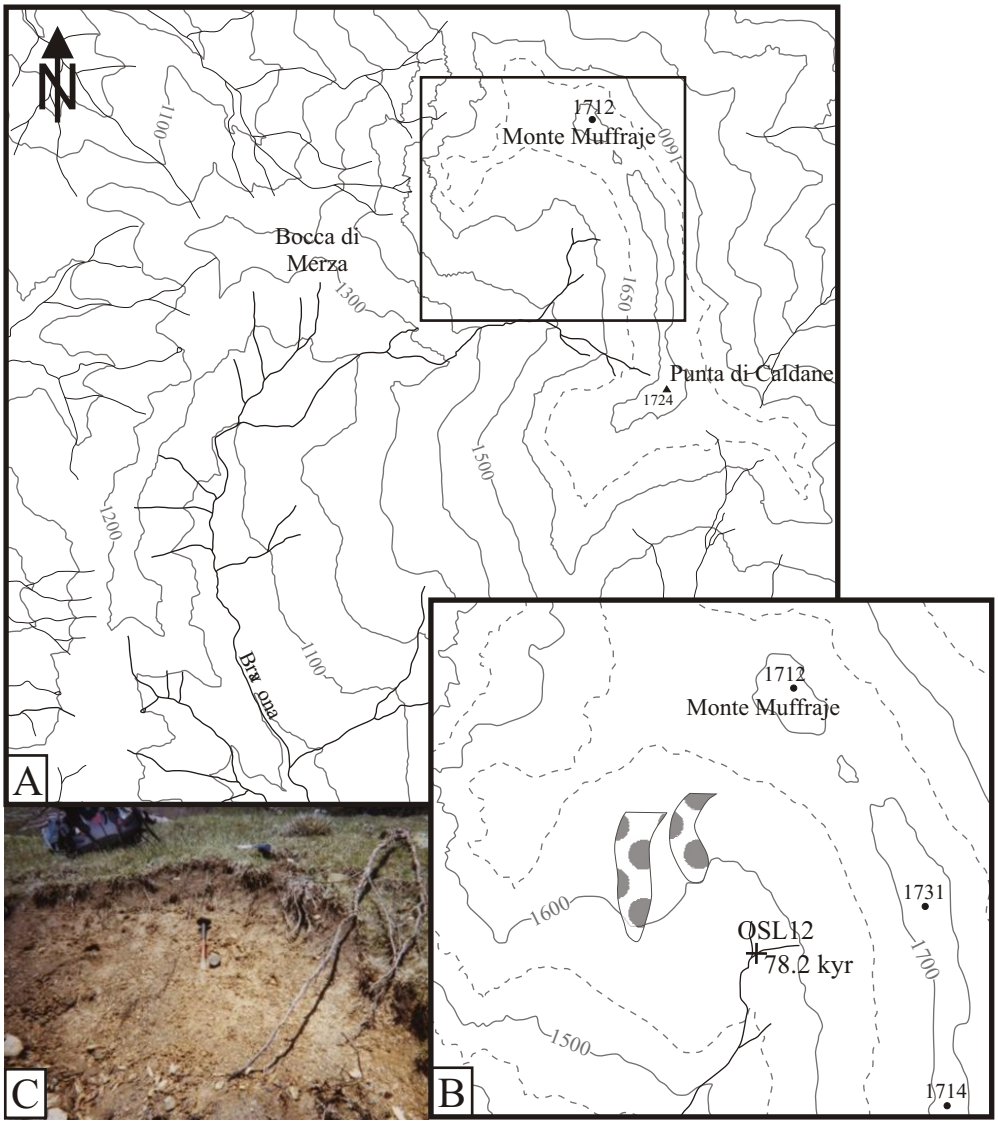

Fig. 31: A) In one of the highest areas of Alpine Corsica, glacial activity formed a flat, up to 800 m wide cirque with shallow slopes between Punta Caldane and Monte Muffraje. Map section ~3.5x3.5 km. B) Two 1 - 1.5 m high, broad moraine ridges with single erratic boulders of schist prove for the presence of small glaciers. Map section ~1.2x1.2 km. C) Sample OSL12 was taken at an undercut slope of a small stream.

in this fairly rugged terrain without being fluvially or glacially eroded is puzzling. Possibly, the sediments were deposited on a river parallel flat that prevented strong erosion (Fig. 30B).

4.2.11. Miscellaneous luminescence samples

There are some luminescence samples yielding ages that cannot be interpreted straightforward as they are either much "too young", a fact that was not expected at all for this kind of depositional environment, or "too old" to fit into the regional context. For the sake of completeness these samples are presented and shortly discussed in the following.

The only dated sample from Alpine Corsica comes from a flat, up to 800 m wide cirque with shallow slopes between Punta Caldane and Monte Muffraje (Fig. 31A and B). Despite its exposition towards the south, areas above 1500 m are covered with snow during winter until April. In the middle of May 2004 when sampling was done snow has just melted away so that soil and sediment were saturated with water. These observations together with first results of Corsican ELA reconstructions led to the idea that the youngest glaciers in the high regions of Alpine Corsica should be at least of LGM age since the average elevation of the reconstructed LGM ELA pattern for the Variscan Corsica makes the existence of LGM glaciers in Alpine Corsica reasonable. In the north/northwestern part of the Caldane cirque, two 1 – 1.5 m high moraine ridges with single boulders of schist prove for the existence of small glaciers (Fig. 31B). At the undercut slope of a small stream sample OSL12 was taken under the assumption that even such small glaciers eroded rock material in the source area causing transport with the possiblity of bleaching and subsequent sedimentation (Fig. 31C). The determined single age of 78.2 ± 4.3 kyr (Fsp-MAA) is not a good base for a solid estimation of the glaciation but it shows that either the sampling assumption was incorrect or the idea of glaciation during the LGM. Age underestimation would have been expectable since foundation walls of shepherd's huts and ruinous terraces show the former agricultural use of the cirque that might have caused erosion or destruction of the original sediments. As the regional ELA pattern for the LGM of Corsica suggests the existence of glaciers in the cirque, the overestimation of the glacier dynamic seems to be the most reasonable explanation for the old age. The small glaciers might have been quite immobile and not able to transport or erode larger amounts of sediment. Additionally, the glaciers shielded the subsurface that the shortly transported sediment could not be bleached sufficiently.

Below the Vizzavona HE2/LGM and HE3 moraines near a holiday camp at 800 m a.s.l. in the Agnone valley, a sand lens was sampled in sediment that was interpreted as moraine material in the field (Fig. 32A). Further morphological studies on air photos and topographic maps revealed that the large boulders belong to a large glacio-fluvial fan. This fan was deposited by the Speloncello River draining the northeastern flank of Mte. d'Oro. In this valley, a large lateral moraine around 1400 m a.s.l. and a small glacial scour basin at 1350 m a.s.l. indicate the position of the glacier that provided the material for the glacio-fluvial fan. The dating result of 26.4 ± 1.5 kyr (Fsp-MAA) and 23.2 ± 1.3 kyr (Fsp-SAR) (OSL10) integrates the glacier into the HE2/LGM glaciation. The obtained ages provide few evidence for the glacial history of the Agnone valley at 800 m a.s.l. except for the fact that late Wuermian glaciation did not reach the fan. The U-shaped valley though continues down to the dissected flat of Tattone, indicating glacial erosion during older glaciations.

Sediments deposited at the level of terraces 70 – 100 m above the recent river were misinterpreted in

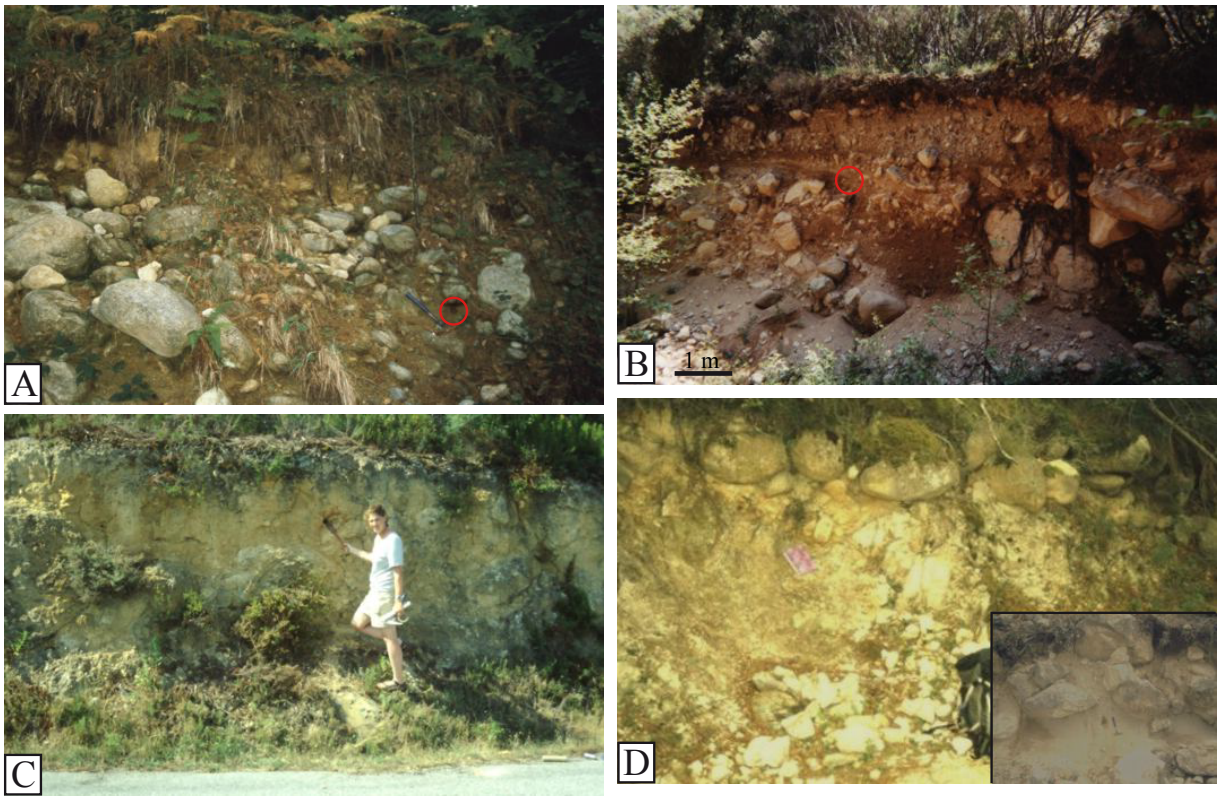

Fig. 32: Luminescence samples from A) a fluvial fan near Tattone in the Agnone valley, B) layered sediments in the southern Asinao valley at the confluence with the Caracutu valley, C) a terrace of the Vecchio river, and D) fluvial sediments above the Fium'Orbu near the settlement Cavu.

the southern Asiano valley in the Bavella (Fig. 32B). Sample OSL18 was taken under the assumption, that the sediment is part of the high terrace. But the obtained very young ages of 14.3 ± 0.8 kyr (Fsp-MAA) and 13.5 ± 0.7 kyr (Fsp-SAR) indicate that the sediment should be correlated to the tributary Caracutu valley.

Fluvial terraces and relics of older valley floors are common geomorphological features in the large Corsican valleys. Tab. 6 shows a try to correlate and tentatively date the different levels found in nine large valleys. In contrast to Conchon (1975, 1986a), who used colour and weathering indexes for her stratigraphy, in this study elevation above the recent river is the main sorting criterion as it is controlled by the incision rate. To confirm the relative dating with luminescence ages turned out to be difficult, first because appropriate sediments are rare, and second because ages seem to be much too young. Sample OSL5 was taken from a terrace in the Vecchio valley (Fig. 32C) ca. 60 m above recent river with an expected Rissian age (220 kyr, incision rate 270-320 mm/kyr). The dating result of 63.4 ± 3.2 kyr (Fsp-MAA) suggests a deposition during HE6 implying a bedrock incision rate of about 1000 mm/kyr. As this value is unreasonably high, re-deposition of the sediment might have caused the younger age. Sample OSL8 taken on a terrace 20 m above the recent river in the Fium' Orbu valley near the settlement Cavu (Fig. 23A, Fig. 32D) is somewhat special because unconsolidated sediment in outcrops on the forest road down to the river suggesting that the terrace was incised in unconsolidated material instead of bedrock. The expected age of a bedrock terrace would be 140 kyr but incision rates in unconsolidated material are quite different and difficult to estimate. So judging the quality of the obtained ages of 25.8 ± 2.1 kyr (Fsp-MAA) and 22.1 ± 2.1 kyr (Fsp-SAR) suggesting deposition during HE2/LGM is difficult, too. Boulders which are too large for fluvial transport under recent climatic conditions are common in the recent river bed.

As indicated by moraines the LGM glacier advance in the Fium'Orbu and its larger tributaries ended 3-4.5 km upstream (Fig. 23A). Boulder transport during floods that far is arguable and might be possible during retreat of LGM glaciers. Another argument for the LGM age is the fact that the youngest terrace maximum 2 m above river is too low for LGM and should be of late-glacial age. The next terrace above, which is the dated terrace, would be expected to be the LGM terrace.

4.3. Conclusion

Mapping and dating of glacial sediments on Corsica indicate a good correlation between late Wuermian cold phases found in marine sediments of the western Mediterranean (Cacho et al., 2002) and the North Atlantic (Bond et al., 1993, Mix et al., 2001). The widespread glaciation during the last Wuermian cold phase of HE2 and LGM left behind the largest moraines which could be dated sufficiently. State of preservation of moraines in general strongly depends on width and gradient of the valley with the best preserved moraines in broad valleys, and poor or any preservation in narrow and steep valleys. Dating results are restricted to the central and southern part of the mountain chain because the volcanic rocks of the Cinto massif do not provide the free quartz and feldspar needed for exposure age dating with ^{10}Be or luminescence dating. Nevertheless, with the dating results in combination with morphological observations correlation is possible. At five dated sites, in the Golo, Tavignano, Agnone, Prunelli and Nursoli valley, the LGM advance produced four or five ridges. Similar staged moraines with the same number of ridges were found in other valleys, also in the Cinto massif, and are assumed to be of the same age. Locally, the Wuermian maximum ice extent precedes the global LGM as in few valleys strongly degraded moraines were found down-valley of the LGM moraines that should be older. Due to bad preservation results of exposure dating of moraine ridges are questionable but in the Cruzini valley, at the eastern Verde flank, and possibly in the Cannareccia valley luminescence dating revealed moraine material of a HE3 advance larger than that of the HE2/LGM. In the Restonica and Marmano valley HE2/LGM advances might have reworked HE3 glacial sediment. The difference in extent between HE3 and HE2/LGM is quite variable as in some cases the older moraines have a short distance to the younger ones; in other cases the moraine relics indicate advances 1 – 2.5 km further down-valley.

Relics of re-advances during the deglaciation, especially during the HE1/Oldest Dryas and the Younger Dryas, are preserved in nearly every valley where also the LGM moraines are preserved. As boulders are mainly small or angular, dating of moraine formation was possible only at few locations. The best dating results were obtained with polished bedrock.

Beside sedimentological observations, the stratigraphy of Conchon (1975, 1989) is based on the assumption, that the Wuermian glaciations were the smaller the younger and that Corsica was free of ice since the Allerød (Conchon, 1984). The now dated moraines of the LGM were nearly continuously placed into the middle Wuermian (N5), the glaciation of the OD into the LGM (N6), and the few moraines taken for OD (N7) are now of YD age. Moreover, ongoing work shows that the high glacial cirques were occupied by small glaciers during the Holocene. This reveals the importance of absolute dating when glacial sediments are correlated supra-regional or with marine data sets.

Pre-Wuermian glaciations larger than the Wuermian glaciations were already postulated by Conchon (1975 and following works) particularly for the Rissian (N3). This idea could be substantiated with few more data but the exact timing and the extent remain unknown.

The applicability of cosmogenic dating strongly depends on the erosion rate. The values of 6 and 20 mm kyr^{-1} that set the limits of the observed ^{10}Be erosion rate range (Kuhlemann et al., 2007) seem to be rare extreme values and not representative for the sampled boulders and polished rocks. Published mean erosion values for crystalline rocks and common values used in exposure age studies lie well below 10 mm kyr^{-1} (e.g. Small et al., 1997; Kaplan et al., 2004; Kelly et al., 2004). As a compromise, most of the cosmogenic ages have been calculated with an erosion rate of 10 mm kyr^{-1}. Samples from surfaces with textures like preserved glacial polish that are geological evidence of insignificant erosion have been calculated without erosion whereas samples from boulders showing a high degree of grusification have been calculated with 15 mm kyr^{-1}.

5. Glaciation and climate

5.1. Reconstruction of late Wuermian glaciation

The results of the glacial sediment dating allow a reconstruction of three different phases of the late Wuermian glaciation, including the Last Glacial Maximum (LGM), the Oldest Dryas (OD), and the Younger Dryas (YD) (Fig. 33A-C). The scarce findings of HE3 glacial sediments do not allow a reconstruction of the glaciation that was partly of a similar extent like the LGM, partly of larger extent. The outlines of the glaciers were drawn on a DEM following morphologic features as trimlines or U-shaped valleys. Trimlines are characterised by a change in slope (steep to moderate in the accumulation area, moderate or low to steep in the ablation area/valley) and a change in the degree of weathering. Bedrock that was eroded by late Wuermian glaciers has a quite smooth surface and shows little to no larger weathering features like tafonis in contrast to bedrock weathering since pre-Wuermian time which is characterised by a rough surface with sharp edges and tafonis. Both, the glaciation of valleys with moraine relics not suitable for dating and that of valleys with scarce moraine relics were reconstructed by careful valley-to-valley correlation. Poor moraine preservation is typical for steep and narrow valleys of the Cinto massif and the Bavella as well as for small catchments like along the Verde chain or in Alpine Corsica. Moreover, the rhyolites of the Cinto massif and the schists of the Alpine Corsica do not have enough free quartz what makes dating impossible with the methods of this study.

5.2. Reconstruction of equilibrium line altitudes and regional climate interpretation

Well-constrained glaciers were chosen to reconstruct the glacial hypsometry and to calculate the equilibrium line altitude (ELA). The hypsometry was constructed on the DEM drawing polygons for each altitude segment (Δ100 m) correcting the isolines for the ice thickness (Fig. 34). The ELA was then calculated with the AAR and the AABR method using a ratio of 0.6 and a balance ratio of 2, respectively (Tab. E8, see chapter 3.3.). ELAs calculated with the AABR method lie manly higher than corresponding AAR ELAs, on average 63 m for the LGM (Fig. 35). For OD and YD this difference is slightly larger with 83 and 86 m, respectively. The overall regional pattern, though, is the same and a climatic interpretation would produce similar results but with a stronger temperature drop for the AAR values. In the following interpretations of regional ELA patterns for the LGM, OD, and YD, the values calculated after the AABR method were used.

5.2.1. Last Glacial Maximum

To construct isolines of ELAs for the Corsican mountains during the LGM 40 calculated ELA values from detailed hypsometry (Tab. E8) and 45 estimated ELA values of the LGM glaciation (Fig. 36A) were used. The average ELA is 1573 m. Without considering moisture, the ELA depression compared to the recent average ELA of 3150 m corresponds to a pure temperature difference of 9.5 °C. The regional ELA pattern shows minima at the steep margins of the northern and eastern mountains (Fig. 36B). These minima are part of strong gradients

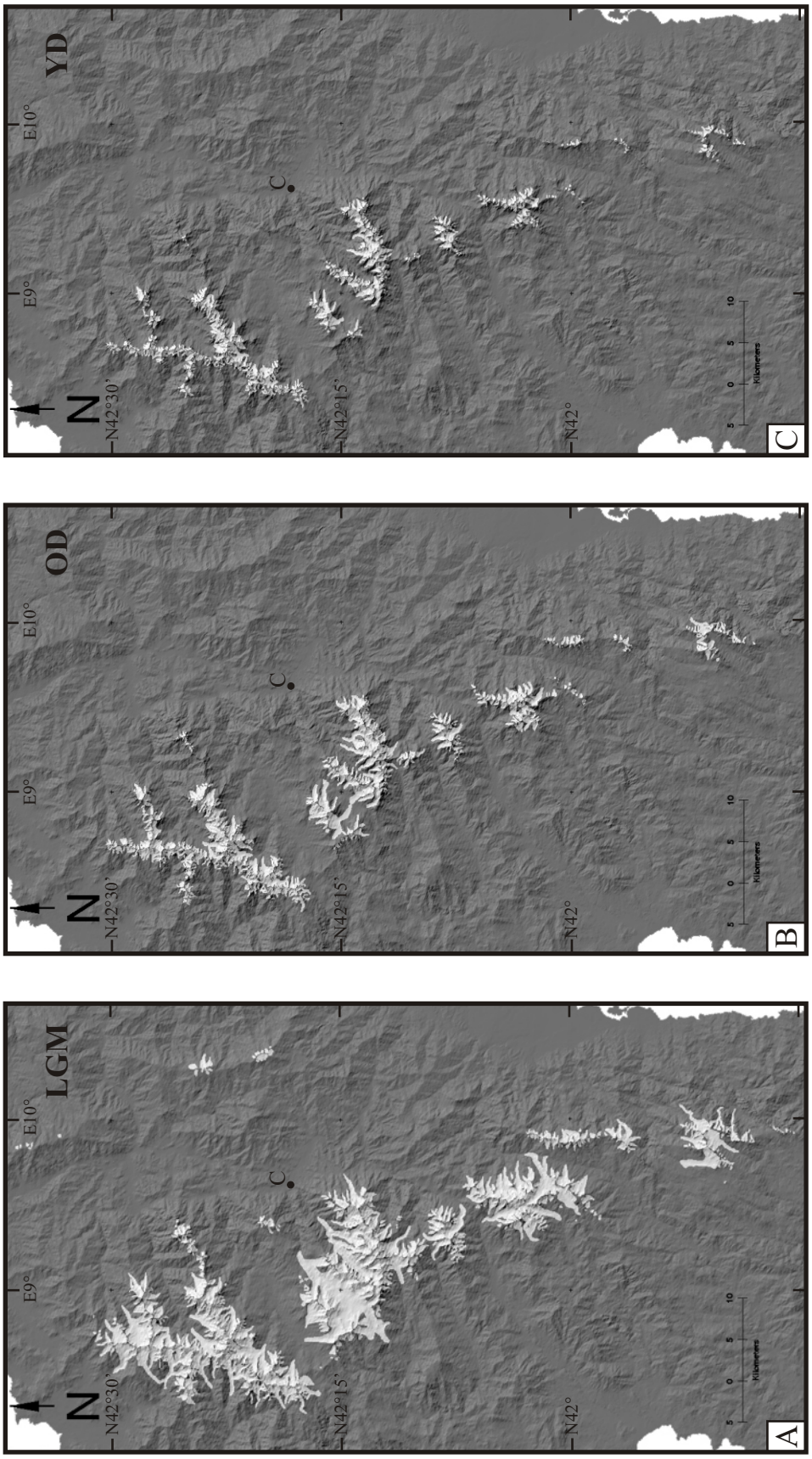

Fig. 33: Reconstructed glaciations of the Last Glacial Maximum (A), the Oldest Dryas (B) and the Younger Dryas (C) on Corsica. C: Corte.

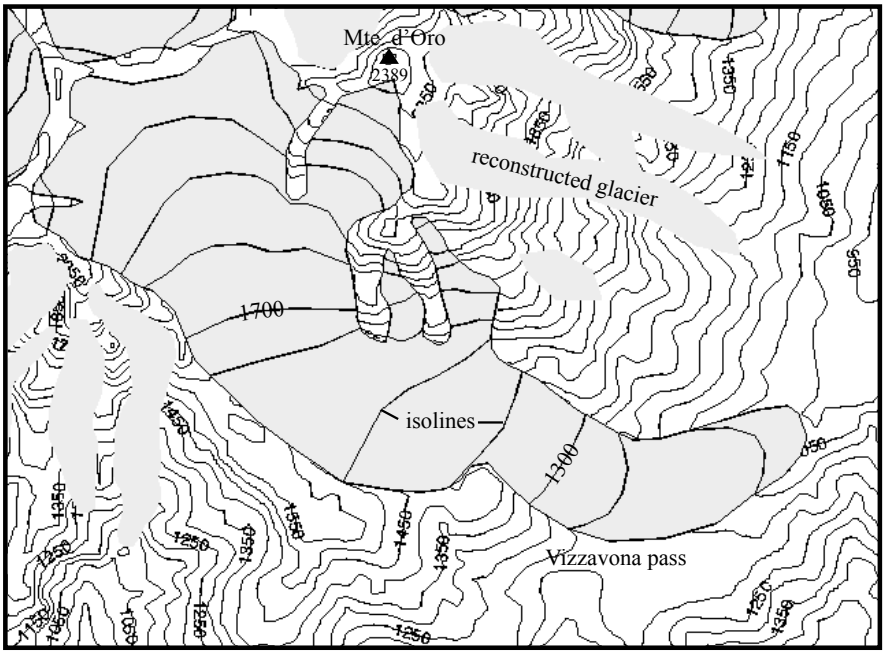

Fig. 34: Illustration of hypsometric reconstruction showing isolines of ice thickness for every 100 m altitude segment.

of the ELA isolines which are parallel to high topographic gradients. Clouds approaching from either westerly or easterly directions were forced to release precipitation at these steep margins. The maximum ELA is located at the southeastern flank of the Cinto massif above the northern Niolo valley. The Cinto massif combines the strongest ELA contrasts with a range of spatial variability up to 800 m, whereas the massifs of Rotondo, Oro and Renoso show only moderate to low variations (Fig. 36B). The low passes of Col de Vergio and Col de Vizzavona display an ELA depression as the isolines of the lower ELA curve towards the passes, towards the east or northeast. The opposite situation is found at Col de Verde where the higher ELA curves towards the northeast (Fig. 36B). This is due to the deep valleys southwest of the passes with a wide and gentle character funneling approaching air masses.

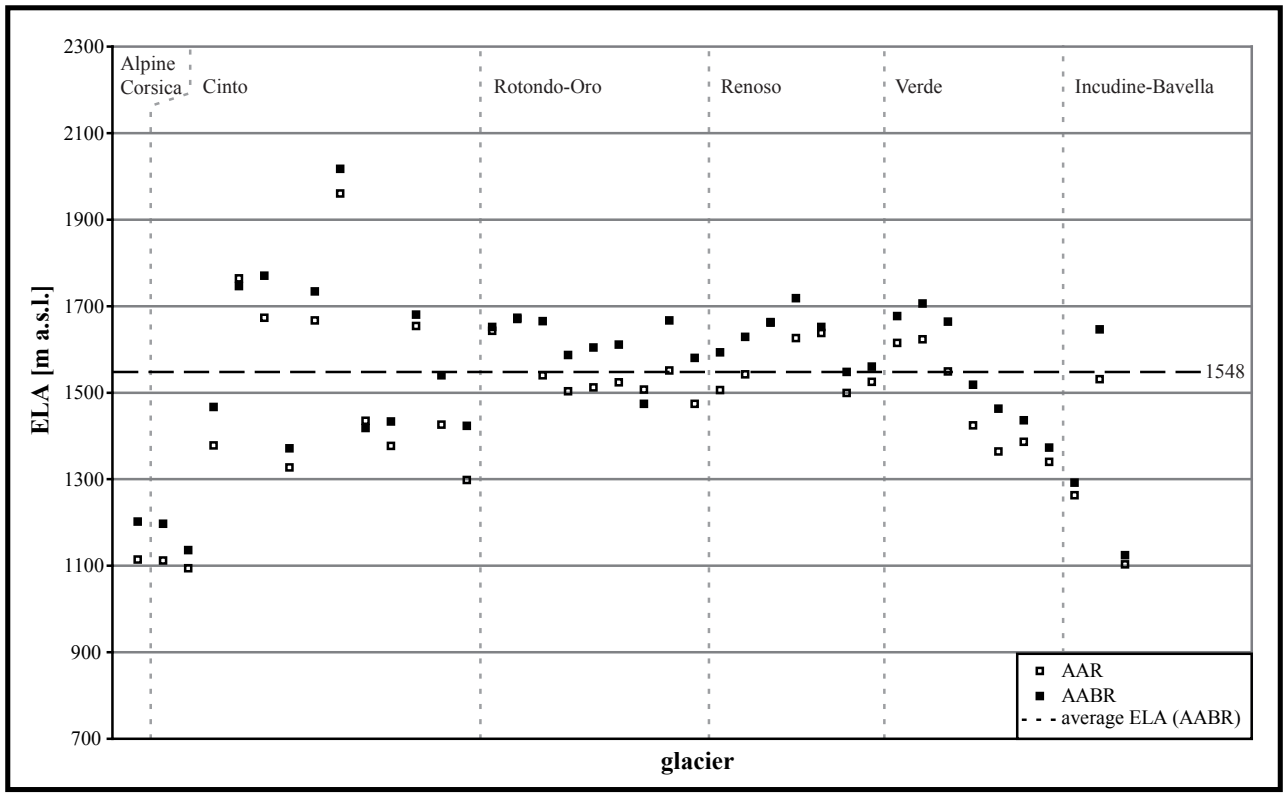

Fig. 35: Equilibrium line altitudes (ELAs) of the LGM calculated with the AAR and AABR method for all hypsometrically reconstructed glaciers sorted from N to S. On average, ELAs calculated with AAR lie 63 m higher than those of the AABR method. The main pattern is similar.

The ELA pattern of Fig. 36B was converted into an anomaly map by subtracting an LGM mean ELA value of 1600 m (Fig. 37A) to extract information about temperature and moisture anomalies. For a first-order de-convolution of the underlying temperature and precipitation components (Figs. 37B and 37C) the relations "100 m ΔELA equivalent to 0.65 ºC temperature change (ΔT)" and "100 m ΔELA equivalent to +11 %/ -9 % of precipitation change (Δpp)" were used (Ohmura et al., 1992). As independent control on palaeotemperature, e.g. from treeline depression, is not available, the differentiation is semi-quantitative, based only on strong relief-controlled gradients.

Generally, positive ELA anomalies (high ELA) are caused by warm and dry local climate whereas negative ELA anomlies (low ELA) are caused by cool and wet local climate. The proportion between temperature and precipitation was chosen analogue to ratios found in climatic data of the Present (Kuhlemann et al., 2008, supplement S1) where the stronger the ELA-anomaly is the larger is the influence of the precipitation. The ELA pattern for the LGM shows a strong positive anomaly in the northern centre (Fig. 37A), which is likely due to an enhanced foehn effect of northwestern winds. Furthermore, the attributed strong moisture deficit of up to 27 % (Fig. 37C) reflects reduced recycling of moisture from reduced vegetation cover (no forest). The wide and

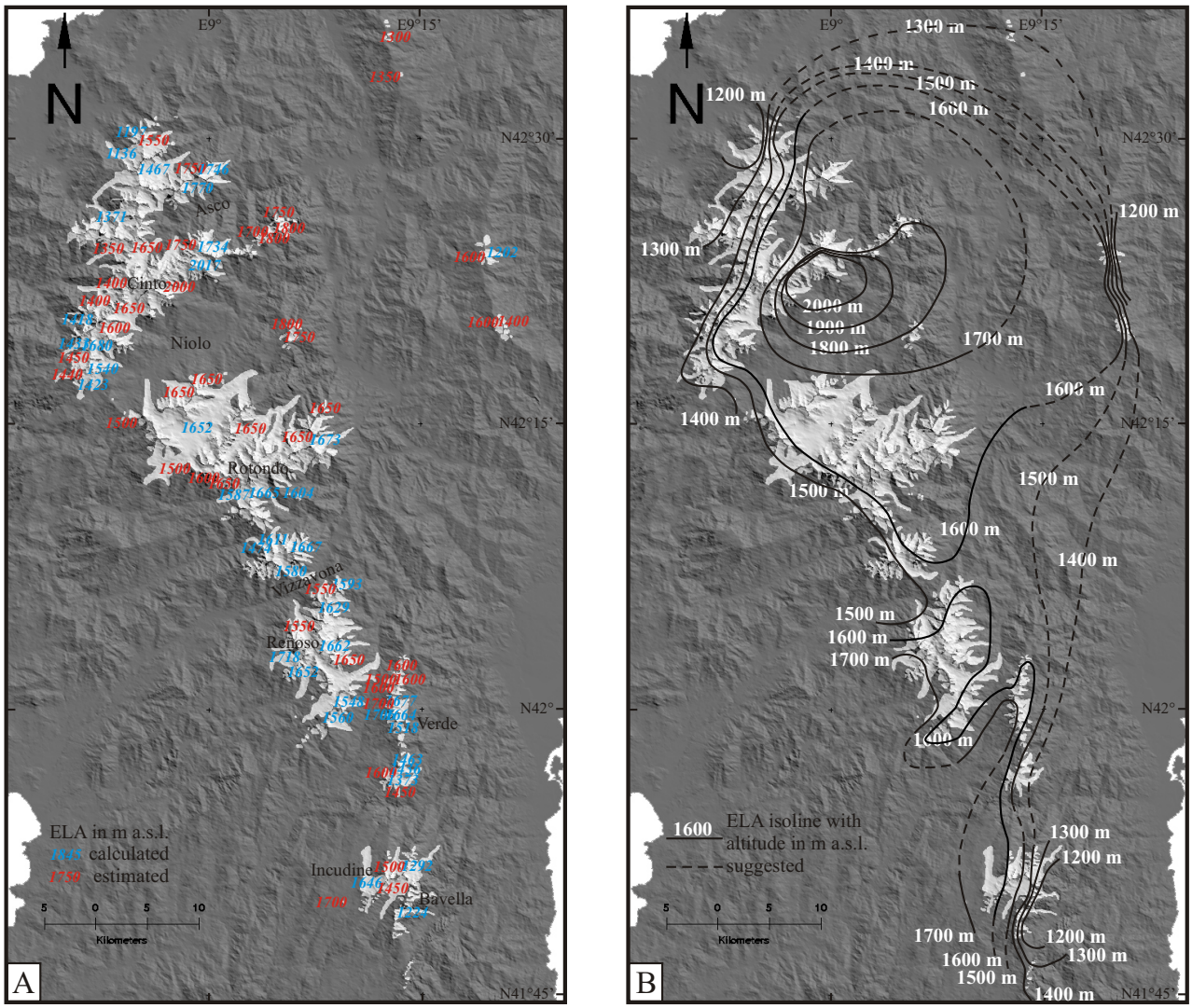

Fig. 36: ELA reconstruction of the LGM. A) Base of the reconstruction of the ELA isoline pattern are calculated ELA values from detailed hypsometry (blue) and estimated values (red). B) Interpolated ELA isolines.

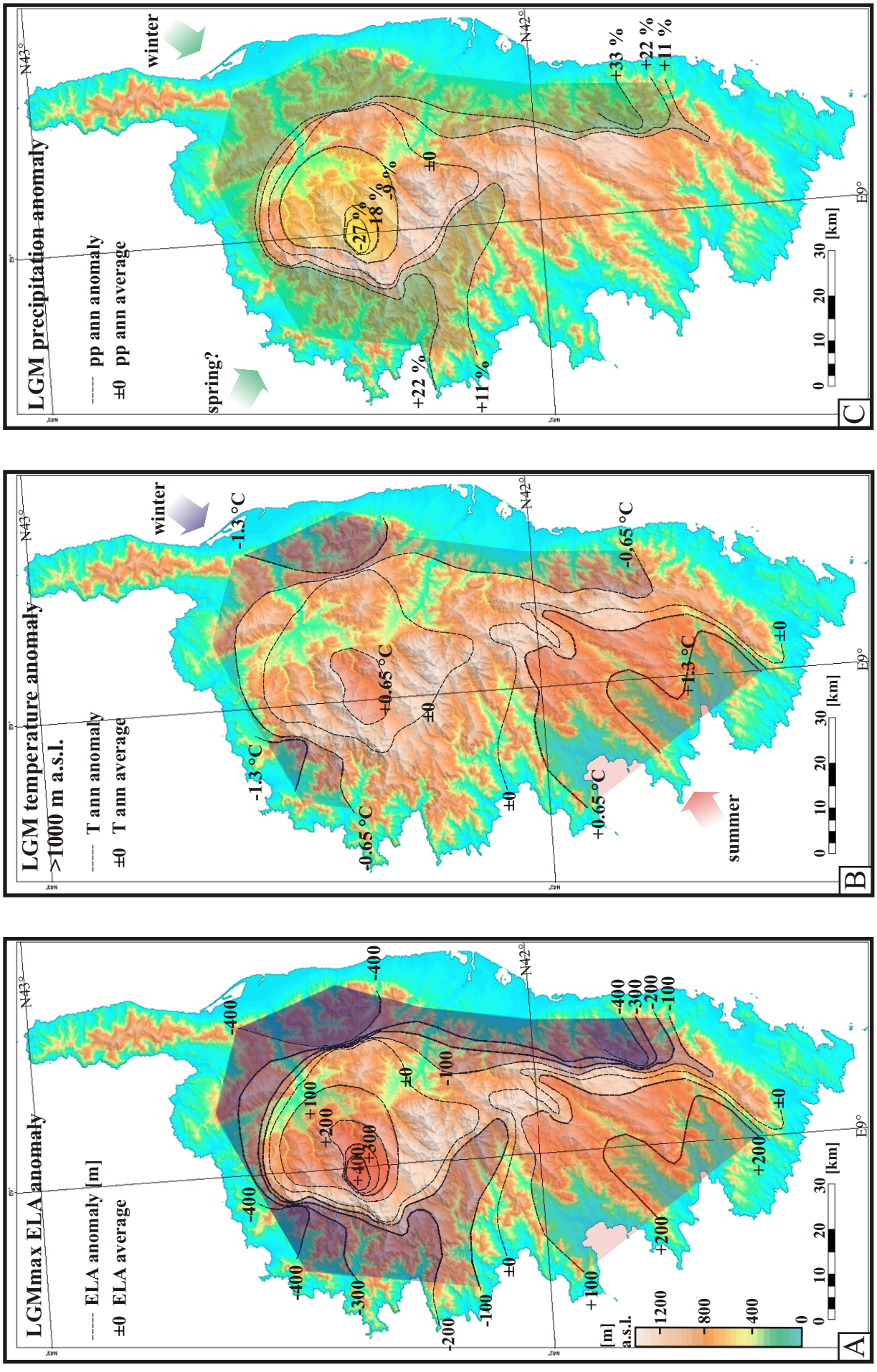

Fig. 37: Last Glacial Maximum ELA anomaly (A) and inferred anomaly patterns of temperature (B) and precipitation (C).

fairly high Niolo valley (above 800 m a.s.l.) appears to favour the development of local high air pressure which tends to hamper clouds from spilling over the surrounding drainage divides. Besides a positive anomaly in the southwest, the ELA pattern of the LGM shows a negative anomaly at the eastern, northern, and northwestern margins. In the N and NE, a stronger temperature component might reflect winter-time (very cold) continental air advection from the N and NE (Fig. 37B). In analogy to a modern positive spring-time precipitation anomaly (Bruno et al. 2001) an additional dominant precipitation component is inferred in the NW (Fig. 37C). In the SE, the precipitation component is assumed to be even larger. The relatively high temperatures in the SW of Corsica (Fig. 37B) might reflect advection of relatively warm and seasonally dry air from the western Sahara, predominantly during summer like at Present. Indicated by the strong negative anomaly in the SE, the warm anomaly might also mirror easterly advection of cold and especially humid air in winter, driven by stationary or slowly moving cyclones in the northern Tyrrhenian Sea, which cause foehn effects in the SW of Corsica.

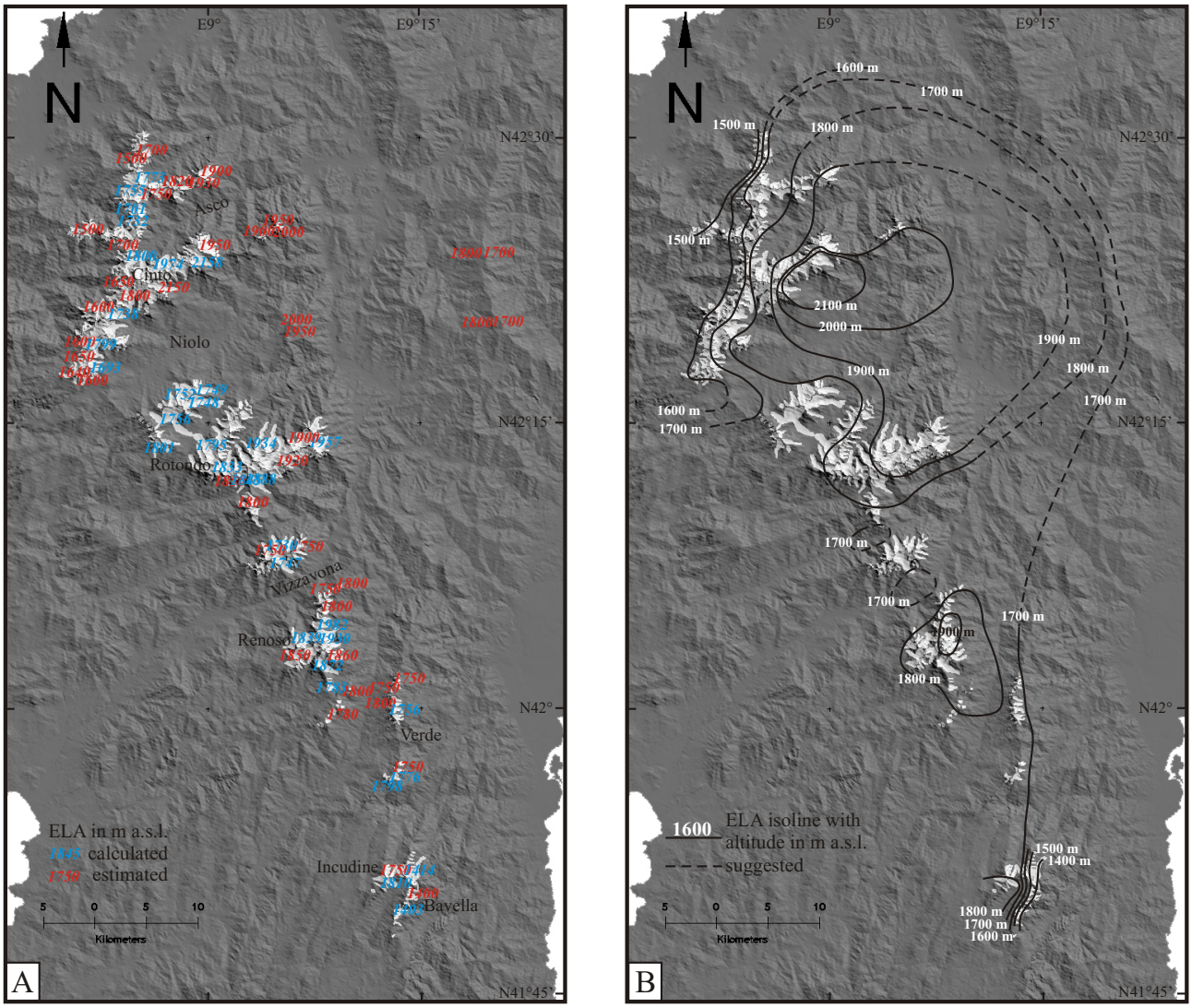

Fig. 38: ELA reconstruction of the Oldest Dryas. A) Base of the reconstruction of the ELA isoline pattern are calculated ELA values from detailed hypsometry (blue) and estimated values (red). B) Interpolated ELA isolines.

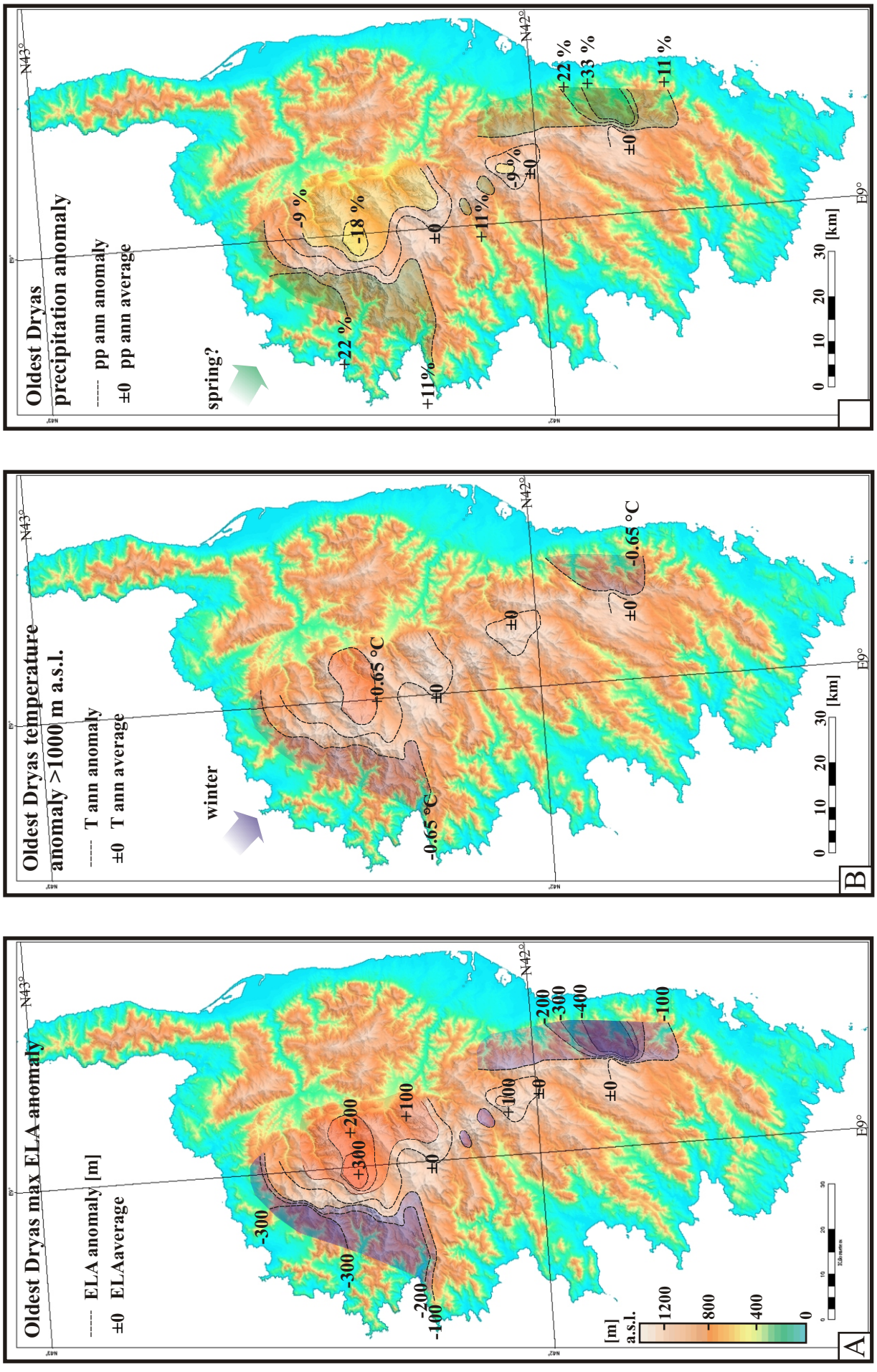

Fig. 39: Oldest Dryas ELA anomaly (A) and inferred anomaly patterns of temperature (B) and precipitation (C).

5.2.2. Oldest Dryas

For the construction of the ELA isolines during the OD 34 calculated ELA values from detailed hypsometry and 35 estimated ELA values of the OD glaciation (Fig. 38A) were used. The average ELA is 1786 m. The altitudinal difference to the recent average ELA of 3150 m gives a temperature difference of 8.2 °C what is 1.3 °C warmer than the LGM. This is similar to the warming found in the Tyrrhenian Sea but slightly lower than in the Alboran Sea (Cacho et al., 2002). The regional ELA pattern during the OD is largely similar to that during the LGM. The trend of the isolines above the Alpine Corsica is a rough estimate based on the LGM pattern since there did not exist any glaciers. So minima of the ELA and strong gradients are only found at the steep margins of the northwestern and southeastern mountains (Fig. 38B). The maximum ELA is still located at the southeastern flank of the Cinto massif above the northern Niolo valley. With 700 m the spatial variability is slightly smaller than in the LGM. Only small variations are found in the southern central region between Mte. Rotondo and the Verde chain where higher ELAs are suggested in the high regions of the massifs and lower ELAs at the low passes (Fig. 38B). Like in the LGM reconstruction, the low pass of Col de Vergio displays an ELA depression with isolines curving towards the pass towards the east/ northeast.

The ELA anomaly map constructed by subtracting an OD mean ELA value of 1800 m displays the strong positive anomaly in the northern centre and the strong negative anomalies in the NW and SE (Fig. 39A). The moisture deficit of the positive anomaly of up to 18 % is smaller than during the LGM indicating a slightly reduced foehn effect of northwestern winds (Fig. 39C). Temperature anomalies are quite moderate with ±0.65 °C whereas the precipitation anomalies are suggested to be stronger (Figs. 39B and C). According to recent observations in the NW the low temperatures are suggested to result from cold winterly air masses and the positive precipitation anomaly from moist air masses in spring time. The warm temperatures in the SW of Corsica found in the LGM pattern cannot be proved for the OD but since the ELA there seems to be above the mean of 1800 m a still warm SW is suggested.

5.2.3. Younger Dryas

The ELA isolines of the YD were constructed with 31 calculated ELA values from detailed hypsometry and 53 estimated ELA values (Fig. 40A). The average ELA is 1883 m. The ELA depression of 1367 m compared to the Present equals 7.6 °C considering a pure temperature effect. In the area of the Gulf of Cadiz and the western Mediterranean, the sea surface temperatures (SST) were 7 and 9 °C colder, respectively, than at Present (Cacho et al., 2002). For the northern Alps, ELA depressions of 450 to 500 m against the Present and a summer temperature depression of 3.5 °C are reported, even less for the central Alps (Kerschner et al., 2000). Compared to those values, the YD cold phase on Corsica reveals quite low ELA values. Comparison to other Mediterranean mountain ranges is hampered by a lack of a robust stratigraphy of late glacial moraines.

The regional ELA pattern during the YD is largely similar to those during the OD and LGM. Minima of the ELA are still found at the steep margins of the northwestern and southeastern mountains but with less strong ELA gradients (Fig. 40B). The spatial variability is again smaller with 600 m. The maximum ELA is also still located at the southeastern flank of the Cinto massif. The ELA pattern south of Mte. Rotondo is nearly the same as during the OD but 100 m higher (Fig. 40B).

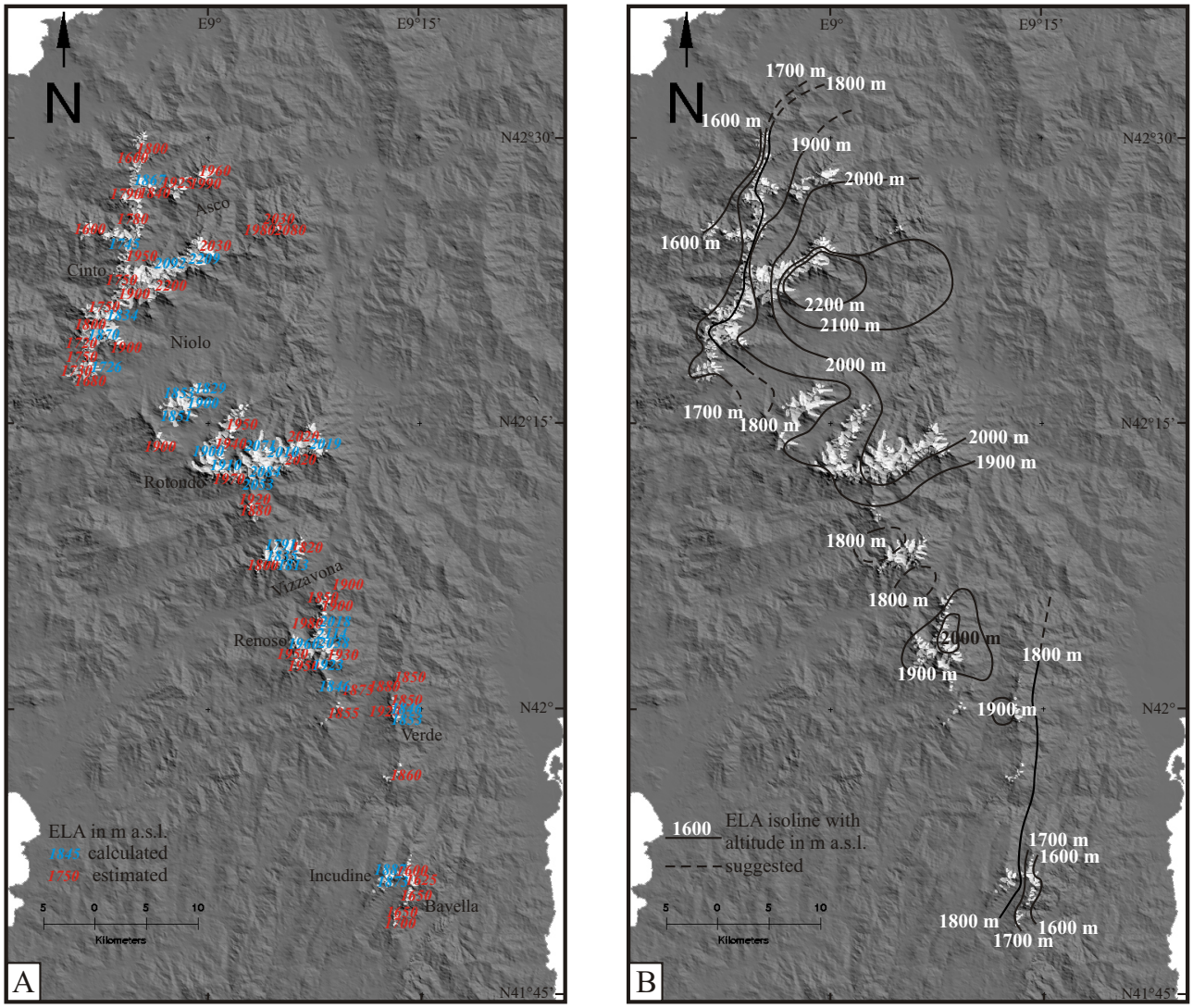

Fig. 40: ELA reconstruction of the Younger Dryas. A) Base of the reconstruction of the ELA isoline pattern are calculated ELA values from detailed hypsometry (blue) and estimated values (red). B) Interpolated ELA isolines.

The ELA anomaly map constructed by subtracting a YD mean ELA value of 1900 m displays the positive anomaly in the northern centre and the negative anomalies in the NW and SE (Fig. 41A). Temperature and precipitation anomalies (Figs. 41B and C) are in the same order as for the OD (Figs. 39B and C)

5.2.4. Climate change

Local change of climate differentiation besides the general warming is indicated by ELA difference plots. In Fig. 42 plots for the difference between LGM and OD, and OD and YD are shown. As the general warming is indicated by the rise of the mean ELA, divergences above or below this value are interpreted in terms of anomalies in moisture supply/ precipitation. Between LGM and OD the mean ELA increased by ~200 m, the difference plot shows values between 0 and >400 m (Fig. 42A). Values above the 200 m indicate less moisture supply for the OD, values below more moisture. The pattern in Fig. 42A shows large areas that were drier during the OD (>200 m ELA difference), especially in areas of high mountain relief (NW, NE, and SE) supporting the idea that the ELA gradients there decreased. Or vice-versa, that the LGM in these regions was quite moist explained

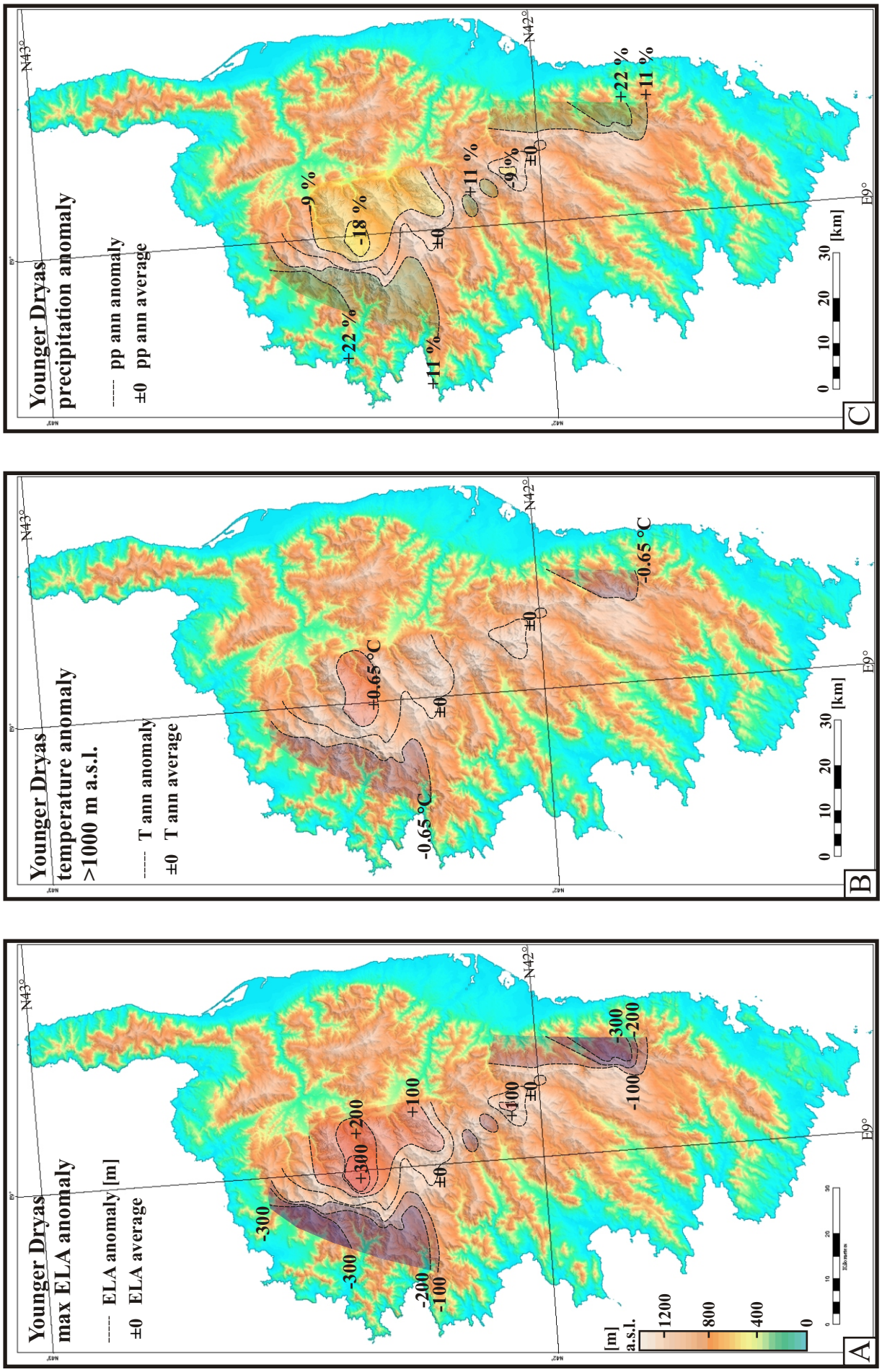

Fig. 41: Younger Dryas ELA anomaly (A) and inferred anomaly patterns of temperature (B) and precipitation (C).

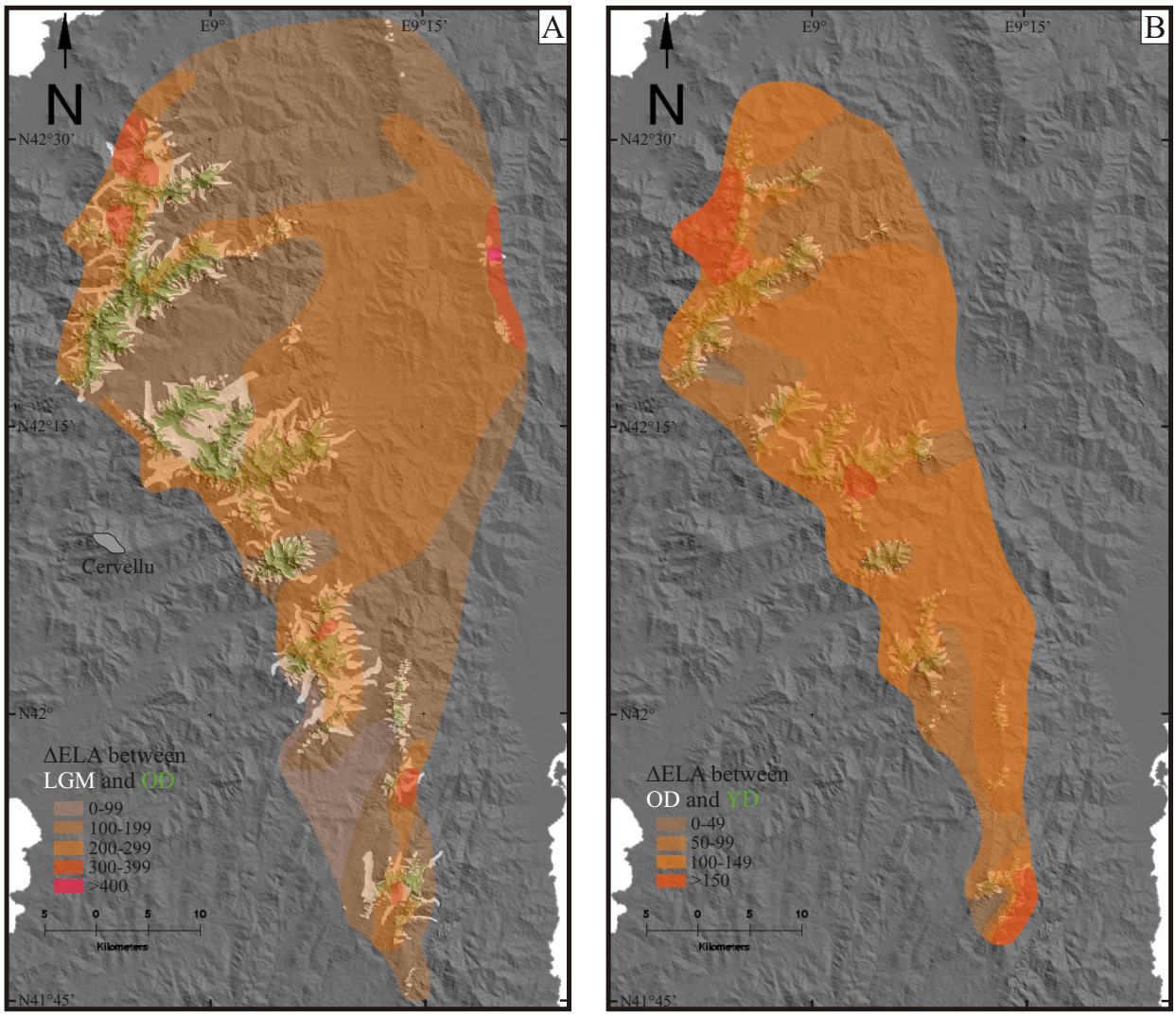

Fig. 42: Difference in m between the ELA of the Last Glacial Maximum and the Oldest Dryas (A) and between the Oldest Dryas and the Younger Dryas (B).

by an increased contribution of convective precipitation. In the Cinto massif, NW exposed flanks become drier, SE exposed flanks wetter, underlining the trend towards decreased gradients along topographic barriers. The drying trend indicates a turn back to a "normal" convective contribution.

An explanation for the anomaly along the W flank of the Tavignano plateau might be the difference between the large outlet glacier of the plateau glacier during the LGM and the quite small, poorly constrained glaciers in steep valleys during the OD. On the other hand the glaciers at the flank are small compared to glaciers on the Tavignano plateau during the OD so that the trend towards slightly less moisture compared to a moister plateau and Vergio pass seems to be a real anomaly. The extreme dryness in the Niolo during the LGM (Fig. 37C) is slightly diminished during the OD as indicated by an ELA difference <200 m, like also found for the northernmost area (Fig. 42A). Moist air seems to come over the Vergio pass from the W or SW since the area around the pass itself shows also a trend towards wetter conditions. Moist air from the SW should have influenced the western flank of the Tavignano plateau as well but seems to be blocked by a small plateau (palaeosurface remnant with mean altitude 1350 m a.s.l.) at the NW flank of Mte. Cervellu (1602 m a.s.l.) (Fig. 42A). This Cervellu plateau might bypass air coming from the SW towards the Vergio and the Vizzavona pass and thus shield the

Tavignano flank. The Oro massif would be shielded from moist air from NW, whereas during W wind phases the Cervellu plateau would not have any effect.

Increased moisture supply from SW during the OD is also indicated by the ELA difference pattern in the south. At the Renoso massif the SW winds caused enhanced foehn during the OD since the SW flank shows a trend towards wetter conditions whereas the NE flank shows a trend towards drier conditions (Fig. 42A). The strong E-W gradients of the mainly wet anomaly along the eastern flank of Verde and Incudine/ Bavella during the LGM are slightly diminished during the OD by the additional moist supply from SW (Fig. 42A) but the wet anomaly in the SE is still present during the OD (Fig. 39C). The dominating moisture advection from the E during the LGM is changed to a mixture of moisture supply from E and SW. The strong ELA difference in the southern Verde chain (Abatesco valley) is not considered here since both glacier extents, LGM and OD, are not well documented, and the difference might be to large.

Between OD and YD the mean ELA increased by ~100 m, the difference plot shows values between 0 and >150 m (Fig. 42B). Values above the 100 m indicate less moisture supply for the YD, values below more moisture. Generally, the differences are much smaller than in the LGM/OD difference pattern. The pattern in Fig. 42B shows two areas that were drier during the OD (>150 m ELA difference), one in the NW and one in the SE. Advection of moisture from the NW and E seems to have been further reduced as well as the ELA gradients. For the NW this would mean that the NW winds, today known as the cold and dry Mistral, may have acquired a more modern character. For the anomaly at the southern flank of Mte. Rotondo (Fig. 42B) no evidence exist for a change in moisture supply. Hence, it is rather suggested that it depends on the increased insolation from the LGM towards the YD, together with the exposition to the south. Along the southwestern rim of the reconstructed area ELA differences smaller than 100 m at Vergio pass, Mte. d'Oro, southern Renoso massif and Incudine massif indicate more moist SW currents during the YD. The small differences in the north and east (Fig. 42B) could be joined with a curve over the Alpine Corsica but since climate proxies for the both Dryas events do not exist there an adequate explanation is not possible.

5.3. Synthesis

Less convection with lower ELA gradients along the steep mountain flanks and more moisture supply from the SW, this is the general conclusion of the climatic reconstructions from the ELA pattern from the LGM to the YD. As the modern atmospheric circulation pattern on the northern hemisphere results in prevailing moist supply from the SW on Corsica, the climatic reconstructions of the Oldest and Younger Dryas clearly shows the transition between full glacial and interglacial atmospheric conditions. Despite steadily increasing insolation from the LGM towards the YD, and following the warm phase of the Bølling/Allerød, the YD is again cold (and dry) in the Northern Atlantic but the atmospheric circulation in the western Mediterranean remained at an intermediate stage.

In detail, following regional changes from the LGM over the OD to the YD show a drying Mistral (NW wind) and increasing moisture supply from the SW:

The great ELA differences along the NW flank of the Cinto massif between each cold phase cannot be

explained only by temperature rise, and an additional decrease in moisture supply is required. This implies that the NW wind was a moist and cold current during the LGM. Coming through the Rhône valley the cold and dry current might have been mixed with the moist air masses of the zonal current of the polar front, from the Bay of Biscay, in the Gulf of Lyon. In autumn and especially in spring, these mixed moist air masses would be cold enough for heavy snowfall in the NW of Corsica during the LGM.

Constantly low ELA differences at Vergio pass, Mte. d'Oro, in the Renoso and southwestern Incudine massif stringently indicate increasing moisture supply from SW or W. The situation at Mte. d'Oro shows that the YD climate remains glacial and only trends towards an interglacial state since it is still far from the recent relative moisture excess and low temperature there (see chapter 6). The extreme cold and moist eastern flanks of the Alpine Corsica and the Bavella during the LGM result from easterly advection of cold and moist air driven by frequent stationary or slowly moving cyclones in the Tyrrhenian Sea. As these anomalies are getting weaker during OD and YD, the frequency of cyclones in the Tyrrhenian Sea seems to diminish.

6. Climate of the Western Mediterranean during the LGM

(Chapter in parts published in: Kuhlemann, J., Rohling, E.J., Krumrei, I., Kubik, P., Ivy-Ochs, S., and Kucera, M. (2008): Regional synthesis of Mediterranean atmospheric circulation during the Last Glacial Maximum. Science, 321, 1338-1340)

In this part of the study, the regional study of Corsica is used to demonstrate how recent climate differentiation compares to that of the LGM, and how the regional pattern reflects Mediterranean atmospheric circulation. A set of regional climatic and palaeoclimatic maps of Corsica demonstrates how recent climate differentiation compares to that of the LGM. As shown in chapter 5.2.1., Corsica is characterized by steep gradients of the ELA (Fig. 36B) and is thus considered to be a highly sensitive palaeoclimatic key area within the Mediterranean. The combination of data on LGM cooling at sea level (SST proxies), low-elevation terrestrial proxy-data, and higher altitudes (ELA draw-down) provides direct constraints on the vertical structure of the LGM atmosphere.

6.1. Present climate and differentiation of temperature and precipitation effects on the ELA

Regional anomalies are highlighted by the calculation of precipitation and temperature differences from average values. The precipitation anomaly at Present (Fig. 43A) is calculated as the difference (%) to the mean elevation-dependent regional precipitation rate which is f(p) = 600 mm yr^{-1} (+640 mm km^{-1} yr^{-1}), valid up to ~1000 m a.s.l. (highest meteorological stations). The empiric function of the elevation-dependent precipitation is calculated from data of meteorological stations (Bruno et al., 2001) marked in Fig. 43A. Because of strong winds during periods of precipitation measurements above ~1000 m a.s.l. are difficult, particularly for snowfall, and therefore precipitation measurements are restricted to altitudes between 200 and 1000 m a.s.l. The temperature anomaly (Figs. 43B and C) is calculated as the difference (Δ°C) to the elevation-dependent annual average temperature to be expected from the free lapse rate of 6.5 °C km^{-1} and 15.5 °C at sea level (Bruno et al., 2001). At elevations above 1000 m a.s.l., seasonal averages are obtained by automatic loggers operating between the years 2003 and 2007 within an own monitoring programme. These loggers are partly placed in well-ventilated rock castles at crests and peaks, partly in half-open boxes attached to the north face of large solitary pine trees at the tree limit, 2 m above the ground. Thus, all loggers were protected from precipitation and direct sunshine. Calibration measurements ensured that even exposed to sunshine the half-open boxes recorded only 0.1 to 0.2 °C higher average temperatures than measured in properly protected sites.

The own monitoring of recent mountain climate yielded average temperatures which are about 0.5 to 1 °C colder than the two high-elevation climate stations of the French meteorological survey. A complete record of climate data from these two stations is not accessible, and thus data have been downloaded from the internet since the year 2002 and digitised in order to extract monthly averages. The reasons for the deviation of the two data sets are not clear. Both climate stations are located on almost flat rocky terrain, and are possibly affected by radiation. In order to avoid artefacts in the higher elevation temperature map, data from these two stations were excluded. The temperature differences at mid elevations as calculated from Bruno et al. (2001), representing averages of about 30 years, are in harmony with the logger data.

The empirical relationship of temperature versus precipitation of temperate Alpine-type glaciers at the ELA

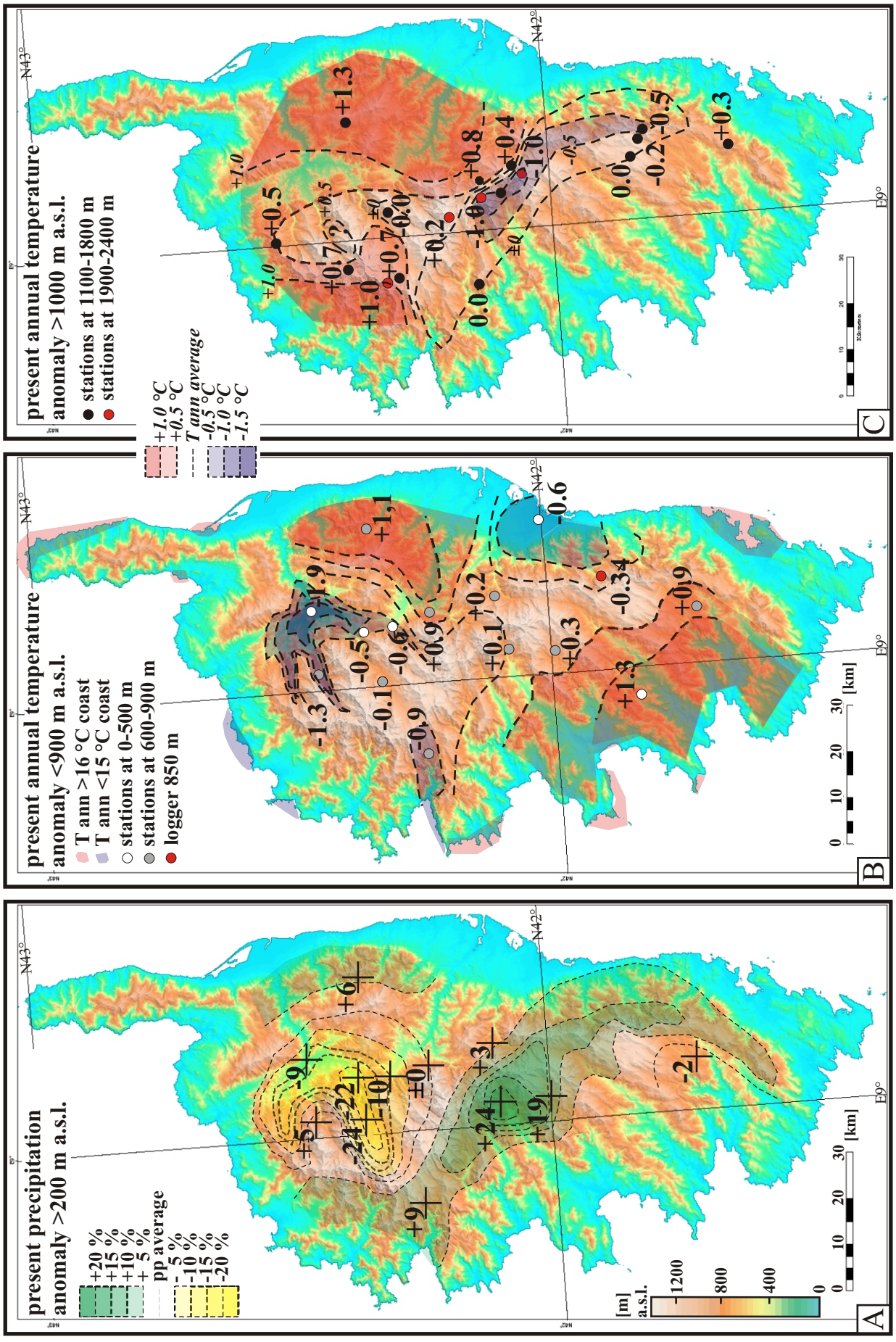

Fig. 43: Present-day anomalies of precipitation (A), low-elevation (Mediterranean climate, B) and high-elevation (montane to alpine climate, C) annual temperatures.

(Ohmura et al., 1992) is used to integrate the present ELA from the anomalies calculated from present day regional averages of annual temperature and precipitation and to construct a map of the present (1960-1990 climate normal) local ELA variability. At about 1500 to 2000 mm of annual precipitation, ±1 ºC summer temperature change (ΔT)is equal to +18 %/ -15 % precipitation change (Δpp)(Ohmura et al., 1992; Hughes et al., 2007). The temperature gradient of 0.6 °C/100 m observed in the Corsican meteorological data therefore equals +11 %/ -9 % of precipitation change. The recent ELA anomaly pattern (Fig. 44A) is based on these correlations resulting in 0.6 °C ΔT = 100 m ΔELA and +11 %/ -9 % Δpp = 100 m ΔELA. The inverse application of this method already provided the differentiation of the ELA anomaly of the LGM into precipitation and temperature anomalies (chapter 5.2.).

A regional ELA map (Fig. 44B) is provided by adding a mean ELA position of 3150 m to the anomaly pattern of Fig. 44A. The mean ELA of 3150 m is an estimate for the standard climate period (1960-1990) temperature records since 2003 at the summits, which have to be corrected for climate warming that occurred during the last decades to give appropriate 'pre-industrial' estimates. A ~250 m ELA rise in the last 20 to 30 years is estimated from: 1) a rise of the tree line by ~150 m that is reflected by a zone of juvenile trees and that is largely driven by temperature (Walther et al., 2005), and 2) ~100 m ELA rise associated with a 10 % precipitation decrease during the period 1991-2000 relative to 1960-1990 (coast-near station of Ajaccio; GHCN).

The precipitation anomaly pattern (Fig. 43A) mirrors dry conditions in the warm northern central interior, likely due to foehn effects, and slightly moist conditions at the margins of the mountain range, especially at the SW margin. The strongest difference from the average precipitation is found in the area of Mte. d'Oro/ Vizzavona pass which coincides with a maximum difference in temperature at altitudes >1000 m a.s.l. (Fig. 43C). This coincidence of a positive precipitation anomaly with cold temperatures is furthermore found along a whole south-central ridge (Figs. 43A and C). Temperatures at higher elevation in well-mixed air masses show a relatively warm north (Fig. 43C) whereas anomalies of low-elevation annual temperature indicate low temperatures in the northern central interior (Fig. 43B). These temperature inversions indicate semi-continental local conditions. Relatively warm air is advected from the SW and NE at lower elevations (Fig. 43B).

Positive ELA anomalies (high ELA) result from warm and dry local climate whereas negative ELA anomalies (low ELA) result from cool and wet local climate. The ELA pattern constructed from the temperature and precipitation anomalies (Figs. 44A and B) reveals a local ELA range of 550 ± 50 m within the relatively small (150 x 50 km) mountain range. In the northern interior, a strong positive anomaly is developed as a result of foehn effects (Kuhlemann et al., 2007). The climatic reason of the negative ELA anomaly (Fig. 44A) in southern-central Corsica with an ELA drawdown to 2800 ± 50 m (Fig. 44B) is not known in detail. Regional topography might be one major reason, with only one prominent drainage divide and frequent local precipitation governed by daily land-sea circulation and insolation-driven convection during the warm season. Moreover, subtropical disturbances typically affect southern-central Corsica stronger than northern Corsica, and southern Corsica is more densely covered by broad-leaf, partly deciduous forest (>1000 m a.s.l.), supporting local recycling of moisture. Moisture data from loggers, amounts of snowfall over the last five years, and the pattern of the temporal snowline and vegetation belts, as compiled from remote sensing, monitoring, and field observations (Kuhlemann et al., 2007) confirm particularly moist conditions in south-central Corsica. Snow patches occasionally

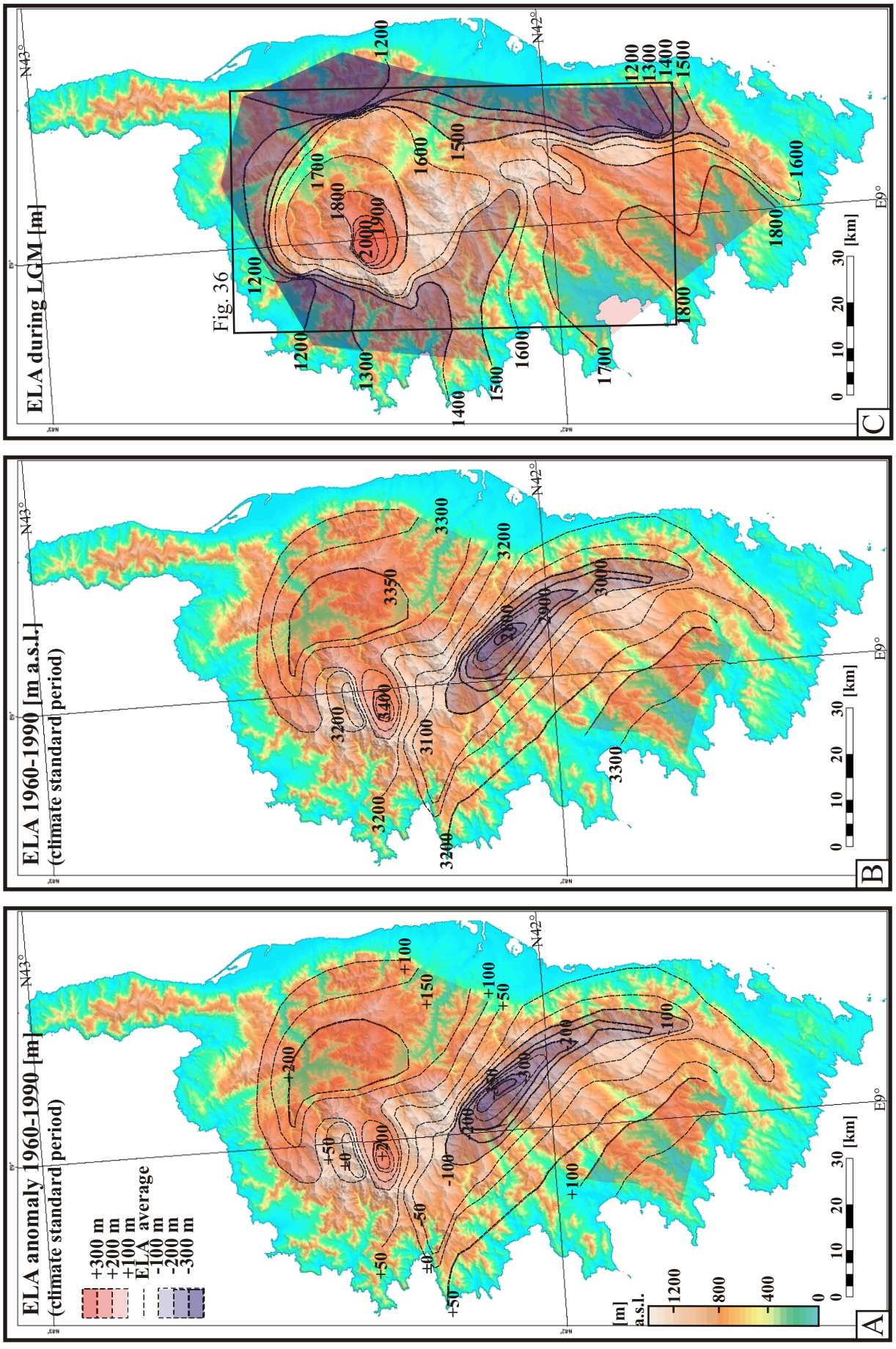

Fig. 44: Present ELA anomaly differing from the average ELA (A), and both Present (B) and LGM (C) ELA in metres above present sea-level.

survive through the summer in cirques at elevations down to 2100 m within this zone. In the same cirques, there is evidence of niche glaciers during the Little Ice Age (Kuhlemann et al., 2005b).

The ELA pattern of the LGM and its differentiation into temperature and precipitation are discussed in chapter 5.2. To simplify comparison with the Present, the ELA pattern of the LGM is shown again in Fig. 44C (ELA isolines from Fig. 36B). Especially at the margins of the island, the climatic conditions appear to differ considerably between the LGM and the Present. These climatic conditions must be explained by larger scale atmospheric circulation, as reflected by the ELA pattern in Mediterranean scale that will be shown below. The same magnitude of differences however indicates that, apart from relief-controlled local climate differentiation, the impact of both precipitation and regional temperature is roughly equal for both periods.

6.3. Mediterranean ELA during the Last Glacial Maximum

Currently available ELA reconstructions for the maximum glaciation in Iberia, Italy, and the southern Dinarides (mainly Greece) lack precise chronology to pin it to the LGM. For the Alps it is known that the maximum extent of glaciers occurred simultaneously with that of the northern hemisphere in the LGM (Florineth and Schlüchter, 2000). For the main part of Corsica, the first part of this study has shown that the ELA during the LGM generally was situated about 50 to 100 m higher than during the maximum glacier extent which occurred earlier in the last glacial cycle, whereas the LGM advance was the strongest in the southern part of the island. Also in the northern Pyrenees, glacier extent was less far during the LGM than during earlier phases in the last glacial cycle (García-Ruiz et al., 2003; Calvet, 2004). This seems also to apply throughout Iberia (Pérez Alberti et al., 2004). Some evidence exists for a stronger advance earlier in the last glacial cycle in the Southern Carpathians as well (Reuther et al., 2007). In northern Greece, maximum glacier extent in the last glacial cycle occurred during the LGM (Woodward et al., 2004; Hughes et al., 2006, 2007). Older ELA maps for Greece and southern Italy show the maximum expansion in the last glacial cycle (Boenzi and Palmentola, 1997), which not necessarily occurred strictly within the LGM (Giraudi, 2004). ELA estimates of Messerli (1967) and Menkovic et al. (2004) on the Balkan peninsula assume a maximum advance in the LGM, recently confirmed by exposure dating in Bulgaria (Kuhlemann et al. in press).

Regional work that has been performed after the earlier compilation of Messerli (1967), who analysed and compiled all relevant older publications, is shown in Appendix F. The table and the reference list give priority to most recent regional work where older references for the particular region are noted. Special priority is given to publications which include geochronological dating of glacier advances. So far, these are scarce.

6.4. Mediterranean ELA and sea surface temperature during the Last Glacial Maximum

The data of the Mediterranean ELAs during the LGM are compiled in a map of ELA isolines (Fig. 45). The isoline pattern shows several meridional lobes which modulate the latitudinal trend. Lobes to the south indicate relatively cold conditions whereas lobes to the north indicate relatively warm conditions. Southward extending lobes of ELA depression are found in mountainous regions of Italy and the Dinarides, which suggests frequent

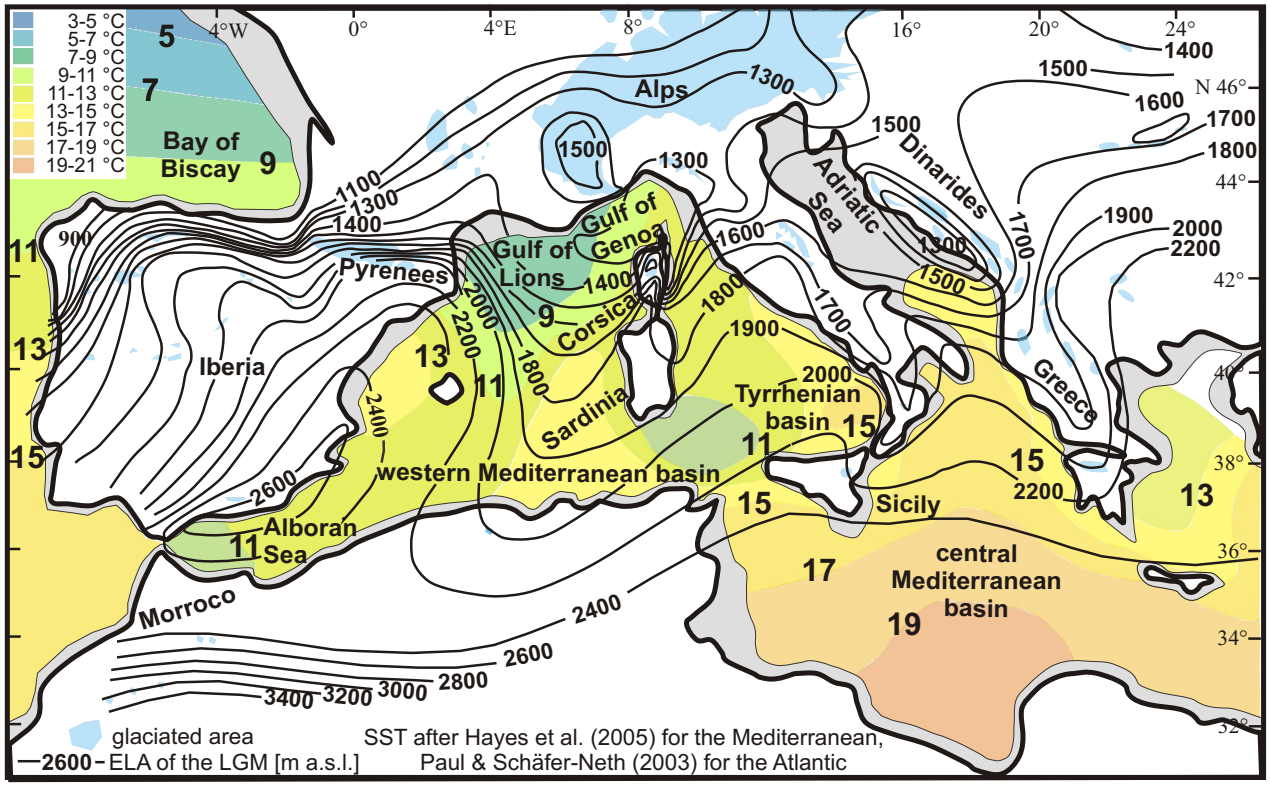

Fig. 45: Map of the equilibrium line altitude (ELA) in the western-central Mediterranean region during the phase of maximum glacier expansion during Heinrich event 2/Last Glacial Maximum (probably 24-23 kyr) and of average annual sea surface temperatures (SST) during the LGM.

higher-altitude southward advances of polar air (Fig. 45). Another lobe of lowered ELA extends from the Gulf of Lions towards the south and east, indicating significant invasion of polar air from the north. Iberia is characterized by a steep gradient from the northern and northwestern coastlines towards the interior and southeast, which likely results predominantly from blocking effects of near-coastal mountain ranges.

Mediterranean surface circulation and sea surface temperature must have been affected by regionally focussed incursions of polar air, as surface currents are deflected by coastlines and their strength and flow direction varies seasonally in response to surface winds and superimposed atmospheric circulation (World Ocean Atlas 1998; Pinardi and Masetti, 2000). Northwesterly winds strongly affect the present-day sea-surface temperature (SST) distribution and surface circulation in the western Mediterranean basin, particularly in the Gulf of Lions (Pinardi and Masetti, 2000). As a consequence, cool waters are frequently upwelling in the Gulf of Lions (Rohling et al., 1998). Glacial SST values calculated from foraminiferal assemblages (Paul and Schäfer-Neth, 2003; Hayes et al., 2005; Kucera et al., 2005) and alkenone data (Cacho et al., 2002) display a roughly similar distribution to modern SST, albeit with a stronger west-east gradient due to stronger cooling in the northwestern Mediterranean than in the central and eastern parts of the basin (Hayes et al., 2005) (Fig. 45). The extraordinary cooling centred on the Gulf of Lions suggests frequent and/or more persistent northerly incursions of cold polar air, probably channelled through the Rhône valley at low elevation (Rohling et al., 1998), and between the glaciated Alps and the Pyrenees at higher elevation.

Comparison of the ELA in the LGM and at Present (largely after Messerli 1967) allows for calculation of the elevation difference between them, called ELA depression (Fig. 46). Above the Mediterranean Sea the modern and ancient ELA is just roughly estimated, which applies also to the ELA depression. The isolines of

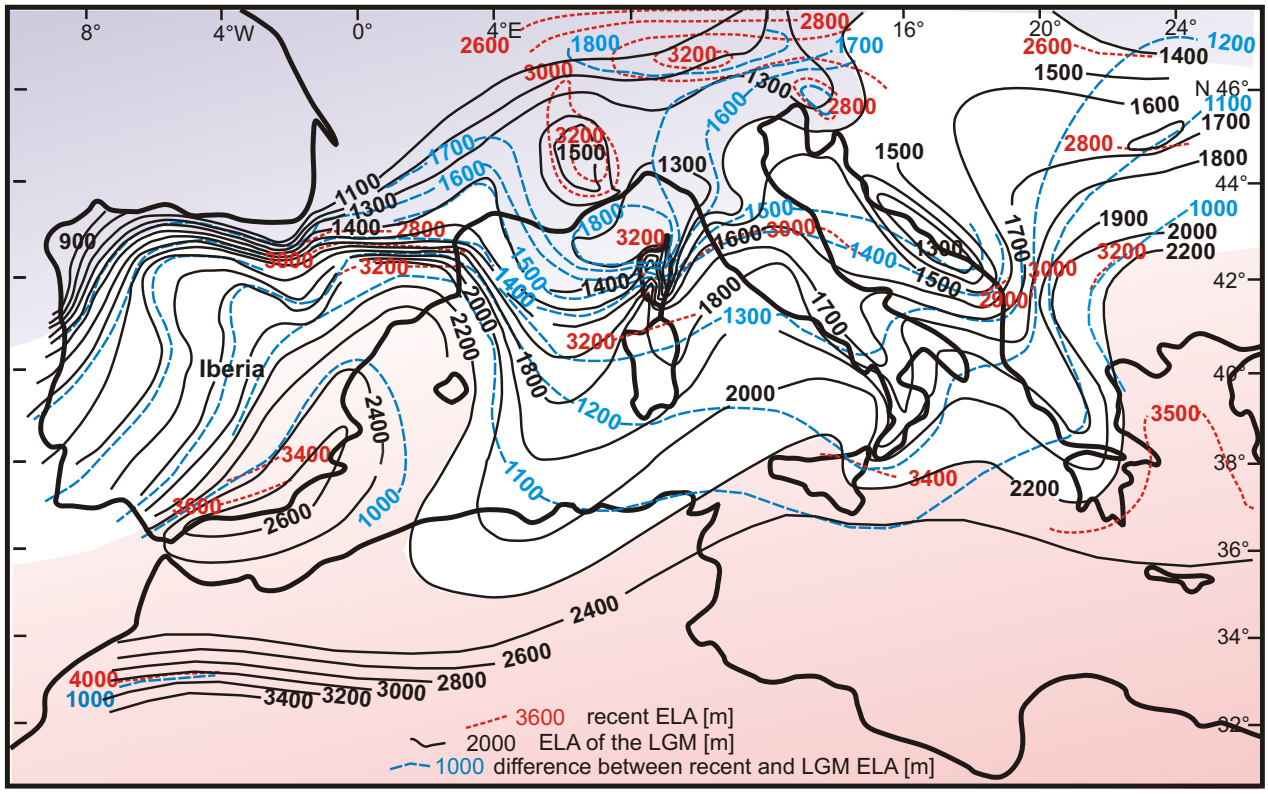

Fig. 46: Comparison of the ELA at Present with that of the LGM used to construct the ELA depression.

the ELA depression roughly follow the ELA lines of the LGM above the Mediterranean Sea, whereas Messerli (1967) plotted a quite straight east-west orientation of present ELA isolines.

To calculate a temperature depression for the LGM in altitudes of 1 to 3 km, the ELA depression is combined with a mean free atmosphere lapse rate of 6.5 °C km^{-1} (Fig. 47). This approach is an end-member scenario applied only to achieve comparison with SST, providing a temperature anomaly pattern which is in fact indicative of precipitation anomalies. The spatial pattern of the LGM reduction of SST (relative to the Present) compared with that of atmospheric temperature as derived from our ELA reconstruction, and with palaeofloral data (Fig. 47) reveal that both SST and ELA-determined atmospheric temperatures (T_{ELA}) had changed, relative to the present. This change was in close harmony (within ±2 ºC) in the northern Bay of Biscay and western parts of the western Mediterranean basin.

The temperature difference between the recent ELA and the LGM reconstruction generally decreases from north (10-11 °C) to south (6-7 °C) (Fig. 47), in agreement with previous reconstructions of a steeper glacial meridional temperature gradient (Messerli, 1967). The differences also generally agree with lower-altitude temperature reconstructions from palaeofloral data (Peyron et al., 1998; Wu et al., 2007). In south-central Italy, the two different palaeoflora temperature estimates of Peyron et al. (1998) and Wu et al. (2007) show a gap between -7 and -9 °C, where the temperature equivalent of the ELA depression indicates about -8.7 ± 1 °C. Further to the south, both land temperature depressions are close and indicate warmer land conditions than indicated by the ELA at higher elevation. Since the SST depression is only 5 °C in this region, causing a significant warm SST anomaly (Figs. 45 and 47), the warmer palaeoflora temperature estimate (Wu et al., 2007) seems to be more realistic and locally enhanced convective precipitation is inferred in this area. All estimates agree well in

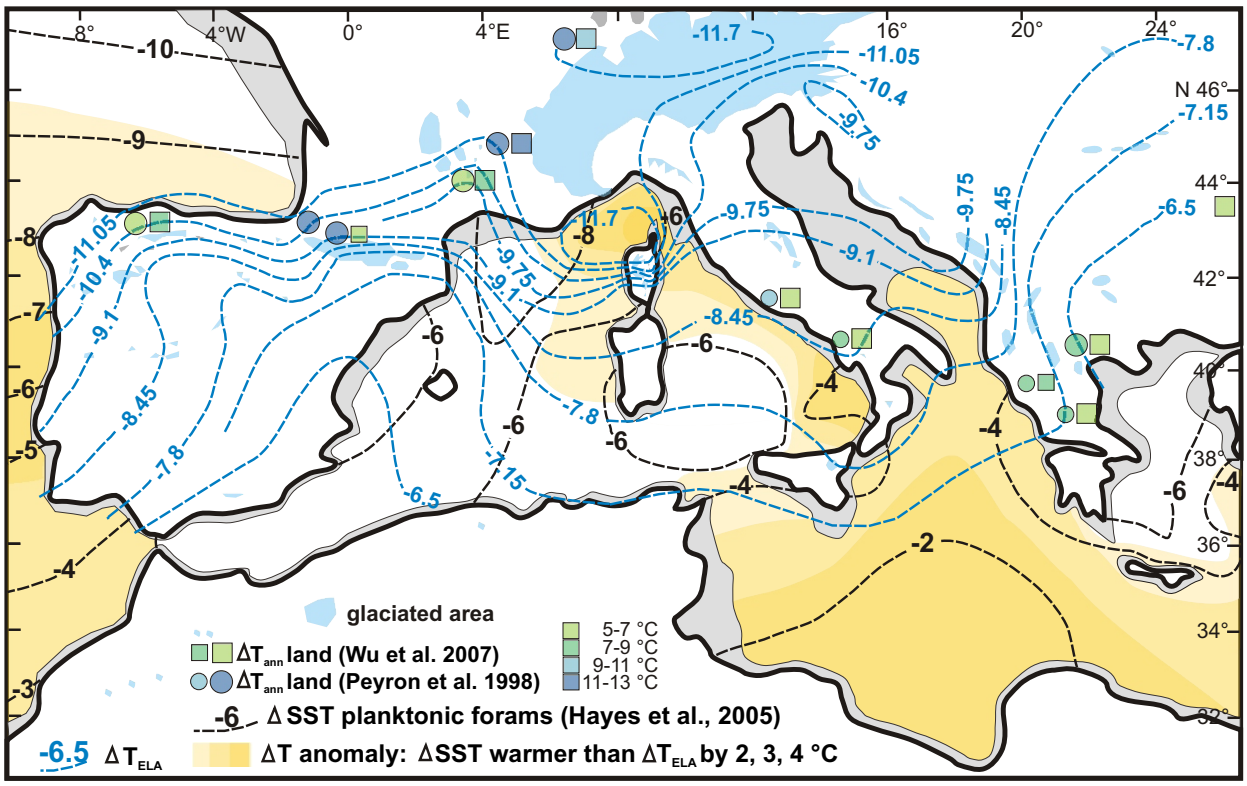

Fig. 47: Map of the temperature difference between recent and LGM SST (black) and temperature equivalent of the ELA depression (lapse rate of 6.5 °C km^{-1}; blue), respectively. In orange-coloured marine regions, LGM SSTs were lowered significantly less than temperatures in the mid troposphere, relative to the present. This implies an anomalously steep lapse rate and unstable layering of the lower troposphere. For comparison, atmospheric cooling values for low-elevation terrestrial sites are given based on palaeo-floral estimates. Small symbols indicate larger, large symbols lesser error of the temperature estimate.

the Rhône valley reflecting relatively cold conditions that are in line with dominant northerly winds. Katabatic winds from the Alpine glaciers possibly contributed to exceptionally cold conditions in the Rhône valley. Slightly warmer land temperatures NW of the Alps compared to the ELA temperature estimate (Fig. 47) might reflect favourable local conditions, out of the reach of katabatic winds. On the southern flank of the French Massif Central, land temperature depressions are somewhat lower than those indicated by the ELA (Peyron et al. 1998), but still close (Wu et al. 2007). The local cooling trend towards the Rhône valley is evident in all data (Fig. 47). In SW France, the land temperature estimates are in conflict and are, as also in NW Iberia, significantly warmer than the ELA temperature depression. In the Atlantic Ocean offshore Morocco SSTs of the LGM also have been reduced less than T_{ELA} (Fig. 47), which likely reflects the southward displacement of the relatively warm Gulf Stream during glacial times (COHMAP 1988; Bond et al., 1993; Kageyama et al., 1999, 2006). This would mean that locally enhanced convective precipitation strongly accounted for the regional ELA depression in NW Iberia. SW France might be affected to a lesser degree. In the central and to a lesser extent also in the eastern Mediterranean, glacial SSTs appear to have dropped considerably less than T_{ELA} (Fig. 47). The considerable warm anomaly in the central basin can hardly be attributed to advection of warm surface waters from the west since quite cool SSTs are found at the southeast of Sardinia (Fig.45) which may reflect leeward upwelling triggered by northwesterly winds. Instead, advection of warm desert air from the Sahara and relatively cloud-free subtropical conditions over the central/ eastern basin might have largely accounted for minimal LGM cooling of

SSTs offshore Lybia.

The fact that the glacial SST dropped considerably less than the calculated T_{ELA} over part of the Mediterranean implies that the atmospheric lapse rate had noticeably increased: up to ~10 °C km^{-1} NW of Corsica, ~9 °C km^{-1} in the southern Adriatic Sea, and ~8.5 °C km^{-1} in the central Mediterranean basin. This has implications for the atmospheric stability, circulation patterns and local precipitation which will be discussed below.

Above, annual averages of SST depression were compared with the ELA depression, although a comparison with summer SST seems to be more appropriate, since the air temperature in the melting season appears to govern the ELA (Ohmura et al. 1992). However, local factors such as cloudiness, spring rainfall or snowfall depending of short-term synoptic conditions, underlying rock types (limestone vs. dark silicates), and other parameters modify the relationship of the ELA to summer air temperature. A plot of summer SST depression relative to the ELA depression (Fig. 48), generated similarly to Fig. 47, exposes the same pattern of regional gradients in the Mediterranean, but shows a cold anomaly, and between Sardinia and Sicily, respectively. The latter anomaly may be explained by upwelling of cold deep water due to persistent NW winds, which are testified by the geometry of fossil dunes in Sardinia and the relatively cool SST in the raw SST pattern (Fig. 45). The cold anomaly around and south of the Balearic Islands (Fig. 48) cannot be reasonably explained by oceanographic processes in the given setting. Moreover, such cold conditions would favour stable stratification of the lower atmosphere causing regionally enhanced dryness of which no evidence exists. For unclear reasons, the annual average Mediterranean SST pattern in the LGM is more reasonable for a comparison with the ELA. This applies also to east Atlantic SSTs off Iberia (Kucera et al., 2005), which are unreasonably warm compared to the ELA temperature depression (end-member).

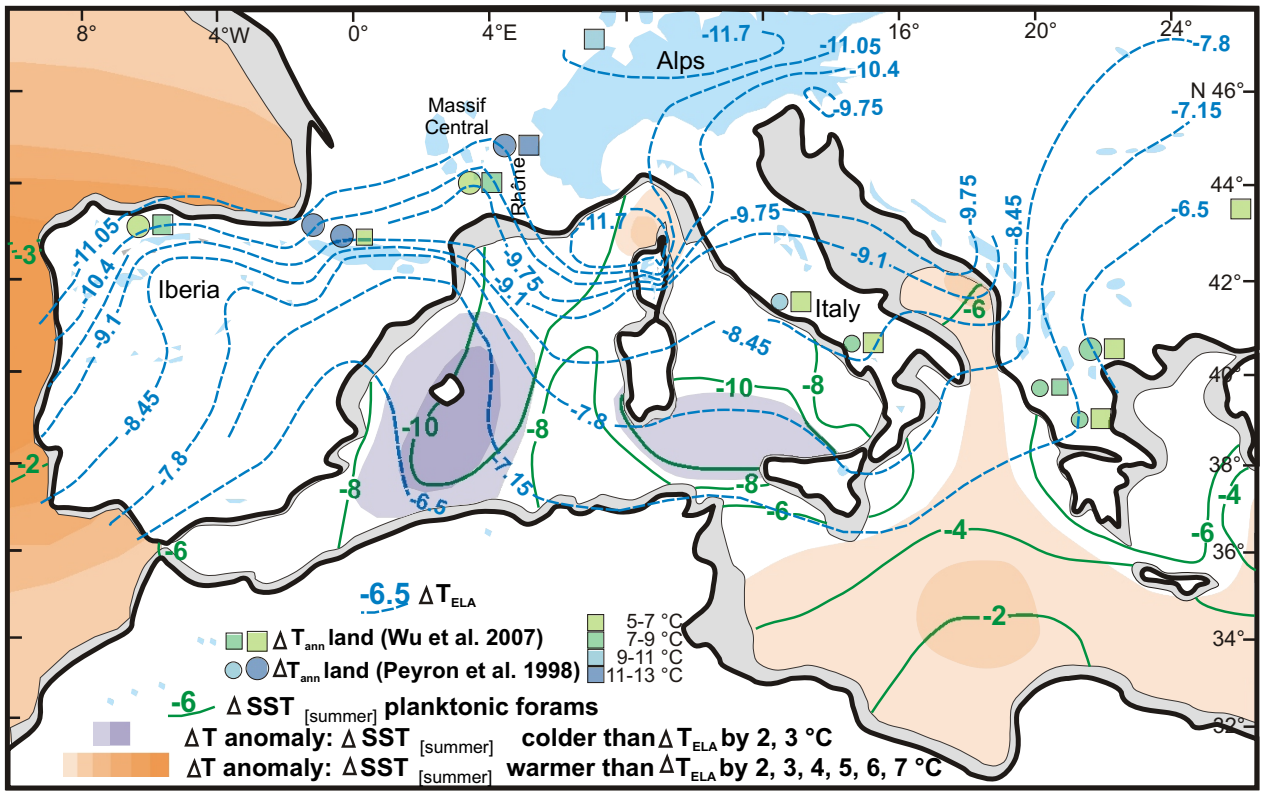

Fig. 48: Modified plot of figure 47 using summer ΔSST instead of annual average ΔSST.

6.4. Atmospheric stability, circulation patterns and local precipitation

As the spatial distributions of SST, T_{ELA}, and of the SST-T_{ELA} gradients in the western-central Mediterranean during the LGM are found to be roughly similar to the Present, though generally enhanced, it is reasonable to expect that cyclones followed similar preferential storm tracks across the basin as well (Fig. 49). Due to the more southerly position of the polar front during cold phases like the LGM (Rohling et al., 1998; Kageyama et al., 2006), cold northerly air outbreaks over the western basin have probably been more frequent and/or persistent than today. Both at present and during the LGM, outbreaks of polar air masses over the western Mediterranean typically are funnelled between the Alps and the Pyrenees, causing conditions inducing cyclogenesis over the Gulf of Genoa (Fig. 49). The funnelling effect may have been stronger with glaciated mountains, as the ice rose several hundreds of meters above the lower watersheds (Florineth and Schlüchter, 1998).

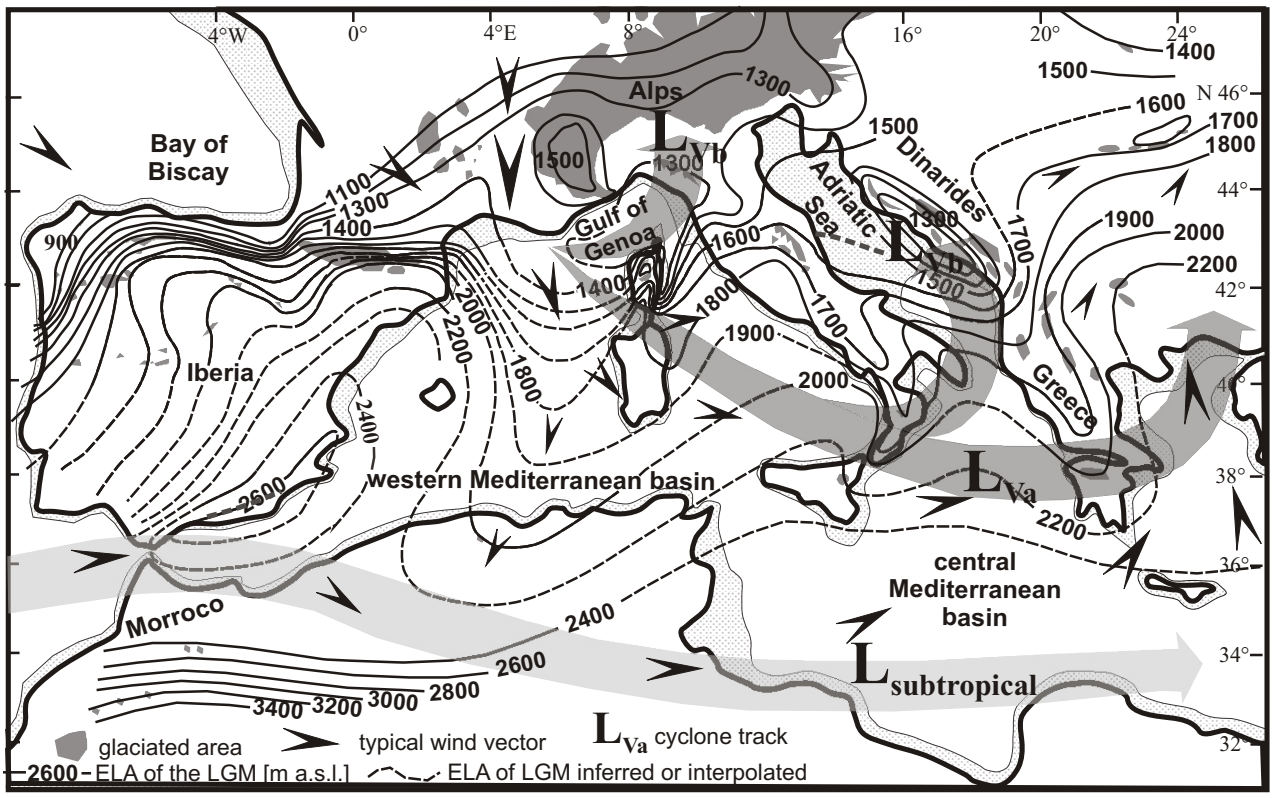

Fig. 49: Map of the ELA of the Mediterranean LGM with resulting wind vectors indicating that cyclone tracks over the western-central Mediterranean were similar to the present tracks labelled Va, Vb, and subtropical by meteorologists.

The incursion of cold air masses would have favoured convection of moist air in regions with relatively warm SSTs, so that considerable local LGM precipitation can be predicted in eastern and northern Corsica, the Apennines, the Dinarides, and Greece, especially at the upwind flank of mountain ranges and close to the coast (Fig. 47). This would be a suitable mechanism to explain steeper precipitation gradients during the LGM relative to the Present, as it is suggested by the data for the steep mountainous margins of Corsica (Figs. 36 and 37). Although this prediction cannot (yet) be confirmed with the data available outside Corsica, it does agree with patterns seen in LGM reconstructions of the high-resolution climate model HadRM (Jost et al., 2005). Locally enhanced precipitation reduces the local lapse rate, which means that a major part of the calculated temperature anomaly pattern is attributed to an effect of a precipitation anomaly. In turn, the locally enhanced precipitation

reduces the vertical thermal gradient by release of condensation energy. In this regard, the temperature-only end-member calculation of the ELA depression represents a time-averaged regional disposition to uplift of air, driven by a steeper thermal gradient between the sea surface and the mid troposphere. This regional disposition to convection interferes with convection driven by typically east-migrating perturbations of cyclones, which typically overwhelm moderate topographic barriers such as the mountain ranges of Europe.

As indicated by the north-extending lobe of the ELA in southeastern Europe, the pronounced southward cold (polar air) expansion towards NW Africa would have triggered a compensatory flow of desert air towards the N and NE (Fig. 45). This is consistent with observations of enhanced wind-blown dust supply from the Sahara into the eastern Mediterranean during glacial times (Larrasoana et al., 2003). Circulation on this spatial scale is generally driven by Rossby waves in the higher atmosphere. Due to ice shield topography and high albedo, spatial variability of the Rossby waves might have been reduced in the LGM as well as stronger channelled by the land-sea distribution and topography compared to the Present. Remote influence of the Laurentide ice shield on atmospheric circulation in the North Atlantic realm is considered to be likely (Kageyama et al., 2006).

A preferentially zonal geostrophic circulation during the LGM is indicated by the difference between strongly reduced SSTs in the western basin and much less reduced SSTs in the central Mediterranean basin. In contrast, a meridional circulation is favoured by a northward extension of the Azores High towards Iceland (North Atlantic ridge), or Greenland, blocking moisture supply of westerly geostrophic flow. The observed cli-

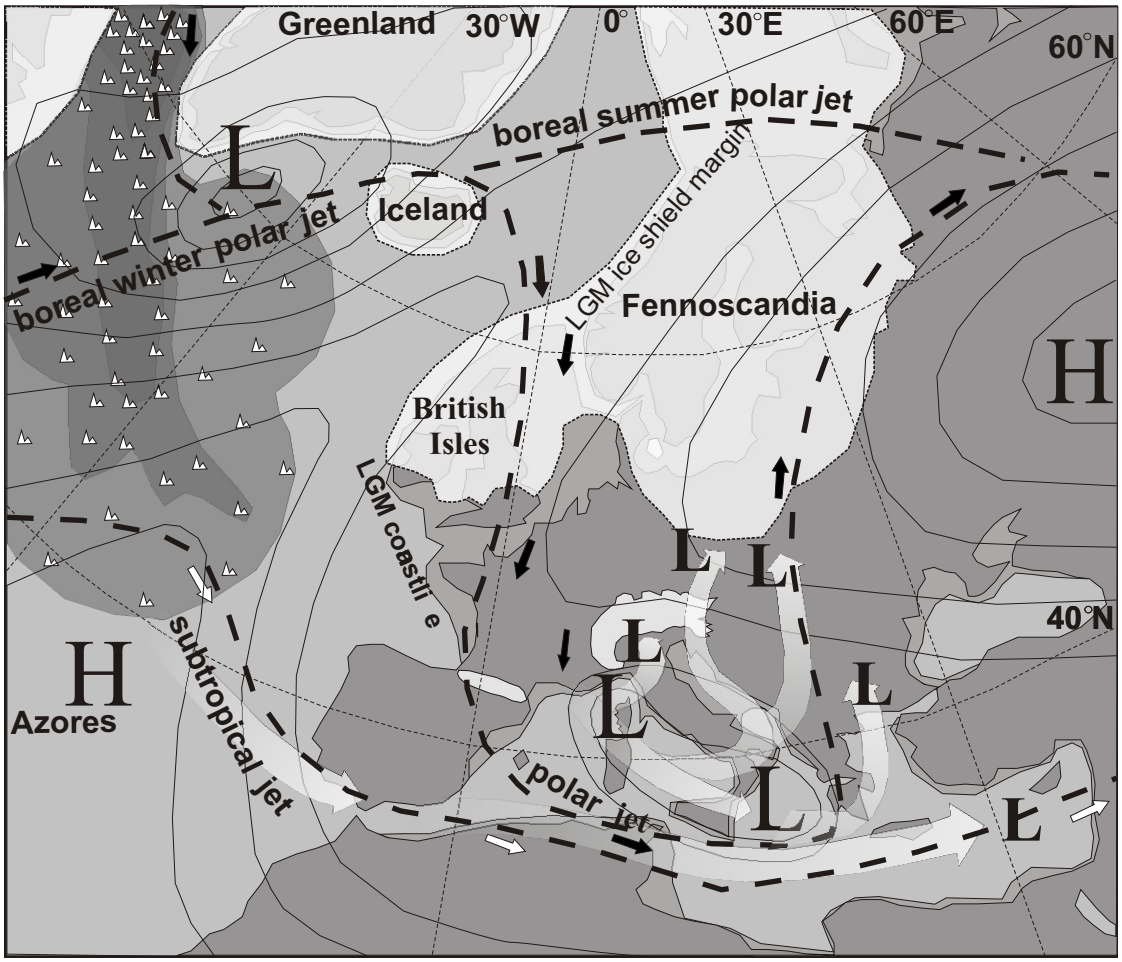

Fig. 50: Synoptic climate model explaining the occurence of more frequent incursions of polar air into the western Mediterranean during the LGM with a strongly sinuous Rossby-wave lobe over central Europe.

mate pattern in the LGM could be explained with a frequent occurrence of a strongly sinuous Rossby wave lobe, forming a narrow trough of polar air over central Europe (Fig. 50). As exemplified in Fig. 50, frequent occurrence means that such an unstable synoptic setting lasting for few days during each phase might have occurred about ten times in the cold season, what is much more than at Present. Nevertheless, this setting would have had strong impact on the accumulation of snow, and would superimpose the climatic effects of longer phases of zonal circulation (westerlies) with low precipitation and dominant high pressure. Polar air over the western Mediterranean basin, combined with low pressure, would trigger convective precipitation there, whereas advection of moist and relatively warm air across southeastern Europe towards the north would favour south-directed growth of the Fennoscandian ice shield.

6.5. Synthesis and discussion

For the Mediterranean perspective, all available ELA data were incorporated which claim to apply for the LGM although several sources cannot provide solid chronostratigraphical constraints. However, scattered age determinations of glacial phases including the Corsican data as well as preliminary data from southeastern Europe (Kuhlemann et al. in press; data to be published) justify a presentation of a new Mediterranean ELA map of the LGM substituting the fundamental compilation of Messerli (1967). Future establishment of a solid chronostratigraphical framework is especially crucial in northern Africa.

The Mediterranean ELA depression of the LGM was transferred directly into a temperature depression to enable comparison to SST temperature depressions. This end-member anomaly pattern is indicative of precipitation anomalies, but represents a regionally variable mixture of the two climate factors temperature and precipitation. Without independent control of either temperature or precipitation, the role of both factors cannot be quantitatively separated. Climate models could tentatively quantify the thermal effect of enhanced convective precipitation on the lapse rate, which would certainly be less steep as a consequence of moisture condensation. Thus, the temperature anomaly map shows a regional disposition to convection and enhanced precipitation.

The evidence on atmospheric circulation in the Mediterranean during the LGM as described above partly contrasts earlier conclusions. Florineth and Schlüchter (2000) assumed that cyclones typically moved from the Alboran Sea towards the southern flank of the Alps and/or across the northern Dinarides to reach the southern Fennoscandian ice shield. The data of this study imply that such cyclone tracks were rarely followed in the LGM, because incursions of polar air between the Alps and the Pyrenees would tend to push cyclones generated in the Alboran Sea towards the northern African coast. In the new scenario, cyclones generated in the Alboran Sea would rather move eastward and hit southern Greece before either moving northward along the polar jet or eastward along the subtropical jet. Since preferential southerly moisture advection to the Alps is evident (Florineth and Schlüchter, 1998, 2000), frequent local formation of Genoa cyclones is assumed which basically followed similar storm tracks as today, possibly moving more slowly and turning northward above the Adriatic realm more frequently than today. The main reason for this assumption is the pronounced wetness and coldness reconstructed on the eastern flank of Corsica, which is necessarily driven by mixing of cold continental air from the east (Bora-type winds) with wet Mediterranean air of the northerly rear side of cyclones passing south of

Corsica on their way to the E and NE.

There is also some misfit with the previously suggested SW-directed pressure ridge of the Scandinavian Mobile Polar High (Sánchez-Goni et al., 2002). The relatively warm and dry conditions in SE Iberia might rather be caused by lee effects of predominant N and NW winds in this region that are driven by the lobe of polar air invading the western Mediterranean basin at higher elevation. Apparently, such SW-directed pressure ridge would conflict with polar air incursions in the Gulf of Lions, too. However, in terms of frequency and persistence of certain synoptic scenarios both scenarios could be of importance, possibly during different seasons.

Although care must be taken to not simply adapt past regional property distributions to modern climate oscillation patterns (Justino and Peltier, 2005), it remains useful to consider instrumental records and proxy-data in order to develop a sense of realistic, analogous climate patterns over the study region. The inferred blocking configuration frequently occurs during a negative mode of the North Atlantic Oscillation (NAO; Broccoli, 2000), and the regional effect in western-central Europe is enhanced when interannual variation of the NAO favours a negative mode in winter and a positive mode in summer (Cassou et al., 2004). Today, blocking in winter triggers a roughly southward geostrophic flow of polar air into the western Mediterranean. During glacial times, this flow is further enhanced by expansion/intensification of the Siberian High in winter (Rohling et al., 2003). Such a configuration is also thought to have been more common during the late Little Ice Age, particularly during the Maunder Minimum (1675-1715) (Jacobeit et al., 2001; Xoplaki et al., 2001; Luterbacher et al., 2001, 2006). The larger scale circulation with frequent blocking during the Maunder Minimum has much in common with the circulation scenario proposed for the LGM (Fig. 50). Because Mediterranean SST data are not available as well as Mediterranean ELA data are absent or vague for the Maunder Minimum except for local studies in the Alps, comparison along similar lines of evidence is not possible.

Finally, the new ideas on Mediterranean-scale circulation during the LGM should be compared to the results of numeric climate models. Older models are out of scope because they have a quite low spatial resolution (see COHMAP, 1988; Kageyama et al., 1999). Some high-resolution climate models like HadRM (Jost et al., 2005) offer solutions for this region that expose striking similarities in temperature and especially precipitation patterns, but there are also models with similar resolution exposing quite different results. Why which one of the various models implies more realistic scenarios is difficult to judge. Recent efforts suggest that CO_2-corrected inverse vegetation models (Wu et al., 2007), which estimate temperatures less cold than previous models, almost close the gap to the modest reduction of LGM winter temperatures (coldest month) indicated by various climate models (Ramstein et al., 2007). Modelling of LGM regional precipitation remains to be a serious problem (Ramstein et al., 2007).

In this part of the study it was highlighted that certain synoptic weather scenarios, particularly in the cold season, may have the potential to govern an anomaly pattern by extreme cold-wet precipitation events, although they may rule for less than a quarter of the year. When climate models expose the average mode of atmospheric circulation (westerlies), this may be both true and misleading. Thus, using the LGM data of this study and the well-studied cold spell of the late Holocene Maunder Minimum may provide a basis for high-resolution climate modelling which includes a small number of typical weather scenarios to separate high-impact from low-impact synoptic settings in the past (see Luterbacher et al., 2006).

Acknowledgements

First of all, I thank my supervisors Prof. Joachim Kuhlemann and Prof. Wolfgang Frisch for the opportunity to work in this interdisciplinary project combining geomorphology, dating and climate reconstruction on the beautiful island of Corsica. Achim, thank you for the intensive, informative phases of field work and for collecting samples whenever possible. Thank you for sharing the room with me (I would have never learned so much about real life at University), and also with my little baby. Thank you for encouraging me to teach students in the "Schotterkurs" and to lead excursions. Wolfgang, thank you for being the critical voice of the project that reminds to begin with the facts and not with the interpretation. Thank you for being more a very experienced colleague than an inapproachable boss.

I am much obliged to Dr. Balász Székely for his help with everything considering GIS and the software ERmapper. Together with his Hungarian colleagues he was able to solve every problem with the DEM. Thanks to Christoph Glotzbach I could calculate the shielding with DEM data as he left his computer including software to me.

My time in Tuebingen was coined by the colleagues in the work group, Martin, Conny, John, Horst, Christian, Andreas, Paul, Volker and many others which were part of the group during their diploma, which left in the early part of my time or which were guests for some time. All of them created a working atmosphere in which the need for help, discussion or just a talk had always its place and answer. John, many thanks to you and your family for your hospitality. Irreplaceable were the lab assistants Gerlinde Höckh, Dagmar Kost and Dorothea Mühlbayer-Renner with their reliable work in the preparation lab separating quartz from the rock samples for cosmogenic dating.

I want to thank Prof. Friedhelm von Blanckenburg teaching me the separation of ^{10}Be from quartz with ultrapure chemistry in the laboratory in Hannover. He also gave advises for the equipment of the laboratory when I installed the ^{10}Be separation in Tuebingen.

I thank Dr. Wolfgang Siebel and especially Elmar Reitter from the Chair of Geochemistry at the University of Tuebingen for the opportunity to use the infrastructure of the geochemistry laboratory where they found a place for me to cook oodles of HF and to separate the ^{10}Be.

Without the help of Dr. Peter Kubik, ETH Zuerich, I would have never understood the pitfalls of the exposure age calculation. Thanks a lot for the helpful email-correspondence. He was also responsible for the AMS measurements of the Be-samples. Dr. Susan Ivy-Ochs, ETH Zuerich, shared her expert knowledge about exposure age dating in some discussions.

I thank Prof. Manfred Frechen from the GGA Hannover for his cooperation in the project and the ability to measure a large amount of luminescence samples. I thank Dr. Astrid Techmer for the measurements and age calculation. Many thanks to Sonja Riemenschneider teaching me the sample preparation of luminescence samples. She understood well to make the time in the dark laboratory a pleasant time.

Many thanks go to Dr. Alexandra Hilgers, Institute of Geography, University of Cologne, for preparation, measurement and age calculation of further luminescence samples as fast as possible. Also thanks for fruitful discussions.

Peter van der Beek, Grenoble, gave me the opportunity for a first study of Corsican stereo air photos that led

to an order of a large pile of quite useful photos.

Financial support was provided by Deutscher Akademischer Austauschdienst (DAAD) and Deutsche Forschungsgemeinschaft (DFG, projects Ku 1298/7-1 and Ku 1298/7-2).

Outside the science world I always had the support of my family and friends. Thomas, thank you for being discussion partner, reviewer, lector, lover, caring husband, father all in one person. I am grateful for my little daughter Ruth, the jabbering, running and springing wholehearted girl, who challenges me every day in a different way. I thank my parents for their unlimited support and numerous worrying thoughts as parents and grandparents. Nicole and Yvonne, we shared different experiences during our time writing a dissertation and I do not want to miss the exchange about it with the necessary mutual understanding and encouragement. I thank Eva Kohlmeier for giving Ruth such a wonderful daycare.

References

Adamiec, G. and Aitken, M.J. (1998): Dose-rate conversion factors: Update. *Ancient TL*, 16, 38-50.

Aitken, M.J. (1985): *Thermoluminescence dating*. Academic Press, London, 359 pp.

Aitken, M.J. (1998): *An introduction to optical dating – The dating of Quaternary sediments by the use of photon-stimulated luminescence*. Oxford University Press, Oxford, 267 pp.

Allen, J.R.M., William, A.W., and Huntley, B. (2000): Weichselian palynostratigraphy, palaeovegetation and palaeoenvironment; the record from Lago Grande di Monticchio, southern Italy. *Quaternary International*, 73/74, 91-110.

Amaudric du Chaffaut, S., Bonin, B., Caron, J.M., Conchon, O., and Rossi, P. (1985): *Carte Géologique de la France (1/50000), feuille Venaco (1114)*. BRGM, Orleans.

Auclair, M., Lamothe, M., and Huot, S. (2003): Measurement of anomalous fading for feldspar IRSL using SAR. *Radiation Measurements*, 37, 487-492.

Balco, G., Stone, J.O., Lifton, N.A. and Dunai, T.J. (2007): A complete and easily accessible means of calculating surface exposure ages or erosion rates from ^{10}Be and ^{26}Al measurements. *Quaternary Geochronology*, doi: 10.1016/j.quageo.2007.12.001.

Benn, D.I. and Evans, D.J.A. (1998): *Glaciers and Glaciation*. Arnold, London. 734 pp.

Boenzi, F. and Palmentola, G. (1997): Glacial features and snow-line trends during the last glacial age in the Southern Apennines (Italy) and on Albanian and Greek mountains. *Zeitschrift für Geomorphologie*, NF Suppl 41, 21-29

Bøtter-Jensen, L., McKeever, S.W.S., and Wintle, A.G. (2003): *Optically Stimulated Luminescence Dosimetry*. Elsevier, Amsterdam, 404 pp.

Boezio, M., Carlson, P., Francke, T., Weber, N., Suffert, M., Hof, M., Menn, W., Simon, M., Stephens, S., Bellotti, R., Cafagna, F., Circella, M., DeMarzo, C., Finetti, N., Papini, P., Piccardi, S., Spillantini, P., Ricci, M., Casolino, M., DePascale, M., Morselli, A., Picozza, P., Sparvoli, R., Barbiellini, G., Schiavon, P., Vacchi, A., Zampa, N., Grimani, C., Mitchell, J., Ormes, J., Streitmatter, R., Bravar, U., Golden, R., and Stochaj, S. (2000): Measurement of the flux of atmospheric muons with the CAPRICE94 apparatus. *Physical Review* D62 (032007).

Bond, G., Broecker, W., Johnson, S., McManus, J., Labeyie, L., Jouzel, J., and Bonani, G., (1993): Correlations between climate records from North Atlantic sediments and Greenland ice. *Nature*, 365, 143-147.

Bond, G. and Lotti, R. (1995): Iceberg discharges into the North Atlantic on millennial time scales during the last glaciation. *Science*, 267, 1005-1010.

Broccoli, A.J. (2000): Tropical Cooling at the Last Glacial Maximum: An atmosphere–mixed layer ocean model simulation. *Journal of Climate*, 13, 951-976

Bruno, C., Dupré, G, Giorgetti, G., Giorgetti, J.P., and Alesandri, J. (2001): *Chì tempu face? Météorologie, climat et microclimats de la Corse*. CNDP-CRDP de Corse/ Météo France, Ajaccio, France.

Cacho, I., Grimalt, J.O., and Canals, M. (2002): Response of the western Mediterranean Sea to rapid climatic variability during the last 50,000 years: a molecular biomarker approach. *Journal of Marine Systems*, 33-34, 253-272 (Elsevier).

Calvet, M. (2004): The Quaternary glaciation of the Pyrenees. In Ehlers, J. and Gibbard, P.L. (eds.): *Quaternary Glaciations – Extent and Chronology, Part I: Europe*. Elsevier, Amsterdam, pp. 119-128.

Cassou, C., Terray, L., Hurrell, J.W., and Deser, C. (2004): North Atlantic Winter Climate Regimes: Spatial asymmetry, stationarity with time, and oceanic forcing. *Journal of Climate*, 17, 1055-1068.

CLIMAP Project 1976: The surface of the ice-age. Earth Science 191, 1131-1136.

Conchon, O., (1975): *Les formations quaternaires de type continental en Corse orientale. Vol. I: Observations et interprètations*, 514 p., *Vol. II: Documents annexes*, 244 p. Thèse Doctorat Etat, Sc., Univ. Paris VI, mult.

Conchon, O. (1977): Les glaciations quaternaires dans le Centre-Sud de la Corse; Comparaison avec la Corse du Nord et les regions periméditerranéennes. *Bulletin de la Société Géologique de France*, 19/5, 1041-1045.

Conchon, O. (1978): Quaternary studies in Corsica (France). *Quaternary Research*, 9/1, 41-53.

Conchon, O. (1979): Maximum extension of Wuermian glaciation around the western Mediterranean. In Sibrava, V., and Shotton, F. (eds.): *Quaternary glaciations in the Northern Hemisphere*. IGCP Project 24/ 5, 77-88.

Conchon, O. (1984): Corrélation entre la sedimentation fluviatile et la sedimentation marine littorale en Corse. *Bulletin de l´Association Française pour l´étude du Quaternaire*, 1/2/3, 151-156.

Conchon, O. (1985): Nouvelles observations sur les formations glaciaires quaternaires en Corse. *Bulletin de l´Association Française pour l´étude du Quaternaire*, 1, 5-11.

Conchon, O. (1986a): Corrélation entre les formations glaciaires, fluviatiles et marines de Corse et les sédiments sousmarins de Méditerranée occidentale au Pléistocène supérieur. *Revue de géologie dynamique et de géographie physique*, 27, 2, 85-93.

Conchon, O., (1986b): Quaternary glaciations in Corsica. In: Sibrava, V., Bowen, D.Q., and Richmond, G.M. (eds.): Quaternary glaciations in the Northern Hemisphere. *Quaternary Science Reviews*, 5, 429-432.

Conchon, O. (1988a): Paléogeographie et paléoclimatologie de la Corse au Quaternaire; chronologie des événements. *Bulletin Societé Géologique de France*, Huitieme Serie, 4/ 4, 587-594.

Conchon, O. (1988b): Manifestations et chronologie de la déglaciation fini-Würmienne en Corse. *Bulletin de l´Association Française pour l´étude du Quaternaire*, 2/3, 91-96.

Conchon, O. (1989): Dynamique et chronologie du détritisme quaternaire en Corse, domaine Méditerranéen montagnard et littoral. *Bulletin de l'Association Française pour l´étude du Quaternaire*, 4, 201-211.

Conchon, O. (1999): Le littoral de Corse (France) au quaternaire. *Quaternaire*, 10, 2-3, 95-105.

Conchon, O. and Gauthier, A. (1977): Les formations quaternaires du massif du Monte Renoso (Corse). *BRGM Section 1, Géologie de la France*, 4, 277-283.

Conchon, O., Loÿe-Pilot, M.-D., Paskoff, R., and Sanlaville, P. (1986): Quaternary marine and lagoonal deposits in the Vadina-Urbino area (Aleria region, eastern Corsica): Radiometric dating and field evidence. *Zeitschrift für Geomorphologie*, Suppl.-Bd. 62, 103-108.

COHMAP Members (1988): Climatic changes of the last 18,000 years: Observations and model simulations. *Science*, 241, 1043-1052.

Dahl-Jensen, D., Mosegaard, K., Gundestrup, N., Clow, G.D., Johnsen, S.J., Hansen, A.W., and Balling, N. (1998): Past temperatures directly from the Greenland Ice sheet. *Science*, 282, 268-271.

Degering, D., Kulig, G., and Krbetschek, M.R. (2006): ADELE – a novel software for age determination based on luminescene and electron spin resonance. Submitted to Radiation Measurements.

Delmas, M., Gunnell, Y., Braucher, R., Calvet, M. and Boulès, D. (2008): Exposure age chronology of the last glaciation in the eastern Pyrenees. *Quaternary Research*, 69, 231-241.

Desilets, D. and Zreda, M. (2003): Spatial and temporal distribution of secondary cosmic-ray nucleon intensities and applications to in-situ cosmogenic dating. *Earth and Planetary Science Letters*, 206, 21-42

Desilets, D., Zreda, M., and Prabu, T. (2006): Extended scaling factors for in situ cosmogenic nuclides: New measurements at low latitude. *Earth and Planetary Science Letters*, 246, 265-276.

Duller, G.A.T. (2004): Luminescence dating of Quaternary sediments: recent advances. *Journal of Quaternary Science*, 19, 183-192.

Dunai, T.J. (2000): Scaling factors for production rates of in-situ produced cosmogenic nuclides: a critical reevaluation. *Earth and Planetary Science Letters*, 176, 157-169.

Dunai, T.J. (2001): Influence of secular variation of the geomagnetic field on production rates of in-situ produced cosmogenic nuclides. *Earth and Planetary Science Letters*, 193, 197-212.

Dunne, A., Elmore, D., and Muzikar, P. (1999): Scaling factors for the rates of production of cosmogenic nuclides for geometric shielding and attenuation at depth on sloped surfaces. *Geomorphology*, 27, 3-11.

Durand-Delga, M. (1978): *Corse-Guides géologiques régionaux*. Masson éd. Paris, 208 pp.

Durand-Delga, M. (1984): Principaux trait de la Corse Alpine et corrélation avec les Alpes ligures. *Memorie della Società Geologica Italiana*, 28, 285-329.

Federici, P.R. (1977): Tracce di glacialismo prewürmiana nell'Appennino parmense. *Rivista Geografica Italiana*, 84, 205-216.

Federici, P.R. (1980): On the Riss glaciation of the Apennines. *Zeitschrift für Geomophologie*, 24, 111-116.

Florineth, D. and Schlüchter, C. (1998): Reconstruction of the Last Glacial Maximum (Wuermian) ice surface geometry and flowlines of the Central Swiss Alps. *Eclogae Geologicae Helvetiae*, 91, 391-407.

Florineth, D. and Schlüchter, C. (2000): Alpine evidence for atmospheric circulation patterns in Europe during the Last Glacial Maximum. *Quaternary Research*, 54, 295-308

Frei, C. and Schär, C. (1998): A precipitation climatology of the Alps from high-resolution rain-gauge observations. *International Journal of Climatology*, 18, 873-900.

GHCN Global Historical Climatology Network

García-Ruiz, J.M., Valero-Garcés, B.L., Martí-Bono, C., and González-Sampériz, P. (2003): Asynchroneity of maximum glacier advances in the central Spanish Pyrenees. *Journal of Quaternary Science*, 18, 61-72.

Giraudi, C. (1998): The Late Quaternary geologic evolution of Campo Felice Abruzzo – Central Italy. *Giornale di Geologia*, 60, 67-82.

Giraudi, C. (2004): The Apennine glaciations in Italy. In Ehlers, J. and Gibbard, P.L. (eds.): *Quaternary Glaciations – Extent and Chronology, Part I: Europe*. Elsevier, Amsterdam, pp. 215-223.

Giraudi, C. and Frezzotti, M. (1997): Late Pleistocene glacial events in the Central Apennines, Italy. *Quaternary Research*, 48, 280-290.

Godfrey-Smith, D., Huntley, D., and Chen, W.-H. (1988): Optical dating studies of quartz and feldspar sediment extracts. *Quaternary Science Reviews*, 7, 373-380.

González-Sampériz, P., Valero-Garcés, B.L., Moreno, A., Jalut, G., García-Ruiz, J.M., Marí-Bono, C., Delgado-Huertas, A., Navas, A., Otto, T., and Dedoubat, J.J. (2006): Climate variability in the Spanish Pyrenees during the last 30 000 yr revealed by the El Portalet sequence. *Quaternary Research*, 66, 38-52.

Gosse, J.C. and Phillips, F.M. (2001): Terrestrial in situ cosmogenic nuclides: theory and application. *Quaternary Science Reviews*, 20, 1475-1560

Granger, D.E., Spagnolo, M., Federici, P., Pappalardo, M., Ribolini, A., and Cyr, A.J. (2006): Last glacial maximum dated by means of 10Be in the Maritime Alps (Italy). In *EOS Transactions: American Geophysical Union* 87, Fall Meeting Supplement, Abstract H53B-0634.

Grootes, P.M., Stuiver, M., White, J.W.C., Johnsen, S., and Jouzel, J. (1993): Comparison of oxygen isotope records from the GISP2 and GRIP Greenland ice cores. *Nature*, 366, 552-554.

Grün, R. (1992): "Age" application software. Risø National Institute, Risø/Denmark.

Guyodo, Y. and Valet, J.-P. (1999): Global changes in intensity of the Earth's magnetic field during the past 800 ka. *Nature*, 399, 249-252.

Harrison, S., Yu, G. and Tarasov, P.E. (1996): Late Quaternary lake-level record from northern Eurasia. *Quaternary Research*, 45, 138-159.

Hayes, A., Kucera, M., Kallel, N., Sbaffi, L., and Rohling, E.J. (2005): Glacial Mediterranean sea surface temperatures based on planktonic foraminiferal assemblages. *Quaternary Science Reviews*, 24, 999-1016.

Heisinger, B., Lal, D., Jull, A.J.T., Kubik, P., Ivy-Ochs, S., Neumaier, S., Knie, K., Lazarev, V., and Nolte, E. (2002a): Production of selected cosmogenic radionuclides by muons: 1. Fast muons. *Earth and Planetary Science Letters*, 200, 345-355.

Heisinger, B., Lal, D., Jull, A.J.T., Kubik, P., Ivy-Ochs, S., Knie, K., and Nolte, E. (2002b): Production of selected cosmogenic radionuclides by muons 2. Capture of negative muons. *Earth and Planetary Science Letters*, 200, 357-369.

Hofmann, H.J., Beer, J., Bonani, G., von Gunten, H.R., Raman, S., Suter, M., Walker, R.L., Wölfli, W., and Zimmermann, D. (1987): ^{10}Be: Half-life and AMS-standards. *Nuclear Instruments and Methods in Physics Research*, B 29, 32-36.

Hollande, D. (1917): Géologie de la Corse. *Bulletin de la Société de Science de l'Histoire Naturelle de la Corse*, 35, 373-384.

Hughes, P.D., Woodward, J.C., and Gibbard, P.L. (2006): Late Pleistocene glaciers and climate in the Mediterranean. *Global and Planetary Change*, 50, 83-98.

Hughes, P.D., Woodward, J.C., and Gibbard, P.L. (2007): Middle Pleistocene cold stage climates in the Mediterranean: New evidence from the glacial record. *Earth and Planetary Science Letters*, 253, 50-56.

Hughes, P.D. and Woodward, J.C. (2008): Timing of glaciation in the Mediterranean mountains during the last cold stage. *Journal of Quaternary Science*, 23, 575-588.

Huntley, D.J. and Lamothe, M. (2001): Ubiquity of anomalous fading in K-feldspars and the measurement and correction for it in optical dating. *Canadian Journal of Earth Sciences*, 38, 1093-1106.

ISO 2533:1975. International Organization for Standardization, Standard Atmosphere, 1975

Ivy-Ochs, S. (1996): *The dating of rock surfaces using in situ produced ^{10}Be, ^{26}Al and ^{36}Cl, with examples from Antarctica and the Swiss Alps*. ETH dissertation No. 11763. 196 p.

Ivy-Ochs, S., Kerschner, H., Reuther, A., Preusser, F., Heine, K., Maisch, M., Kubik, P.W. and Schlüchter, C. (2008): Chronology of the last glacial cycle in the European Alps. *Journal of Quaternary Science*, 23, 559-573.

Ivy-Ochs, S., Schlüchter, Ch., Kubik, P.W., and Denton, G.H. (1999): Moraine exposure dates imply synchronous Younger Dryas glacier advances in the European Alps and in the Southern alps of new Zealand. *Geografiska Annaler*, 81 A, 313-323.

Ivy-Ochs, S., Schäfer, J., Kubik, P.W., Synal, H.-A., and Schlüchter, Ch. (2004): Timing of deglaciation on the northern Alpine foreland (Switzerland). *Eclogae geologicae Helvetiae*, 97, 47-55.

Jacobeit, J., Jönsson, P., Bärring, L., Beck1, C., and Ekström, M. (2001): Zonal Indices for Europe 1780–1995 and Running Correlations with Temperature. *Climatic Change*, 48, 219-241.

Jost, A., Lunt, D., Kageyama, M., Abe-Ouchi, A., Peyron, O., Valdes, P.J., and Ramstein, G. (2005): High-resolution simulations of the last glacial maximum climate over Europe: a solution to discrepancies with continental palaeoclimatic reconstructions? *Climate Dynamics*, 24, 577-590

Justino, F., and Peltier, W.R. (2005): The glacial North Atlantic Oscillation, *Geophysical Research Letters*, 32, L21803.1-L21803.4

Kageyama, M., D'Andrea, F., Ramstein, G., Valdes, P.J., and Vautard, R. (1999): Weather regimes in past climate atmospheric general circulation model simulations. *Climate Dynamics*, 15, 773-793

Kageyama, M., Laîne, A., Abe-Ouchi, A., Braconnot, P., Cortijo, E., Crucifix, M., de Vernal, A., Guiot, J., Hewitt, C.D., Kitoh, A., Kucera, M., Marti, O., Ohgaito, R., Otto-Bliesner, B., Peltier, W.R., Rosell-Melé, A., Vettoretti, G., Weber, S.L., Yu, Y., and MARGO Project Members (2006): Last Glacial Maximum temperatures over the North Atlantic, Europe and western Siberia: a comparison between PMIP models, MARGO sea-surface temperatures and pollen-based reconstructions. *Quaternary Science Reviews*, 25, 2082–2102

Kaplan, M.R., Ackert, R.P.jr., Singer, B.S., Douglass, D.C., and Kurz, M.D. (2004): Cosmogenic nuclide chronology of millennial-scale glacial advances during O-isotope stage 2 in Patagonia. *Geological Society of America Bulletin*, 116, 308-321.

Kaser, G., and Osmaston, H. (2002): *Tropical Glaciers*. Cambridge University Press, Cambridge. 207 pp.

Kelly, M.A., Kubik, P.W., von Blanckenburg, F., and Schlüchter, Ch. (2004): Surface exposure dating of the Great Aletsch Glacier Egesen moraine system, western Swiss Alps, using the cosmogenic nuclide ^{10}Be. *Journal of Quaternary Science*, 19, 431-441.

Kerschner, H., Kaser, G., and Sailer, R. (2000): Alpine Younger Dryas glaciers as palaeo-precipitation gauges. *Annals of Glaciology*, 31, 80-84.

Klaer, W. (1956): Verwitterungsformen im Granit auf Korsika. *Petermanns geographische Mitteilungen*, Ergänzungsheft 261, 146 pp.

Klasen, N. (2007): *Lumineszenzdatierung glazifluvialer Sedimente im nördlichen Alpenvorland*. PhD. Thesis, University of Cologne, 210 pp.

Knutti, R., Flückiger, J., Stocker, T.F., and Timmermann, A. (2004): Strong hemispheric coupling of glacial climate through freshwater discharge and ocean circulation. *Nature*, 430, 851-856.

Kohl, C.P., and Nishiizumi, K. (1992): Chemical isolation of quartz for measurement of in-situ produced cosmogenic nuclides. *Geochimica et Cosmochimica Acta*, 56, 3583-3587.

Korte, M. and Constable, C. (2005): Continuous geomagnetic field models for the past 7 millennia: 2. CALS7K. *Geochemistry, Geophysics, Geosystems*, 6, Q02H16. doi: 10.1029/2004GC000801.

Kotarba, A., Hercman, H., and Dramis, F. (2001): On the age of Campo Imperatore glaciations, Gran Sasso Massif, Central Italy. *Geografia Fisica e Dinamica Quaternaria*, 24, 65-69.

Krbetschek, M. (1995): *Lumineszenz-Datierung quartärer Sedimente Mittel-, Ost- und Norddeutschlands*. Dissertation TU Bergakademie Freiberg.

Krbetschek, M., Rieser, U., Zöller, L., and Heinicke, J. (1994): Radioactive disequilibria in the palaeodosimetric dating of sediments. *Radiation Measurements*, 23, 485-489.

Krbetschek, M., Götze, J., Dietrich, A., and Trautmann, T. (1997): Spectral information from minerals relevant for luminescence dating. *Radiation Measurements*, 27, 695-748.

Kubik, P.W., Ivy-Ochs, S., Masarik, J., Frank, M., and Schlüchter, C. (1998): ^{10}Be and ^{26}Al production rates deduced from an instantaneous event within the dendro-calibration curve, the landslide of Köfels. Ötz valley, Austria. *Earth and Planetary Science Letters*, 161, 231-241.

Kucera, M., Weinelt, M., Kiefer, T., Pflaumann, U., Hayes, A., Weinelt, M., Chen, M.-T., Mix, A.C., Barrows, T.T., Cortijo, E., Duprat, J., Juggins, S., and Waelbroeck, C. (2005): Reconstruction of sea-surface temperatures from assemblages of planktonic foraminifera: multi-technique approach based on geographically constrained calibration data sets and its application to glacial Atlantic and Pacific Oceans. *Quaternary Science Reviews*, 24, 951-998

Kuhlemann, J., Frisch, W., Székely, B., Dunkl, I., and Danišik, M. (2005a): Wuermian maximum glaciation in Corsica. *Austrian Journal of Earth Sciences*, 97, 68-81.

Kuhlemann, J., Székely, B., Danisik, M., Dunkl, I., Molnár, G., Timár, G., and Frisch, W. (2005b): DEM analysis of mountainous relief in a crystalline basement block: Cenozoic relief generations in Corsica (France). *Zeitschrift. für Geomorphologie* N.F., 49, 1-21

Kuhlemann, J., van der Borg, K., Danišík, M., and Frisch, W. (2007): In situ 10Be-erosion rates in granites of subalpine Miocene palaeosurfaces in the western Mediterranean (Corsica, France). *International Journal of Earth Sciences*, doi: 10.1007/s00531-007-0169-z

Kuhlemann, J., Rohling, E.J., Krumrei, I., Kubik, P., Ivy-Ochs, S. and Kucera, M. (2008): Regional synthesis of Mediterranean atmospheric circulation during the Last Glacial Maximum. *Science*, 321, 1338-1340. Data supplements S1 to S3 (13 pages) at www.sciencemag.org/cgi/content/full/1157638/DC1

Kuhlemann, J., Milivojević, M., Krumrei, I., and Kubik, P. (in press): Last glaciation of the Šara Range (Balkan peninsula): Increasing dryness from the LGM to the Holocene.

Lamothe, M., Auclair, M., Hamzaoui, C., and Huot, S. (2003): Towards a prediction of long-term anomalous fading of feldspar IRSL. *Radiation Measurements*, 37, 493-498

Larrassoana, J., Roberts, A.P., Rohling, E.J., Winklhofer, M., and Wehausen, R. (2003): Three million years of monsoon variability over the northern Sahara. *Climate Dynamics*, 21, 689-698

Lifton, N., Bieber, J., Clem, J., Duldig, M., Evenson, P., Humble, J., and Pyle, R. (2005): Addressing solar modulation and long-term uncertainties in scaling secondary cosmic rays for in situ cosmogenic nuclide applications. *Earth and Planetary Science Letters*, 239, 140-161.

Liritzis, I. and Kokkoris, M. (1992): Revised dose-rate data for thermoluminescence/ESR dating. *Nuclear Geophysics*, 6 (3), 423-443.

Loewe, F. (1971): Considerations on the origin of the Quaternary ice sheet of North America. *Arctic and Alpine Research*, 3, 331-344.

Lucerna, R. (1911): Les anciens glaciers de la Corse et les oscillacions pléistocènes de la Méditerranée. *Annales de Géographie*, XX, 44-51.

Luterbacher, J., Rickli, R., Xoplaki, E., Tinguely, C., Beck, C., Pfister, C., and Wanner, H. (2001): The Late Maunder Minimum (1675-1715) – a key period for studying decadal scale climate change in Europe. *Climatic Change*, 49, 441-462.

Luterbacher, J. and 48 coauthors (2006): Mediterranean climate variability over the last centuries: A review. In: Lionello, P., Malanotte-Rizzoli, R., and Boscolo, R. (eds.): *The Mediterranean Climate: an overview of the main characteristics and issues*. Elsevier, pp 27-148.

Masarik, J. and Reedy, R.C. (1995): Terrestrial cosmogenic nuclide production systematics calculated from numerical simulations. *Earth and Planetary Science Letters*, 136, 381-395.

Masarik, J. and Wieler, R. (2003): Production rates of cosmogenic nuclides in boulders. *Earth and Planetary Science Letters*, 216, 201-208.

McElhinny, M.W. and Senanayake, W.E. (1982): Variations in the geomagnetic dipole 1: The past 50.000 years. *Journal of Geomagnetism and Geoelectricity*, 34, 39-51.

Meier, M.F. and Post, A.S. (1962): Recent variations in mass net budgets in western North America. *IUGG/IASH Committee on Snow and Ice*, General Assembly, Obergurl, International Association of Science and Hydrology, 58, 63-77.

Meierding, T.C. (1982): Late Pleistocene glacial equilibrium-line in the Colorado Front Range: a comparison of methods. *Quaternary Research*, 18, 289-310.

Menkovic, L., Markovic, M., Cupkovic, T., Pavlivic, R., Trivic, B., and Banjac, N. (2004): Glacial morphology of Serbia, with comments on the Pleistocene Glaciation of Monte Negro, Macedonia and Albania. In Ehlers, J. and Gibbard, P.L. (eds.): *Quaternary Glaciations – Extent and Chronology, Part I: Europe. Elsevier*, Amsterdam, pp. 379-384.

Messerli, B. (1967): Die eiszeitliche und gegenwärtige Vergletscherung im Mittelmeergebiet. *Geographica Helvetica*, 22, 105-228.

Michard, A. (1965): *Etude géologique des hautes vallées du Taravo et du Fium Orbo (Corse)*. Thèse 3e cycle (Pétrographie), Clermont-Ferrand.

Mix, A.C., Bard, E., and Schneider, R. (2001): Environmental processes of the ice age: land, oceans, glaciers (EPILOG). *Quaternary Science Reviews*, 20, 627-657.

Murray, A.S. and Wintle, A.G. (2000): Luminescence dating of quartz using an improved single-aliquot regenerative-dose protocol. *Radiation Measurements*, 32, 57-73.

Murray, A.S. and Wintle, A.G. (2003): The single aliquot regenerative dose protocol: potential for improvements in reliability. *Radiation Measurements*, 37, 377-381.

Nambi, K. and Aitken, M.J. (1986): Annual dose conversion factors for TL and ESR dating. *Archaeometry*, 28, 202-205.

Nishiizumi, K., Finkel, R.C., Klein, J., and Kohl, C.P. (1996): Cosmogenic production of ^{7}Be and ^{10}Be in water targets. *Journal of Geophysical Research*, 101, 22,225-22,232.

Nishiizumi, K., Winterer, E.L, Kohl, C.P., Klein, J., Middleton, R., Lal, D., and Arnold, J.R. (1989): Cosmic ray production rates of ^{10}Be and ^{26}Al in quartz from glacially polished rocks. *Journal of Geophysical Research*, B94, 17907-17915.

Ohmura, A., Kasser, P., and Funk, M. (1992): Climate at the equilibrium line of glaciers. *Journal of Glaciology*, 38, 397-411.

Ohno, M. and Hamano, Y. (1992): Geomagnetic poles over the past 10.000 years. *Geophysical Research Letters*, 19, 1715-1718.

Olley, J.M., Murray, A., and Roberts, R.G. (1996): The effects of disequilibria in the uranium and thorium decay chains on burial dose rates in fluvial sediments. *Quaternary Science Reviews*, 15, 751-760.

Osmaston, H.A. (1965): *The past vegetation and climate of Ruwenzori and its neighbourhood*. D.Phil. Thesis, University of Oxford.

Osmaston, H.A. (1975): Models for the Estimation of Firnlines of Present and Pleistocene Glaciers. In: Peel, R.F., Chisholm, M.D.I., and Haggett, P. (Eds.): *Processes in Physical and Human Geography*. Bristol Essays, pp. 218-245.

Osmaston, H. (2005): Estimates of glacier equilibrium line altitudes by the Area × Altitude, the Area × Altitude Balance Ratio and the Area × Altitude Balance Index methods and their validation. *Quaternary International*, 138-139, 22-31.

Pallàs, R., Rodés, Á, Braucher, R., Carcaillet, J., Ortuño, M., Bordonau, J., Bourlès, D., Vilaplana, J.M., Masana, E. and Santanach, P. (2007): Late Pleistocene and Holocene glaciation in the Pyrenees: a critical review and new evidence from ^{10}Be exposure ages, south-central Pyrenees. *Quaternary Science Reviews*, 25, 2937-2963.

Palmentola, G. and Acquafredda, P. (1983): Gli effetti dei ghiacciai quaternari sulla Montagno del Matese, al confine Molisano-Campao. *Geografia Fisica e Dinamica Quaternaria*, 6, 117-130.

Peña, J.L., Sancho, C., Lewis, C., McDonald, E. and Rhodes, E. (2004): Datos cronológicos de las morrenas terminals del glaciar del Gállego y su relación con las terrazas fluvioglaciares (Pirineo de Huesca). In *Geografía Física de aragón, Aspectos generales y temáticos*, Peña, J.L., Longares, L.A. and Sánchez, M. (eds). Universidad de Zaragoza e Institución Fernando el Católico, Zaragoza; 71-84.

Pérez Alberti, A., Valcárel Díaz, M., and Blanco Chao, R. (2004): Pleistocene glaciation in Spain. In Ehlers, J., and Gibbard, P.L. (eds.): *Quaternary Glaciations – Extent and Chronology, Part I: Europe*. Elsevier, Amsterdam, pp. 389-394.

Peyron, O., Guiot, J., Cheddadi, R., Tarasov, P., Reille, M., de Beaulieu, J.L., Bottema, S., and Andrieu, V. (1998): Climatic reconstruction in Europe for 18,000 yr B.P. from pollen data. *Quaternary Research*, 49/2, 183-196.

Pinardi, N., and Masetti, E. (2000): Variability of the large scale general circulation of the Mediterranean Sea from observations and modelling: a review. *Palaeogeography Palaeoclimatology Palaeoecology*, 158, 153-174.

Porter, S.C. (1975): Equilibrium line altitudes of late Quaternary glaciers in the Southern Alps, New Zealand. *Quaternary Research*, 5, 27-47.

Porter, S.C. (2001): Snow line depression in the tropics during the last glaciation. *Quaternary Science Reviews*, 20, 1067-1091.

Prescott, J.R.. and Hutton, J. (1988): Cosmic ray and gamma ray dosimetry for TL and ESR. *Nuclear Tracks and Radiation Measurements*, 14, 223-227.

Prescott, J.R.. and Hutton, J. (1994): Cosmic ray contributions to dose rates for Luminescence and EST Dating: large depths and long-term variations. *Radiation Measurements*, 23, 497-500.

Prescott, J.R. and Stephan, L.G. (1982): The contribution of cosmic radiation to the environmental dose for thermoluminescence dating. *PACT*, 6, 17-25.

Preusser, F. and Schlüchter, C. (2004): Dates from an important early Late Pleistocene ice advance in the Aare valley, Switzerland. *Eclogae Geologicae Helvetiae*, 97, 245-253.

Preusser, F., Andersen, B.G., Denton, G.H., and Schlüchter, C. (2005): Luminescence chronology of late Pleistocene glacial deposits in North Westland, New Zealand. *Quaternary Science Reviews*, 24, 2207-2227.

Pumpelly, R. (1859): Sur quelques glaciers dans l'île de Corse. *Bulletin de la Société Géologique de France*, (2), XVII, p. 78.

Ramstein, G., Kageyama, M., Guiot, J., Wu, H., Hély, C., Krinner, G., and Brewer, S. (2007): How cold was Europe at the Last Glacial Maximum? A synthesis of the progress achieved since the first PMIP model-data comparison. *Climate of the Past*, 3, 331-339

Reille, M. (1975): *Contribution pollenanalytique à l'histoire tardiglaciaire et holocène de la végétation de la montagne Corse*. Thèse Doct. Etat, Marseille, 189 pp.

Reille, M. (1992): New pollen-analytical researches in Corsica: the problem of Quercus ilex L. and Erica arborea L., the origin of Pinus halepensis Miller forests. *New Phytologist*, 122, 359-378.

Reille, M. and Andrieu, V. (1995): The late Pleistocene and Holocene in the Lourdes Basin, Western Pyrénées, France: new pollen analytical and chronological data. *Vegetation History and Archaeobotany*, 4, 1-21.

Reille, M., Gamisans, J., Andrieu-Ponel, V., and de Beaulieu, J.-L. (1999): The Holocene at Lac de Creno, Corsica, France: a key site for the whole island. *New Phytologist*, 141, 291-307.

Reille, M., Gamisans, J., de Beaulieu, J.-L., and Andrieu, V. (1997): The late-glacial at Lac de Creno (Corsica, France): a key site in the western Mediterranean basin. *New Phytologist*, 135, 547-559.

Reuther, A., Urdea, P., Geiger, C., Ivy-Ochs, S., Niller, H.-P., Kubik, P., and Heine, K. (2007): Late Pleistocene glacial chronology of the Pietrele valley, Retezat Mountains, Southern Carpathians, constrained by ^{10}Be exposure ages and pedological investigations. *Quaternary International*, 164, 151-169.

Roberts, R., Spooner, N., Questiaux, G. (1994): Palaeodose underestimates caused by extended duration preheats in the optical dating of quartz. *Radiation Measurements*, 23, 647-653.

Rohling, E.J., Hayes, A., Kroon, D., De Rijk, S., and Zachariasse, W.J. (1998): Abrupt cold spells in the NW Mediterranean. *Paleoceanography*, 13, 316-322

Rohling, E.J., Mayewski, P.A., and Challenor, P. (2003): On the timing and mechanism of millennial-scale climate variability during the last glacial cycle. *Climate Dynamics*, 20, 257-267

Rohling, E.J., Abu-Zied, R.H., Casford, J.S.L., Hayes, A. and Hoogakker, B.A.A. (2008): The Mediterranean Sea: present and past. In *The Physical Geography of the Mediterranean*. Woodward, J.C. (ed.). Oxford University Press, Oxford, UK.

Rondeau, A. (1961): *Recherches géomorphologiques en Corse*. (La part de la tectonique et de l'érosion différentielle dans le relief de l'île). Armand Colin, Paris, 586 pp.

Rossi, P., Rouire, J., and Durand-Delga, M. (1980): *Carte Géologique de la France, A 1/250 000, Corse*, sheet 44/45, Notice explicative de la feuille, BRGM, Orléans, 80 pp.

Rossi, P., Durand-Delga, M., Caron, J.M., Guieu, G., Conchon, O., Libourel, G., Loye-Pilot, M.D., Oll, J.J., Pequignot, G., Potdevin, J.L., Lieuf, M., Rodriguez, G., Sedan, O., Vellutini, P.J., and Rouire, J. (1995): *Carte Géologique de la France (1/50000), feuille Corte (1110)*, BRGM, Orleans.

Sánchez Goñi, M.F., Cacho, I., Turon, J.-L. Guiot, J., Sierro, F.J., Peypouquet, J.-P., Grimalt, J.O., and Shackleton, N.J. (2002): Synchroneity between marine and terrestrial responses to millennial scale climatic variability during the last glacial period in the Mediterranean region. *Climate Dynamics*, 19, 95-105.

Sancho, C., Peña Monné, J.L., Lewis, C., McDonald, E. and Rhodes, E. (2002): Preliminary dating of glacial and fluvial deposits in the Cinca River Valley (NE Spain): chronological evidences for the Glacial Maximum in the Pyrenees?. In *Quaternary Climatic Changes and Environmental Crises in the Mediterranean Region*, Ruíz-Zapata, B., Borado-Valiño, M., Valdemillos, A., Gil-García, M.J., Badají, T., Bustamante, I. and Mendizábal, I. (eds). Universidad de Alcalá de Henares, Madrid; pp 453-456.

Schäfer-Neth, C. and Paul, A. (2003): The Atlantic Ocean at the Last Glacial Maximum: 1. Objective Mapping of the GLAMAP Sea-Surface Conditions. In *The South Atlantic in the Late Quaternary: Reconstruction of Material Budgets and Current Systems*, Wefer, G., Mulitza, S., and Ratmeyer, V. (eds). Springer-Verlag Berlin Heidelberg New York Tokyo; pp 531-548.

Schaller, M., von Blanckenburg, F., Veldkamp, A., Tebbens, L.A., Hovius, N., and Kubik, P.W. (2002): A 30.000 yr record of erosion rates from cosmogenic ^{10}Be in Middle European river terraces. *Earth and Planetary Science Letters*, 204, 307-320.

Severinghaus, J.P., Sowers, T., Brook, E.J., Alley, R.B., and Bender, M.L. (1998): Timing of abrupt climate change at the end of the Younger Dryas interval from thermally fractionated gases in polar ice. *Nature*, 391, 141-146.

Shackleton, N.J., Sánchez-Goñi, M.F., Pailler, D., and Lancelot, Y. (2003): Marine Isotope Substage 5e and the Eemian Interglacial. *Global and Planetary Change*, 36, 151-155.

Small, E.E., Anderson, R.S., Repka, J.L., and Finkel, R. (1997): Erosion rates of alpine bedrock summit surfaces deduced from in situ ^{10}Be and ^{26}Al. *Earth and Planetary Science Letters*, 150, 413-425.

Smith, B.W., and Rhodes, E.J. (1994): Charge movements in quartz and their relevance to optical dating. *Radiation Measurements*, 23, 329-333.

Spooner, S. (1994): On the optical dating signal from quartz. *Radiation Measurements*, 23, 601-605.

Stanford, J.D., Rohling, E.J., Hunter, S.E., Roberts, A.P. Rasmussen, S.O., Bard, E., McManus, J., and Fairbanks, R.G. (2006): Timing of meltwater pulse 1a and climate responses to meltwater injections. *Paleoceanography*, 21, doi:10.1029/2006PA001340.

Stokes, S. (1994): The timing of OSL sensitivity changes in a natural quartz. *Radiation Measurements*, 23, 601-606.

Stone, J.O. (2000): Air pressure and cosmogenic isotope production. *Journal of Geophysical Research*, 105, 23,753-23,759.

Svendsen, J.I., Alexanderson, H., Astakhov, V.I., Demidov, I., Dowdeswell, J.A., Funder, S., Gataullin, V., Henriksen, M., Hjort, C., Houmark-Nielsen, M., Hubberten, H.W., Ingólfsson, Ó. Jakobsson, M., Kjær, K.H., Larsen, E., Lokrantz, H., Lunkka, J.P., Lysså, A., Mangerud, J., Matiouchkov, A., Murray, A., Möller, P., Niessen, F., Nikolskaya, O., Polyak, L., Saarnisto, M., Siegert, C., Siegert, M., Spielhagen, R.F., and Stein, R. (2004): Late Quaternary ie sheet history of northern Eurasia. *Quaternary Science Reviews*, 23, 1229-1271.

Templer, R.H. (1986): The localized transition model of anomalous fading. *Radiation Protection Dosimetry*, 17, 493-497.

Visocekas, R. (1985): Tunnelling radioactive recombination in labradorite: its association with anomalous fading of thermoluminescence. *Nuclear Tracks and Radiation Measurements*, 10, 521-529.

von Blanckenburg, F., Hewawasam, T., and Kubik, P. (2004): Cosmogenic nuclide evidence for low weathering and denudation in the wet, tropical highlands of Sri Lanka. *Journal of Geophysical Research*, 109, doi: 10.1029/2003JF000049.

Wallinga, J., Bos, A.J.J., Dorenbos, P., Murray, A.S., and Schokker, J. (2007): A test case for anomalous fading correction in IRSL dating. *Quaternary Geochronology*, 2, 216-221.

Wallinga, J., Murray, A.S., and Wintle, A.G. (2000): The single-aliquot regenerative-dose (SAR) protocol applied to coarse-grain feldspar. *Radiation Measurements*, 32, 529-533.

Walther, G.-R., Beißner, S., and Burga, C.A. (2005): Trends in upward shift of alpine plants. *Journal of Vegetation Science*, 16, 541–548.

Wilhelm, F. (1975): *Schnee- und Gletscherkunde*. De Gruyter, Berlin, New York. 434 pp.

Wintle, A.G. (1977): Detailed study of a thermoluminescent mineral exhibiting anomalous fading. *Journal of Luminescence*, 15, 385-393.

Wintle, A.G. and Murray, A.S. (1999): Luminescence sensitivity changes in quartz. *Radiation Measurements*, 30, 107-118.

Woodward, J.C., Macklin, M.G., and Smith, G.R. (2004): Pleistocene glaciation in the mountains of Greece. In Ehlers, J. and Gibbard, P.L. (eds.): *Quaternary Glaciations – Extent and Chronology, Part I: Europe*. Elsevier, Amsterdam, pp. 155-173.

World Ocean Atlas (1998) vol. 2

Wu, H., Guiot, J., Brewer, S., and Guo, Z. (2007): Climatic changes in Eurasia and Africa at the last glacial maximum and mid-Holocene: reconstruction from pollen data using inverse vegetation modelling. *Climate Dynamics*, 29, 211-229.

Xoplaki, E., Gonzalez-Rouco, J.F., Luterbacher, J., and Wanner, H. (2004): Wet season Mediterranean precipitation variability: influence of large-scale dynamics and trends. *Climate Dynamics*, 23, 63-78

Yang, S., Odah, H., and Shaw, J. (2000): Variations in the geomagnetic dipole moment over the last 12,000 years. *Geophysical Journal International*, 140, 158-162.

Appendix A

Sample preparation

Separation of quartz from whole rock

The samples are cleaned with a brush, placed into 30 % H_2O_2, and finally dried.

The clean rock peaces have to be carefully grinded with a jaw crusher until all grains are smaller than 630 µm; the dust is removed with the 250 µm sieve. The fraction of 250 – 630 µm is used for further separation. 100 g of the grinded sample is placed in 1 litre of a mixture of 30 % HCl and 0.03 % H_2O_2 (1:2) in a warm water bath overnight, then rinsed well and dried. In the next step, the sample is covered with 2 % HNO_3 for 30 minutes, rinsed acid free, and dried in an oven at 100 °C overnight.

The quartz is separated by gravitational separation with Na-Polytungstate solution, starting with a density of 2.75 g/cm³. The solution is thinned step-by-step until the quartz containing fraction is nearly pure. After gravitational separation, the sample has to be rinsed thoroughly and dried. To get rid of remaining feldspars, nine portions with 6 g of the quartz fraction are placed in 1 litre of acid (2 % HNO_3 and 2 % HF, 1:2) in 50 °C warm water bath for 45 hours, in-between shaken in ultrasonic bath from time to time. The used acid is discarded. The quartz is washed free from acid, rinsed with deionised water, and dried. To get rid of remaining processing residues or skeletal quartz, the dried quartz is milled in a small agate mill without pressure for 3 – 5 minutes, washed and dried. The resulting quartz concentrate should be inspected under a microscope. Eventually, gravitational separation has to be repeated.

Separation of ^{10}Be from quartz (ultra pure chemistry)
(after von Blanckenburg et al., 2004)

The dry quartz concentrate is weighted into clean Teflon beakers. 7M ultra pure (Δ) HF is added so that the sample is just all covered with HF plus 5 mm excess liquid height, and heated one hour at max. 120 °C with lid. The cooled sample is washed with ultra pure water. In order to remove fluorides, ultra pure (Δ) Aqua regia (ΔHNO_3 conc (15M) : ΔHCl conc (6M) = 1:3) is added covering the sample with acid plus 5 mm excess liquid height. After a possible exothermic reaction, the cooled sample is then heated for minimum 1 h at 120 °C with lid on the beaker. Then the sample is washed, rinsed, and shaken thoroughly 4-5 times with ultra pure water. The dried sample has to be weighted precisely as this weight will be used in the age calculation.

28 M ΔHF is added to the dry sample covering it with acid plus 5 mm excess liquid height. The first and second additions must be done with care because of possible strong exothermic reactions, therefore adding the HF should be done in increments. When the reaction has stopped and the sample is cooled down, the acid is boiled down without lid at 120 °C until it has evaporated to dryness. For the third and following additions, the HF is added, the closed beaker put on the hot plate for minimum 2 hours, and only now with open lid evaporated to dryness. Repeat this until all quartz is dissolved. In-between, the white precipitate has to be dissolved with

ultra pure H_2O and evaporated.

For sample weights below 50 g 0.15 ml ^9Be carrier is added, for sample weights above 50 g 0.3 ml carrier. The precise weight of the carrier solution has to be documented since precise amount of carrier is needed for age calculation (depending on carrier concentration in the solution, carrier amount has to be corrected for the calculation). 12 ml ΔAq reg (3 ml ΔHNO_3 conc + 9 ml 6M ΔHCl) are added ensuring that carrier and sample are well mixed. The samples are heated until all residue is dissolved and evaporated gently. Then exactly 10 ml 6M ΔHCl are added and the samples heated gently. All material, liquid and solid, is transferred into cleaned 10 ml centrifuge tubes and centrifuged for 5 minutes at 3000 rpm. The liquid only is transferred into 50 ml centrifuge tubes (make sure that no solid material comes with the liquid).

Into the centrifuge tubes, 3M NH_4OH (NH_4OH conc suprapur : Millipore H_2O =1:4) is added to the sample liquid until pH 8,5 – 9 is reached. While adding NH_4OH, continuous shaking is necessary as well as regular checks of the pH with pH-strips (drop solution on test stripes). Around pH 9 a precipitation and sometimes a change in colour should be visible. The samples are centrifuged for 5 minutes at 3000 rpm. The liquid is decanted and discarded. The precipitate is washed with 10 ml pH 8 – ultra pure H_2O by shaking it lightly. Centrifugation is repeated and the liquid decanted again. Finally, the precipitate is dissolved in 1 ml 6M ΔHCl, if 1 ml is not enough to dissolve a larger amount of precipitate, 2 ml 6M ΔHCl should be used.

In the following step, 7.5 ml RKBN104704 columns filled with 2 ml resin (Biorad 1X8 100-200 mesh) are used to clean the samples from most of the iron. The columns are stored in ultra pure H_2O which first has to dropp out. The resin is then cleaned in two steps with 5 ml + 5 ml 0.3M ΔHCl. In the next three steps, the resin is conditioned with 2 ml + 2 ml + 2 ml 6M ΔHCl. During the following steps, the Be (+Al) is collected in a cleaned Savillex beaker: the dissolved sample is loaded and then washed down with 1 ml + 2 ml + 2 ml 6M ΔHCl, if it is dissolved in 1 ml acid, otherwise with 2 ml + 2 ml + 2 ml 6M ΔHCl. The Savillex beakers are put on the hotplate over night to evaporate the HCl from the beaker. The resin is cleaned with 5 ml +5 ml 0.3M ΔHCl, and the column stored with resin sealed in Millipore H_2O.

For the second chromatographic step in which the Be is completely separated, 4 ml 0.4M oxalic acid (50.43 g Oxal-Dihydrat / 1 l Millipore H_2O = 0.4M oxalic acid) are added to the dry sample, and heated with lid (at ~100 °C) to ensure complete dissolution. The 7.5 ml RKBN104704 columns filled with 1 ml resin (Biorad AG50-X8 200-400 mesh) are stored in H_2O that has to drop out. In two steps the resin is cleaned with 2 ml + 3 ml 6M ΔHCl. With 2 ml + 3 ml Millipore H_2O the HCl is removed from the resin and it is conditioned with 2 ml + 3 ml 0.4M oxalic acid. Then the dissolved sample is loaded and then washed down with 1 ml 0.4M oxalic acid. Also, Al is eluted. With the next 1 ml 0.4M oxalic acid, the sample is washed further down and Al eluted. To elute Fe, Al, Ti and other elements, 5 ml + 5 ml 0.4M oxalic acid are added. 1 ml + 2 ml Millipore H_2O remove the oxalic acid from the columns. For the next steps the molar concentration of the acid has to be accurate to elute only the Na and then the Be, therefore titrated ΔHCl must be used. First 1 ml + 3 ml 0.5M titrated ΔHCl are added. Then the collecting beaker has to be changed to collect the Be in a fresh 7 ml Savillex vial with 1 ml + 1 ml + 5 ml 1M titrated ΔHCl. Again, the collecting beaker is changed and the resin cleaned with 10 ml 6M ΔHCl. 5 ml H_2O remove the 6M HCl from the resin, which is sealed and stored in Millipore H_2O. The sample is dried down on the hotplate over night.

In the last part of the Be extraction, silver nitrate solution is needed: 38 g $AgNO_3$ are dissolved into 1 l ultrapure H_2O or 380 mg $AgNO_3$ into 10 ml ultrapure H_2O. This solution has to be stored in dark bottles and cupboards because of fast oxidation. Samples are fumed after columns 3x with minimum 0.5 ml ΔHNO3 conc to eliminate the Cl. The aim of the following steps is to get a Ag:Be ratio of 20. For 0.3 (0.15) mg ^{9}Be carrier 9.25 (4.625) mg AgNO3 are needed. So 0.25 (0.125) ml ΔHNO3 conc + 0.25 (0.125) ml Ag solution are added to the dried sample. In the case of 0.3 mg carrier, the solution is then fumed to 200 µl (half), in the case of 0.15 mg carrier only the evaporate is dissolved completely. The solution is transferred to quartz crucibles and the samples dried in a ceramic holder (at ca. 150 °C). Dusk mask and/or fume hood are necessary for all following steps and Pt-coated tongs should be used. Each sample is oxidised separately in the Bunsen burner by first drying the sample outside of the flame and then holding it in the dark blue part of the flame. The crucible can glow shortly.

The cooled sample is scratched from the crucible wall with a metal spatulum and loaded from the rear (side with iron ring) into the cleaned targets. It is pressed down in the target by hammering often but slightly on a metal pin that should have the same diameter as the target drill. To fill the hole, copper (powder Cu p.a., 2703, 63 µm) is added from the rear and pressed down thoroughly with the hammer. All instruments have to be cleaned with methanol between each sample.

Appendix B

Physical basis of luminescence dating

A physical model for the luminescence of solids is the energy-level diagram that illustrates electron transitions and energy levels of electrons in an ideal crystal lattice. Under normal circumstances all electrons are found within the valence band of crystalline isolators. When energy is added to the system, the electron may jump from the valence band to the higher energy conduction band. Between the valence band, representing the ground state, and the conduction band, where electrons move freely, is the "forbidden gap". Due to crystal defects electrons can stay between the energy bands. The crystal defects are characterised by positive or negative deficits in charge compared to regular occupied sites and therefore are traps for free moving charges. Typical defects are vacancies (Schottky defect), interstitials (Frenkel defect), and impurities. The traps have different energy levels and are called recombination level above the valence band ("Aktivatorterm"), and trap level below the conduction band ("Haftterm").

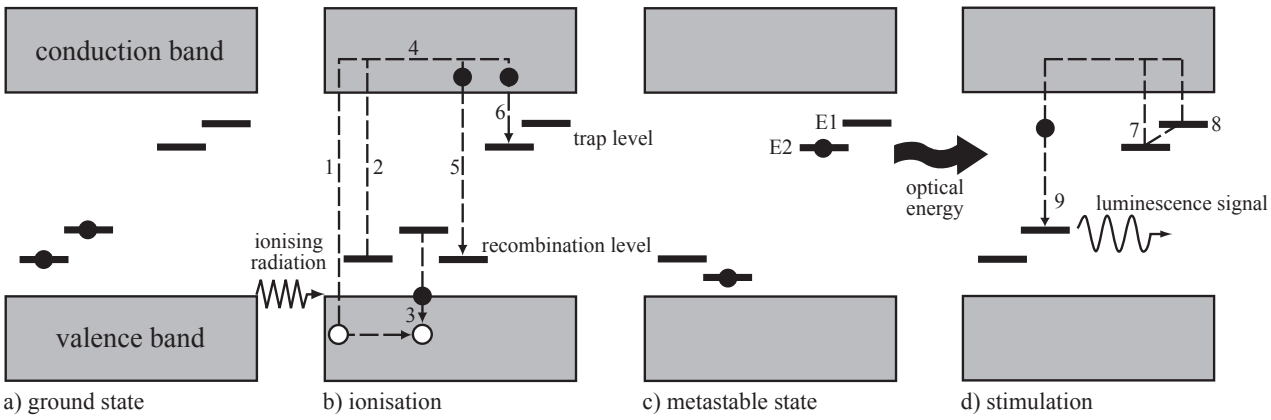

Fig. B1: Energy level diagramm as physical model explaining the optically stimulated luminescence (after Krbetschek, 1995). The four steps a) to d) are explained in the text.

The recombination levels are filled with electrons in the ground state, trap levels are empty (Fig. B1a). After absorbing energy from ionising radiation, electrons may jump from the valence band or the recombination level to the conduction band (Fig. B1b, transition 1, 2). The resulting positively charged holes move through the band until they can recombine with an electron from the recombination level (transition 3). The electrons move freely in the conduction band (transition 4). Most of these electrons recombine after a very short stay by emitting photons (fluorescence) or by non-radiative relaxation (transition 5). Only a small part of the electrons is captured in the trap level and stored in a meta-stable state (transition 6). The depth of the level, that is the energetic distance to the conduction band (Fig. B1c, E1<E2), equals the amount of energy needed for releasing the electron from the trap level. It determines the average stability of the meta-stable states (Aitken, 1985). Electrons in shallow trap levels already recombine at room temperature whereas emptying deeper levels needs a larger amount of energy. Thus meta-stable states can be conserved over geological times.

Electrons captured in trap levels are excited by sufficient supply of energy (heat or light) and reach directly

(Fig. B1d, transition 7) or via intermediate levels (transition 8) the conduction band, from where they recombine with an empty recombination level releasing their stored energy as photons. This emission of photons as light is the signal recorded during the luminescence dating. There the intensity of luminescence gives the quantity of captured electrons. The wavelength of the emitted light depends on the distance of the conduction band to the recombination level.

Appendix C

Schematic preparation path of luminescence samples

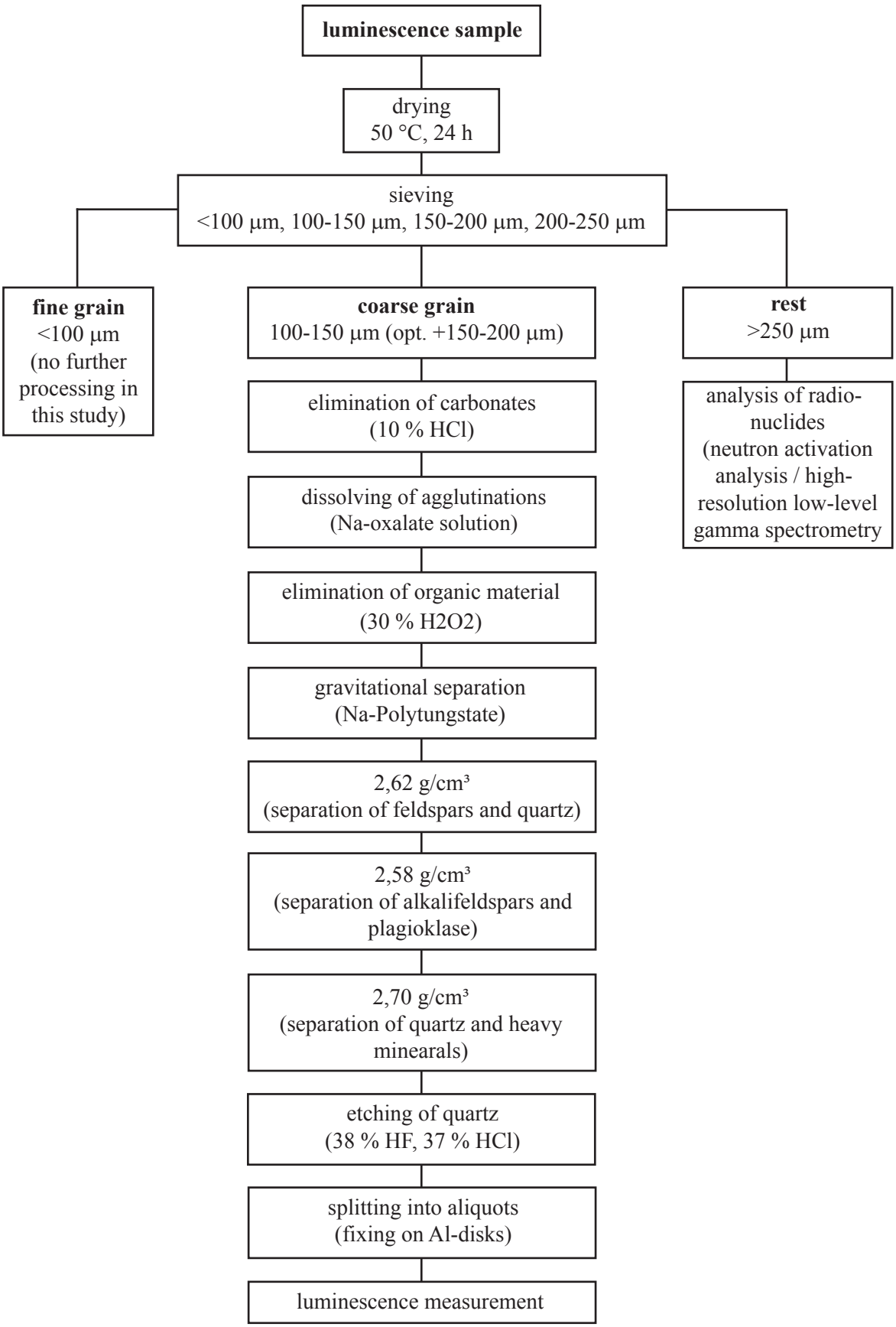

Appendix D

Determination of dose rate

The contribution of natural radioactivity is calculated with the content of natural radionuclides in the surrounding material. The dose rate is then calculated from the nuclide concentrations relevant for it by conversion factors (Adamiec and Aitken, 1998; Liritzis and Kokkoris, 1992; Nambi and Aitken, 1986).

As the determination of the radionuclide concentration is done with dried material, a moisture corrected dose rate has to be used in the calculation of the total dose rate. This is calculated for each kind of radiation with the moisture factor W (mass water/dry weight of the sediment) with following equations (Aitken, 1985):

$$D_{\alpha} = \frac{D_{\alpha,dry}}{1+1.50W} \quad (1) \qquad D_{\beta} = \frac{D_{\beta,dry}}{1+1.25W} \quad (2) \qquad D_{\gamma} = \frac{D_{\gamma,dry}}{1+1.14W} \quad (3)$$

For the calculation of the total dose rate the moisture corrected parts of the dose rate are used.

The percentage of cosmic radiation in the total dose rate is generally small in relation to the doses derived from decay of radionuclides. However, at high geographic latitude and altitude in combination with low radionuclide contents it can be significantly. The dose rate of the cosmic radiation can be calculated with the equations given by Prescott and Hutton (1988) and Prescott and Stephan (1982). The first equation applies to sea level and 55° geomagnetic latitude and allows for sediment thickness as well as density (Prescott and Hutton, 1988):

$$D_0 = 0.21 * e^{(-0.070x+0.0005x^2)} \quad (4)$$

with D_0 the cosmic dose rate [Gy/kyr] (Prescott and Hutton, 1988), and x the cover factor [g/cm²] (sediment thickness [m]/density [g cm^{-3}]).

The second equation given by Prescott and Stephan (1982) allows in addition for the geomagnetic latitude and the altitude of the sampling point:

$$D_c = D_0 * \left[F + J * e^{(h/H)}\right] \quad (5)$$

with D_0 the cosmic dose rate [Gy/kyr] (eq. 4), D_c the cosmic dose rate [Gy/kyr] (Prescott and Stephan, 1982), h the altitude a.s.l. [km], and F, J, H functions of geomagnetic latitude (Prescott and Stephan, 1982).

The part of the radiation components in the total dose rate depends on grain size. The external α-radiation penetrates only the outer rim of mineral grains with a diameter of 100-200 µm. For quartz its share is eliminated by removing the outer layer of the grain (etching) and is therefore not included into dating of coarse grains. For feldspars, an alpha-efficiency factor is used to correct for the α-radiation. The part of the β-radiation has to be multiplied by a grain size specific correction factor (Aitken, 1985). The total dose rate is calculated as follows:

$$D_{total} = 0.90D_{\beta} + D_{\gamma} + D_c \quad (6).$$

Appendix E

Documentation of Corsican data

Tab. E1: Data required for exposure age calculation with the Cronus calculator: sample name, latitude, longitude, elevation in metres a.s.l., atmosphere model (elev flag, set to standard atmosphere), sample thickness and density, erosion rate, and the concentration of cosmogenic nuclides. The nuclide concentrations are corrected for chemical blanks. Additionally, rock type (alk - alkaline; calk - calc-alkaline) and sampled surface (B - boulder; S - polished rock surface) are indicated.

sample	lat [°]	long [°]	elev [m]	elev flag	rock type	B/ S	sample thickn. [cm]	sample density [g/cm³]	shielding	erosion rate [cm/yr]	^{10}Be conc [at/g]	error in ^{10}Be [at/g]
Ku10	42.30	8.88	1370	std	granite	B	4	2.7	0.9958	0.001	252288	11643
Ku11	42.17	9.10	1038	std	granite	S	4	2.7	0.9825	0.001	252926	12147
Ku16	42.26	8.93	1762	std	granite	S	4	2.7	0.9999	0.001	249937	8860
Ku27	42.12	9.13	890	std	granite	B	1	2.7	0.9884	0.0015	119761	25839
Ku29	42.28	9.11	640	std	granite	B	4	2.7	0.9790	0.0003	189680	9570
Ku34	42.31	8.95	950	std	granite	S	4	2.7	0.9978	0.001	222394	13241
Ku37	42.20	8.92	1120	std	granite	S	2	2.7	0.9976	0.001	200876	8520
Ku41	42.23	9.06	2063	std	granite	S	1	2.7	0.9997	0.001	39410	17885
Ku47	42.03	9.19	1460	std	granite	B	2	2.7	0.9974	0.001	303316	11849
Ku49	41.97	9.09	1200	std	granite	S	4	2.7	0.9884	0.001	161266	9177
Ku51	42.02	9.11	1260	std	granite	B	3	2.7	0.9866	0.001	173546	13424
Ku52	42.02	9.11	1250	std	granite	B	2	2.7	0.9866	0.001	208452	11990
Ku53	42.01	9.10	1250	std	granite	B	3	2.7	0.9958	0.0008	822622	29080
Ku63	42.24	9.06	1500	std	granite	B	2	2.7	0.9958	0.001	49798	3927
Ku81	41.85	9.18	1450	std	granite	S	2	2.7	0.9968	0.001	227836	11264
Ku84	41.87	9.18	1465	std	granite	B	2	2.7	0.9994	0.001	315380	12217
Ku85	42.20	9.05	1910	std	granite	S	2	2.7	0.9562	0.001	221042	10949
Ku86	42.15	9.06	1070	std	granite	B	3	2.7	0.9594	0.001	184919	10897
Ku88	42.03	9.15	1750	std	granite	B	2	2.7	0.9986	0.001	264843	12783
Ku89	42.30	8.88	1550	std	alk granite	B	3	2.7	0.9971	0.0003	2357994	130494
Ku90	42.30	8.90	1210	std	granite	B	4	2.7	0.9931	0.001	204844	15331
Ku91	42.30	8.90	1230	std	granite	B	1	2.7	0.9931	0.001	237166	14423
Ku93	42.25	8.96	1695	std	granite	B	2	2.7	0.9814	0.001	227783	12961
Ku95	42.24	8.98	1545	std	granite	B	4	2.7	0.9979	0.001	242752	9334
Ku98	42.21	9.06	2338	std	granite	B	2	2.7	0.9985	0.0006	227249	33869
Ku99	42.21	9.06	2335	std	granite	S	3	2.7	0.9985	0.0006	113997	19315
Ku100	42.18	9.06	1540	std	granite	B	3	2.7	0.9958	0.001	876589	59109
Ku102	42.15	9.08	1422	std	granite	S	3	2.7	0.9944	0.001	73767	7844
Ku103	42.11	9.12	1190	std	gneiss	B	2	2.7	0.9903	0.001	198923	14013
Ku104	42.13	9.13	985	std	granite	B	2	2.7	0.9927	0.0015	210072	14251
Ku105	42.22	9.02	1570	std	alk granite	S	1	2.7	0.9614	0.0003	739469	28389
Ku106	42.23	9.09	1480	std	granite	S	1	2.7	0.9581	0.001	157210	12589
Ku107	42.04	9.14	1800	std	granite	S	1	2.7	0.9694	0.001	270294	32721
Ku110	42.12	9.12	1110	std	granite	B	3	2.7	0.9900	0.0015	210380	17593
Ku111	42.12	9.12	1130	std	granite	B	3	2.7	0.9811	0.0015	183673	18514
Ku112	42.12	9.12	1115	std	granite	B	3	2.7	0.9880	0.0015	197393	22008
Ku117	42.01	9.23	1405	std	granite	B	2	2.7	0.9888	0.001	258504	11333
Ku118	42.24	9.06	1520	std	granite	B	1	2.7	0.9884	0.001	252585	11752
Ku119	42.28	8.93	1170	std	granite	B	2	2.7	0.9940	0.001	284304	41471
Ku121	42.06	9.13	2120	std	granite	B	2	2.7	0.9484	0.001	229644	8459
Ku122	42.28	9.11	682	std	granite	B	2	2.7	0.9828	0.0003	78229	13010
Ku123	42.28	9.00	1741	std	granite	S	2	2.7	0.9429	0.001	216324	15938

Tab. E1 (continued)

sample	lat [°]	long [°]	elev [m]	elev flag	rock type	B/ S	sample thickn. [cm]	sample density [g/cm³]	shielding	erosion rate [cm/yr]	^{10}Be conc [at/g]	error in ^{10}Be [at/g]
Ku125	42.28	9.01	1553	std	granite	B	3	2.7	0.9954	0.001	284822	11581
Ku126	42.28	9.02	1547	std	granite	B	3	2.7	0.9985	0.001	204701	15758
Ku127	42.28	9.02	1538	std	granite	B	3	2.7	0.9969	0.001	258849	13265
Ku128	42.06	9.13	2104	std	granite	B	2	2.7	0.9484	0.001	146215	18100
Ku129	42.21	9.06	2267	std	aplit	S	2	2.7	0.9800	0	418357	17691
Ku131	42.21	9.06	2345	std	granite	S	3	2.7	0.9768	0	315913	16128
Ku132	42.21	9.03	1710	std	alk granite	S	3	2.7	0.9748	0	252323	16088
Ku133	42.21	9.02	1950	std	alk granite	S	3	2.7	0.9699	0	219016	12312
Ku135	42.06	9.17	1260	std	granite	B	1	2.7	0.9923	0.001	171911	21060
Ku138	42.28	9.01	1575	std	granite	B	2	2.7	0.9972	0.001	287067	14411
CO-Gro	42.23	9.03	1442	std	granite	B	2	2.7	0.8789	0.001	33882	4677
CO-Ver	42.30	8.88	1494	std	calk granite	B	2	2.7	0.9891	0.001	242661	13185

Tab. E2: Results of the Cronus calculator: Scaling factors independent of scaling scheme, the internal uncertainty contains only the uncertainty of the AMS measurements; production rate due to spallation after the Lal/Stone scaling system; exposure ages according to the different scaling schemes with the external uncertainty including also the uncertainty in the reference nuclide production rate for spallation and the uncertainty in the nuclide production rate by muons (Balco et al. 2007).

	Results not dependent on spallogenic production rate model		Exposure ages -- constant production rate model		Exposure ages -- time-varying production models											
			Scaling scheme for spallation:		Lal(1991) / Stone(2000)			Desilets et al. (2003; 2006)		Dunai (2001)		Lifton et al. (2005)		Time-dependent Lal (1991)/Stone (2000)	
Sample name	thickness scaling factor	shield. factor	prod. rate (muons) [at/g/yr]	internal uncert. [yr]	expos. age [yr]	external uncert. [yr]	prod. rate (spallation) [at/g/yr]	expos. age [yr]	external uncert. [yr]	expos. age [yr]	external uncert. [yr]	expos. age [yr]	external uncert. [yr]	expos. age [yr]	external uncert. [yr]
Ku10	0.967	0.9958	0.31	1148	20680	2443	14.16	21450	3214	21674	3243	20991	2708	20500	2375
Ku11	0.967	0.9825	0.278	1803	28915	3721	10.78	30072	4910	30307	4942	29361	4125	28381	3570
Ku16	0.967	0.9999	0.351	589	14600	1556	18.99	15048	2065	15318	2099	14734	1725	14579	1523
Ku27	0.9916	0.9884	0.267	3638	14002	3921	9.88	15179	4540	15413	4620	14940	4307	14079	3934
Ku29	0.967	0.979	0.244	1365	25216	2714	7.8	26585	3590	26748	3601	26166	3065	25023	2646
Ku34	0.967	0.9978	0.27	1975	26204	3488	10.23	27503	4556	27725	4587	26918	3889	25871	3380
Ku37	0.9833	0.9976	0.287	977	19375	2222	11.88	20415	2997	20631	3023	20026	2523	19282	2169
Ku41	0.9916	0.9997	0.389	752	1634	766	24.07	1763	838	1858	884	1720	810	1682	788
Ku47	0.9833	0.9974	0.32	1131	23469	2754	15.35	24085	3624	24311	3652	23526	3023	23122	2653
Ku49	0.967	0.9884	0.293	937	14486	1708	12.26	15387	2259	15622	2291	15126	1937	14518	1685
Ku51	0.9751	0.9866	0.3	1308	14829	1965	12.94	15687	2495	15923	2531	15412	2185	14848	1943
Ku52	0.9833	0.9866	0.299	1239	18306	2241	12.95	19212	2926	19438	2957	18840	2503	18221	2194
Ku53	0.9751	0.9958	0.299	14134	134966	37434	12.96	131361	45231	131856	45434	121992	33055	121079	29073
Ku63	0.9833	0.9958	0.325	256	3162	381	15.86	3483	500	3577	512	3409	438	3233	385
Ku81	0.9833	0.9968	0.319	972	16917	1962	15.18	17635	2578	17881	2610	17285	2185	16850	1919
Ku84	0.9833	0.9994	0.321	1185	24543	2905	15.39	25137	3816	25361	3844	24535	3179	24122	2790
Ku85	0.9833	0.9562	0.369	641	11683	1293	20.5	12022	1671	12333	1713	11754	1414	11668	1269
Ku86	0.9751	0.9594	0.282	1362	19439	2423	10.88	20534	3182	20745	3210	20151	2727	19353	2373
Ku88	0.9833	0.9986	0.351	862	15561	1772	19.03	16012	2297	16282	2334	15677	1943	15512	1735
Ku89	0.9751	0.9971	0.329	33575	266190	62400	16.36	248197	67798	247491	67222	231278	52109	238650	50140
Ku90	0.967	0.9931	0.294	1653	18698	2529	12.49	19629	3203	19850	3237	19247	2790	18611	2483
Ku91	0.9916	0.9931	0.298	1560	21225	2717	13.01	22153	3508	22371	3538	21698	3004	21052	2649
Ku93	0.9833	0.9814	0.345	895	13909	1631	18.05	14419	2098	14689	2136	14126	1793	13908	1605
Ku95	0.967	0.9979	0.327	758	16949	1868	16.16	17555	2483	17800	2514	17190	2080	16872	1823
Ku98	0.9833	0.9985	0.421	1266	8132	1464	28.73	8190	1609	8544	1679	7949	1472	8061	1443
Ku99	0.9751	0.9985	0.419	698	4035	785	28.44	4208	881	4333	906	4101	817	4086	791
Ku100	0.9751	0.9958	0.328	34643	132274	56425	16.18	123177	57283	123757	57763	112631	41058	115223	39791
Ku102	0.9751	0.9944	0.316	567	5100	732	14.78	5535	909	5643	925	5423	816	5163	734
Ku103	0.9833	0.9903	0.294	1504	18169	2386	12.43	19125	3053	19347	3086	18764	2649	18098	2342
Ku104	0.9833	0.9927	0.275	2562	26374	4158	10.61	27878	5438	28152	5497	27214	4652	26012	4022
Ku105	0.9916	0.9614	0.333	2263	51031	5589	16.26	49663	6915	49844	6918	47760	5675	48348	5154
Ku106	0.9916	0.9581	0.324	985	11153	1452	15.15	11746	1823	12028	1866	11517	1598	11162	1436

Tab. E2 (continued)

	Results not dependent on spallogenic production rate model		Exposure ages -- constant production rate model		Exposure ages -- time-varying production models											
			Scaling scheme for spallation:		Lal(1991) / Stone(2000)			Desilets et al. (2003; 2006)		Dunai (2001)		Lifton et al. (2005)		Time-dependent Lal (1991)/Stone (2000)	
Sample name	thickness scaling factor	shield. factor	prod. rate (muons) [at/g/yr]	internal uncert. [yr]	expos. age [yr]	external uncert. [yr]	prod. rate (spallation) [at/g/yr]	expos. age [yr]	external uncert. [yr]	expos. age [yr]	external uncert. [yr]	expos. age [yr]	external uncert. [yr]	expos. age [yr]	external uncert. [yr]
Ku107	0.9916	0.9694	0.358	2178	15657	2678	19.31	16059	3089	16332	3143	15718	2797	15599	2647
Ku110	0.9751	0.99	0.285	2697	23472	3885	11.58	24733	4912	24995	4970	24158	4279	23217	3783
Ku111	0.9751	0.9811	0.287	2545	19445	3356	11.66	20613	4155	20865	4211	20184	3694	19353	3304
Ku112	0.9751	0.988	0.286	3202	21495	4056	11.6	22722	4942	22974	5004	22231	4425	21336	3983
Ku117	0.9833	0.9888	0.315	1081	20534	2396	14.6	21283	3162	21509	3191	20829	2658	20347	2327
Ku118	0.9916	0.9884	0.328	971	17812	2053	16.11	18436	2690	18678	2722	18045	2269	17707	2003
Ku119	0.9833	0.994	0.292	5352	28397	6226	12.32	29337	7097	29571	7159	28621	6481	27851	6039
Ku121	0.9833	0.9484	0.394	425	10513	1086	23.47	10709	1418	11049	1462	10448	1183	10483	1062
Ku122	0.9833	0.9828	0.248	1613	9448	1819	8.24	10268	2135	10473	2176	10129	2003	9500	1820
Ku123	0.9833	0.9429	0.35	1094	13209	1689	17.94	13680	2105	13958	2147	13397	1831	13209	1667
Ku125	0.9751	0.9954	0.329	981	20156	2310	16.36	20722	3036	20955	3065	20257	2541	19961	2241
Ku126	0.9751	0.9985	0.329	1198	13777	1804	16.34	14397	2260	14656	2299	14118	1974	13789	1783
Ku127	0.9751	0.9969	0.328	1097	18206	2156	16.21	18807	2794	19046	2827	18404	2368	18084	2103
Ku128	0.9833	0.9484	0.392	858	6548	1048	23.21	6754	1209	7084	1270	6570	1092	6516	1035
Ku129	0.9833	0.98	0.412	653	15378	1489	26.89	15315	1880	15548	1901	14995	1585	15295	1453
Ku131	0.9751	0.9768	0.42	570	11143	1124	28	11150	1404	11452	1437	10894	1192	11101	1101
Ku132	0.9751	0.9748	0.346	885	13830	1493	17.96	14252	1877	14477	1901	13999	1624	13825	1470
Ku133	0.9751	0.9699	0.373	573	10170	1053	21.21	10426	1335	10716	1368	10202	1142	10146	1034
Ku135	0.9916	0.9923	0.301	1988	14297	2435	13.24	15145	2907	15384	2954	14882	2647	14326	2422
Ku138	0.9833	0.9972	0.332	1180	19723	2356	16.8	20269	3042	20506	3074	19814	2571	19542	2290
CO-Gro	0.9833	0.8789	0.319	356	2524	420	13.4	2799	515	2924	537	2739	472	2589	429
CO-Ver	0.9833	0.9891	0.324	1112	17513	2094	15.7	18158	2710	18400	2743	17780	2306	17422	2047

Tab E3: Sampling location (geographical name, latitude, longitude, and altitude a.s.l.), sediment type, depth below ground surface, and used grain size fraction of luminescence samples measured in Cologne

sample	location	lat [°]	long [°]	altitude [m]	sediment type	depth [m]	grain size [µm]
Cruz1	Cruzini valley	42°08'29"	9°01'20"	490	fluvial	8	150-350
Cruz2	Cruzini valley	42°08'29"	9°01'20"	490	glaciofluvial	8	100-250
Cruz3	Cruzini valley	42°08'29"	9°01'20"	491	glaciofluvial	7	100-200
Cruz4	Cruzini valley	42°08'29"	9°01'20"	494	glaciofluvial	4	90-250
Guagno	Fiume Grossu valley	42°10'26"	8°53'21"	465	glaciofluvial	4	100-200
Cann1	Cannareccia valley	42°03'32"	9°10'26"	1239	fluvial	2	100-200
Cann2	Cannareccia valley	42°03'31"	9°10'24"	1235	fluvial	5	100-200
Cann3	Cannareccia valley	42°03'30"	9°10'18"	1240	fluvial	3	100-200

Tab. E4: Radionuclide concentrations (Uranium, Thorium, Kalium) as determined with neutron activation analysis (NAA) of the luminescence samples measured in Cologne.

sample	U [ppm]	error [ppm]	Th [ppm]	error [ppm]	K [%]	error [%]
Cruz1	7.21	0.27	13.94	0.43	3.21	0.25
Cruz2	6.74	0.25	12.88	0.40	3.87	0.27
Cruz3	6.32	0.24	11.14	0.35	3.20	0.26
Cruz4	6.07	0.24	13.43	0.42	3.59	0.30
Guagno	12.29	0.42	25.66	0.78	3.78	0.31
Cann1	3.41	0.28	15.44	0.48	1.75	0.39
Cann2	3.64	0.23	11.56	0.37	2.77	0.38
Cann3	2.75	0.20	10.71	0.34	2.45	0.40

Tab. E5: Age determinations, results of the equivalent dose (D_e) estimations derived from regenerative single aliquot dose (SAR) measurements of feldspars and one quartz sample, and calculated dose rates for potassium-rich feldspars and quartz (Cologne). RSD is the relative standard deviation of the n D_e values finally used for D_e determination, the number of all measured aliquots is shown in parenthesis. The errors of the D_e estimates include the systematic uncertainty from the calculation of the beta source of 5 %. All uncertainties represent the 1σ confidence interval.

sample	Equivalent Dose [Gy]	error [Gy]	Dose Rate [Gy/kyr]	error [Gy/kyr]	RSD [%]	n	Luminesc. age [kyr]	error [kyr]
Cruz1	191	13	5.69	0.29	15	11 (12)	33.6	2.9
			Fading corrected (fading rate 3.3 % per decade)				44.7	4.5
Cruz2	182	10	5.95	0.27	14	8 (8)	30.7	2.2
Cruz3	158	14	5.22	0.25	11	11 (11)	30.3	3.0
Cruz4	141	15	5.68	0.29	21	12 (12)	24.8	2.9
Guagno-Fsp	351	21	7.93	0.33	9	10 (10)	44.2	3.2
Guagno-Qz	301	36	6.92	0.32	22 (34)	15 (24)	43.5	5.6
Cann1	59	4	3.79	0.34	11	11 (12)	15.5	1.7
Cann2	143	12	4.36	0.33	20	14 (15)	32.7	3.7
Cann3	412	27	3.9	0.34	12	12 (12)	106	11
			Fading corrected (fading rate 5.8 % per decade)				186	23

Tab E6: Sampling location (geographical name, latitude, longitude, and altitude a.s.l.), sediment type, depth below ground surface, and used grain size fraction of luminescence samples measured in Hannover.

sample	location	lat [°]	long [°]	altitude [m]	sediment type	depth [m]	grain size [μm]
OSL1	Polischellu	41°49'04"	9°15'36"	493	glaciofluvial	2	100 - 200
OSL2	Gravona N 193	42°06'03"	9°05'41"	848	glaciofluvial	3	206 - 212
OSL3	Gravona	42°06'00"	9°06'05"	935	glaciofluvial	2	100 - 200
OSL4	Vizzavona Pass	42°07'39"	9°09'43"	1053	glaciofluvial	2	106 - 212
OSL5	Vecchio	42°12'43"	9°11'43"	312	fluvial	1	106 - 212
OSL6	Restonica	42°17'33"	9°06'19"	655	glaciofluvial	7	100 - 200
OSL7	Soccia-Creno	42°12'55"	8°55'26"	1050	glaciofluvial	3	106 - 212
OSL8	Fium Orbo/Cavu	42°04'41"	9°11'51"	635	fluvial	2	100 - 200
OSL9	M.Forest. Verde	42°00'23"	9°11'45"	971	glaciofluvial	2	106 - 212
OSL10	Camp Tattone/Agnone	42°14'46"	9°10'25"	802	fluvial	1	100 - 200
OSL11	St. Pietro di Venaco	42°07'57"	9°08'56"	741	glaciofluvial	5	100 - 200
OSL12	Punta Caldane	42°20'16"	9°20'24"	1595	glaciofluvial	1	100 - 200
OSL13	Ghisoni oxbow	42°05'53"	9°13'41"	518	fluvial	0.3	106 - 212
OSL15	l'Abatesco at Gite	41°57'54"	9°15'39"	525	glaciofluvial	4	100 - 200
OSL16	San Gavino	41°59'17"	9°15'38"	539	glaciofluvial	3	106 - 212
OSL17	north. Asinao valley	41°52'55"	9°16'19"	676	fluvial	2	106 - 212
OSL18	Caracutu valley	41°47'27"	9°12'19"	831	fluvial	2	100 - 200
OSL19	Pont de Marmano	42°02'22"	9°11'43"	967	glaciofluvial	2	106 - 212
OSL20	Cruzini 489m	42°08'30"	9°01'02"	489	glaciofluvial	7	100 - 200
OSL21	M.Forest. Vizzavona	42°07'04"	9°08'03"	1032	glaciofluvial	2	106 - 212

Tab E7: Results of the luminescence measurements from Hannover: equivalent dose (ED) from K-feldspar (FSP) after the additive multiple aliquot (MAA) and regenerative single aliquot (SAR) protocol, and quartz after the SAR protocol; cosmic dose rate considering latitude, depth below ground surface, and altitude a.s.l.; calculated dose rates for K-feldspars and quartz; infrared-stimulated luminescence (IRSL) age estimates of feldspars and optical stimulated luminescence (OSL) age estimate of quartz.

sample	FSP- MAA ED [Gy]	error [Gy]	FSP- SAR ED [Gy]	error [Gy]	Qz- SAR ED [Gy]	error [Gy]	Cosmic Dose Rate [µGy/yr]	error [µGy/yr]	Dose Rate^{Fsp} [Gy/kyr]	error [Gy/kyr]	Dose Rate^{Qz} [Gy/kyr]	error [Gy/kyr]	IRSL- Age FSP - MAA [kyr]	error [kyr]	IRSL- Age FSP - SAR [kyr]	error [kyr]	OSL-Age Qz-SAR [kyr]	error [kyr]
OSL1	97.9	4.1	111.3	2.0	52.6 (9)	5.7	162	0.16	5.87	0.59	5.32	0.53	16.7	1.1	18.9	1	9.9	1.2
OSL2	101.9	3.4	91.1	1.0	66.5 (13)	4.8	137	0.14	4.59	0.46	4.01	0.4	22.2	1.3	19.8	1	16.6	1.5
OSL3	512.3	1.6	380.1	13.2	387.2 (19)	13.7	164	0.16	4.41	0.44	3.86	0.39	116	6	86.3	5.3	100	6
OSL4	50.3	1.9	55.3	0.9	54.7 (23)	2.2	167	0.17	4.62	0.46	4.04	0.4	10.9	0.7	12	0.6	13.5	0.9
OSL5	299.3	1.6	-	-	202.8 (11)	18.3	175	0.18	4.72	0.47	4.14	0.41	63.4	3.2	-	-	49	5.1
OSL6	192.8	4.1	173.7	2.7	31.3 (3)	26.2	87	0.09	7.06	0.71	6.5	0.65	27.3	1.5	24.6	1.3	4.8	4
OSL7	508.6	1.8	402.1	12.1	37.5 (5)	2.6	148	0.15	5.11	0.51	4.53	0.45	99.5	5	78.6	4.6	8.3	2.8
OSL8	113.9	2.8	97.6	1.5	41.5 (12)	2.2	160	0.16	4.41	0.44	3.87	0.39	25.8	1.4	22.1	1.2	10.7	0.8
OSL9	272.9	2.0	246.3	7.1	82.0 (3)	14.6	167	0.17	5.73	0.57	5.14	0.51	47.6	2.4	43	2.5	16	3
OSL10	119.2	3.2	104.8	2.2	47.8 (5)	12.0	161	0.16	4.52	0.45	3.98	0.4	26.4	1.5	23.2	1.3	12	3.1
OSL11	75.3	1.7	77.2	1.0	206.2 (15)	16.5	111	0.11	3.71	0.37	3.18	0.32	20.3	1.1	20.8	1.1	64.9	6.2
OSL12	193.7	2.4	-	-	77.5 (4)	14.8	232	0.23	2.48	0.25	1.95	0.2	78.2	4.3	-	-	39.7	7.9
OSL13	1.5	2.4	1.7	0.0	1.3 (11)	0.1	198	0.2	4.64	0.46	4.06	0.41	0.32	0.5	0.37	0.02	0.32	0.03
OSL15	65.1	1.2	56.9	1.1	27.7 (12)	3.3	121	0.12	4.86	0.49	4.32	0.43	13.4	0.7	11.7	0.6	6.4	0.8
OSL16	123.7	3.7	122.7	2.5	30.1 (9)	4.4	138	0.14	4.06	0.41	3.48	0.35	30.5	1.8	30.2	1.7	8.6	1.3
OSL17	124.7	1.4	123.4	3.0	85.7 (15)	5.3	161	0.16	4.89	0.49	4.31	0.43	25.5	1.3	25.2	1.4	19.9	1.6
OSL18	74.3	1.8	69.9	1.4	48.3 (8)	6.8	176	0.18	5.19	0.52	4.64	0.46	14.3	0.8	13.5	0.7	10.4	1.6
OSL19	149.3	3.9	120.1	3.0	66.2 (18)	2.0	167	0.17	4.1	0.41	3.7	0.37	36.4	2.1	29.3	1.7	17.9	1.1
OSL20	133.2	1.1	127.1	2.9	-	-	85	0.09	5.2	0.52	-	-	25.6	1.3	24.4	1.3	-	-
OSL21	96.3	2.0	85.2	1.8	44.6 (7)	5.5	169	0.17	4.32	0.43	3.74	0.37	22.3	1.2	19.7	1.1	11.9	1.6

Tab. E8: Equilibrium line altitudes (ELA) of Corsican glaciers during the Last Glacial Maximum (LGM), Oldest Dryas (OD), and Younger Dryas (YD) as derived from detailed hypsometry according to the AAR and AABR method and the altitudinal difference between both methods.

glacier		massif	LGM ELA [m a.s.l.]		difference [m]	OD ELA [m a.s.l.]		difference [m]	YD ELA [m a.s.l.]		difference [m]
			AAR 0.6	AABR 2		AAR 0.6	AABR 2		AAR 0.6	AABR 2	
Mte. San Petrone E		Alpine Corsica	1114	1202	88			no glacier			
Mte. Grosso N		Cinto	1112	1197	85						
Frintogna/ Calenzana		Cinto	1094	1136	42						
Tartagine/ Mte. Corona		Cinto	1378	1467	89	1690	1773	83	1772	1867	95
Mandriaccia/ Capu Ladroncellu		Cinto				1690	1755	65			
Rau du Ladroncellu		Cinto				1628	1701	73			
Mte. Padru E		Cinto	1764	1746	-18						
Mte. Padru S		Cinto	1673	1770	97						
Spasimata	P. Ghialla/ C. a u Carrozzu	Cinto	1327	1371	44	1684	1732	48			
Muvrella SW		Cinto							1651	1745	94
Asco		Cinto				1689	1800	111			
Manica		Cinto				1869	1974	105	1982	2092	110
Latoncello		Cinto	1667	1734	67						
Capu Biancu S		Cinto	1960	2017	57	2064	2158	94	2124	2209	85
Paglia Orba E		Cinto				1637	1738	101	1734	1834	100
Fango		Cinto	1435	1418	-17						
Lonca		Cinto	1377	1433	56						
Golo		Cinto	1654	1680	26	1701	1799	98	1756	1870	114
Catamalzi/ Vergio		Cinto	1426	1540	114	1586	1693	107	1620	1726	106
Vergio/ Aitone		Cinto	1298	1423	125						
Fragica		Rotondo-Oro				1667	1752	85	1755	1853	98
	Scrocchiella					1653	1749	96	1726	1829	103
	Punta Artica E					1697	1748	51	1850	1900	50
Tavignano[1]	Tavignano N	Rotondo-Oro	1643	1652	9	1643	1756	113	1739	1851	112
	Cimatella S					1698	1801	103			
	Tavignano S					1690	1795	105	1829	1900	71
	Timozzo					2002	1934	-68	2040	2071	31
Restonica	Rivisecco	Rotondo-Oro							1974	2010	36
	Melo					1781	1833	52	1819	1910	91
Misognu/ Mte. Cardo E		Rotondo-Oro	1670	1673	3	1884	1957	73	1937	2019	82
Rotondo S	Vallee de Petra Piana	Rotondo-Oro	1540	1665	125	1813	1888	75	2051 1978	2084 2053	33 75
Fium Grosso	Punta Mozzella	Rotondo-Oro	1503	1587	84	1801	1845	44			
Punta di Petra Facciata		Rotondo-Oro	1512	1604	92			no glacier			
Grottaccia/ Mte. d´Oro NW		Rotondo-Oro	1524	1611	87	1651	1730	79	1715	1791	76

[1]: AABR calculated with BR=3

Tab. E8 (continued)

glacier		massif	LGM ELA [m a.s.l.]		difference [m]	OD ELA [m a.s.l.]		difference [m]	YD ELA [m a.s.l.]		difference [m]
			AAR 0.6	AABR 2		AAR 0.6	AABR 2		AAR 0.6	AABR 2	
Coracchia/Cruzini Migliarello N		Rotondo-Oro	1507	1474	-33						
Speloncello/ Mte. d'Oro NE		Rotondo-Oro	1551	1667	116						
Agnone/ Vizzavona	Oro S	Rotondo-Oro	1474	1580	106	1680	1747	67	1755	1835	80
									1755	1813	58
Alzeta		Renoso	1506	1593	87						
Punta di l´Oriente		Renoso	1542	1629	87						
Sce. de Pizzolo		Renoso				1889	1982	93	1930	2018	88
Gravona		Renoso				1715	1839	124	1883	1960	77
Tragette-Bastani	Bastani Niellucio	Renoso				1872	1930	58	2025	2114	89
									1934	2038	104
Cannareccia		Renoso	1663	1662	-1						
Punta Capannella W		Renoso	1626	1718	92						
Pozzi Marmano		Renoso				1757	1872	115	1793	1923	130
Prunelli		Renoso	1638	1652	14						
Ese-Scaldasole		Renoso				1689	1783	94	1747	1846	99
Mte. Giovanni NE		Renoso	1499	1548	49						
Mte. Giovanni S		Renoso	1525	1560	35						
l'Argentuccio		Verde	1615	1677	62						
Punta Capella W		Verde	1623	1706	83						
Nursoli	Nursoli N	Verde	1549	1664	115	1645	1743	98	1761	1846	85
	Nursoli S								1753	1853	100
Aria		Verde	1424	1518	94						
Punta Mozza		Verde	1364	1463	99						
l´AbatescoN		Verde	1386	1436	50						
l'AbatescoS		Verde	1340	1373	33	1689	1776	87			
Usciolu		Verde				1706	1798	92			
Asinao N		Bavella-Incudine	1263	1292	29	1356	1414	58			
Incudine/ Tremoli		Bavella-Incudine							1799	1887	88
Incudine NW		Bavella-Incudine	1531	1646	115						
Asinao S		Bavella-Incudine				1687	1810	123	1777	1873	96
Polischellu		Bavella-Incudine	1103	1124	21	1291	1403	112			
mean			1485	1548	63	1712	1794	83	1838	1923	86

Appendix F

Late Pleistocene equilibrium line altitudes in the Western Mediterranean

Tab. F1: Wuermian Mediterranean equilibrium line altitudes [m a.s.l.] with emphasis on the LGM. Mountain ranges are sorted from west to east. The peak altitude [m a.s.l.] is given as a reference for the altitude of the massif. Dating with cosmogenic radionuclides (CRN) is indicated according to the cited source.

region	mountain range	massif	lat [°] N	long [°]	peak alt. [m]	ELA Wuermian			Ref.
						Early	LGM	CRN	
Spain	Galician M.	Sierra del Faro	42°17'	8°15' W	1129	900			(1)
	Galician M.	Sierra Cabrera	42°10'	6°46' W	2012	1500- 1700			(1)
	Cord. Cantabrica	Sierra de Picos	42°49'	6°50' W	1923	1400			(1)
	Cord. Cantabrica	West	43°04'	6°09' W	2417	1450			(1)
	Cord. Cantabrica	East	43°01'	4°44' W	2615	1500			(1)
	Cord. Iberica	Sierra Demanda	42°08'	2°58' W	2305	1900-1950			(1)
	Cord. Iberica	Sierra Moncayo	41°46'	1°50' W	2316	1950			(1)
	Sistema Central	Sierra Gredos	40°15'	5°24' W	2592	1800-1850			(1)
	Sistema Central	Sierra Guadarrama	40°58'	3°41' W	2469	2000			(1)
	Sierra Nevada		37°03'	3°19' W	3481	2500			(1)
	Pyrenees	Aneto (Maladetta)	42°37'	0°39' E	3404	1700-1800			(2)
	Pyrenees	Monte Perdido	42°40'	0°02' E	3355	1700-1800			(2)
France	Pyrenees	Carlit	42°34'	1°56' E	2921	1600 - 2200			(2)
	Pyrenees	Aston	42°41'	1°40' E	3141	1700-1800			(2)
	Pyrenees	Arres d'Anie	42°53'	0°44' E	2504	1500			(2)
	Pyrenees	Ossau	42°48'	0°23' E	2884	1500			(2)
	Pyreness	N Pyrenees	43°00'	0°45' E	2000	1400			(2)
	Pyrenees	Canigou	42°31'	2°27' E	2785	1600 - 2200			(2)
	Pyrenees	Néouvielle	42°50'	0°07' E	3091				(2)
	Vosges		48°02'	6°52' E	1424	900	1100	^{14}C	(3)
	Massif Central	Mont-Dore	45°34'	2°50' E	1886		1000-1200		(4, 5, 6)
	Massif Central	Cantal	45°05'	2°45' E	1858		1000-1200		(5, 6, 7, 8)
	Massif Central	Aubrac	44°38'	3°00' E	1471		1250		(5, 6)
	Massif Central	Forez	45°34'	3°51' E	1640		1280		(4)
	Jura	French Jura	46°30'	5°50' E	1723		1000		(5, 6)
	Corsica	N + E margin	42°	9° E	1971		1400	^{10}Be	this study
	Corsica	N central	42°23'	8°57' E	2706		1900	^{10}Be	this study
Helvetia	Alps	Rhine glacier	47°36'	9°25' E	3614		950		(9)
Italy	Apennine	northern part	44°17'	10°24' E	2165		1400		(10)
	Apennine	Gran Sasso	42°27'	13°36' E	2912		1750	^{14}C	(10, 11)
	Apennine	S Apennine	40°07'	15°51' E	2267		1700		(10)
Croatia		Snezniska Planota	45°35'	14°27' E	1643		1400-1500		(10)
		Velebit	44°21'	15°30' E	1686		1200-1300		(12)
Bosnia		Plocna	43°36'	17°35' E	2228		1900-2000		(12)
		Prenje	43°33'	17°54' E	2155		1500		(12)
Mte Negro		Veliko Vetao	43°13'	18°45' E	2396		1600		(12)
		Durmitor	43°08'	19°03' E	2522		1800		(12)
		Orjen	42°34'	18°32' E	1894		1300		(13, 14, 15)
Albania		Shara Range	42°02'	20°52' E	2748		2000		(14)
		E Albanian Alps	42°32'	20°08' E	2656		1650		(14, 15)
		W Albanian Alps	42°23'	19°48' E	2693		1500		(11, 14)
		Albanian Mtns	41°45'	20°14' E	2767		1600		(11, 14)

Tab. F1 continued.

region	mountain range	massif	lat [°] N	long [°]	peak alt. [m]	ELA Wuermian Early	ELA Wuermian LGM	CRN	Ref.
Greece	W-Greece	Smolikas/ Tymphi	40°01'	20°52' E	2637		2200-1700	U-Th	(11, 16, 17)
		Helmos	37°58'	22°12' E			1900		(11, 16)
		Taigetos	37°06'	22°18' E	2407		2000		(11, 16)
	E-Greece	Olymp	40°05'	22°21' E	2917		2200-1900		(17)
	Crete	Psiloriti (Ida)	35°13'	24°47° E	2500		2500		(12)
Romania	S Carpathians	Fagarasi	45°30'	23°40' E	2535		1900		(12)
	S Carpathians	Retezat	45°20'	23°35' E	2502		1800	^{10}Be	(18)
N-Africa	High Atlas	Jbel Toubkal	31°03'	7°57' W	4165		3500		(17)
		Irhil M'Goun	31°30'	6°27' W	4070		3400		(17)
		Jbel Ayachi	32°29'	4°56' W	3751		3300		(17)
	Middle Atlas	Jbel Bou Iblane	33°41'	4°03' W	3340		2400-2500		(17)
		Jbel Bou Naceur	33°33'	3°54' W	3310				(17)
	Saharan Atlas	Djurdjura	36°28'	4°08' E	2308		1900-2100		(12)

References of Table F1:

(1) Pérez Alberti, A., Valcárel Díaz, M., and Blanco Chao, R. (2004): Pleistocene glaciation in Spain. In Ehlers, J., and Gibbard, P.L. (eds.): *Quaternary Glaciations – Extent and Chronology, Part I: Europe*. Elsevier, Amsterdam, pp. 389-394.

(2) Calvet, M. (2004): The Quaternary glaciation of the Pyrenees. In Ehlers, J. and Gibbard, P.L. (eds.): *Quaternary Glaciations – Extent and Chronology, Part I: Europe*. Elsevier, Amsterdam, pp. 119-128.

(3) Mercier, J.-L. and Jeser, M. (2004): The glacial history of the Vosges Mountains. In Ehlers, J. and Gibbard, P.L. (eds.): *Quaternary Glaciations – Extent and Chronology, Part I: Europe*. Elsevier, Amsterdam, pp. 113-116

(4) Etlicher, B. (1985): Corrélations glaciares-periglacieare dans l'Est du Massif Central Français. *Bulletin de l'Association Française pour l'Etude du Quaternaire*, 2/3, 117-124.

(5) Buoncristiani, J.-F. and Campy, M. (2004a): Palaeogeography of the last two glacial episodes in the Massif Central, France. In Ehlers, J. and Gibbard, P.L. (eds.): *Quaternary Glaciations – Extent and Chronology, Part I: Europe*. Elsevier, Amsterdam, pp. 111-112.

(6) Buoncristiani, J.-F. and Campy, M. (2004b): The palaeogeography of the last two glacial episodes in France: the Alps and Jura. In Ehlers, J. and Gibbard, P.L. (eds.): *Quaternary Glaciations – Extent and Chronology, Part I: Europe*. Elsevier, Amsterdam, pp. 101-110

(7) de Goër, H. (1972): La Planèze de Saint Flour: formes et dépots glaciaires. *Annales de la faculté des sciences de Clermont-Ferrand*, 48, 204 pp.

(8) Veyret, Y. (1981): *Les modelés et formations d'origines glaciaire dans le Massif Central français: problème de distribution et de limites dans le milieu de la moyenne montagne*. Thèse d'état de Paris I, Presse universitaire de Lille, 783 pp.

(9) Benz, C. (2003): Der würmzeitliche Rheingletscher-Maximalstand, Digitale Rekonstruktion, Modellierung und Analyse mit einem Geographischen Informationssystem. *Physical Geography*, 43, Geographisches Institut der Universitaet Zuerich, 180 pp.

(10) Giraudi, C. (2004): The Apennine glaciations in Italy. In Ehlers, J. and Gibbard, P.L. (eds.): *Quaternary Glaciations – Extent and Chronology, Part I: Europe*. Elsevier, Amsterdam, pp. 215-223.

(11) Hughes, P.D., Woodward, J.C., and Gibbard, P.L. (2007): Middle Pleistocene cold stage climates in the Mediterranean: New evidence from the glacial record. *Earth and Planetary Science Letters*, 253, 50-56.

(12) Messerli, B. (1967): Die eiszeitliche und gegenwärtige Vergletscherung im Mittelmeergebiet. *Geographica Helvetica*, 22, 105-228.

(13) Cvijic, J. (1899): Glacijalne i morfološke studije o planinama Bosne, Hercegovine i Crne Gore. Glas *Srpske Kraljevske Akademije Nauka*, LVII, 1-196, Belgrade.

(14) Menković, L., Marković, M., Cupkovic, T., Pavlivic, R., Trivic, B., and Banjac, N. (2004): Glacial morphology of Serbia, with comments on the Pleistocene Glaciation of Monte Negro, Macedonia and Albania. In Ehlers, J. and Gibbard, P.L. (eds.): *Quaternary Glaciations – Extent and Chronology, Part I: Europe*. Elsevier, Amsterdam, pp. 379-384.

(15) Milivojević, M., Menković, L., and Calić, J. (2008): Pleistocene glacial relief of the central part of Mt. Prokletije (Albanian Alps). *Quaternary International*, 190, 112-122.

(16) Woodward, J.C., Macklin, M.G., and Smith, G.R. (2004): Pleistocene glaciation in the mountains of Greece. In Ehlers, J. and Gibbard, P.L. (eds.): *Quaternary Glaciations – Extent and Chronology, Part I: Europe*. Elsevier, Amsterdam, pp. 155-173.

(17) Hughes, P.D., Woodward, J.C., and Gibbard, P.L. (2004): Quaternary glaciation in the Atlas Mountains of North Africa. In: J. Ehlers, P.L. Gibbard (Eds.), *Quaternary Glaciations – Extent and Chronology, Part III: South America, Asia, Africa, Australia, Antarctica*. Elsevier, Amsterdam, 255-260

(18) Reuther, A., Urdea, P., Geiger, C., Ivy-Ochs, S., Niller, H.-P., Kubik, P., and Heine, K. (2007): Late Pleistocene glacial chronology of the Pietrele valley, Retezat Mountains, Southern Carpathians, constrained by ^{10}Be exposure ages and pedological investigations. *Quaternary International*, 164, 151-169.